# Improved Tools for Point-of-Care Nucleic Acid Amplification Testing

Thesis by

Erik Bradley Jue

In Partial Fulfillment of the Requirements for the Degree of

Doctor of Philosophy


CALIFORNIA INSTITUTE OF TECHNOLOGY

Pasadena, California

2020

(Defended May 18th, 2020)

Erik Bradley Jue
ORCID: 0000-0001-7585-3794

# ACKNOWLEDGMENTS

This work was only made possible by the numerous people who have helped and supported me. I express my sincere gratitude to those listed below and many others not mentioned explicitly.

**I thank my scientific advisor and research mentor**:

Dr. Rustem Ismagilov – I thank you for accepting me into the lab and for training me to become a scientifically rigorous researcher. Throughout my Ph.D., you have challenged me to solve difficult real-world problems and to make meaningful impact with my work. You have given me multiple opportunities to demonstrate leadership in my projects, and through these experiences I have seen myself grow as an independent researcher. In your lab, I developed a broad set of skills including grant writing, project planning, project execution, data analysis, figure generation, scientific writing, inventory management, and working directly with companies/consultants. I appreciate that not everyone has had the same opportunities or resources throughout their Ph.D. research. Though a challenging and arduous journey, it is through these trials that you have mentored and trained me to become a better version of myself. I thank you for your guidance and scientific expertise. I further appreciate you for your flexibility, adaptability, and understanding in challenging situations. You always think carefully when confronted with new problems, and have an openness to hearing different frames of view. I sincerely appreciate you as a mentor, and recognize that the experiences I have had here will positively influence me for years to come.

**I thank my thesis committee members:**

I thank all of my thesis committee members for their time, wisdom, and guidance.

Dr. Murray – I thank you for your advice, mentoring, and foresight. I appreciate your suggestions which have helped shape my project and thesis planning.

Dr. Shapiro – I thank you for taking me in as a rotation student and for your support throughout the years. You always ask thoughtful questions and push me to think more carefully about my research.

Dr. Yang – I thank you for always having your door open for me. I appreciate your words of wisdom, guidance, and understanding throughout my doctoral studies.

**I thank our lab's Scientific Research Group Manager and Administrative Assistant:**

Natasha Shelby – Writing alone cannot express how influential you have been in and throughout my Ph.D. It is likely that each chapter of this thesis has been improved in some way through your work. You help the lab to run smoothly, and you are constantly looking for ways to make the lab environment operate even better. Last but not least, you have been a great friend throughout my Ph.D. studies.

Sohee Lee – I thank you all of your help, from scheduling professors to processing rebates to spending reports. You really do a lot to make the lab run smoothly!

**I thank the administrative staff that has enabled this work:**

I thank building and maintenance staff including janitorial services, waste management, electricians, HVAC technicians, and others not mentioned for allowing my work to proceed safely and smoothly.

Joe Drew, Armando Villasenor, and Greg Rolette – This work would not be possible without properly functioning facilities and great processes for shipping and receiving given the sheer number of packages that our lab orders. I thank you for solving any and all building problems which allows our work to proceed smoothly.

John Van Deusen – Thank you for training me on all of the machining equipment in the Jim Hall Design and Prototyping Lab. This equipment has granted us new capabilities such as machining heating blocks using the waterjet that have been critical to my projects.

Dr. Nate Siladke – Thank you for ensuring our lab stays safe!

Dr. Lauriane Queenee – Thank you for ensuring our lab stays safe with regards to biosafety, and for your quick responses on all emails!

**I thank my Ismagilov Lab colleagues, co-authors, and contributors on projects:**

Dr. Justin Rolando – It is impossible for me to express all of my appreciation for you in a single paragraph. You took me in under your wing (insert airplane joke) as a rotation student, and I have always looked up to you as a mentor. You are the first person I look to for a myriad of issues in the lab (chemistry, vacuum gauges, chemical safety, etc.). Collaborations with you have been easy, quick, and fun owing to your hard work, dedication, and great sense of humor. I admire your positive attitude, unrelenting work ethic, and of course – your lab pranks which bring joy to our hearts. Last but not least, I appreciate you as a friend who has been there with me since the very beginning of my Ph.D. Though our future paths may separate, I know the bond we formed will last a lifetime.

Dr. Daan Witters – Working with you was truly a pleasure. You have always been a rigorous scientist, dedicated to your work, a strong communicator, and extremely responsible which made collaborating with you easy. I am proud to call you a friend and appreciate the many hours we've spent together in and out of the lab.

Dr. Nathan Schoepp – You have always been professional and strive to improve the lab, from initiating chemical inventory to ensuring lab equipment is properly managed. I thank you for this, and for being generous with your time and expertise in biochemistry and molecular diagnostics. I further thank you for your detailed documentation and carefully managed inventories of primers and NA extracts. Though this may seem a bit trivial because documentation is "part of your job", I mean this as a sincere compliment because I am not certain your level of rigor could have been replicated by anyone else. It is this extreme care and attention to detail that has enabled my work.

Dr. Dmitriy Zhukov – I thank you for taking me in and training me during my first year of research. I learned many of my lab techniques (AutoCAD, device fabrication, pumping lid, etc.) under your mentorship and guidance. I enjoyed working on the pumping lid C-clamp and the micromachined washer for SlipChip projects with you. You have been a constant presence throughout my Ph.D., and you have been a great friend.

Dr. Stefano Begolo – I thank you for passing on your knowledge for the autonomous device project. Although our overlap was short, I especially value the advice I received from you. Yours insights have been deeply appreciated and helpful throughout the years.

Dr. Jesus Rodriguez-Manzano – I thank you for training me on biochemistry and passing on your knowledge for the autonomous device project. I also learned a lot about figure-generation with Adobe Illustrator from you.

Dr. Si Hyung Jin – I thank you for being such a generous, intelligent, and responsible colleague and collaborator. You have learned a lot within the last few months, and I am excited to see how your progress and publications. I thank you for taking the lead on many of these grants and for pushing projects forward. I also appreciate that you always wear a smile and bring such a strong positive energy to the lab.

Roberta Poceviciute – I thank for you putting up with me as your desk neighbor for many years. I appreciate you for your advice and for helping me think through challenging situations. Your perspectives have helped me to grow as a researcher. I thank you for the many years of friendship.

Dr. Said Bogartyrev – You have been a strong foundation of support throughout my Ph.D., and a wonderful friend throughout the years. You are the first person I consult when I need to work something out, or when I just need to take a break from labwork. Thanks buddy.

**I thank the biosafety team:**

Dr. Eugenia Khorosheva, Emily Savela, and Mary Arrastia – We have been through many hours of training, IBCs, IRBs, and back-and-forth biosafety emails. I thank you for your countless hours and attention to detail, which have allowed me to feel safe while working with biohazardous pathogens.

**I thank other members of the lab**:

Dr. Liang Ma, Dr. David Selck, Dr. Travis Schlappi, Matthew Curtis, Dr. Asher Preska-Steinberg, Dr. Tahmineh Khazaei, Dr. Octavio Mondragon-Palomino, Dr. Joanne Lau, Jacob Barlow, Michael Porter, Eric Liaw, Alex Winnett, Matt Cooper, Anna Romano, and Sarah Simon.

**I thank my mentees who have contributed greatly to my projects**:

Sasha Alabugin, Kana Moriyama, Eric Chen, Yu Kim, Pedro Ojeda, Ashay Gore, Andrew Friedman, Duncan Chadly, Selina Zhou, and Kevin Winzey

**I thank my parents for raising me, supporting me, and shaping me into who I have become today:**

Lawrence Jue – The way that you lead by example and care for the people in your life inspires me to be a better person. I know that you are always there to solve any problem I might have, and I thank you being there for me every step of the way.

Jan Jue – I thank you for being an endless source of love and care. You are always encouraging me to chase after my goals, and you are supportive of all of my endeavors, regardless of how ridiculous or crazy they might be. I know that I can always talk to you about my problems and that you'll have goodies for me whenever I visit home.

**I thank my sisters and brother:**

Lauren Gee, Brian Gee, Michelle Jue, and Kianna Jue – You have been a solid pillar of support throughout my life, and I thank all of you for your love, care, and encouragement throughout the many years.

**I thank my large and incredibly loving extended family:**

A sincere thank you to each and every one of you, for having believed, encouraged, and supported me from the very beginning.

**I thank the many friends who have supported me along the way**:

Samuel Clamons, Andrey Shur, Kevin Cherry, Colin Mitchell, Eric Kao, Christopher Lim, Gordon Oh, Jonathan Gavino, John Pang, Val Kung, Steven Bailon, Taylor Manners, Alex Barrick, Shela Ma, Crystal Shen, Elaine Wu, Elaine Tam, Jonathan Liu, Loko Kung, Jerry Feng, Lillian Tong, Mitchell Lee, Oliver Pei, Dr. Daniel Kamei, Dr. Ricky Chiu, Dr. Garrett Mosley, Dr. Kristine Maylee, Johnny Wang, Cameron Yamanishi, Bob Lamm, Stephanie Wang, Allison Yip, Phuong Nguyen, Samantha Cheng, and Alison Thach.

**I acknowledge that this work would not have been possible without the grants and fellowships that have funded my research:**

Rose Hills Fellowship, NSF Graduate Research Fellowship, NIH Training Grant Program, Caltech Innovation Initiative, DARPA-LRS (HR0011-11-2-0006), DTRA (MCDC-18-01-01-007), and the Burroughs Wellcome Fund Innovation in Regulatory Science (1014981).

# ABSTRACT

There is a critical need for improved diagnostic tools to detect infectious diseases, especially in low-resource regions. A sample-to-answer point-of-care nucleic acid amplification test (NAAT) would be incredibly valuable for many different applications (e.g. COVID-19, Chlamydia/Gonorrhoeae, Influenza, Ebola, Zika/Chikungunya/Dengue, etc.). However, sample preparation (purification of pure nucleic acids) is a challenging bottleneck. In Chapter 2, commercial NA extraction methods were studied and improved. In Chapter 3, commercial stocks of SARS-CoV-2 RNA used in FDA emergency-use authorizations were found to be inaccurate and were independently quantified using reverse transcription digital PCR. In Chapter 4, a 3D printed meter-mix device was developed for initial processing prior to the sample preparation device. In Chapter 5, a 3D printed sample-to-device interface was prototyped to facilitate loading multi-volume SlipChip devices with purified template mixed with LAMP reactants. In Chapters 6-7, advancements were made for image processing of commercial chips to study digital LAMP reactions. In Chapter 8, additional tools were developed towards sample-to-answer point-of-care NAAT including a sample preparation module, amplification module, cell-phone readout, and automated base station.

# PUBLISHED CONTENT AND CONTRIBUTIONS

**E. Jue, D. Witters, and R.F. Ismagilov. 2020. "Two-phase wash to solve the ubiquitous contaminant-carryover problem in commercial nucleic-acid extraction kits"** ***Scientific Reports*****. 10(1940). doi:10.1038/s41598-020-58586-3**

EJ acquired funding. Planned and analyzed buffer dilution experiments for **Figure 2.2**. Planned, ran, and analyzed all remaining experiments. Generated all figures and wrote the manuscript.

DW Ran preliminary experiments evaluating the use of TPW to reduce buffer carryover.

**E. Jue, N.G. Schoepp, D. Witters, and R.F. Ismagilov. 2016. "Evaluating 3D printing to solve the sample-to-device interface for LRS and POC diagnostics: example of an interlock meter-mix device for metering and lysing clinical urine samples"** ***Lab on a Chip*****. 16:1852-1860. doi:10.1039/c6lc00292g**

EJ contributed to the invention, design, and validation of the meter-mix device. This includes the invention and design of the plunger system (chambers, plungers, valves, stoppers), invention and design of the multivalve and interlock system, design of the sealing mechanisms, design of the static mixer, and the design of the urine suction tube. EJ validated device function, user operation, device assembly, urine suction tube anti-drip feature, accurate metering and dispensing, mixer efficacy, and compatibility with qPCR.

NS contributed to the invention of the multivalve and interlock system as well as testing of the meter-mix device using biological samples, including development and validation of polymerase chain reaction (PCR) and loop-mediated isothermal amplification (LAMP) assays for the detection of Ct and Ng. All device validation and control experiments extracting urine spiked with either Ct or Ng prior to mixing with the device were performed by NS. Amplification of extracted nucleic acids using either PCR or LAMP was performed by NS, including data analysis.

DW contributed to the initial invention and design of the meter-mix device as well as the writing, editing, and finalization of both the outline and manuscript.

***J. Rodriguez-Manzano,*M.A. Karymov, S. Begolo, D.A. Selck, D.V. Zhukov, E. Jue, and R.F. Ismagilov. 2016 "Reading Out Single-Molecule Digital RNA and DNA Isothermal Amplification in Nanoliter Volumes with Unmodified Camera Phones"** ***ACS NANO*****. 10(3):3102-3113. doi:10.1021/acsnano.5b07338**

*These authors contributed equally

JRM developed the idea, designed experiments, and prepared the manuscript. Took the lead for TOC, **Figure 5.1-4**, **Figure 5.7-9**, **Figure 5.14**, and **Table 5-1**. Shared responsibility for **Figure 5.6**. Developed idea for enhanced constrast by image processing and predicting RGB ratiometric signal output based on transmittance spectra. Involved in writing ImageJ macro for image processing.

MAK developed idea, designed experiments, and helped prepare the manuscript. Took the lead for **Figure 5.6** and **Figure 5.12**. Shared responsibility for **Figure 5.4** and **Figure 5.5**. Wrote ImageJ macro for image processing and automatic counting

SB developed the idea and designed experiments. Shared responsibility for **Figure 5.1-3**. Developed the idea of enhancing contrast between positive and negative reaction by image processing. Wrote imageJ macro for image processing.

DAS took the lead for **Figure 5.13** and shared responsiblitiy for **Figure 5.2** and **Figure 5.5**. Helped with fluorescent images for **Figure 5.4** and **Figure 5.6**. Developed idea of enhancing constrast between positive and negative reaction by image processing. Developed idea for predicting RGB ratiometric signal output based on trasmittance spectra.

DZ took the lead for **Figure 5.10-11, Figure 5.15-16**. Designed, optimized, and fabricated rotational multivolume SlipChip device for **Figure 5.4-5**. Designed and fabricated the two-step SlipChip device for **Figure 5.6**. Helped JRM for multivolume experiments.

EJ designed and tested C-clamp interface for the pumping lid. Used the C-clamp pumping lid to help load the multivolume device for a handful of experiments until JRM was trained. Designed and fabricated multivolume device with insertable washer features to aid slipping. Multivolume device with washer was used for TOC, **Figure 5.4-5**.

**J.C. Rolando, E. Jue, N.G. Schoepp, and R.F. Ismagilov. 2018. "Real-time, digital LAMP with commercial microfluidic chips reveals the interplay of efficiency, speed, and background amplification as a function of reaction temperature and time"** ***Analytical Chemistry*****. 91(1):1034–1042. doi:10.1021/acs.analchem.8b04324**

JCR conceptualized the method, generated and analyzed data. Wrote the paper, constructed figures, and performed all revisions.

EJ wrote the MATLAB software script for automated analysis of digital LAMP image sequences. Provided minor input to experimental design; and minor edits and inputs to the figures and manuscript.

NGS prepared and quantified nucleic acid stocks. Optimized buffer conditions for Bst 2.0. Provided minor input to experimental design and minor edits and inputs to the figures and manuscript.

**J.C. Rolando, E. Jue, J. Barlow, and R.F. Ismagilov. 2020. "Real-time kinetics and high-resolution melt curves in single-molecule digital LAMP to differentiate and study specific and nonspecific amplification"** ***Nucleic Acids Research*****. 48(7):42. doi:10.1093/nar/gkaa099**

EJ wrote the MATLAB software script for automated analysis of digital LAMP image sequences.

# TABLE OF CONTENTS

# LIST OF ILLUSTRATIONS AND/OR TABLES

*Number* *Page*

*Chapter 1*

# OVERVIEW

## Background

The global burden of communicable disease has been estimated at 3.2 billion DALYs (disability-adjusted life years) per year for 2017.[1] Notable examples of communicable disease include ongoing pandemics COVID-19[2] and HIV/AIDS;[3] recent outbreaks of 2014-2016 Ebola,[4] 2015-2016 Zika virus,[5] and 2009-2010 H1N1 Influenza;[6] and ongoing challenges including respiratory diseases (Tuberculosis, Pertussis, Measles, etc.), diarrheal diseases (Rotavirus, E. coli, Norovirus, etc.), mosquito-borne pathogens (West Nile Virus, Dengue, Chikungunya, Malaria, etc.), and sexually transmitted infections (Chlamydia, Gonorrhoeaea, Syphilis, etc.).

The appropriate treatment and containment of communicable diseases requires timely and effective diagnostics to identify the causative pathogen. A strong screening response enables pandemic tracking, quarantining of individuals, guidance of appropriate treatments, contact tracing, public policy advising, and proper resource allocation. Because pandemics do not discriminate by international borders, an effective containment approach necessitates testing on a global scale. However, current infrastructure and supplies are lacking for such wide-scale testing capabilities, even in the most well-equipped countries.

Diagnosing pathogens is not an effortless endeavor. Communicable diseases take many forms such as bacterial, viral, parasitic, and fungal infections. Furthermore, pathogens can be located in different sample matrices such as water, food, respiratory droplets, urine, blood, saliva, sputum, stool, and more. An ideal diagnostic platform would have the flexibility to detect different pathogens in different types of sample matrices. Furthermore, routes of transmission also vary by pathogen and include direct contact, indirect contact, respiratory droplets, food contamination, insect bites, and sexual transmission. Because an unknown sample could contain an unknown pathogen (different than the pathogen being tested for)

with an unknown route of transmission, all human-derived samples should be handled with care (e.g. minimum BSL-2). While some pathogens can be easily diagnosed by clinical presentation, many pathogens cannot be detected without diagnostics.[7] This occurs when clinical presentations are shared among diseases, there is a high asymptomatic rate, or there exists a long incubation period.

Accessibility is also a critical factor to consider when evaluating the effectiveness of a diagnostic tool. The 2013-2016 Ebola Virus outbreak demonstrated the vital role of diagnostics for confirming cases, monitoring disease progression, and resource allocation planning. Notably, long transport times (several days) and the lack of rapid diagnostics in both resource-rich and resource-limited settings contributed to the initial failure to contain the outbreak.[8]

In considering the requirements for global-scale testing, the ideal test would be applicable at the point-of-care (POC, at the site of sample collection) and in limited-resource settings (LRS). Globally distributed testing imposes stringent requirements on diagnostics devices that can be summarized by the ASSURED criteria published by the World Health Organization.[9] The ASSURED criteria stands for affordable, sensitive, specific, user-friendly, rapid, robust, equipment-free, and deliverable. It is worth taking some time to elaborate on each requirement.

Considering the global nature of pandemics, affordability is required to enable wide-scale testing, especially in the most vulnerable populations. The cost of a test must be weighed against the benefits, and is typically measured by disability-adjusted life years, or DALYs, avoided.[10] The advantages of an on-site POC diagnosis include reduced required infrastructure, laboratory workload, and turn-around-time. Overall, the patient experiences improved quality of care. However, cost comparison of POC tests to centralized laboratory testing is a controversial issue. Perspectives vary among patients, insurance companies, laboratory employees, and hospital employees.[11] While labor costs and the cost per test are quantifiable values, improvements in quality of care are more difficult to assess. Considering

the tricky cost landscape, it is prudent for diagnostic developers to weigh the cost of a new POC test against its clinical benefit.

The combined properties of sensitivity and specificity refer to the accuracy of the test. It is clear that test accuracy is the benchmark feature of a diagnostic test; and yet, a number of diagnostic tests have been developed and sold with poor accuracy.[12-14] While no test will be 100% accurate, it is important to strive for high sensitivity and high specificity from the beginning of diagnostic assay design. Generally, a test with over 90% sensitivity and 90% specificity has good diagnostic performance, but the utility of a test also depends on the specific application, prevalence of the pathogen, and rate of testing.

The ideal POC test would be user-friendly, equipment-free, and deliverable – an example of an ideal POC test (though not designed for disease detection) is the pregnancy test. The pregnancy test can be performed in the comfort of one's home by an untrained user provided with a simple page of instruction. In contrast, many gold-standard diagnostic tests require a trained user working in a temperature-controlled laboratory with access to expensive equipment.[15-17] However, much of the developing world does not have access to centralized lab testing. Even in developed countries, during times of high diagnostic demand such as a global pandemic, centralized lab facilities cannot meet testing demands. In the recent COVID-19 pandemic, we have observed long shipping times, lack of trained personnel to process samples, and a shortage of diagnostic testing supplies.[18] This has resulted in both a shortage of testing and long time-to-results for patients that are tested.

The ideal POC test should also be robust. This is especially important for globally distributed diagnostics because reagents must withstand longer shelf-times, various temperature conditions, and operation by untrained users. If the POC test is not sufficiently robust, the accuracy and utility of the test would suffer.

Lastly, the ideal POC should be rapid. This is an important requirement for on-site testing. For example, it is highly preferably for a doctor's office or mobile clinic to test patients within the timespan of their visit. If this were the case, the health provider could prescribe

the appropriate treatment and consult the patient during the visitation (rather than in a follow-up call). The shorter the test, the more likely it is that patients will wait, the less space is required for waiting rooms, and the more tests can be processed for any given amount of time.

In addition to the ASSURED criteria, we have learned that it is important for tests to be highly parallelizable. In recent years, tests have been developed with turn-around time as fast as 45 min,[19] but throughput (and associated costs) is still a concern since only one specimen can be tested at a time.

For disease diagnostics, there are three commonly employed test strategies: (1) cell culture, (2) protein-based testing (lateral-flow immune assay or enzyme-linked immunosorbent assay, LFA or ELISA), and (3) nucleic acid amplification testing (NAAT).

Cell culture is one of the earliest developed methods of testing, and involves growing the target pathogen and diagnosing the pathogen using some other method (visually, microscopy, ELISA, NAAT). However, cell culture requires long incubation times of many hours (rapid systems are still 8 h) which is not suitable or testing at the POC.[15]

There are two common implementations of protein-based testing: the enzyme-linked immunosorbent assay (ELISA) and the lateral-flow immunoassay (LFA). Both of these methods rely on antibodies which bind to the target antigen or protein of interest. Usually these antigens are peptides displayed on the surface of the pathogen or antibodies developed by the host (serology testing). A common concern for protein-based testing is non-specific protein adsorption or off-target binding, which leads to low specificity of the assay.[20,21] For ELISA specifically, assay times are long, and there are many user steps making ELISA unsuitable for POC testing.[22,23] Meanwhile, the LFA, which is commonly utilized in the off-the-shelf pregnancy test is ideally suited for POC testing, but lacks the sensitivity required for many diagnostic applications.[24-28]

NAAT is perhaps the most powerful of these three approaches, with its relatively short time-to-result, high sensitivity, and high specificity. For many pathogens, NAAT is the preferred gold-standard testing method. There are 3 components to a NAAT: (1) nucleic acid extraction, (2) nucleic acid amplification, and (3) readout. First, nucleic acids (NAs) are purified and concentrated from the patient sample to eliminate inhibitors present in the sample matrix. Secondly, the purified nucleic acids (NAs) are amplified, typically using polymerase chain reaction (PCR), to generate billions of DNA copies. This approach works by using conserved primer sequences that are specific to the pathogen of interest. Therefore, if the pathogen is present, many DNA copies will be generated. Lastly, the amplified NAs can be detected in a number of ways such as fluorescence or visual readout.

While NAAT excels with its high sensitivity and specificity, NAAT does not meet any of the remaining POC requirements (requires highly trained users in centralized labs with expensive and bulky equipment). In recent years, research labs have made developments towards POC NAAT.[29-33] The diagnostics industry has also been developing integrated POC NAAT assays, the two most POC-amenable being the Cepheid GeneXpert system and the Abbott ID Now.[19] Nevertheless, more improvements can still be made to ensure fulfillment of all the ASSURED criteria.

**Outline**

In this doctoral thesis, I document my contributions towards improved POC NAAT.

In Chapter 2, I identify extraction buffer carry-over in commercial NA extraction kits as a major culprit for inhibition in downstream NA amplification.[34,35] I address this concern with the addition of a two-phase wash (TPW) which acts to reduce carry-over. By improving sample preparation purification, this enables the use of greater volumes of purified eluent, thereby improving sensitivity and limit-of-detection of downstream tests.

In Chapter 3, I identify a problem with the titer reported for commercial stocks when examining the analytical sensitivity of the CDC-recommend RT-qPCR protocol for diagnosing SARS-nCoV-2. I used an ultrasensitive and precise assay, reverse transcription digital PCR (RT-dPCR), to independently quantify the concentrations of commercial nucleic acid stocks. This work has broader implications because one of the commercial stocks was genomic RNA from BEI and measured 270% and 300% compared to the label concentration. This stock has been used in at least 11 approved FDA Emergency Use Authorizations as of April 27, 2020. The precise and accurate reporting of stock concentrations is necessary to improve the evaluation of different NAAT kits.

In Chapters 4 and 5, I develop tools for solving the sample-to-answer interface problem. While much of the published literature has focused on individual components (NA extraction, NA amplification, or readout), relatively less work has been shown towards the integration of these components. I designed and developed a meter-mix device (Chapter 4) which addresses urine sample transfer to a NA extraction device while simultaneously lysing the sample (thereby simplifying the NA extraction).[36,37] I also designed a 3D printed C-clamp (Chapter 5) which facilitated sample loading into glass microfluidic devices for nucleic acid amplification.[38,39]

In Chapter 6 and 7, I developed MATLAB image processing scripts to automatically analyze images of a digital nucleic acid amplification tracked over time. Each experiment set contained 20,000 wells and 100s of images. The first script (Chapter 6) analyzed images with a single fluorescent channel,[40] and the second script (Chapter 7) utilized dual-channel fluorescence to enable melt-curve analysis.[41]

Lastly, in Chapter 8, I describe additional tools developed for integrated sample-to-answer NAAT diagnostics.[42] In particular, I developed a parallel-filled amplification module for conducting lyophilized and multiplexed loop-mediated isothermal amplification reactions (LAMP). I designed and developed an automated base station featuring Arduino-controlled motor rotation and a heating element to automatically operate a nucleic acid extraction device and nucleic acid amplification device. Lastly, I showed a cell-phone modified for

fluorescence readout and automated MATLAB image analysis for readout of the parallel-filled amplification module.

**References**


1. Roser, M. & Ritchie, H. Burden of disease. *Our World In Data* (2016).

2. Organization, W. H. WHO Director-General's opening remarks at the media briefing on COVID-19-11 March 2020. *Geneva, Switzerland* (2020).

3. Cohen, M. S., Hellmann, N., Levy, J. A., DeCock, K. & Lange, J. The spread, treatment, and prevention of HIV-1: evolution of a global pandemic. *The Journal of clinical investigation* **118**, 1244-1254 (2008).

4. Control, C. f. D. & Prevention. 2014-2016 Ebola outbreak in west Africa. *Centers Dis Control Prev* (2016).

5. Organization, W. H. WHO Director-General summarizes the outcome of the Emergency Committee regarding clusters of microcephaly and Guillain-Barré syndrome. February 1, 2016. *Available from:.[Last accessed on 2016 Feb 14]* (2016).

6. Organization, W. H. Pandemic H1N1 2009. (WHO Regional Office for South-East Asia, 2009).

7. Washington, J. A. Principles of diagnosis. *Medical microbiology* **4**, 134-143 (1996).

8. Shorten, R. J. *et al.* Diagnostics in Ebola virus disease in resource-rich and resource-limited settings. *PLoS neglected tropical diseases* **10** (2016).

9. Kosack, C. S., Page, A.-L. & Klatser, P. R. A guide to aid the selection of diagnostic tests. *Bulletin of the World Health Organization* **95**, 639 (2017).

10. Chin, C. D., Linder, V. & Sia, S. K. Commercialization of microfluidic point-of-care diagnostic devices. *Lab on a Chip* **12**, 2118-2134 (2012).

11. Hortin, G. L. Does point-of-care testing save money or cost more? *Laboratory Medicine* **36**, 465-467 (2005).

12. Brook, G. The performance of non-NAAT point-of-care (POC) tests and rapid NAAT tests for chlamydia and gonorrhoea infections. An assessment of currently available assays. *Sexually transmitted infections* **91**, 539-544 (2015).

13. Khuroo, M. S., Khuroo, N. S. & Khuroo, M. S. Diagnostic accuracy of point-of-care tests for hepatitis C virus infection: a systematic review and meta-analysis. *PloS one* **10**, e0121450 (2015).

14. Dheda, K., Ruhwald, M., Theron, G., Peter, J. & Yam, W. C. Point-of-care diagnosis of tuberculosis: Past, present and future. *Respirology* **18**, 217-232 (2013).

15. Yager, P., Domingo, G. J. & Gerdes, J. Point-of-care diagnostics for global health. *Annual review of biomedical engineering* **10** (2008).

16. Peeling, R. W., Holmes, K. K., Mabey, D. & Ronald, A. Rapid tests for sexually transmitted infections (STIs): the way forward. *Sexually transmitted infections* **82**, v1-v6 (2006).

17. Niemz, A., Ferguson, T. M. & Boyle, D. S. Point-of-care nucleic acid testing for infectious diseases. *Trends in biotechnology* **29**, 240-250 (2011).

18. Ward, D. *Sampling Bias: Explaining Wide Variations in COVID-19 Case Fatality Rates*. (2020).

19. Vashist, S. K. *In Vitro Diagnostic Assays for COVID-19: Recent Advances and Emerging Trends*. (2020).

20. Güven, E. *et al.* Non-specific binding in solid phase immunoassays for autoantibodies correlates with inflammation markers. *Journal of immunological methods* **403**, 26-36 (2014).

21. Farajollahi, M. M., Cook, D. B., Hamzehlou, S. & Self, C. H. Reduction of non-specific binding in immunoassays requiring long incubations. *Scandinavian journal of clinical and laboratory investigation* **72**, 531-539 (2012).

22. Liu, D. *et al.* A fully integrated distance readout ELISA-Chip for point-of-care testing with sample-in-answer-out capability. *Biosensors and Bioelectronics* **96**, 332-338 (2017).

23. Thiha, A. & Ibrahim, F. A colorimetric enzyme-linked immunosorbent assay (ELISA) detection platform for a point-of-care dengue detection system on a lab-on-compact-disc. *Sensors* **15**, 11431-11441 (2015).

24. Fu, X. *et al.* A SERS-based lateral flow assay biosensor for highly sensitive detection of HIV-1 DNA. *Biosensors and Bioelectronics* **78**, 530-537 (2016).

25. Tang, R. *et al.* Improved sensitivity of lateral flow assay using paper-based sample concentration technique. *Talanta* **152**, 269-276 (2016).

26. Jue, E., Yamanishi, C. D., Chiu, R. Y., Wu, B. M. & Kamei, D. T. Using an aqueous two-phase polymer-salt system to rapidly concentrate viruses for improving the detection limit of the lateral-flow immunoassay. *Biotechnology and bioengineering* **111**, 2499-2507 (2014).

27. Chiu, R. Y. *et al.* Simultaneous concentration and detection of biomarkers on paper. *Lab on a Chip* **14**, 3021-3028 (2014).

28. Fu, E. *et al.* Enhanced sensitivity of lateral flow tests using a two-dimensional paper network format. *Analytical chemistry* **83**, 7941-7946 (2011).

29. Song, J. *et al.* Instrument-free point-of-care molecular detection of Zika virus. *Analytical chemistry* **88**, 7289-7294 (2016).

30. Stumpf, F. *et al.* LabDisk with complete reagent prestorage for sample-to-answer nucleic acid based detection of respiratory pathogens verified with influenza A H3N2 virus. *Lab on a Chip* **16**, 199-207 (2016).

31. Rodriguez, N. M., Wong, W. S., Liu, L., Dewar, R. & Klapperich, C. M. A fully integrated paperfluidic molecular diagnostic chip for the extraction, amplification, and detection of nucleic acids from clinical samples. *Lab on a Chip* **16**, 753-763 (2016).

32. Lafleur, L. K. *et al.* A rapid, instrument-free, sample-to-result nucleic acid amplification test. *Lab on a Chip* **16**, 3777-3787 (2016).

33. Shin, D. *et al.* Mobile nucleic acid amplification testing (mobiNAAT) for Chlamydia trachomatis screening in hospital emergency department settings. *Scientific reports* **7**, 1-10 (2017).

34. Jue, E., Witters, D. & Ismagilov, R. F. Two-phase wash to solve the ubiquitous contaminant-carryover problem in commercial nucleic-acid extraction kits. *Scientific reports* **10**, 1-16 (2020).

35. Ismagilov, R. F., Witters, D. & Jue, E. Methods and systems and related compositions for mixtures separation with a solid matrix.

36. Jue, E., Schoepp, N. G., Witters, D. & Ismagilov, R. F. Evaluating 3D printing to solve the sample-to-device interface for LRS and POC diagnostics: example of an

interlock meter-mix device for metering and lysing clinical urine samples. *Lab on a Chip* **16**, 1852-1860 (2016).

37. Ismagilov, R. F., Jue, E. & Schoepp, N. G. Devices and methods for preparing biological samples.

38. Rodriguez-Manzano, J. *et al.* Reading out single-molecule digital RNA and DNA isothermal amplification in nanoliter volumes with unmodified camera phones. *ACS nano* **10**, 3102-3113 (2016).

39. Ismagilov, R. F. *et al.* Devices and methods for direct visual detection and readout of single nucleic acid molecules.

40. Rolando, J. C., Jue, E., Schoepp, N. G. & Ismagilov, R. F. Real-Time, Digital LAMP with Commercial Microfluidic Chips Reveals the Interplay of Efficiency, Speed, and Background Amplification as a Function of Reaction Temperature and Time. *Analytical chemistry* **91**, 1034-1042 (2018).

41. Rolando, J. C., Jue, E., Barlow, J. T. & Ismagilov, R. F. Real-time kinetics and high-resolution melt curves in single-molecule digital LAMP to differentiate and study specific and non-specific amplification. *Nucleic Acids Research* **48**, e42-e42 (2020).

42. Ismagilov, R. F., Witters, D. & Jue, E. Purification and detection of analytes.

*Chapter 2*

# TWO-PHASE WASH TO SOLVE THE UBIQUITOUS CONTAMINANT-CARRYOVER PROBLEM IN COMMERCIAL NUCLEIC-ACID EXTRACTION KITS

E. Jue, D. Witters, and R.F. Ismagilov. 2020. *Scientific Reports*. 10(1940). doi:10.1038/s41598-020-58586-3

**Abstract**

The success of fundamental and applied nucleic acid (NA) research depends on NA purity, but obtaining pure NAs from raw, unprocessed samples is challenging. Purification using solid-phase NA extractions utilizes sequential additions of lysis and wash buffers followed by elution. The resulting eluent contains NAs and carryover of extraction buffers. Typically, these inhibitory buffers are heavily diluted by the reaction mix (e.g., 10x dilution is 1 µL eluent in 9 µL reaction mix), but in applications requiring high sensitivity (e.g., single-cell sequencing, pathogen diagnostics) it is desirable to use low dilutions (e.g., 2x) to maximize NA concentration. Here, we demonstrate pervasive carryover of inhibitory buffers into eluent when several commercial sample-preparation kits are used following manufacturer protocols. At low eluent dilution (2-2.5x) we observed significant reaction inhibition of polymerase chain reaction (PCR), loop-mediated isothermal amplification (LAMP), and reverse transcription (RT). We developed a two-phase wash (TPW) method by adding a wash buffer with low water solubility prior to the elution step. The TPW reduces carryover of extraction buffers, phase-separates from the eluent, and does not reduce NA yield (measured by digital PCR). We validated the TPW for silica columns and magnetic beads by

demonstrating significant improvements in performance and reproducibility of qPCR, LAMP, and RT reactions.

## Introduction

Polymerase chain reaction (PCR) is a widely used tool in molecular biology for generating many nucleic acid (NA) copies from a starting DNA template. PCR may also be combined with reverse transcription (RT) to amplify many DNA copies from a starting RNA template. The amplified NAs then serve different purposes, such as detection, quantification, library preparation for sequencing, or generating constructs for cloning [1,2]. NA amplification is crucial in highly sensitive applications (few DNA copies) such as single-cells analyses or the detection of SNPs, cell-free circulating DNA, or pathogens [3-5]. Isothermal amplifications are an attractive alternative to PCR that eliminate the stringent temperature cycling requirements [6]. Specifically, loop-mediated isothermal amplification (LAMP) is faster than PCR and is especially promising for diagnostic devices in point-of-care settings [7,8]. PCR, RT, and LAMP typically require purified NAs as a starting template; however, extracting purified NAs from raw, unprocessed samples is challenging [9]. Though commonly overlooked, the efficient and effective extraction of pure NAs is of paramount importance [10].

A primary function of NA extractions is to eliminate inhibitors. If inhibitors are transferred into the eluent, they can delay or completely inactivate downstream applications such as PCR and LAMP [11,12]. Inhibitors have also been implicated in failed RT, molecular cloning, and sequencing experiments [13-15]. We anticipate two potential sources of inhibitors: (1) those present in the raw, unprocessed sample and (2) those introduced during the NA extraction [16]. There have been numerous studies demonstrating the adverse effects of inhibitors in challenging sample matrices, such as humic acids, food particles, cellular debris, urine, blood, and stool [11,12,17-25]. To remove these inhibitors, solid-phase extractions are an effective choice because they have been found to yield higher purity compared with other extraction methods [19,20,26-29]. The two most common solid-phase extraction methods use either spin

columns or magnetic beads [28,30]. In both methods, the sample is first mixed with a lysis/binding buffer, the lysed sample contacts the solid phase allowing NAs to bind, the solid phase is cleansed with one or more wash buffers, and the NAs are eluted with water. Typically, the lysis/binding buffer contains a chaotropic salt (e.g., guanidinium isothiocyanate) whereas the wash buffer contains a high concentration of ethanol (or isopropanol). Any carryover of these extraction buffers (lysis buffer or wash buffer) into the eluent could be greatly inhibitory to downstream analyses.

The purified eluent contains NAs and any carried-over extraction buffers at their highest concentration. To run a downstream reaction, a volume of eluent is mixed with a volume of reaction mix. For research applications, it is standard to dilute the eluent 10x (e.g., 1 µL eluent and 9 µL reaction mix) [31,32], 25x (e.g., 1 µL eluent and 24 µL reaction mix) [33], or more [34,35]. At these high eluent dilutions, concentrations of inhibitors present in the eluent are reduced and thus their potential negative effects on the reaction are mitigated. However, the dilution of inhibitors equally dilutes the NAs, which may be detrimental when the original sample has low NA concentrations [3] and/or when high sensitivity is desired. For example, single nucleotide polymorphisms [5], cell-free circulating DNA [4], and single-cell analyses all require maximizing the concentration of NA loaded into the amplification mix. Maximizing NA concentration is also important for infectious disease diagnostics and monitoring the water supply, food supply, and environment [32,36-38]. For these applications, a higher NA concentration could be achieved with a lower dilution (e.g., a 2.5x dilution would be 4 µL eluent and 6 µL reaction mix). The theoretical maximum NA concentration could be attained by eliminating the dilution altogether, which is only possible by adding eluent directly to a dried reaction mix (e.g., 10 µL eluent and dry reaction mix to make ~10 µL reaction). This can be achieved with lyophilization, wherein reagents are freeze-dried to a powder, or other approaches for generating dry reaction mixes. The use of dry reagents has additional benefits: simple assay protocols, lenient reagent-storage conditions, and long reagent shelf-life, all of which are desirable characteristics for the development of point-of-care devices. However, in using low dilutions or no dilution, extraction buffers in the eluent are used at higher concentrations, which may have adverse effects on downstream reactions.

Few studies have directly investigated inhibition resulting from solid-phase extraction kit buffers [39,40]. In this manuscript, we aimed to quantify and reduce inhibition arising from buffer carryover in commercial extraction kits from well-known suppliers. We first identified that kit buffer carryover is indeed a concern when using low eluent dilutions (≤2.5x) for both commercial silica-column and magnetic-bead extractions (following manufacturer protocols). To improve our understanding of inhibition, we performed a detailed study using a range of buffer dilutions from different extraction kits. To address the carryover of kit buffers, we developed modified extraction protocols utilizing an additional two-phase wash (TPW) that would integrate easily with the existing manufacturer protocols [41]. The TPW is a compound with low water solubility, can be added in between the wash and elution steps, and phase-separates with water after the elution step. We identified an optimized set of TPW candidates among several potential compounds and then evaluated TPW performance by testing kit protocols from leading manufacturers (Zymo and Qiagen) at both low and high eluent dilutions. To unambiguously show that inhibition is due to kit buffer inhibitors, as opposed to sample inhibitors or losses of NAs, we performed extractions on pure water samples with or without the TPW, and added the resulting kit extract to spiked qPCR, LAMP, and RT assays.

## Materials and Methods

### *NA Stocks and Primers*

Lambda (λ) phage DNA (linear double-stranded 500 µg/mL, N3011L, New England Biolabs (NEB)) was purchased from NEB and the stock was quantified at $1.1x10^{10}$ cp/µL using digital PCR (dPCR). *Escherichia coli* DNA was extracted from an NEB 5-alpha strain using Epicentre QuickExtract DNA Extraction Buffer (Lucigen Corporation,Middleton, WI, USA), and the stock was quantified at $1.4 \times 10^7$ cp/µL using dPCR. *Neisseria gonorrhoeae* live infectious stock (Z017, Zeptometrix, Buffalo, NY, USA) was resuspended to $5 \times 10^7$ cfu/mL in pre-warmed (37 °C) Hardy Diagnostics FB Broth (K31, Hardy Diagnostics, Santa

Maria, CA, USA) and diluted an additional 10-fold in urine to 5 x $10^6$ cfu/mL. Urine from healthy human donors (>18 years of age) was acquired and used in accordance with approved Caltech Institutional Review Board (IRB) protocol 15-0566. Informed consent was obtained from all participants. Urine sample donations were never tied to personal identifiers, and all research was performed in accordance with the approved IRB protocol and relevant institutional biosafety regulations. Urine samples were stored at room temperature and used within 1 h of collection. Spiked urine (125 µL) was mixed with DNA/RNA Shield (125 µL) and lysis buffer (500 µL) for a total lysed sample volume of 750 µL. Both DNA and RNA were extracted simultaneously with a ZR Viral DNA/RNA Kit, and *N. gonorrhoeae* 16S RNA was found to be in over 200-fold excess of 16S DNA as verified by dPCR with or without an RT step. All NA stocks were diluted at least 100-fold into all reactions, thereby eliminating the effects of any inhibitors that could be present in the NA stock. Lambda LAMP primers [42], Lambda PCR primers [43], *E. coli* 23S rRNA gene LAMP primers [44], *E. coli* 23S rRNA gene PCR primers [45], and *N. gonorrhoeae* 16S rRNA gene PCR primers [46] have been previously published and were supplied by Integrated DNA Technologies using standard desalting purification.

*Kit Extractions*

We tested three different silica-column kits: Zymo ZR Viral DNA/RNA Kit (outdated protocol, D7021), Zymo Quick-DNA/RNA Kit (updated protocol, D7021), and the QIAquick PCR Purification Kit (28104, Qiagen). For all silica-column kits, fresh collection tubes were used after each spin, and centrifugation speeds were set to 16,000xg. Centrifugation was performed on either an Eppendorf 5415D centrifuge (Eppendorf, Hauppauge, NY, USA) or a Thermo Fisher Scientific AccuSpin Micro 17R centrifuge (13-100-676). We note that the QIAquick protocol calls for 17,900xg, but we instead ran at 16,000xg which was the max speed for the Eppendorf 5415D. For both Zymo kits, 750 µL lysed sample was prepared by mixing 125 µL sample with 125 µL Zymo 2x DNA/RNA Shield and 500 µL Viral DNA/RNA Buffer. For the Zymo ZR Viral DNA/RNA kit, 750 µL

lysed sample was centrifuged for 1 min, 500 µL Zymo Viral Wash Buffer was centrifuged for 2 min, and 50 µL nuclease-free water was centrifuged for 30 s into a clean 1.5 mL tube. Optionally, either a dry spin or 300 µL TPW was centrifuged for 2 min in between the Viral Wash Buffer and elution steps. For the Zymo Quick-Viral DNA/RNA kit, 750 µL lysed sample was centrifuged for 1 min, 500 µL Zymo Viral Wash Buffer was centrifuged for 30s, an additional 500 µL Zymo Viral Wash Buffer was centrifuged for 30s, 500 µL 200 proof ethanol was centrifuged for 1 min, and 50 µL nuclease-free water was centrifuged for 30 s into a clean 1.5 mL tube. Optionally, either a dry spin or 300 µL TPW was centrifuged for 1 min in between the ethanol and elution steps. For the QIAquick PCR Purification Kit, 125 µL sample was mixed with 625 µL Buffer PB without indicator. 750 µL lysed sample was centrifuged for 30s, followed by 750 µL Buffer PE for 30s, a dry spin for 1 min, and 50 µL nuclease-free water for 1 min. Optionally, the dry spin was skipped or the dry spin was replaced with a 300 µL TPW and centrifuged for 1 min.

We tested the Zymo Quick-DNA/RNA Viral MagBead (R2140). For the Zymo MagBead kit, 200 µL sample was mixed with 200 µL Zymo 2x DNA/RNA Shield, 4 µL Proteinase K, and 800 µL Zymo Viral DNA/RNA Buffer. 1204 µL was added to each tube, mixed with 20 µL MagBinding Beads, and placed on an UltraRocker Rocking Platform (1660709EDU, Bio-Rad, Hercules, CA, USA) for 10 min at max speed. Tubes were transferred to a DynaMag-2 magnetic rack (12321D, Thermo Fisher Scientific) and we followed manufacturer instructions for the remainder of the protocol. Optionally, the 10 min dry step was skipped or the dry step was instead replaced with the addition of 500 µL TPW. In the modified protocol for the Zymo MagBead kit, we waited at least one additional minute and performed a second aspiration after each aspiration step in the manufacturer's protocol.

*qPCR Mix*

qPCR reactions contained 1X Bio-Rad SsoFast Supermix (1725201, Bio-Rad), PCR primers (IDT) at 0.5 µM each, and were supplemented with nuclease-free water up to 10 µL. Each

96-well plate (thin-wall clear well, HSP9641, Bio-Rad) was sealed (Microseal B, MSB1001, Bio-Rad) and briefly spun in a Mini Plate Spinner Centrifuge (14-100-141, Fisher Scientific). Heating and real-time imaging were performed on the Bio-Rad CFX-96 Touch Real-Time PCR Detection System by heating to 95 °C for 5 min, cycling 40 times between 95 °C for 15 s, 60 °C for 15s, and 72 °C for 20s, and taking a melt-curve analysis. For the *E. coli* DNA dilution experiment, qPCR was run for 60 cycles. Fluorescence readings were taken at the end of each extension step. Quantification cycle ($C_q$) was determined when the software's automated baseline corrected fluorescence reached 200 RFU.

*LAMP Mix*

LAMP reactions contained the following concentrations of reagents: 1X Isothermal Amplification Buffer (20 mM Tris-HCl pH 8.8, 10 mM $(NH_4)_2SO_4$, 50 mM KCl, 5 mM $MgSO_4$, 0.1% Tween-20, B0537S, NEB, Ipswich, MA, USA), an additional 2 mM $MgSO_4$ (B1003S, NEB), 1.4 mM deoxynucleotide mix (N0447L or N0446S, NEB), 2 µM Invitrogen Syto-9 (S34854, Thermo Fisher Scientific), 2 µM Invitrogen bovine serum albumin (15561020, Thermo Fisher Scientific), 320 U/mL WarmStart Bst 2.0 (M0538L, NEB), and were supplemented with nuclease-free water (not DEPC-Treated, 4387936, Thermo Fisher Scientific) up to 10 µL. LAMP primers (Integrated DNA Technologies (IDT), Coralville, IA, USA) were designed, ordered, and added at NEB's recommended concentrations of 1.6 µM FIP/BIP, 0.2µM F3/B3, and 0.4 µM LoopF/B. Each 96-well plate was sealed and briefly spun. Heating and real-time imaging were performed on the Bio-Rad CFX-96 Touch Real-Time PCR Detection System (1855195, Bio-Rad). Each 96-well plate was cooled to 12 °C for 2 min, held at 68 °C for 47 min with 35-second fluorescence read intervals, and we performed a melt-curve analysis. For the *E. coli* DNA dilution experiment, the 68 °C step was held for 105 min. Time-to-positive (TTP) was determined when the software's automated baseline corrected fluorescence reached 1000 RFU.

*Buffer Inhibition*

For studying kit buffer inhibitors, LAMP and qPCR reactions were spiked to 5 x $10^4$ cp/rxn λ phage DNA (NEB) and supplemented with half-log dilutions of either Koptec 200-proof ethanol (V1001, Decon Labs, King of Prussia, PA, USA), Viral RNA Wash Buffer 1X (R1034-2-48, Zymo Research, Tustin, CA, USA), Buffer PE (19065, Qiagen, Germantown, MD, USA), Zymo DNA/RNA Shield 1X (R1200-125), Zymo Viral DNA/RNA Buffer (D7020-1-100), or Qiagen Buffer PB (19066) to the appropriate final concentration. For selecting the optimal TPW, LAMP and qPCR reactions were spiked with 1 µL of 5 x $10^4$ cp/µL λ phage DNA, diluted to 10 µL, and an additional 1 µL was added of either nuclease-free water, 200 proof ethanol, isopropanol (BP2618-500, Thermo Fisher Scientific, Waltham, MA, USA), 1-butanol (3000-04, Mallinckrodt Chemicals), isopentanol (2992-04, Mallinckrodt Chemicals), 1-hexanol (H13303-100mL, MilliporeSigma, St. Louis, MO, USA), 1-heptanol (H2805-250mL, MilliporeSigma), 1-octanol (SHBH2844V, MilliporeSigma), 1-nonanol (131210-100mL, MilliporeSigma), 1-decanol (2397563-50g, MilliporeSigma), 1-undecanol (MKCG3271, MilliporeSigma), 2-dodecanol (D221503-5G, MilliporeSigma), 5 cSt silicone oil (317667-250mL, MilliporeSigma), or Fluorinert FC-40 (ZF-0002-1308-0, 3M, St. Paul, MN, USA).

*dPCR Mix*

Droplet digital PCR (dPCR) experiments were performed on a Bio-Rad QX200 Droplet Digital PCR System (1864001, Bio-Rad). dPCR mixes were made with 1X QX200 dPCR EvaGreen Supermix (1864034, Bio-Rad), 200 nM forward primer, and 200 nM reverse primer. Eluent was diluted 10x in separate tubes and an additional 10x into the reaction mix. All samples were made to 50 µL and duplicates were run by adding 22 µL to two sample wells in the DG8 Cartridge for droplet generator (1864008, Bio-Rad). Droplet generation, droplet transfer, and foil sealing followed the manufacturer's instructions. Thermocycling took place on a C1000 Touch Thermal Cycler (Bio-Rad) with a pre-melt at 95 °C for 3 min,

40 cycles of 95 °C for 30s, 60 °C for 30s, and 68 °C for 30s, and a stabilization at 4 °C for 5 min, 90 °C for 5 min, and a hold at 12 °C until droplet analysis. A temperature ramp rate of 2C/s was used for temperature transitions. Droplets were read according to the manufacturer's instructions. Analysis thresholds were manually set at the valley between negative and positive droplets. Final concentrations were determined using the merge setting on the QuantaSoft analysis software. No template controls (NTC) were always run and showed negligible normalized counts (<0.1%).

*RT Mix*

The RT reaction contained 1X Isothermal Amplification Buffer, 0.5 mM dNTP Mix, 0.2 µM primers, 1U/µL Riboguard RNase Inhibitor (RG90910K, Lucigen, Middleton, WI, USA), and 0.15 U/µL WarmStart Rtx (M0380L, NEB). The extracted *N. Gonorrhoeae* RNA was diluted 10x in a separate tube and an additional 10x by adding 2.5 µL into the 25 µL reaction mix (100x dilution total). Kit extracts were spiked in the reaction mix by adding either 2.5 µL (10x) or 12.5 µL (2x). We added water to a total reaction volume of 25 µL. Temperature was set to anneal for 5 min at 25 °C, incubate for 10 min at 55 °C, and inactivate for 10 min at 80 °C in a C1000 Touch Thermal Cycler (1851196, Bio-Rad).

**Results and Discussion**

*Establishing the presence and prevalence of inhibitors in buffers*

We first carefully designed an experiment to evaluate the presence, prevalence, and effects of buffer carryover when using standard commercial NA extraction kits. To eliminate the confounding effects of NAs or inhibitors originating from the sample, we performed NA extractions on pure water samples (**Figure 2.9**). When extracting from pure water samples, we refer to the eluent as the "kit extract," which only contains water and inhibitors originating

from buffers in the extraction kits. Here, we tested a centrifugation-based NA extraction using a Zymo ZR Viral DNA/RNA Kit and followed the manufacturer's protocol. Next, we mixed the kit extract into a qPCR reaction spiked with $\lambda$ phage DNA at either a 10x dilution (1 µL kit extract, 0.5 µL template DNA, 5.5 µL reaction mix) or 2.5x dilution (4 µL kit extract, 0.5 µL template, 5.5 µL reaction mix). We used heavily diluted purified $\lambda$ phage DNA to ensure no inhibition originated from the template. The 10x and 2.5x dilution reactions contained different volumes of kit extract, but each had a final volume of 10 µL and contained the same concentration of $\lambda$ phage template, $\lambda$ phage primers, and qPCR components. We ran qPCR on a thermocycler for 40 cycles while taking readings at the end of each cycle. If the kit extracts have no inhibitory effect, we would expect the same quantification cycle ($C_q$) for both reactions. Given the amount of input DNA ($5 \times 10^4$ copies), we expect amplification to occur at ~20 cycles.

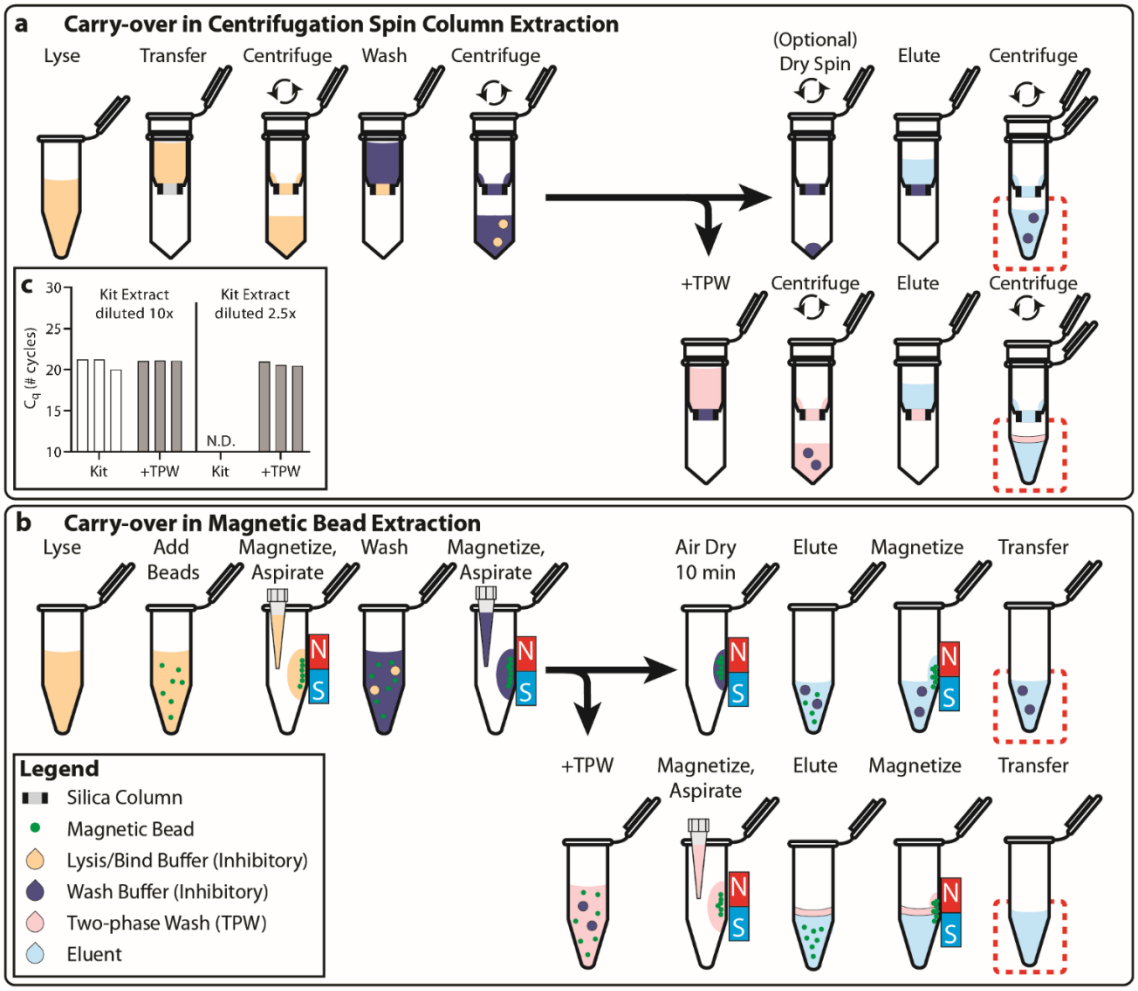


**Figure 2.1: Schematic depicting the carryover of buffers during sample preparation when nucleic acids (NA) are extracted using either (a) spin column centrifugation or (b) magnetic beads.**

Dashed red boxes highlight carryover of buffer into the eluent. Carryover buffer from the previous wash either mixes with the eluent (top dashed box in each panel) or phase separates (bottom dashed box in each panel) when the two-phase wash (TPW) is used. (c) Inset graph shows a qPCR run spiked with 5 x 104 copies λ phage DNA and λ phage primers into which we added Zymo ZR "kit extract." (When extracting from pure water samples, we refer to the eluent as the "kit extract," which only contains water and inhibitors originating from buffers in the extraction kits.) The graph compares the reaction inhibition in a 10x extract dilution and a 2.5x extract

dilution and shows the effect of adding a TPW (+TPW) during the nucleic-acid extraction step. Inhibition is similarly observed for magnetic bead extraction kits. N.D. stands for not detected. We ran 6 extractions (3 silica columns x 2 conditions) and used the same kit extract to make the high- and low-dilution conditions.

Using the centrifugation sample-preparation protocol (**Figure 2.1a**) and a 2.5x dilution of kit extract, amplification in qPCR was completely inhibited (**Figure 2.1c**). In contrast, using the 10x dilution, all three kit extracts (three separate columns) amplified at ~20 cycles as expected. The only variable that differed between the two conditions was that the 2.5x dilution (4 µL kit extract) contained four times the concentration of buffer compared with the 10x dilution (1 µL kit extract). This result led us to conclude that carryover of inhibitory buffers is inhibiting the qPCR reaction.

We suspect that carryover results from residual buffer trapped in the column that is picked up during elution. Although centrifugation moves most of the extraction buffers to the waste tube for removal, some lysis/binding buffer and/or wash buffers may remain stuck in the column after each centrifugation step (**Figure 2.1a**). This could occur due to physical entrapment, surface tension, or physicochemical interactions with either the silica column or the walls of the tube. Furthermore, it is possible for some of the inhibitory components contained in the buffer to become unevenly trapped on the column. During the elution step, water could mix with these trapped buffers/inhibitors and carry them into the final eluent. We emphasize that for a standard elution volume of 50 µL water, even low volumes of carryover may correspond to a sufficiently inhibitory percentage of buffer in the eluent. For example, 500 nL buffer carryover corresponds to 1% buffer in the eluent and 2.5 µL corresponds to 5% buffer in the eluent.

Buffer carryover also occurred when using magnetic-bead extraction. In these protocols, magnetic beads that bind to NAs in the appropriate buffer conditions are added to the sample. Extraction buffers are then added (lysis and multiple washes) by sequential rounds of buffer addition, magnetization to pull the magnetic beads to the side of the tube, and aspiration of

each buffer. (**Figure 2.1b**). For the elution step, water is added which releases the NAs from the magnetic beads, the magnetic beads are drawn to the sides of the tube, and the eluent is transferred to a clean tube. During this process, however, some buffer components may stick to the magnetic beads or adhere to the walls of the tube. Thus, although most of the buffers are removed during aspiration, a low concentration of extraction buffers transfer into the eluent when using the standard manufacturer protocols. Below (section "TPW validation for magnetic-bead extractions"), we explicitly examine the extent of buffer carryover for magnetic-bead extractions using low and high dilutions of eluent.

We hypothesized that we could address the issue of extraction buffer carryover in commercial NA extraction kits by the addition of a TPW. The TPW is composed of an immiscible compound that phase separates with water, and we added it in between the wash step and the final elution (**Figure 2.1a bottom, Figure 2.1b bottom**). Our aim was to develop a TPW that would be simple, inexpensive, and that would integrate easily with existing protocols. If successful, the TPW would greatly reduce buffer carryover and improve downstream assay performance. In our study (**Figure 2.1c**), incorporating the TPW recovered qPCR (2.5x dilution of kit extract) and provided the expected Cq of ~20 cycles. This was a drastic performance improvement compared with the complete reaction inhibition we observed when the same dilution was run using the manufacturer protocol.

*Exploring the effects of buffer inhibition on amplification*

Having established that buffer carryover is a problem, we next aimed to better understand the effects of inhibition on amplification in qPCR and LAMP. We selected extraction buffers from a Zymo viral DNA/RNA kit and a Qiagen PCR purification kit. We chose these two commercial kits in particular because they both utilize minimal protocols (lysis, wash, elute) with no added steps (e.g. bacterial pellet spins, proteinase K, lysozyme, DNase/RNase, filtration, etc.). Specifically, we wanted to identify the concentration at which each buffer inhibits qPCR and LAMP. First, we added buffers at half-log dilutions (from 10% down to

0.032%) into $\lambda$ phage spiked qPCR or LAMP reactions (1 µL diluted buffer, 1 µL template, 8 µL reaction mix). We were also curious to see whether qPCR and LAMP were affected differently by inhibitors. We expected differences between the two amplification methods because qPCR amplification is temperature-gated, whereas LAMP amplifies continuously. Previous literature on this topic shows "mixed results;" many studies have shown that LAMP is more robust than PCR in the presence of inhibitors, [47-50] whereas others have shown that inhibition of PCR and LAMP depends on which inhibitor was used [40].

We found that all extraction buffers were inhibitory to both types of reactions, but at different concentrations (**Figure 2.2**). As a control, for each kit, we ran the protocol with 0% buffer and found amplification with qPCR to yield a $C_q$ of ~20.0 ± 0.3 cycles and amplification with LAMP to have a TTP of 7.1 ± 0.6 min. As a general trend, we found that wash buffers (ethanol, Zymo Viral Wash Buffer, and Qiagen Buffer PE; **Figure 2.2a-c,g-l**) were less inhibitory than lysis buffers (Zymo DNA/RNA Shield, Zymo DNA/RNA Viral Buffer, and Qiagen Buffer PB; **Figure 2.2d-f,j-l**). For qPCR, we observed a statistically significant ($P < 0.05$) $C_q$ delay of at least 0.5 cycles for wash buffer concentrations starting at 10% (**Figure 2.2a-c, Table 2-1**) and for lysis buffers starting between 0.32 – 1% (**Figure 2.2d-f, Table 2-2**). For LAMP, we observed a statistically significant ($P < 0.05$) TTP delay of at least 0.5 min for wash buffer concentrations starting at 1–3.2% (**Figure 2.2g-i, Table 2-3**) and for lysis buffers starting at 0.32–3.2% (**Figure 2.2j-l, Table 2-4**). These results imply that the extent of inhibition on qPCR and LAMP reactions is inhibitor-dependent, which may help explain the "mixed results" in the literature.

Next, we observed the presence of inhibitors at very low concentrations using melting temperature (Tm), as compared with $C_q$, TTP, or endpoint fluorescence (**Figure 2.10-13**). Interestingly, we observed that the presence of extraction buffers raised or lowered the Tm of the DNA product even at very low concentrations (1% - 3.2% for ethanol buffers, 0.32% - 1% for lysis buffers). Detecting a change in the Tm of an NA product could be a useful tool for diagnosing the presence or absence of extraction buffers in a reaction.

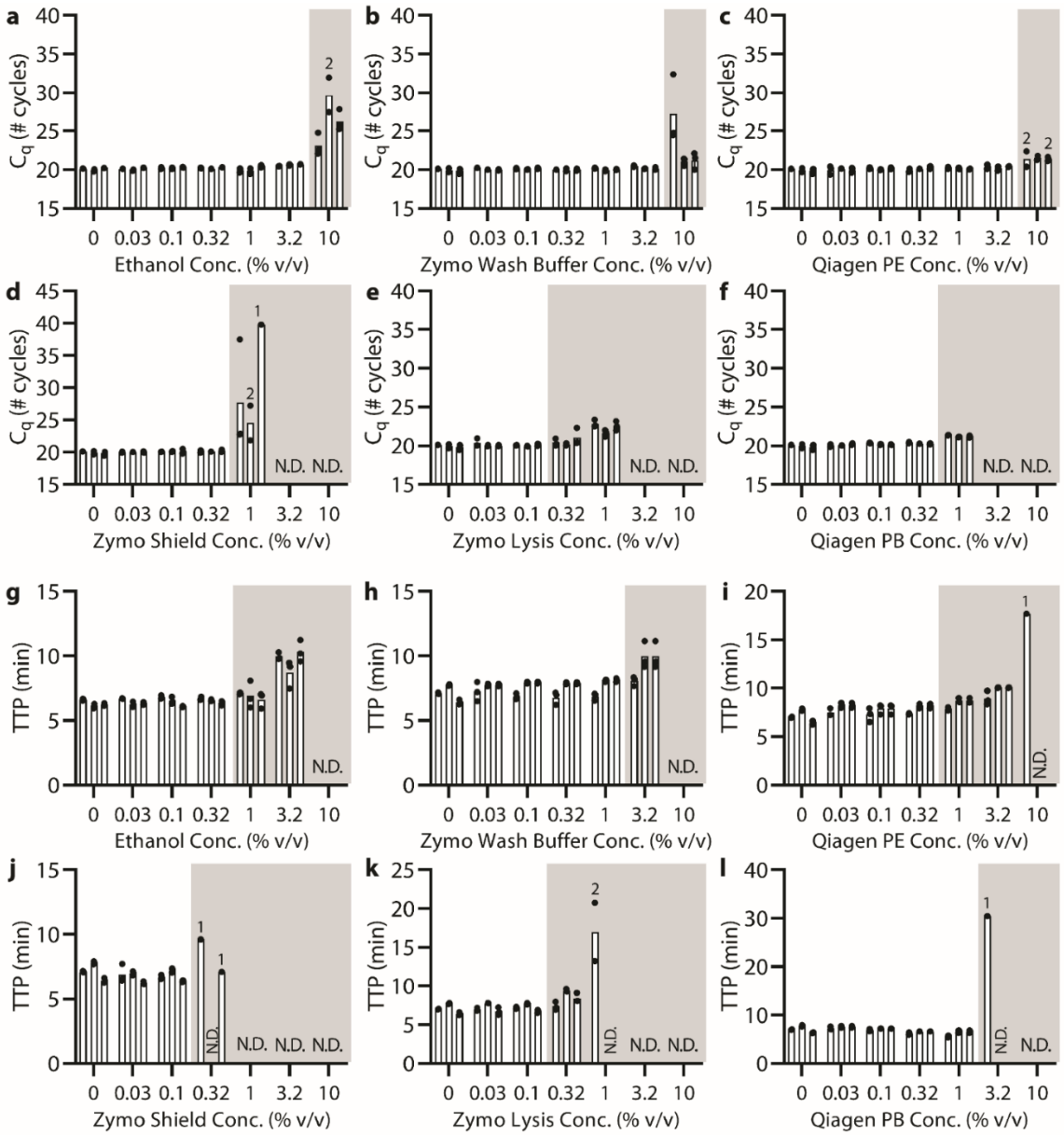


**Figure 2.2: (a-f) qPCR and (g-l) LAMP experiments demonstrate reaction inhibition from NA extraction kit buffers.**

Quantification cycles ($C_q$) for qPCR or time to positive (TTP) for LAMP spiked with $5 \times 10^4$ copies λ phage DNA and primers with increasing concentrations of extraction kit buffers. For ethanol dilutions (a,g), three separate amplification mixes were each combined with an independent ethanol dilution series. All remaining buffer dilutions (b-f, h-l) shared the same set of three amplification mixes (same 0% condition), and

each amplification mix was combined with an independent dilution series of each buffer. Each bar is the average of qPCR or LAMP technical triplicates (black circles). Where shown, numbers above a bar indicate the number of samples that amplified out of technical triplicates. Gray shading indicates when inhibition (>0.5 cycles or >0.5 min) was observed according to changes in $C_q$ or TTP. Samples marked N.D. were not detected within either 40 cycles or 40 min.

*Inhibition in samples with low NA concentrations*

We next wished to test the effects of buffer-related inhibition in samples containing low NA concentrations. For applications requiring high sensitivity (e.g., single-cell sequencing, cell-free circulating DNA, SNP genotyping, and diagnostics), amplification reactions are often run at or near the limit-of-detection (LOD). Samples starting with low NA concentrations thus require the polymerase to replicate more DNA than in samples that start with a high NA concentration. Therefore, we hypothesized that the inhibition effect resulting from buffer carryover would be stronger for these low NA samples (and detected as delayed $C_q$ or TTP). Additionally, it has been recorded that PCR reactions with different primers and targets can respond differentially to inhibitors [11]. To ensure the inhibitory effects we saw with $\lambda$ phage DNA were not specific to just the set of DNA and primers we used, we ran this experiment using *Escherichia coli* DNA and *E. coli* primers.

With qPCR, we found that the cycle delay as a result of buffer inhibitors was higher at lower NA concentrations (**Figure 2.3a,b**). We started with a medium concentration of target (5 x $10^4$ *E. coli* 23S copies) and tested 4-fold dilutions down to 0.05 copies with either control (no inhibition) or in the presence of 1% Zymo Viral DNA/RNA Buffer. We chose 1% lysis buffer because we had found 1% lysis buffer to be weakly inhibitory, and we suspected inhibition may worsen with decreasing DNA concentration.

Our control reactions matched our expectations; we found 5 x $10^4$ copies yielded a $C_q$ of 19.55 ± 0.04, the cycle increased by ~2 for every 4-fold dilution, and we detected the target

down to 3 copies. Compared with the 1% lysis buffer condition, we found that the reaction for the highest concentration (5 x $10^4$ copies) was greatly impaired by 4.65 ± 0.13 (95% CI: 4.33 – 4.97) cycles (**Figure 2.3b**). The delay worsened and variance increased as the NA concentration was decreased. At 3 copies/rxn, there was an 8.45 ± 0.94 (95% CI: 6.11 – 10.79) cycle delay and all three triplicates amplified, but we needed to increase the number of cycles in this experiment in order to detect the delayed $C_q$. Our results showed that the presence of lysis buffer caused a decrease in the amplification efficiency with each cycle. This conclusion was also supported by the shallower amplification curves (**Figure 2.15**).

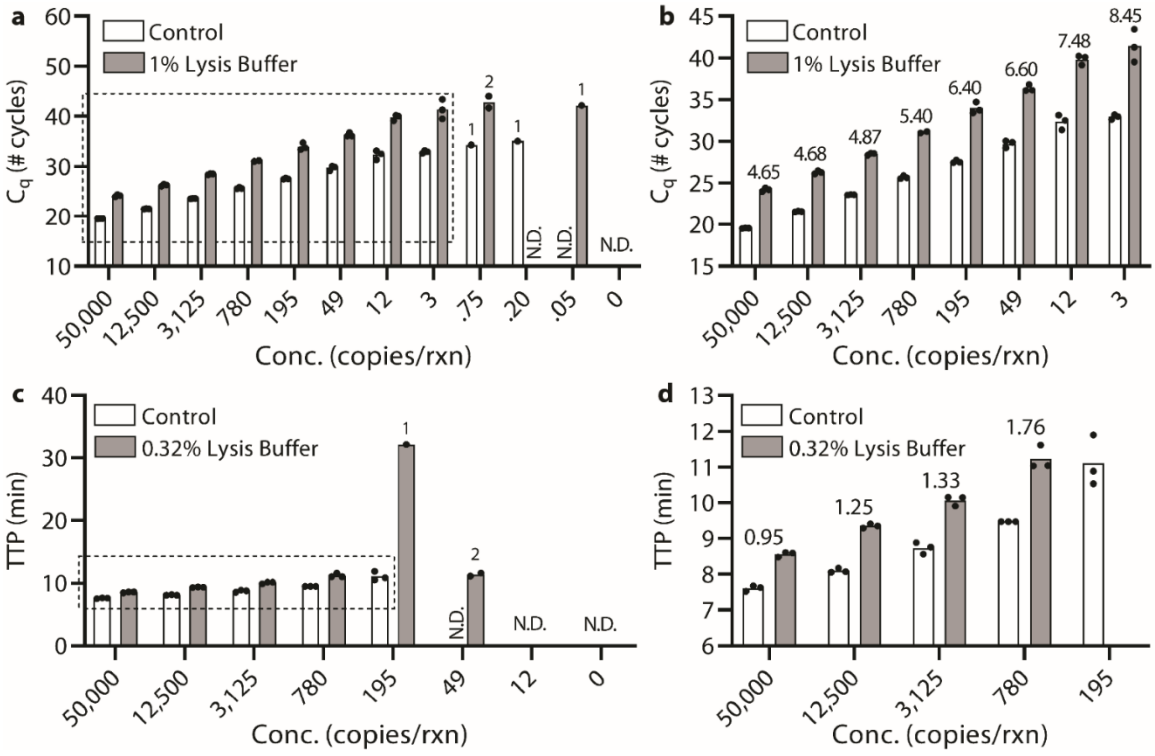


**Figure 2.3: (a-b) qPCR and (c-d) LAMP experiments targeting *E. coli* 23S rRNA gene, which shows increased impact of reaction inhibition at low NA concentrations.**

(a) qPCR and (c) LAMP spiked with 4-fold dilution series of *E. coli* 23S rRNA gene copies and comparing with and without Zymo Viral DNA/RNA Buffer. Each bar

represents the average of technical qPCR or LAMP triplicates (black circles). Numbers above a bar indicate the number of samples which amplified if not all triplicates were detected. Dashed boxes indicate axes for zoomed-in graphs of (b) qPCR and (d) LAMP. Numbers above each pair of bars indicate the difference in either $C_q$ or TTP between the control and the reaction with added lysis buffer. Samples marked N.D. were not detected within either 60 cycles or 40 min.

With LAMP, we also found that the delay as a result of buffer inhibitors was higher at lower NA concentrations (**Figure 2.3c,d**). Because LAMP was more sensitive to inhibitors than qPCR, we compared the control to 0.32% lysis buffer. The control reaction TTP was 7.61 ± 0.08 min at 5 x $10^4$ copies and the TTP increased with increasing dilutions up to 11.1 ± 0.7 min at 195 copies. LAMP failed to amplify at higher concentrations of DNA than when using qPCR (amplification for 3 or fewer copies was stochastic). The addition of 0.32% lysis buffer caused a 0.95 ± 0.06 (95% CI: 0.80 – 1.10) min delay in TTP at the highest concentration (5 x $10^4$ copies/rxn), which increased as the *E. coli* DNA concentration was lowered to a 1.76 ± 0.19 (95% CI: 1.29 – 2.23) min delay at the lowest detectable concentration (780 copies/rxn). At lower concentrations, amplification was stochastic. LAMP was unable to detect down to 195 copies/rxn in the presence of lysis buffer, indicating a loss in analytical sensitivity that was not observed with qPCR. Another difference between LAMP and qPCR is that although the LAMP TTP was delayed, the amplification rate and endpoint fluorescence in LAMP were not strongly affected (**Figure 2.15**).

*Identifying a suitable TPW*

Next, we identified a suitable wash buffer that would reduce the carryover of extraction buffer and integrate easily into existing protocols. The ideal wash buffer would be added after the final ethanol wash but prior to the elution and it would have the following properties: (1a) it would be non-inhibitory or (1b) it would not transfer to downstream assays such as

qPCR or LAMP, (2) it would remove previous washes from the column by an appropriate combination of solid-liquid and liquid-liquid interfacial properties and solubility of inhibitory components, and (3) it would not prematurely elute NAs from the column. We directly investigated criterion 1a by performing qPCR and LAMP reactions. We spiked reactions with $\lambda$ phage DNA, diluted up to 10 µL, and we added an additional 1 µL of different wash buffer candidates to a total of 11 µL. As additional wash candidates, we tested increasing chain lengths of primary alcohols (or secondary alcohols if the primary form was unavailable), 5 centistokes (cSt) silicone oil, and FC-40 fluorocarbon oil (**Figure 2.4a,b**). As an experimental control, we tested a "No Additive" condition, which was a 10 µL reaction with optimized reaction conditions and no inhibitors. To control for the effects of a 1 µL dilution on the reaction, we also tested a "Water" condition which was an 11 µL reaction with no inhibitors.

The "No Additive" control case showed a qPCR $C_q$ of 20.09 ± 0.01 cycles (95% CI: 20.07 – 20.12) and a LAMP TTP of 6.54 ± 0.05 min (95% CI: 6.42 – 6.66). We note that 1 µL in 11 µL is a large fraction of the reaction mix (~9%), so we are overestimating buffer carry-over concentrations compared to normal operating conditions. The "Water" control showed no delay for qPCR and a 0.55 min delay for LAMP due to the dilution of LAMP reactants. For both qPCR and LAMP reactions, we found that long-chain alcohols with ≥ 9 chain lengths, silicone oil, and FC-40 were non-inhibitory for qPCR (within 1 cycle) and LAMP (within 1 min) compared to the "No Additive" condition (**Figure 2.4a,b**). Octanol showed delays for qPCR (3.54 cycle difference) and LAMP (4.63 min difference), and only 2 out of 3 replicates amplified for qPCR. All alcohols with ≤ 8 chain lengths either had delayed amplification or the reaction was completely inhibited. Because long-chain alcohols, silicone oil, and FC-40 showed little to no inhibition of qPCR and LAMP, these candidates fulfilled criterion 1a.

These non-inhibitory wash candidates (long-chain alcohols, silicone oil, and FC-40), which we refer to as TPW, have low solubility in water (**Table 2-7**) and resulted in phase separation (**Table 2-8**). The TPW separates to either the top phase or the bottom phase (density dependent) while interacting minimally with the aqueous solution. As a result of reduced

interactions with the aqueous solution, the TPW is less toxic to downstream reactions. In LAMP reactions with added alcohols (**Figure 2.4b**), we also noticed that the TTP delay decreased as the solubility decreased (from 1-octanol to 2-dodecanol). The 1-octanol had the greatest delay (without completely inhibiting the reaction). We suspect that although 1-octanol mostly occupied its own phase, some 1-octanol dissolved in the aqueous phase and disrupted polymerase activity. Furthermore, we also noticed that the TTP for the very low solubility TPWs matched the "No Additive" condition rather than the "Water" condition, implying the reaction mix was not diluted by the 1 µL of added TPW.

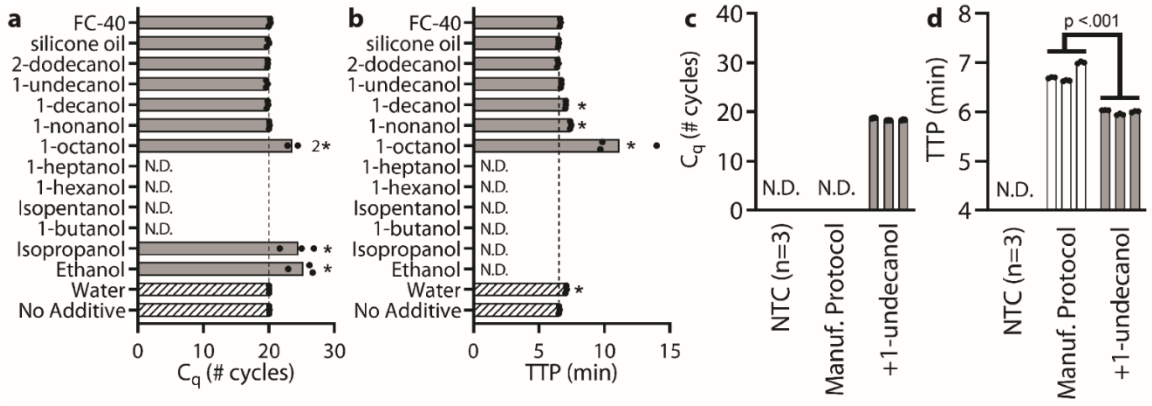


**Figure 2.4: Identifying the most effective TPW in (a) qPCR and (b) LAMP reactions and subsequent validation of 1-undecanol as a candidate TPW with (c) qPCR and (d) LAMP at low eluent dilutions.**

TPW candidates for (a) qPCR and (b) LAMP reactions were spiked with 5 x $10^4$ copies λ phage DNA and primers, made to 10 µL, and 1 µL of each wash candidate was added to yield 11 µL total. The number 2 next to the 1-octanol bar indicates that only two of the three replicates amplified. The dashed lines show the $C_q$ or TTP of the uninhibited 10 µL "No Additive" control. (c) qPCR with 2.2x diluted eluent and (d) LAMP with 2x diluted eluent on a λ phage DNA sample extracted with a Zymo Quick-Viral DNA/RNA kit. Protocol was performed according to manufacturer instructions as provided or with an additional TPW (+1-undecanol) between the

ethanol wash and elution steps. Each bar represents the average of technical triplicates (black circles). We ran 6 extractions (3 silica columns x 2 conditions) and used the same eluent for both the qPCR and LAMP analyses. Samples marked N.D. were not detected within either 40 cycles or 40 min. NTC, no-template control. (a,b) We asked whether TPW candidates fell within the 99% CI of the "No Additive" control (qPCR: 20.01-20.17, LAMP: 6.25-6.83) with outliers indicated with a *. (d) We asked whether the average TTP was statistically different between the manufacturer protocol and the +1-undecanol condition using a t-test.

Next, we evaluated criterion 1b (ensuring that the TPW does not transfer to qPCR and LAMP) as well as criterion 2 (the ability of the TPW to remove previous washes from the column) by running a NA extraction with or without TPW and adding the resulting eluent into qPCR and LAMP (**Figure 2.4c,d**). Of our TPW candidates, we selected 1-undecanol for further evaluation because (i) it was non-inhibitory for qPCR and LAMP reactions and (ii) as an alcohol, 1-undecanol may function similarly to ethanol- or isopropanol-based washes. In these experiments (testing criteria 1b and 2), we first diluted a commercially purified $\lambda$ phage DNA sample to 2.5 x $10^6$ copies and ran an NA extraction using the Zymo Quick-DNA/RNA Viral Kit. We either followed the manufacturer protocol or added an additional 300 µL 1-undecanol wash in between the Viral Wash Buffer and elution step. Using the manufacturer's protocol, the resulting eluent is approximately 49 µL, but with the added TPW the resulting eluent is approximately 48 µL aqueous phase and ~1-2 µL 1-undecanol phase. Because we wanted to emphasize any potential inhibitory effects, we used a low dilution of eluent. For qPCR, we diluted 2.2x by adding 4.5 µL of eluent, 0.5 µL primers, and 5 µL qPCR reaction mix. For LAMP, we diluted 2x by adding 5 µL eluent, 0.5 µL primers, and 4.5 µL reaction mix. During the transfer of eluent into the reaction mix, we noticed that the phase separation yielded by the TPW resulted in minimal transfer of the TPW into downstream reactions (criterion 1b). The ~1-2 µL TPW separates from the aqueous phase and adheres to the walls of the tube, making it is easy to use a pipette to capture just the eluent.

Overall, we found that the addition of the 1-undecanol TPW greatly improved qPCR and LAMP performance at low dilution (**Figure 2.4c-d**). Without the inclusion of the TPW, qPCR run at low dilution of eluent, and following the manufacturer's NA extraction protocol led to failed amplification in all 9 samples. However, with the TPW, the reaction completely recovered with a $C_q$ of 18.46 ± 0.22 cycles. For LAMP and low dilution, we found that the manufacturer protocol amplified in 6.78 ± 0.17 min, whereas our modified TPW protocol amplified in 6.00 ± 0.04 min (**Figure 2.4d**). Not only was there a 0.78 min reduction in TTP ($p < .01$), variance was also reduced. Observing improvements for both qPCR and LAMP, we concluded there was reduced carryover of previous washes (criterion 2).

To confirm our result that the 1-undecanol TPW with low eluent dilutions led to significant improvements in qPCR and LAMP, we repeated this experiment twice more and found similar results. In total (**Figure 2.4-5**), we ran 27 reactions (9 columns) following the manufacturer protocol and compared to 27 reactions (9 columns) with the added 1-undecanol wash. Each set of 3 columns showed a statistically significant ($p < 0.01$) difference comparing with and without 1-undecanol wash ($p < 0.01$) for qPCR and LAMP. For qPCR (triplicate) with the manufacturer protocol, we found 2/27 reaction wells with $C_q$ between 18-22 cycles, 3/27 wells were delayed by 4 or more cycles, and 22/27 wells did not amplify. Of the 5 wells that amplified, the average $C_q$ and standard deviation was 28.6 ± 9.2 cycles. Meanwhile, adding the 1-undecanol wash resulted in 25/27 wells with $C_q$ between 18-22 cycles, 2/27 wells with a delayed $C_q$, and all reactions amplified. The average $C_q$ with the added 1-undecanol wash was 19.7 ± 2.5 cycles. We emphasize that in addition to more samples amplifying, we found that the $C_q$ dropped and the measured variance among samples was reduced, thereby improving the accuracy, speed, and robustness of the diagnostic assay. For LAMP (triplicates), all 27 wells with TPW (10.23 ± 0.06 min) had a faster TTP than all 27 wells following manufacturer protocols (11.36 ± 0.27 min). Again, we find that the 1-undecanol wash improved the speed and robustness (reduced variance) of the assay.

Next, we investigated whether this result was specific to 1-undecanol or TPWs in general (**Figure 2.5a,b,d,e**). For this experiment, we chose 2-dodecanol because it is the longest

chain alcohol we tested, and 1-octanol because it is the shortest chain alcohol for which both qPCR and LAMP still amplified (**Figure 2.4a,b**). We expect 2-dodecanol to perform similarly to 1-undecanol because they are compositionally similar, and both were previously found to be non-inhibitory for qPCR and LAMP (**Figure 2.4a,b**). Accordingly, we expect 1-octanol might perform worse given its higher solubility and previously observed delays. We also chose silicone oil and FC-40 to evaluate nonalcoholic forms of TPW. The result of our study found that all five TPW candidates outperformed the manufacturer protocol. In qPCR reactions, 7/9 reactions amplified with 2-dodecanol wash, 5/9 for 1-octanol, 5/9 for silicone oil, and 4/9 for FC-40, whereas without the TPW (following the manufacturer protocol) amplification often failed (5/27). For LAMP, all TPWs conditions amplified with a faster TTP than manufacturer protocol. ($P < 0.01$).

We hypothesize 1-undecanol and 2-dodecanol performed best (greatest number of successfully amplified qPCR reactions and faster LAMP TTPs) because these two TPW candidates met all of our criteria (1a. non-inhibitory, 1b. low transfer to downstream assays, 2. remove previous wash, and 3. do not elute NAs). Meanwhile, we hypothesize 1-octanol performs slightly worse because 1-octanol is inhibitory to qPCR and LAMP (criterion 1a). However, these inhibitory effects are minimal because 1-octanol phase-separated from the eluent and, as a result, only a small volume of 1-octanol was carried-over into the downstream reactions (criterion 1b). Lastly, we observed that both silicone oil and FC-40 demonstrated slightly worse performance than the other TPW candidates. A potential explanation for the poor performance of silicone oil and FC-40 is that during the TPW step, the alcohols mixed with the previous ethanol-based wash, whereas silicone oil and FC-40 did not (**Table 2-8**). As a result, this allows the alcohol-based TPWs to dilute and more effectively cleanse droplets of ethanol trapped in the column (criterion 2).

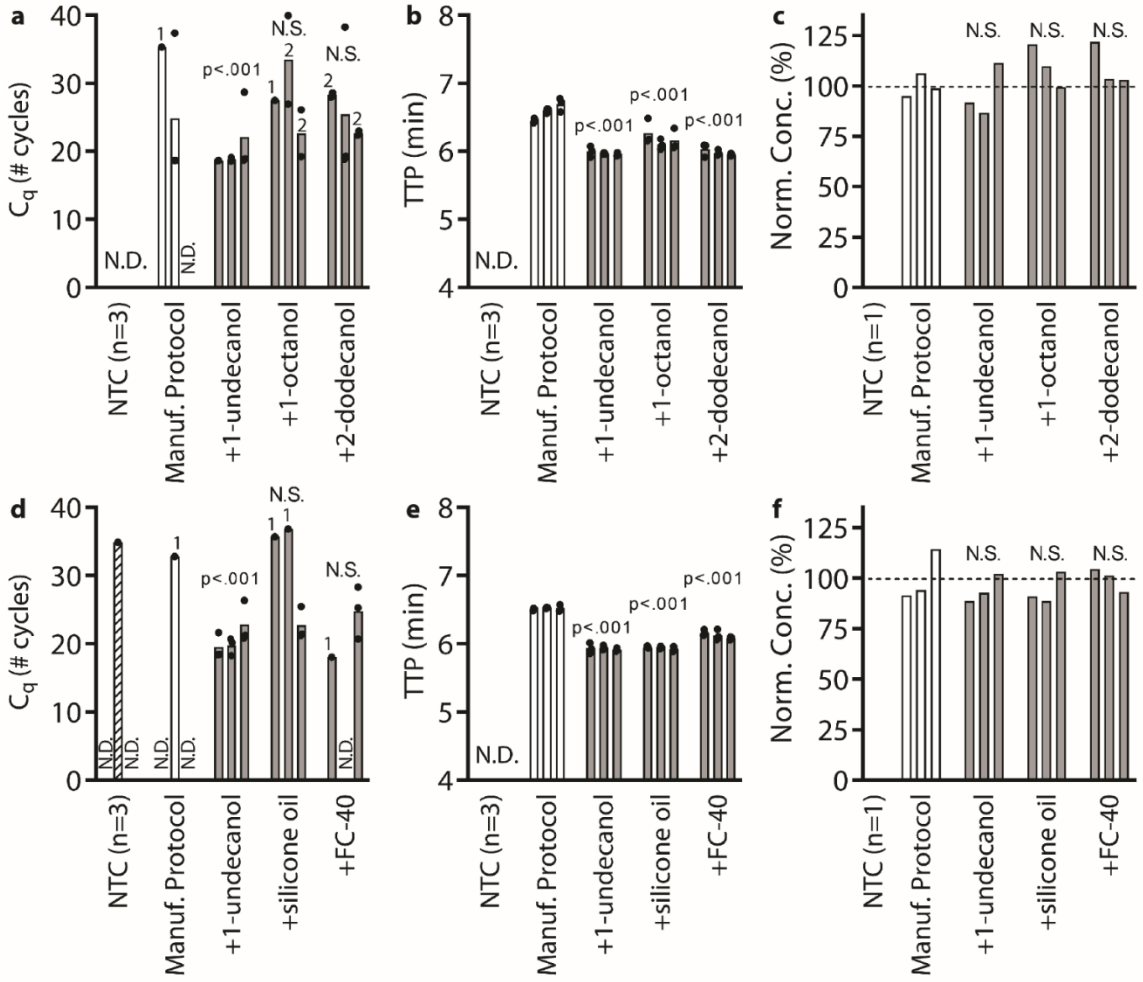


**Figure 2.5: Comparing the performance of different TPWs with eluent at 2.2x dilution in qPCR (a,d), 2x dilution in LAMP (b,e), and 100x dilution in digital PCR (dPCR) (c,f).**

Samples were spiked with 2.5 x $10^6$ copies λ phage DNA and extracted in 50 µL water with a Zymo Quick-Viral DNA/RNA kit. We compared each manufacturer's protocol (Manuf. protocol) with the same protocol plus an additional TPW of either 1-undecanol, 1-octanol, 2-dodecanol, silicone oil, or FC-40. To observe inhibition, a low eluent dilution was used in qPCR and LAMP with λ phage primers. To get a highly accurate quantification of NAs (for comparing these results), we ran each sample using dPCR with a high dilution of eluent (100x), which eliminates the effects of inhibitors. Each bar represents the average of qPCR or LAMP technical triplicates

(black circles) or single dPCR measurements. We ran 24 extractions (3 silica columns x 8 conditions) and the same eluent was used to run the qPCR, LAMP, and dPCR analyses. Where shown, numbers above a bar indicate the number of samples which amplified if not all triplicates were detected. Dashed lines (panels c and f) indicate the average NA recovery following manufacturer protocol. Samples marked N.D. were not detected within 40 cycles by qPCR or 40 min by LAMP. (a-f) For each of the five TPW candidates, we asked whether the mean value was statistically different from the manufacturer protocol by t-test. N.S. stands for not significant ($P > 0.05$).

Next, we evaluated whether or not the TPW meets criterion 3 (NAs are effectively eluted from the column during the TPW or lost due to premature elution or incomplete elution) (**Figure 2.5c,f**). For this experiment, we used a 100x dilution to reduce buffer concentrations to non-inhibitory levels followed by digital PCR (dPCR); dPCR is a highly sensitive method for quantifying NAs that detects the same target (same primers) as qPCR. Although triplicates are commonly tested for qPCR and LAMP, for dPCR experiments we ran duplicates measurements each with more than 15,000 individual reactions. We merged the results from both experiments and used the Poisson distribution to calculate the final concentration using Bio-Rad's QuantaSoft analysis software. We normalized all dPCR concentrations to the average concentration of the three extractions following the manufacturer protocols. We found that the TPW did not appreciably affect the NA recovery, fulfilling our final criterion (3) for an ideal wash buffer. Furthermore, all highly diluted dPCR measurements showed similar NA recovery between manufacturer protocol and TPW conditions, whereas low dilutions resulted in stark differences for both qPCR and LAMP, further confirming that inhibitors are responsible for delays in $C_q$ and TTP.

*TPW validation for different kits with high and low dilution*

To evaluate the generality of our approach and better understand the mechanism, we tested three extraction kit protocols with and without the added TPW. We also wanted to evaluate whether there is a difference in downstream amplification between high eluent dilution (10x) and low eluent dilution (2x or 2.5x). We evaluated Zymo's kit D7021 using either the newer protocol (Zymo Quick-DNA/RNA Viral Kit) or the older protocol (Zymo ZR Viral DNA/RNA Kit). Although both protocols use the same buffers, the Zymo Quick Kit has three wash steps (two viral wash buffers and one ethanol wash), whereas the Zymo ZR kit has one viral wash buffer step. By default, the Zymo kits do not include a "dry spin." The Qiagen QIAquick uses a different set of buffers, has one wash step, and by default includes a "dry spin." In this experiment, all kits extractions were performed on pure water (there are no NAs during the extraction, **Figure 2.9**) to ensure we were only evaluating the effects of buffer inhibitors. The subsequent qPCR and LAMP reactions were then spiked with $5 \times 10^4$ $\lambda$ DNA copies. As a control, water was added to qPCR or LAMP (rather than kit extract) to represent the best-case reaction without inhibitors ("No Extract").

We did not observe inhibition at 10x dilution following manufacturer protocols (**Figure 2.6**), which confirmed that the standard 10x or more dilution into qPCR and LAMP prevents the inhibitory effects we see at lower dilutions. With a 10x dilution, we noticed that the "No Dry Spin" condition using the Qiagen kit with LAMP resulted in ~1 min delay. We note that the Qiagen kit manufacturer protocol requires the dry spin. Without the dry spin, we noticed the Qiagen kit extract had substantially more volume (~65 µL) than when the dry spin was included (~49 µL). This implies ~16 µL (25%) carryover of Buffer PE into the kit extract. The volume of kit extract from Zymo kits, however, was not noticeably affected by the addition of the dry spin (~49 µL with or ~49 µL without).

*TPW validation for different reaction mixes with high and low dilution*

To understand how different reaction mixes respond to buffer carry-over, we compared NEB's SsoFast mix to NEB's Luna mix and our manually prepared LAMP mix to NEB's

pre-made LAMP mix. Using a Zymo Quick-DNA/RNA Viral Kit for extractions, we found that the Luna mix amplified at a 2.2x dilution of kit eluent, whereas the SsoFast mix did not (**Figure 2.14a,b**). This result implies that the Luna kit is more tolerant to the Zymo extraction buffer inhibitors than to those in the SsoFast mix. When we compared experiments with and without the TPW, we again observed that the inclusion of the TPW improved downstream assay performance, recovering amplification for the SsoFast mix and reducing the $C_q$ from 19.1 to 18.4 cycles for the Luna qPCR assay. The manually prepared LAMP mix performed similarly to the pre-made LAMP kit, and again the TPW improved performance at low eluent dilution (2.86x). The TTP for the home-made mix was reduced from 7.4 to 7.0 min, and the TTP for the pre-made mix was reduced from 7.9 to 7.4 min (**Figure 2.14c,d**).

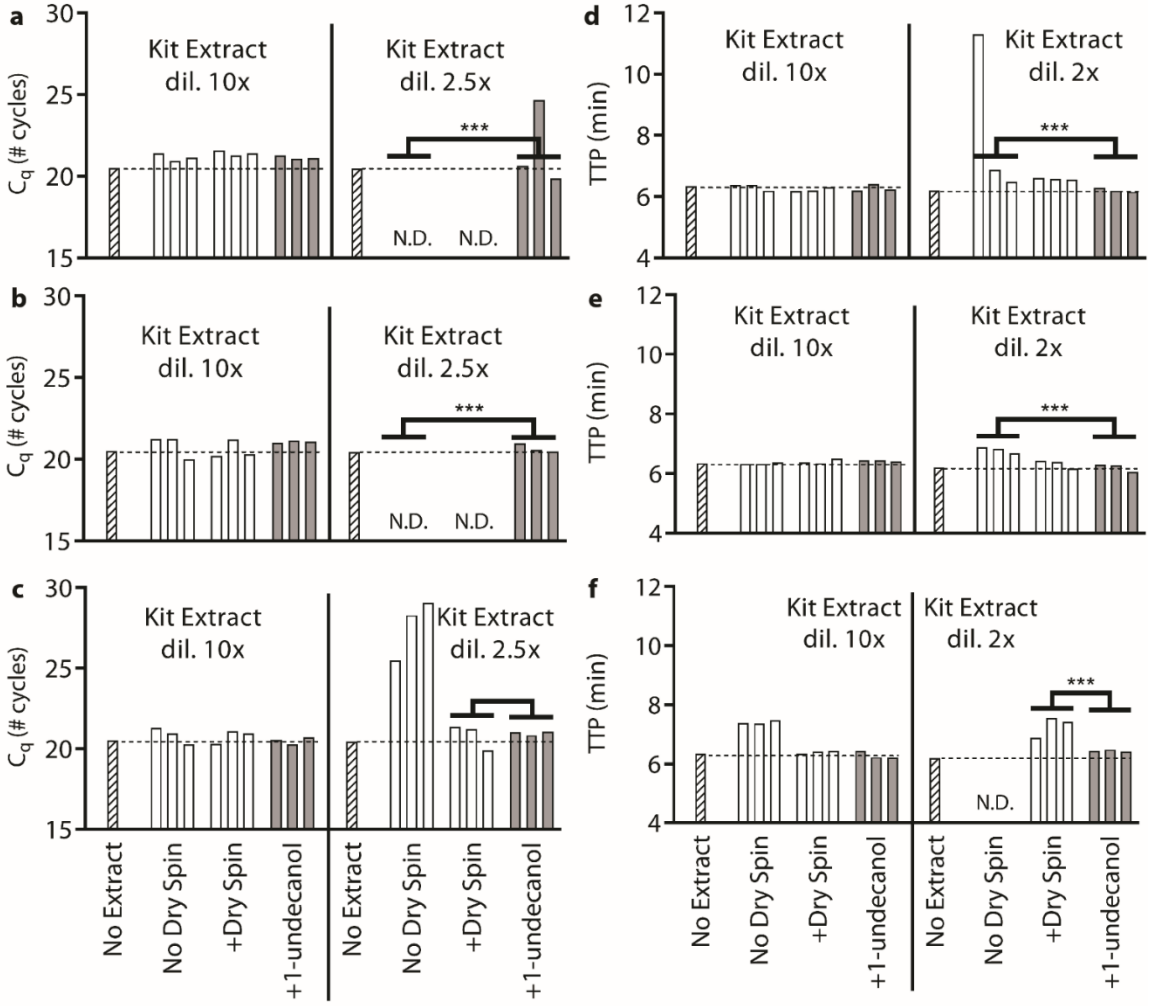


**Figure 2.6: Evaluation of TPW for different silica-column NA extraction kit protocols on pure water samples using (a-c) qPCR and (d-f) LAMP.**

All reactions were spiked with 5 x $10^4$ copies λ phage DNA and primers. By manufacturer protocol, the (a,d) Zymo Quick-DNA/RNA Viral Kit and (b,e) Zymo ZR Viral DNA/RNA Kit do not include the dry spin (+dry spin), whereas the (c,f) Qiagen QIAquick PCR Purification Kit does. The left of each graph shows high dilution and the right shows low dilution. Each bar represents the result from a single qPCR or LAMP measurement. We ran 27 silica-column extractions (3 silica columns x 3 conditions x 3 extraction protocols), and the kit extract was shared between high and low dilutions of both qPCR and LAMP. Dashed lines show the $C_q$ or TTP for a reaction without inhibitors ("No Extract"). Samples marked N.D. were not detected

within either 40 cycles or 40 min. (a-f) We asked whether the manufacturer protocol replicates ("No Dry Spin for Zymo kits, "+dry spin" for Qiagen kit) fell within the 95% CI of the corresponding +1-undecanol condition for the low kit extract dilution case. The number of replicates that lie outside the 95% CI were indicated by the number of *s.

However, when we used 2x or 2.5x dilutions, we observed significant inhibition (**Figure 2.6**). With the Zymo kits and qPCR, there was no amplification whether or not an additional dry spin was added (**Figure 2.6a,b**), contradicting Zymo's "no buffer contamination" claim. For the Qiagen kit (**Figure 2.6c**) and qPCR, the dry spin performs quite well, matching the No Extract control. With the Zymo kits and LAMP (**Figure 2.6d,e**), there are delays when following the protocol (no dry spin) but this is slightly improved by adding a dry spin. With the Qiagen kit and LAMP (**Figure 2.6f**), we observe total reaction inhibition without the dry spin and a 1.1 min delay following the manufacturer protocol. In summary, these results prove that inhibitors are carried into the elution, the additional dry step is helpful for removing wash buffers, and high dilution is the responsible for reducing concentrations to non-inhibitory levels.

Lastly, we used our modified protocol utilizing 1-undecanol TPW and found substantially improved performance, even at low dilutions of the kit extract. We calculated the 95% confidence interval (C.I.) for each 1-undecanol condition at the low dilution and counted the number of outliers when following the manufacturer protocol. For all kits and combinations, we find that the TPW matches performance (Qiagen qPCR) or substantially improved performance (Zymo ZR and Zymo Quick qPCR, all LAMP conditions). The most drastic improvement is for the Zymo ZR kit and qPCR, which failed to amplify with the manufacturer protocol but completely recovered when we added the TPW (**Figure 2.1c** is a subset of **Figure 2.6b** showing "No Dry Spin" and "+1-undecanol"). Given the dramatic improvements and ease of adding the TPW, we recommend silica-column kit manufacturers further evaluate the TPW and consider inclusion with their kits.

We evaluated whether in some cases the TPW could be considered as an alternative for ethanol-based washes (**Figure 2.16**). As a comparison, we used the Zymo ZR kit, which only has one wash step (viral wash buffer). We either replaced the viral wash-buffer step with a dry spin (control), ethanol (control), or different TPW solutions. Briefly, we found that at least under these clean conditions, ethanol wash slightly outperforms the viral wash buffer, long-chain alcohol washes have the best performance, and non-alcohol washes (silicone oil and fluorocarbon oil) led to failed amplifications.

*TPW validation for magnetic-bead extractions*

We next tested whether TPW would improve magnetic bead extractions. Sur et al. previously found that transferring magnetic particles through a hydrophobic liquid effectively reduced PCR inhibitors [51]. This method, termed immiscible phase filter (IPF), allowed for the replacement of multiple wash steps with a single pass through an immiscible liquid. At a 5x dilution of eluent into RT-qPCR, the IPF method showed no statistical difference in detected copies compared to commercial kits for HIV-1 spiked into plasma, Chlamydia and Gonorrhea spiked into urine, and proviral HIV-1 DNA integrated with peripheral blood mononuclear cells in whole blood. Another previous study conducted by Berry et al. described the IFAST (immiscible filtration assisted by surface tension) device [52], and further analyzed their method by examining surface tensions and energies associated with the aqueous phase, immiscible phase, and their device material. The IFAST device reduced total NA extraction operation time to less than 5 min while showing similar performance to commercial extraction kits with operation times between 15 to 45 min (eluent dilution unspecified).

Here with test the TPW with a commercial magnetic bead extraction kit and evaluate both high and low dilution of eluent into LAMP and qPCR. A schematic of the magnetic-bead protocol is shown in **Figure 2.1b**. Using a Zymo Quick-DNA/RNA MagBead Extraction kit, we started with 1 x $10^6$ copies $\lambda$ DNA and eluted with 50 µL. By default, the protocol requires

a 10 min air dry step to allow residual ethanol from the wash step to evaporate. We tested the manufacturer protocol, protocol without the air dry step, and the protocol where the air dry step was replaced with a 1-undecanol TPW. At 10x dilution into qPCR (**Figure 2.7a**), omitting the dry step has no effect. Adding the 1-undecanol TPW led to a 1.1 cycle delay, which corresponds to a decrease in NA extraction efficiency (**Figure 2.7c**) rather than an inhibitory delay. At 10x dilution into LAMP (**Figure 2.7b**), omitting the air dry step causes a 1 min delay, and including the TPW leads to a 0.7 min TTP improvement. At low dilutions, the inhibitory effects are more drastic, and the TPW clearly outperformed the kit protocol with 2 of 3 manufacturer protocol samples performing worse by qPCR and 3 of 3 manufacturer protocol non-detects.

Further experimentation with the MagBead kit revealed that the greater the volume of 1-undecanol carryover, the lower NA recovery we observed. In the experiment shown (**Figure 2.7**), the three extractions had approximately 30 µL, 24 µL, and 22 µL of 1-undecanol carryover as measured by pipette. We found that following the initial 1-undecanol aspiration, a significant volume of 1-undecanol remains stuck to the magnetic beads and walls of the tube. To improve NA yield, we developed a modified protocol in which we aspirate the 1-undecanol, wait at least 1 min, and aspirate any remaining 1-undecanol that slid down the tube due to gravity. This modification led to high yield of NAs after TPW for 1-undecanol (**Figure 2.7c**) and for other compounds (**Figure 2.17**).

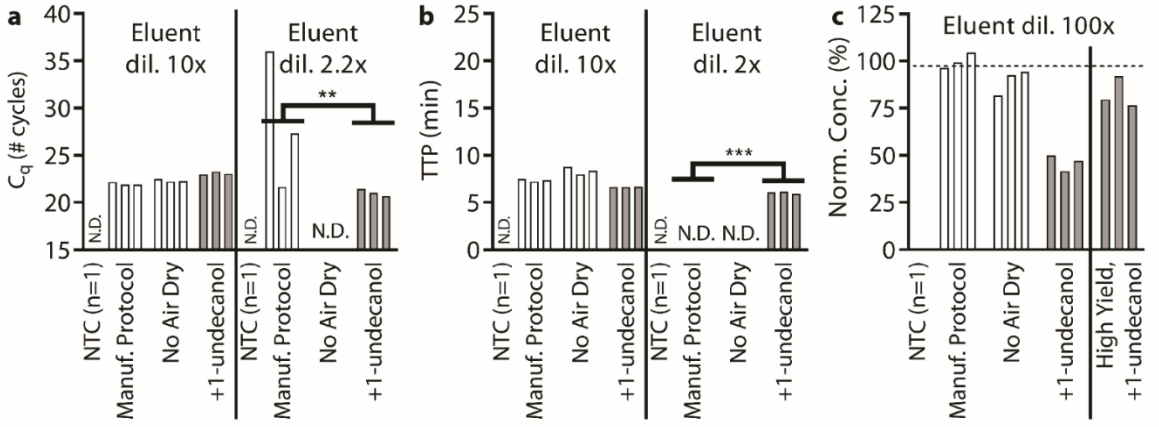


**Figure 2.7: Evaluating TPW for compatibility with Zymo Quick-DNA/RNA MagBead extraction with (a) qPCR, (b) LAMP, and (c) dPCR.**

Extraction performed on 1 x $10^6$ λ phage DNA copies with either a 10 min air dry (Manuf. protocol), no air dry, or with the air dry replaced by a TPW (+1-undecanol) step. The resulting eluent is spiked at either high dilution or low dilution into (a) qPCR and (b) LAMP or 100x dilution into (c) dPCR. For dPCR (d), the bars to the right of the solid black line show the results for an extraction protocol with a +1-undecanol wash using a high-yield protocol from a separate experiment (normalized to the no TPW control in that experiment). Bars represent single qPCR and LAMP or the merged result from a duplicate dPCR measurement. Dashed line in dPCR (c) indicates the average NA recovery following manufacturer protocol. We ran 9 extractions (3 magnetic-bead extractions x 3 conditions), and the eluent was shared among qPCR, LAMP, and dPCR analyses. Samples marked N.D. were not detected within either 40 cycles for qPCR or 40 min for LAMP. (a-b) We asked whether the manufacturer protocol replicates fell within the 95% CI of the corresponding +1-undecanol condition for the low eluent dilution case. The number of replicates that lie outside the 95% CI were indicated by the number of *s.

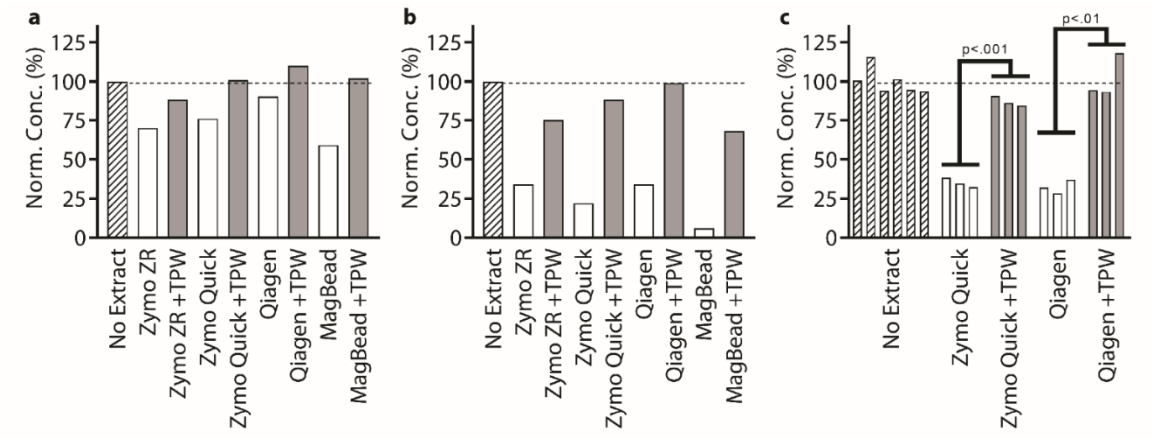


**Figure 2.8: Measurement of reverse transcription (RT) efficiency on *Neisseria gonorrhoeae* RNA using 16S rRNA gene primers with (a) 10x dilution or (b,c) 2x dilution of extractions from different commercial kits into RT reaction mix.** NA concentration quantified by digital PCR after 100x dilution of post-transcribed RT mix. (c) We asked whether RT yield comparing with and without TPW was statistically different using a t-test.

*TPW validation for RT*

We next tested how extraction buffer carryover and TPW would affect RT. For applications requiring high sensitivity, the starting sample might only contain a few cells. In these scenarios, it is beneficial to detect RNA because many RNA copies can be made from a single DNA copy. To evaluate whether or not buffer carryover affects RT, we ran an RT experiment using RNA from *N. gonorrhoeae*, a pathogen with clinical and diagnostic relevance (**Figure 2.8**). First, a high concentration of RNA was extracted using a Zymo ZR Viral DNA/RNA Kit, and the extracted RNA was diluted 100-fold to reduce the concentration of inhibitors. Separately, we ran kit extractions on pure water samples for all previously examined NA extraction kits. We combined RNA with kit extractions into RT reactions containing WarmStart Rtx, NG 16S rRNA PCR primers, and other reaction components. We emphasize that all reactions contained equal concentrations of RNA, and were expected to produce equal levels of DNA. In each RT reaction, we either added 1 µL

kit extract to 9 µL reaction mix (10x) or 5 µL kit extract to 5 µL RT reaction mix (2x). For the "No Extract" condition, we added either 1 µL or 5 µL water. Following RT, the transcribed DNA was then diluted an additional 100x and added to dPCR mix (reaction mix, PCR primers) for quantitative analysis. By separating the RT reaction and quantification with dPCR, we can clearly investigate the effects of buffer inhibition on RT alone (whereas with a 1-step RT-dPCR reaction, it is difficult to determine whether inhibition affects RT or dPCR). We observed a clear trend: using kit extracts while following manufacturer protocols led to a reduction in the amount of DNA that was transcribed. This trend was observed even at a 10x dilution of kit extract into the RT reaction, implying that RT is more strongly inhibited than qPCR or LAMP (**Figure 2.8a**). However, when the TPW was added to the NA extraction kit, transcription efficiency was improved for all kits. These trends are even more pronounced when examining a 2x dilution of kit extract into the RT reaction (**Figure 2.8b**). These results were further confirmed with greater sample size in a separate experiment for 2x dilution of kit extract into RT reaction (**Figure 2.8c**). We found that the TPW significantly improved the efficiency of the RT reaction.

## Conclusions

In this chapter, we evaluated how the buffers from solid-phase silica-column centrifugation and magnetic-bead extraction kits are carried over into the eluent and inhibit downstream amplification reactions. Using kits from leading manufacturers, we repeatedly observed that as expected, a high (10x) dilution of eluent showed little to no inhibition of qPCR or LAMP reactions. However, carried-over extraction buffers caused delays or completely inhibited amplification and reverse transcription at low (2–2.5x) dilutions of eluent. We observed reaction inhibition using two different silica-column centrifugation kits (3 protocols: Zymo ZR, Zymo Quick, Qiagen QIAquick) and a magnetic-bead kit (Zymo MagBead) when using the manufacturer protocols.

We reduced the inhibition due to carryover by developing a TPW protocol that improved eluent purity and led to more efficient and reproducible reactions. We showed that the inclusion of a dry spin step, although helpful, still generated buffer carryover which inhibited qPCR and LAMP at low eluent dilutions. We discovered that the inclusion of a TPW step greatly reduced buffer carryover, and we found that low solubility compounds exhibited the best performance. Using the TPW protocol improved eluent purity, leading to more efficient (reduced delays in $C_q$ or TTP) reactions. The addition of the TPW also improved the efficiency of RT reactions.

Furthermore, TPW improved reproducibility of amplification reactions by reducing $C_q$ and TTP variations between measurements (**Figure 2.7a**, 2.2x dilution), and at low target concentrations leading to more repeatable detection (**Figure 2.7b**, 2x dilution). Reproducibility is an important aspect of nucleic-acid assays in biological research and diagnostic assays. Given the high degree of sensitivity of reactions to levels of carryover (**Figure 2.2**), especially at low target NA concentrations (**Figure 2.3**), it is expected that slight variation in the extent of carryover can lead to high variation in the performance of a NA assay. High purity eluent from TPW was compatible with low dilutions into amplification mix, improving assay sensitivity because more NAs could be added to each reaction.

We anticipate the addition of the TPW would improve NA extraction purity and performance of downstream assays in a variety of applications. We have demonstrated performance of TPW for a range of commercial extractions kits and a range of nucleic-acid targets. One limitation of this study is that it is not exhaustive: we have not tested every possible kit, every possible sample type, every possible NA reaction, and every possible nucleic-acid target. However, TPW is inexpensive and easy to incorporate into both silica-column (one additional spin) and magnetic-bead extractions (one additional aspiration), and therefore we encourage researchers and commercial suppliers to test TPW in their specific workflows and protocols. In particular, we expect to use the TPW extraction in combination with lyophilized reagents, which requires no dilution, and is highly desirable for point-of-care diagnostics.

Finally, the TPW will enable the field to develop new methods of sample preparation, such as pressure- or vacuum-based NA extractions, that are simpler, quicker, and more portable than current protocols.

In addition to reducing extraction buffer carryover, we hypothesize the TPW could also reduce carryover of some compounds originating from the sample by removing them from the solid phase. For example, long-chain alcohols might remove nonpolar compounds better than traditional wash buffers (ethanol or isopropanol). This hypothesis remains to be tested in future work. Furthermore, we anticipate that improved eluent purity from the added TPW would enable high-sensitivity analyses that were previously difficult or impossible because high dilution of eluent has been the *de facto* standard. Improved eluent purity would be especially valuable for more challenging reactions, including long amplicons (DNA and RNA), targets with high GC content, and highly structured or chemically modified RNA targets (e.g. rRNA, tRNA). By enabling the use of lower dilutions, this method would enhance performance of NA analysis in applications where sensitivity and reproducibility are critical, including single-cell sequencing, cell-free circulating DNA analyses and SNP detection, and molecular diagnostics.

## Data Availability Statement

Full dataset available through CaltechDATA, DOI: 10.22002/D1.1298; https://data.caltech.edu/records/1298

## References

1. SR, K. PCR Technique with its Application. *Research & Reviews: Journal of Microbiology and Biotechnology* **4**, 1-12 (2015).

2. Valones, M. A. *et al.* Principles and applications of polymerase chain reaction in medical diagnostic fields: a review. *Braz. J. Microbiol.* **40**, 1-11, doi:10.1590/s1517-83822009000100001 (2009).

3. Day, E., Dear, P. H. & McCaughan, F. Digital PCR strategies in the development and analysis of molecular biomarkers for personalized medicine. *Methods* **59**, 101-107 (2013).

4. Gielis, E. M. *et al.* Cell-Free DNA: An Upcoming Biomarker in Transplantation. *Am. J. Transplant.* **15**, 2541-2551, doi:10.1111/ajt.13387 (2015).

5. Klein, D. Quantification using real-time PCR technology: applications and limitations. *Trends Mol. Med.* **8**, 257-260 (2002).

6. 6Craw, P. & Balachandran, W. Isothermal nucleic acid amplification technologies for point-of-care diagnostics: a critical review. *Lab on a chip* **12**, 2469-2486, doi:10.1039/c2lc40100b (2012).

7. Notomi, T. *et al.* Loop-mediated isothermal amplification of DNA. *Nucleic Acids Res.* **28**, E63, doi:10.1093/nar/28.12.e63 (2000).

8. Tanner, N. A. & Evans, T. C., Jr. Loop-mediated isothermal amplification for detection of nucleic acids. *Curr. Protoc. Mol. Biol.* **105**, Unit 15.14., doi:10.1002/0471142727.mb1514s105 (2014).

9. Yager, P., Domingo, G. J. & Gerdes, J. Point-of-care diagnostics for global health. *Annu. Rev. Biomed. Eng.* **10**, 107-144, doi:10.1146/annurev.bioeng.10.061807.160524 (2008).

10. Boesenberg-Smith, K. A., Pessarakli, M. M. & Wolk, D. M. Assessment of DNA yield and purity: an overlooked detail of PCR troubleshooting. *Clin. Microbiol. Newsl.* **34**, 1-6 (2012).

11. Huggett, J. F. *et al.* Differential susceptibility of PCR reactions to inhibitors: an important and unrecognised phenomenon. *BMC Res. Notes* **1**, 70, doi:10.1186/1756-0500-1-70 (2008).

12. Kaneko, H., Kawana, T., Fukushima, E. & Suzutani, T. Tolerance of loop-mediated isothermal amplification to a culture medium and biological substances. *J. Biochem. Biophys. Methods* **70**, 499-501, doi:10.1016/j.jbbm.2006.08.008 (2007).

13. Bustin, S. A., Benes, V., Nolan, T. & Pfaffl, M. W. Quantitative real-time RT-PCR--a perspective. *J. Mol. Endocrinol.* **34**, 597-601, doi:10.1677/jme.1.01755 (2005).

14. Tebbe, C. C. & Vahjen, W. Interference of humic acids and DNA extracted directly from soil in detection and transformation of recombinant DNA from bacteria and a yeast. *Appl. Environ. Microbiol.* **59**, 2657-2665 (1993).

15. Simbolo, M. *et al.* DNA qualification workflow for next generation sequencing of histopathological samples. *PLoS One* **8**, e62692, doi:10.1371/journal.pone.0062692 (2013).

16. Rossen, L., Norskov, P., Holmstrom, K. & Rasmussen, O. F. Inhibition of PCR by components of food samples, microbial diagnostic assays and DNA-extraction solutions. *Int. J. Food Microbiol.* **17**, 37-45, doi:10.1016/0168-1605(92)90017-w (1992).

17. Wilson, I. G. Inhibition and facilitation of nucleic acid amplification. *Appl. Environ. Microbiol.* **63**, 3741 (1997).

18. Nolan, T., Hands, R. E., Ogunkolade, W. & Bustin, S. A. SPUD: a quantitative PCR assay for the detection of inhibitors in nucleic acid preparations. *Anal. Biochem.* **351**, 308-310, doi:10.1016/j.ab.2006.01.051 (2006).

19. Schrader, C., Schielke, A., Ellerbroek, L. & Johne, R. PCR inhibitors - occurrence, properties and removal. *J. Appl. Microbiol.* **113**, 1014-1026, doi:10.1111/j.1365-2672.2012.05384.x (2012).

20. Alaeddini, R. Forensic implications of PCR inhibition--A review. *Forensic science international: Genetics* **6**, 297-305, doi:10.1016/j.fsigen.2011.08.006 (2012).

21. Hu, Q., Liu, Y., Yi, S. & Huang, D. A comparison of four methods for PCR inhibitor removal. *Forensic science international: Genetics* **16**, 94-97, doi:10.1016/j.fsigen.2014.12.001 (2015).

22. Radstrom, P., Lofstrom, C., Lovenklev, M., Knutsson, R. & Wolffs, P. Strategies for overcoming PCR inhibition. *CSH protocols* **2008**, pdb.top20, doi:10.1101/pdb.top20 (2008).

23. Opel, K. L., Chung, D. & McCord, B. R. A study of PCR inhibition mechanisms using real time PCR. *J. Forensic Sci.* **55**, 25-33, doi:10.1111/j.1556-4029.2009.01245.x (2010).

24. Mahony, J. *et al.* Urine specimens from pregnant and nonpregnant women inhibitory to amplification of Chlamydia trachomatis nucleic acid by PCR, ligase chain reaction, and transcription-mediated amplification: identification of urinary substances associated with inhibition and removal of inhibitory activity. *J. Clin. Microbiol.* **36**, 3122-3126 (1998).

25. Demeke, T. & Jenkins, G. R. Influence of DNA extraction methods, PCR inhibitors and quantification methods on real-time PCR assay of biotechnology-derived traits. *Anal. Bioanal. Chem.* **396**, 1977-1990, doi:10.1007/s00216-009-3150-9 (2010).

26. Chacon-Cortes, D. & Griffiths, L. R. Methods for extracting genomic DNA from whole blood samples: current perspectives. *Journal of Biorepository Science for Applied Medicine* **2014**, 1-9 (2014).

27. Abd El-Aal, A. A., Abd Elghany, N. A., Mohamadin, A. M. & El-Badry, A. A. Comparative study of five methods for DNA extraction from whole blood samples. *International Journal of Health Science* **3** (2010).

28. Price, C. W., Leslie, D. C. & Landers, J. P. Nucleic acid extraction techniques and application to the microchip. *Lab on a chip* **9**, 2484-2494, doi:10.1039/b907652m (2009).

29. Bergallo, M. *et al.* Evaluation of six methods for extraction and purification of viral DNA from urine and serum samples. *The new microbiologica* **29**, 111-119 (2006).

30. Ali, N., Rampazzo, R. C. P., Costa, A. D. T. & Krieger, M. A. Current Nucleic Acid Extraction Methods and Their Implications to Point-of-Care Diagnostics. *BioMed research international* **2017**, 9306564, doi:10.1155/2017/9306564 (2017).

31. Priye, A. *et al.* A smartphone-based diagnostic platform for rapid detection of Zika, chikungunya, and dengue viruses. *Sci. Rep.* **7**, 44778, doi:10.1038/srep44778 (2017).

32. Goldberg, C. S., Sepulveda, A., Ray, A., Baumgardt, J. & Waits, L. P. Environmental DNA as a new method for early detection of New Zealand mudsnails (Potamopyrgus antipodarum). *Freshwater Science* **32**, 792-800 (2013).

33. Rudi, K., Hagen, I., Johnsrud, B. C., Skjefstad, G. & Tryland, I. Different length (DL) qPCR for quantification of cell killing by UV-induced DNA damage. *Int. J. Env. Res. Public Health* **7**, 3376-3381, doi:10.3390/ijerph7093376 (2010).

34. Qiu, J., Chen, P. & Lin, S. Development of a Real-Time Polymerase Chain Reaction Method to Measure Ligation Efficiency. *Journal of Experimental Microbiology and Immunology* (2015).

35. Mason, W. J. *et al.* Multiplex PCR protocol for the diagnosis of staphylococcal infection. *J. Clin. Microbiol.* **39**, 3332-3338, doi:10.1128/jcm.39.9.3332-3338.2001 (2001).

36. Kamau, E., Alemayehu, S., Feghali, K. C., Saunders, D. & Ockenhouse, C. F. Multiplex qPCR for detection and absolute quantification of malaria. *PLoS One* **8**, e71539, doi:10.1371/journal.pone.0071539 (2013).

37. Crotchfelt, K. A., Welsh, L. E., DeBonville, D., Rosenstraus, M. & Quinn, T. C. Detection of Neisseria gonorrhoeae and Chlamydia trachomatis in genitourinary specimens from men and women by a coamplification PCR assay. *J. Clin. Microbiol.* **35**, 1536-1540 (1997).

38. Biava, M. *et al.* Evaluation of a rapid and sensitive RT-qPCR assay for the detection of Ebola Virus. *J. Virol. Methods* **252**, 70-74, doi:10.1016/j.jviromet.2017.11.009 (2018).

39. Peist, R., Honsel, D., Twieling, G. & Löffert, D. PCR inhibitors in plant DNA preparations. *Qiagen news* **3**, 7-9 (2001).

40. Nixon, G. *et al.* Comparative study of sensitivity, linearity, and resistance to inhibition of digital and nondigital polymerase chain reaction and loop mediated isothermal amplification assays for quantification of human cytomegalovirus. *Anal. Chem.* **86**, 4387-4394, doi:10.1021/ac500208w (2014).

41. Jue, E., Witters, D. & Ismagilov, R. F. How to diagnose and solve the ubiquitous contaminant-carryover problem in commercial nucleic acid extraction kits. *PittCon 2020*, Oral Presentation.

42. Goto, M., Honda, E., Ogura, A., Nomoto, A. & Hanaki, K. Colorimetric detection of loop-mediated isothermal amplification reaction by using hydroxy naphthol blue. *BioTechniques* **46**, 167-172, doi:10.2144/000113072 (2009).

43. Kuehnelt, D. M., Kukovetz, E., Hofer, H. P. & Schaur, R. J. Quantitative PCR of bacteriophage lambda DNA using a second-generation thermocycler. *PCR Methods Appl.* **3**, 369-371 (1994).

44. Schoepp, N. G. *et al.* Rapid pathogen-specific phenotypic antibiotic susceptibility testing using digital LAMP quantification in clinical samples. *Sci. Transl. Med.* **9**, eaal3693, doi:10.1126/scitranslmed.aal3693 (2017).

45. Matsuda, K., Tsuji, H., Asahara, T., Kado, Y. & Nomoto, K. Sensitive quantitative detection of commensal bacteria by rRNA-targeted reverse transcription-PCR. *Appl. Environ. Microbiol.* **73**, 32-39, doi:10.1128/aem.01224-06 (2007).

46. Lee, S. R., Chung, J. M. & Kim, Y. G. Rapid one step detection of pathogenic bacteria in urine with sexually transmitted disease (STD) and prostatitis patient by multiplex PCR assay (mPCR). *J. Microbiol.* **45**, 453-459 (2007).

47. Francois, P. *et al.* Robustness of a loop-mediated isothermal amplification reaction for diagnostic applications. *FEMS Immunol. Med. Microbiol.* **62**, 41-48, doi:10.1111/j.1574-695X.2011.00785.x (2011).

48. Yamazaki, W., Ishibashi, M., Kawahara, R. & Inoue, K. Development of a loop-mediated isothermal amplification assay for sensitive and rapid detection of Vibrio parahaemolyticus. *BMC Microbiol.* **8**, 163, doi:10.1186/1471-2180-8-163 (2008).

49. Sriworarat, C., Phumee, A., Mungthin, M., Leelayoova, S. & Siriyasatien, P. Development of loop-mediated isothermal amplification (LAMP) for simple detection of Leishmania infection. *Parasites & vectors* **8**, 591, doi:10.1186/s13071-015-1202-x (2015).

50. Kogovšek, P. *et al.* Rapid loop-mediated isothermal amplification assays for grapevine yellows phytoplasmas on crude leaf-vein homogenate has the same performance as qPCR. *Eur. J. Plant Pathol.* **148**, 75-84 (2017).

51. Sur, K. *et al.* Immiscible phase nucleic acid purification eliminates PCR inhibitors with a single pass of paramagnetic particles through a hydrophobic liquid. *The Journal of molecular diagnostics* **12**, 620-628, doi:10.2353/jmoldx.2010.090190 (2010).

52. Berry, S. M., Alarid, E. T. & Beebe, D. J. One-step purification of nucleic acid for gene expression analysis via Immiscible Filtration Assisted by Surface Tension (IFAST). *Lab on a chip* **11**, 1747-1753, doi:10.1039/c1lc00004g (2011).

## Supporting Information

*Kit extractions on "pure water"*

Typically, it makes sense to run controls with nucleic acids (NAs) spiked into the sample prior to the NA extraction step. However, in our "pure water" experiments we wanted to observe the effects of buffer carry-over independently of NA yield. We subsequently ran NA extractions on "pure water" samples to obtain eluent containing buffer carry-over (kit extract). We then used the original "pure water" sample as the non-inhibited control and compared to the kit extract (elution from kit extraction performed on pure water) in NA spiked downstream reactions. This approach was used to generate **Figure 2.1c, Figure 2.6,** and **Figure 2.8**.

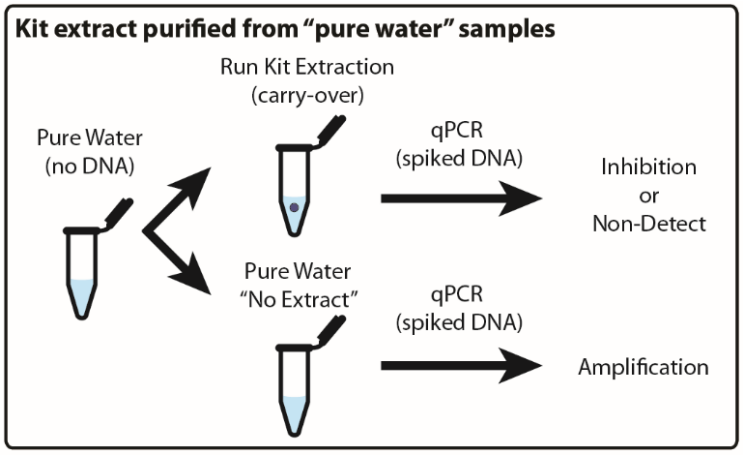


**Figure 2.9: Example protocol used for experiments performed on "pure water."**

*Full data set for buffer inhibitors in qPCR and LAMP*

**Figure 2.10-13** show the full data set for buffer dilutions in qPCR and LAMP. The A-C panels of each figure (providing $C_q$ and TTP data) were presented in the main text. Changes in the endpoint RFU were highly concordant with changes in $C_q$ or TTP. The melting-temperature (Tm) effects showed up at low concentrations of inhibitors, suggesting that Tm can be an effective indicator for the presence or absence of inhibitors in sample.

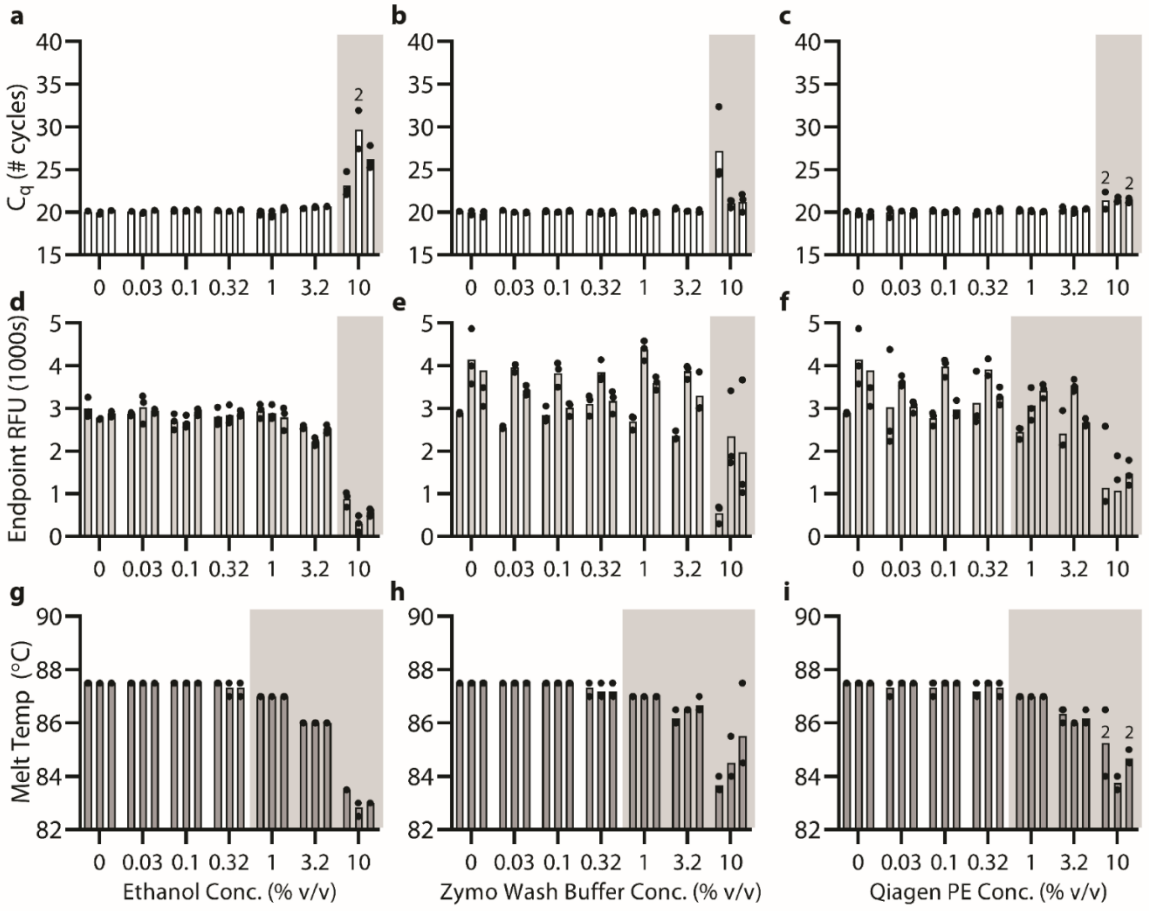


**Figure 2.10: (a-c) $C_q$, (d-f) endpoint fluorescence, and (g-i) melting temperature for qPCR on 5 x $10^4$ λ phage DNA copies in the presence of ethanol, Zymo Viral Wash Buffer, or Qiagen PE Buffer.**

Gray background indicates an average $C_q$ delay of at least 0.5 cycles, RFU decrease of at least 500 RFU, or a melting temperature change of at least 0.5 °C compared with the 0% buffer condition.

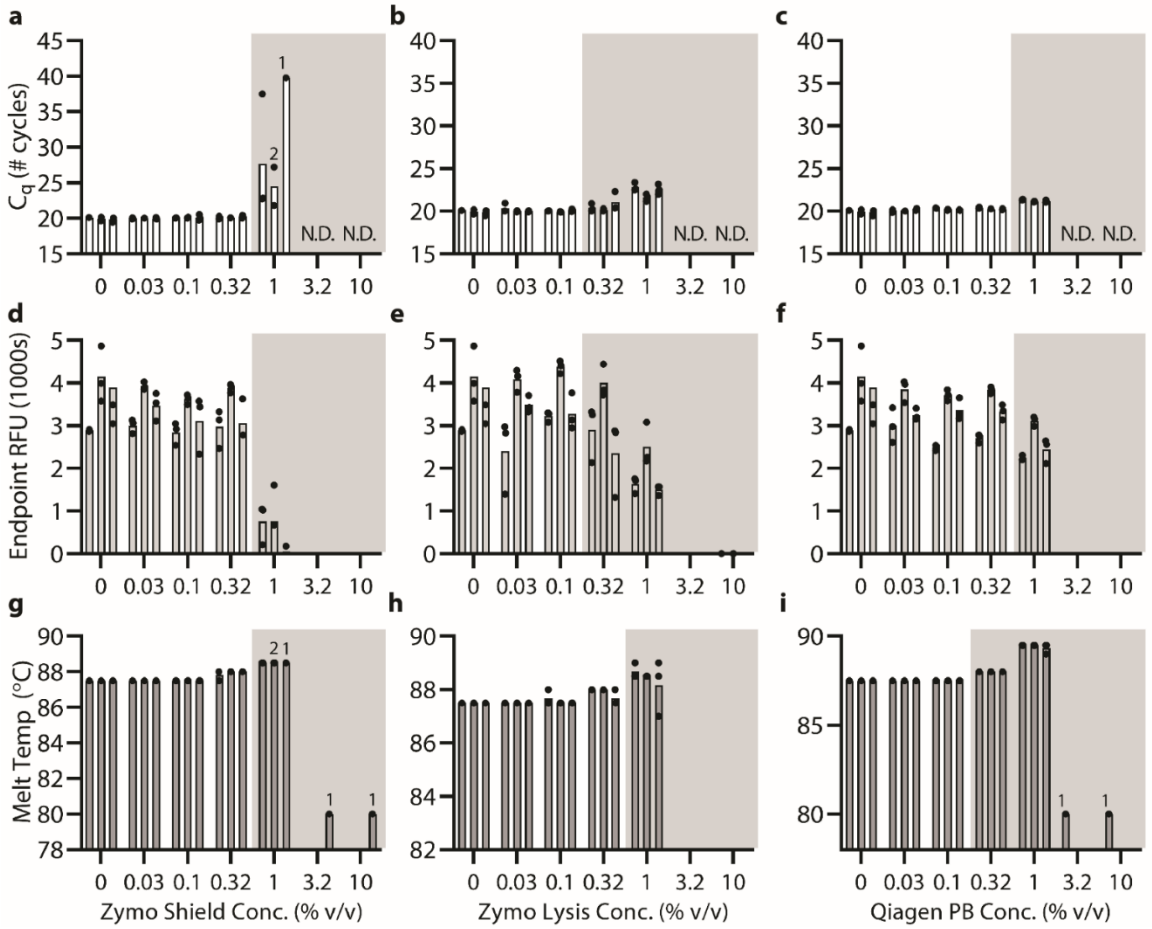


**Figure 2.11: (a-c) $C_q$, (d-f) endpoint fluorescence, and (g-i) melting temperature for qPCR on 5 x $10^4$ λ phage DNA copies in the presence of Zymo DNA/RNA Shield, Zymo Viral DNA/RNA Buffer, or Qiagen PB Buffer.**

Gray background indicates an average $C_q$ delay of at least 0.5 cycles, RFU decrease of at least 500 RFU, or melting temperature change of at least 0.5 °C compared with the 0% buffer condition.

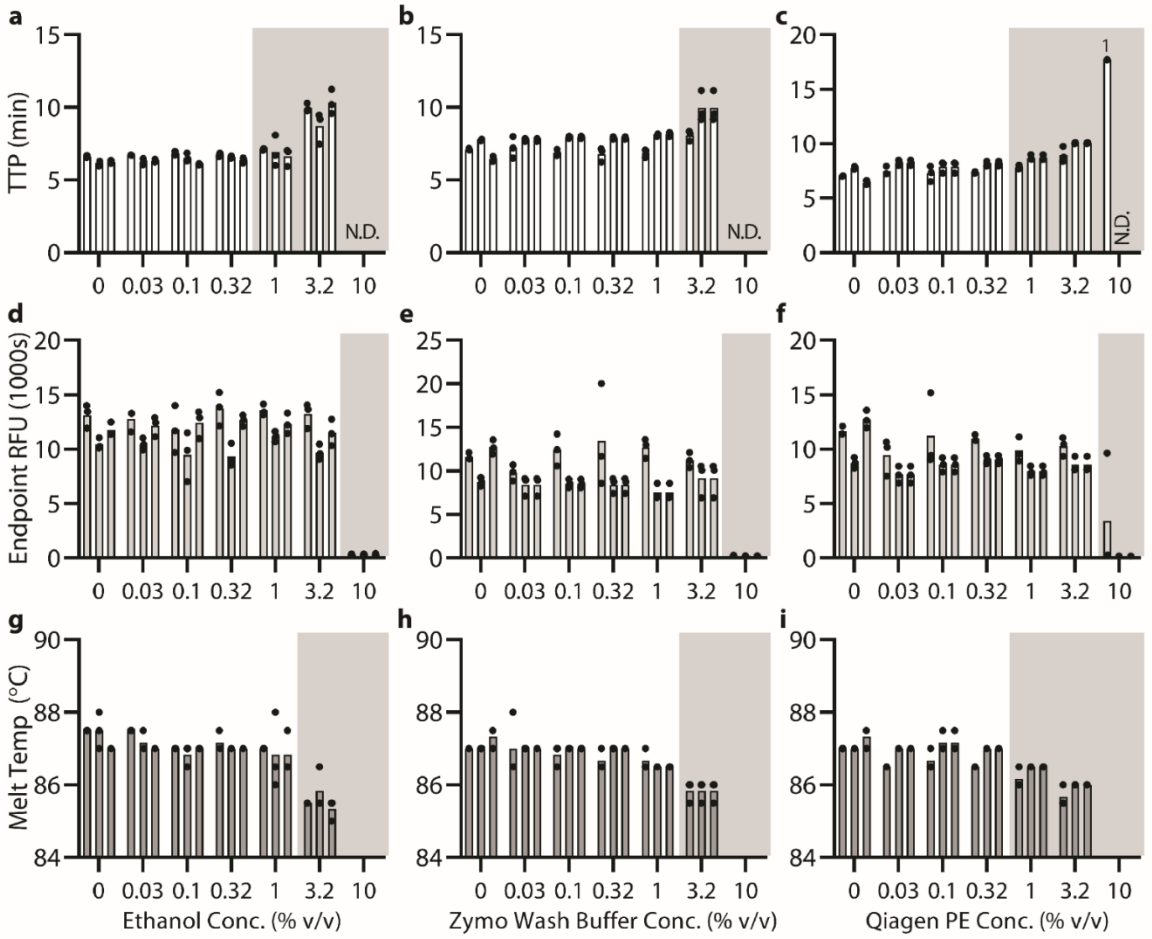


**Figure 2.12: (a-c) TTP, (d-f) endpoint fluorescence, and (g-i) melting temperature for LAMP on 5 x $10^4$ λ phage DNA copies in the presence of ethanol, Zymo Viral Wash Buffer, or Qiagen PE Buffer.**

Gray background indicates an average TTP delay of at least 0.5 min, RFU decrease of at least 5000 RFU, or melting temperature change of at least 0.5 °C compared with the 0% buffer condition.

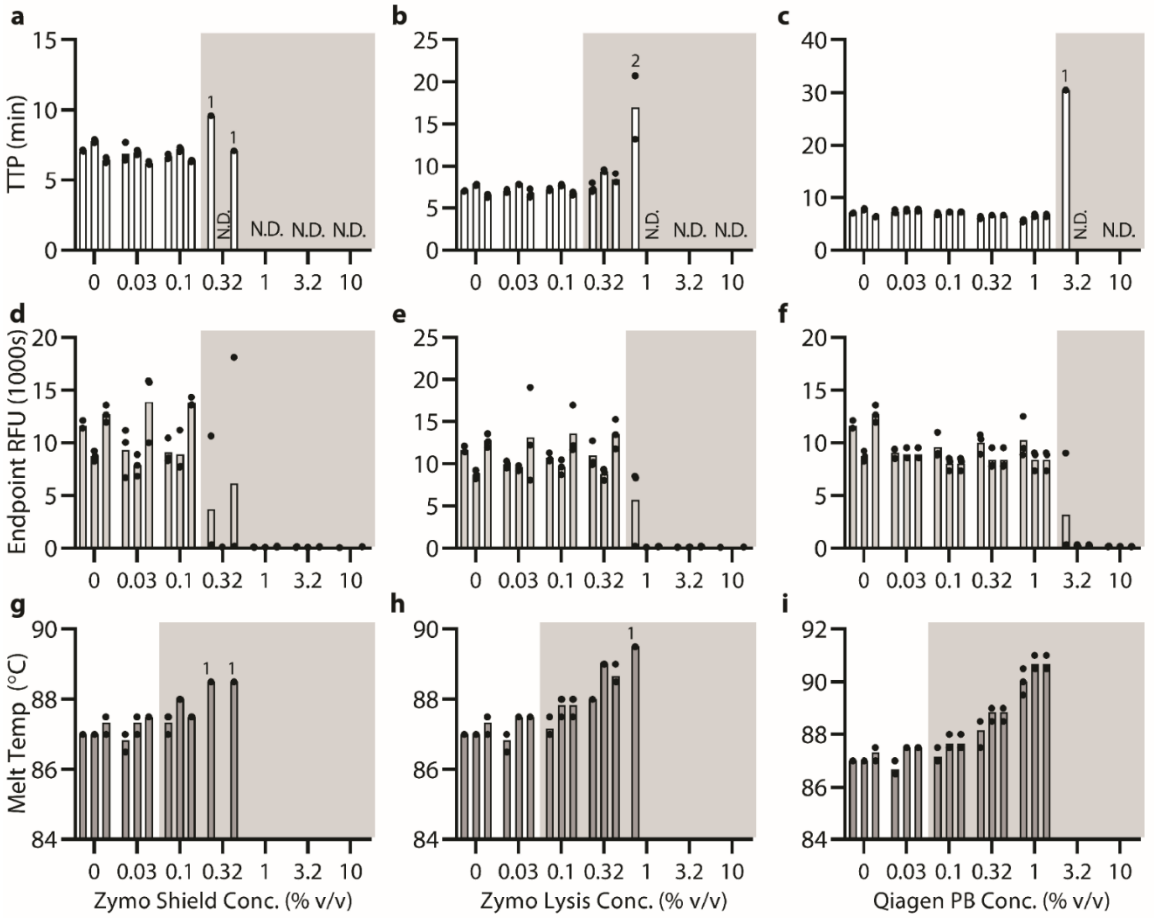


**Figure 2.13: (a-c) TTP, (d-f) endpoint fluorescence, and (g-i) melting temperature for LAMP on 5 x $10^4$ λ phage DNA copies in the presence of Zymo DNA/RNA Shield, Zymo Viral DNA/RNA Buffer, or Qiagen PB Buffer.**
Gray background indicates an average TTP delay of at least 0.5 min, RFU decrease of at least 5000 RFU, or melting temperature change of at least 0.5 °C compared with the 0% buffer condition.

*TPW validation for different reaction mixes with high and low dilution*

We compared NEB's SsoFast EvaGreen Supermix to NEB's Luna Universal qPCR master mix and a manually prepared LAMP mix to NEB's pre-made WarmStart LAMP Kit. For the SsoFast mix, we used 500 nM primers (NEB recommended 300-500 nM), and for the Luna

mix we used 250 nM primers (NEB recommendation). The same primer concentration was used for the manually prepared LAMP mix and NEB's pre-made mix. For the LAMP comparison, the lowest possible dilution was 2.86x because NEB's pre-made LAMP mix required 65% of the reaction volume (WarmStart LAMP 2X master mix, 50x fluorescent dye, primers).

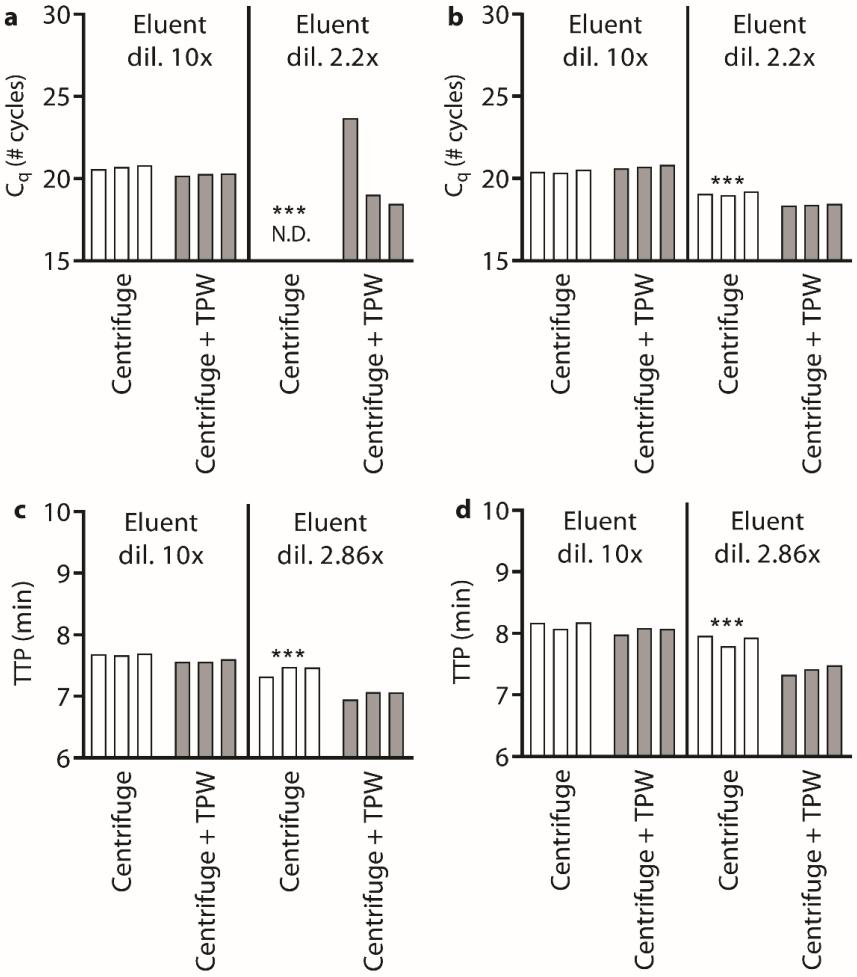


**Figure 2.14: Evaluation of extraction buffer inhibition on different assays and improvements due to the addition of a TPW.**

We compared the (a) NEB SsoFast mix to the (b) NEB Luna mix, and we compared a (c) manually prepared LAMP mix to an (d) NEB pre-made LAMP mix. Kit eluent

was obtained by performing a Zymo Quick-DNA/RNA Viral Kit on 2.5 x 105 copies λ phage DNA and eluting with 50 µL water. The left side of each graph shows high dilution and the right side shows low dilution. We ran six silica-column extractions in total, and the same kit extract was shared among the high and low dilutions of all assays. Samples marked "N.D." indicate not detected within either 40 cycles (qPCR) or 40 min (LAMP). All negative controls were clean (not shown). For the low eluent dilution conditions, we asked how many replicates following the standard centrifugation protocol fell outside of the 95% confidence interval for the corresponding centrifuge +TPW condition (indicated by number of *).

*Buffer inhibitors in qPCR and LAMP*

We note that 3.2% Qiagen PE Buffer in LAMP caused a large delay (6.0 min ΔTTP), but this difference does not measure as statistically significant by t-test. This is due to a bias introduced by a single non-detect (8 out of 9 amplified) which greatly increased the measured standard deviation. If we exclude the non-detect from the analysis (rather than assigning the non-detect to a value of 46.7 min), the t-test measures a *P*-value of 0.002. Also of potential interest, Qiagen PB Buffer appears to have sped up LAMP at low concentrations (0.1% - 1%). This result is unexpected, and further testing is required to validate this surprising result, which we hypothesize is not generalizable (e.g. could be primer or reaction mix dependent).

**Table 2-1: Summary of ethanol-based buffer dilutions for qPCR.**

The average and standard deviation were calculated from 9 replicates. The $\Delta C_q$ is calculated by subtracting the average value for a given buffer concentration from the water condition (0%). A positive value indicates a cycle delay when adding the buffer. *P*-values were calculated by a 1-tailed unequal variance t-test compared to the water condition (0%). A * indicates a delay of at least 0.5 cycles and *P*-value <0.05. Non-detects were assigned a value of 40 cycles. VWB = Zymo Viral Wash Buffer; PE = Qiagen PE Buffer.

| | Ethanol | | | | | VWB | | | | | PE | | | | |
|---|---|---|---|---|---|---|---|---|---|---|---|---|---|---|---|
| | Avg | Std | ΔCq | p | * | Avg | Std | ΔCq | p | * | Avg | Std | ΔCq | p | * |
| 0% | 20.1 | 0.2 | | | | 20.0 | 0.3 | | | | 20.0 | 0.3 | | | |
| 0.03% | 20.1 | 0.1 | 0.0 | 0.499 | | 20.1 | 0.1 | 0.1 | 0.171 | | 20.0 | 0.3 | 0.0 | 0.431 | |
| 0.1% | 20.2 | 0.1 | 0.1 | 0.065 | | 20.1 | 0.1 | 0.1 | 0.109 | | 20.1 | 0.1 | 0.1 | 0.141 | |
| 0.32% | 20.2 | 0.1 | 0.1 | 0.152 | | 20.0 | 0.1 | 0.0 | 0.449 | | 20.1 | 0.2 | 0.1 | 0.165 | |
| 1% | 20.1 | 0.4 | 0.0 | 0.465 | | 20.1 | 0.1 | 0.1 | 0.302 | | 20.1 | 0.1 | 0.1 | 0.081 | |
| 3.2% | 20.6 | 0.1 | 0.5 | <0.001 | | 20.3 | 0.2 | 0.3 | 0.011 | | 20.3 | 0.2 | 0.3 | 0.006 | |
| 10% | 27.5 | 5.5 | 7.4 | 0.002 | * | 23.2 | 3.8 | 3.2 | 0.019 | * | 25.5 | 8.2 | 5.5 | 0.039 | * |

**Table 2-2: Summary of lysis buffer dilutions for qPCR.**

The average and standard deviation were calculated from 9 replicates. The $\Delta C_q$ is calculated by subtracting the average value for a given buffer concentration from the water condition (0%). A positive value indicates a cycle delay when adding the buffer. *P*-values were calculated by a 1-tailed unequal variance t-test compared to the water condition (0%). A * indicates a delay of at least 0.5 cycles and *P*-value <0.05. Non-detects were assigned a value of 40 cycles. PB = Qiagen PB Buffer.

| | Shield | | | | | Lysis | | | | | PB | | | | |
|---|---|---|---|---|---|---|---|---|---|---|---|---|---|---|---|
| | Avg | Std | ΔCq | p | * | Avg | Std | ΔCq | p | * | Avg | Std | ΔCq | p | * |
| 0% | 20.0 | 0.3 | | | | 20.0 | 0.3 | | | | 20.0 | 0.3 | | | |
| 0.03% | 20.0 | 0.1 | 0.0 | 0.445 | | 20.1 | 0.3 | 0.1 | 0.184 | | 20.1 | 0.2 | 0.1 | 0.101 | |
| 0.1% | 20.1 | 0.2 | 0.1 | 0.126 | | 20.0 | 0.1 | 0.0 | 0.340 | | 20.2 | 0.1 | 0.2 | 0.023 | |
| 0.32% | 20.2 | 0.2 | 0.2 | 0.047 | | 20.5 | 0.7 | 0.5 | 0.029 | * | 20.3 | 0.1 | 0.3 | 0.004 | |
| 1% | 32.4 | 8.5 | 12.4 | 0.001 | * | 22.3 | 0.7 | 2.3 | <0.001 | * | 21.2 | 0.1 | 1.2 | 0.000 | * |
| 3.2% | 40.0 | 0.0 | 20.0 | <0.001 | * | 40.0 | 0.0 | 20.0 | <0.001 | * | 40.0 | 0.0 | 20.0 | 0.000 | * |
| 10% | 40.0 | 0.0 | 20.0 | <0.001 | * | 40.0 | 0.0 | 20.0 | <0.001 | * | 40.0 | 0.0 | 20.0 | 0.000 | * |

**Table 2-3: Summary of ethanol-based buffer dilutions for LAMP.**

The average and standard deviation were calculated from 9 replicates. The ΔTTP is calculated by subtracting the average value for a given buffer concentration from the water condition (0%). A positive value indicates a cycle delay. *P*-values were calculated by a 1-tailed unequal variance t-test compared to the water condition (0%). A * indicates a delay of at least 0.5 min and *P*-value <0.05. Non-detects were assigned a value of 46.7 min. VWB = Zymo Viral Wash Buffer; PE = Qiagen PE Buffer.

| | Ethanol | | | | | VWB | | | | | PE | | | | |
|---|---|---|---|---|---|---|---|---|---|---|---|---|---|---|---|
| | Avg | Std | ΔTTP | p | * | Avg | Std | ΔTTP | p | * | Avg | Std | ΔTTP | p | * |
| 0% | 6.3 | 0.2 | | | | 7.1 | 0.6 | | | | 7.1 | 0.6 | | | |
| 0.03% | 6.4 | 0.2 | 0.1 | 0.277 | | 7.2 | 0.7 | 0.1 | 0.420 | | 7.4 | 0.8 | 0.3 | 0.185 | |
| 0.1% | 6.5 | 0.4 | 0.1 | 0.182 | | 7.2 | 0.6 | 0.1 | 0.368 | | 7.2 | 0.8 | 0.1 | 0.380 | |
| 0.32% | 6.6 | 0.2 | 0.2 | 0.022 | | 7.1 | 0.7 | 0.0 | 0.494 | | 7.3 | 0.8 | 0.2 | 0.230 | |
| 1% | 6.9 | 0.6 | 0.5 | 0.019 | * | 7.2 | 0.7 | 0.1 | 0.333 | | 7.8 | 0.8 | 0.7 | 0.021 | * |
| 3.2% | 9.7 | 1.0 | 3.3 | <0.001 | * | 8.6 | 1.2 | 1.5 | 0.003 | * | 13.1 | 12.6 | 6.0 | 0.096 | |
| 10% | 46.7 | 0.0 | 40.3 | <0.001 | * | 46.7 | 0.0 | 39.6 | <0.001 | * | 43.5 | 9.6 | 36.4 | <0.001 | * |

**Table 2-4: Summary of lysis buffer dilutions for LAMP.**

The average and standard deviation were calculated from 9 replicates. The ΔTTP is calculated by subtracting the average value for a given buffer concentration from the water condition (0%). A positive value indicates a cycle delay. *P*-values were calculated by a 1-tailed unequal variance t-test compared to the water condition (0%). A * indicates a delay of at least 0.5 min and *P*-value <0.05. Non-detects were assigned a value of 46.7 min. PB = Qiagen PB Buffer.

| | Shield | | | | | Lysis | | | | | PB | | | | |
|---|---|---|---|---|---|---|---|---|---|---|---|---|---|---|---|
| | Avg | Std | ΔTTP | p | * | Avg | Std | ΔTTP | p | * | Avg | Std | ΔTTP | p | * |
| 0% | 7.1 | 0.6 | | | | 7.1 | 0.6 | | | | 7.1 | 0.6 | | | |
| 0.03% | 6.7 | 0.5 | -0.4 | 0.078 | | 7.2 | 0.5 | 0.1 | 0.401 | | 7.0 | 0.8 | -0.1 | 0.338 | |
| 0.1% | 6.8 | 0.4 | -0.3 | 0.095 | | 7.2 | 0.4 | 0.1 | 0.331 | | 6.7 | 0.5 | -0.4 | 0.083 | |
| 0.32% | 38.2 | 16.9 | 31.1 | <0.001 | * | 8.4 | 1.0 | 1.3 | 0.002 | * | 6.3 | 0.5 | -0.8 | 0.005 | |
| 1% | 46.7 | 0.0 | 39.6 | <0.001 | * | 40.1 | 13.2 | 33.0 | <0.001 | * | 6.5 | 0.9 | -0.6 | 0.053 | |
| 3.2% | 46.7 | 0.0 | 39.6 | <0.001 | * | 46.7 | 0.0 | 39.6 | <0.001 | * | 44.9 | 5.4 | 37.8 | <0.001 | * |
| 10% | 46.7 | 0.0 | 39.6 | <0.001 | * | 46.7 | 0.0 | 39.6 | <0.001 | * | 46.7 | 0.0 | 39.6 | <0.001 | * |

*Inhibitory effects on NA amplification curves*

We observed that qPCR reactions with lysis buffer (**Figure 2.15a**, dashed lines) had lower amplification efficiency with each cycle compared with reactions lacking lysis buffer (**Figure 2.15a**, solid lines). This experiment demonstrates that the presence of lysis buffer causes a delay in the $C_q$ and a reduction in the endpoint fluorescence intensity. Meanwhile,

LAMP reactions with lysis buffer experienced an initiation delay, but the amplification rate and endpoint fluorescence intensity were not strongly affected (**Figure 2.15b**).

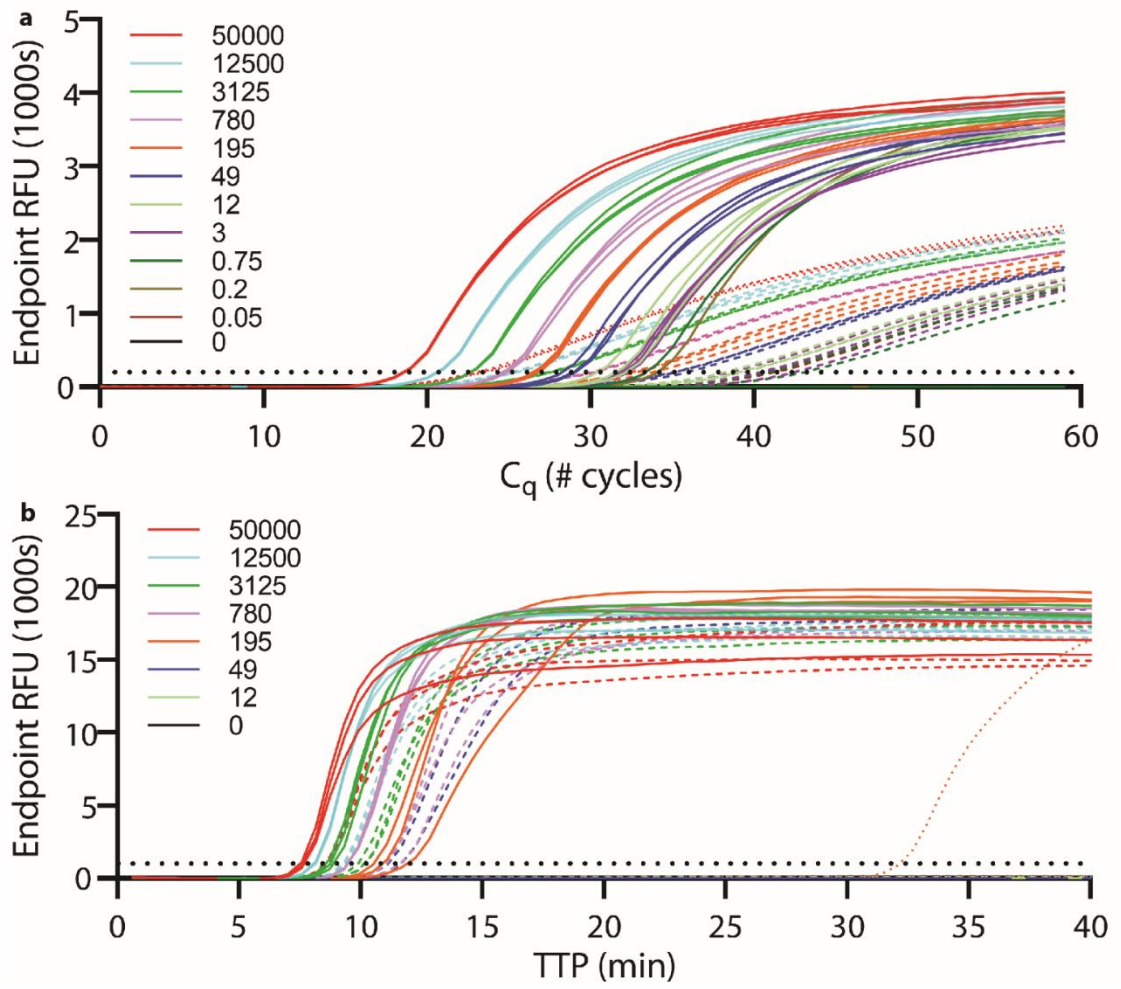


**Figure 2.15: (a) qPCR and (b) LAMP amplification curves with (dashed lines) or without (solid lines) Zymo Viral DNA/RNA Buffer for 4-fold dilutions of *E. coli* 23S rRNA gene copies.**

For qPCR we used 1% lysis buffer, and for LAMP we used 0.32% lysis buffer. Time-to-positive (TTP) threshold of 200 RFU for qPCR or 1000 RFU for LAMP is drawn as a dotted black line. Legend indicates the number of *E. coli* 23S rRNA gene

copies/rxn. The qPCR amplification curves correspond to the experiment in **Figure 2.3** of the main text.

*TPW screen with qPCR and LAMP*

**Table 2-5: TPW screen with qPCR.**

$\Delta C_q$ calculated by subtracting the "No additive" control from each condition.

| | Avg | Std | ΔCq | N |
|---|---|---|---|---|
| No additive | 20.09 | 0.01 | | 3 |
| water | 20.03 | 0.02 | -0.06 | 3 |
| Ethanol | 25.30 | 2.03 | 5.21 | 3 |
| Isopropanol | 24.54 | 2.66 | 4.44 | 3 |
| 1-butanol | N.D. | | | 0 |
| isopentanol | N.D. | | | 0 |
| 1-hexanol | N.D. | | | 0 |
| 1-heptanol | N.D. | | | 0 |
| 1-octanol | 23.63 | 1.10 | 3.54 | 2 |
| 1-nonanol | 20.07 | 0.07 | -0.03 | 3 |
| 1-decanol | 19.80 | 0.10 | -0.29 | 3 |
| 1-undecanol | 19.67 | 0.13 | -0.42 | 3 |
| 2-dodecanol | 19.81 | 0.03 | -0.28 | 3 |
| silicone oil | 19.86 | 0.19 | -0.23 | 3 |
| FC-40 | 20.15 | 0.17 | 0.06 | 3 |

**Table 2-6: TPW screen with LAMP.**

ΔTTP calculated by subtracting the "No additive" control from each condition.

| | Avg | Std | ΔTTP | N |
|---|---|---|---|---|
| No additive | 6.54 | 0.05 | | 3 |
| water | 7.09 | 0.05 | 0.55 | 3 |
| Ethanol | N.D. | | | 0 |
| Isopropanol | N.D. | | | 0 |
| 1-butanol | N.D. | | | 0 |
| isopentanol | N.D. | | | 0 |
| 1-hexanol | N.D. | | | 0 |
| 1-heptanol | N.D. | | | 0 |
| 1-octanol | 11.18 | 2.44 | 4.63 | 3 |
| 1-nonanol | 7.41 | 0.06 | 0.87 | 3 |
| 1-decanol | 7.06 | 0.03 | 0.51 | 3 |
| 1-undecanol | 6.70 | 0.03 | 0.16 | 3 |
| 2-dodecanol | 6.43 | 0.05 | -0.11 | 3 |
| silicone oil | 6.49 | 0.02 | -0.06 | 3 |
| FC-40 | 6.64 | 0.04 | 0.09 | 3 |

*Solubility table and ethanol phase separation for TPW candidates*

**Table 2-7: Solubility table for two-phase wash (TPW) candidates**

| Candidate TPW | Solubility of TPW Candidate in water | Solubility of water in TPW Candidate |
|---|---|---|
| FC-40 [1] | <0.0050 % | < 0.0007 g / 100 g |
| Silicone oil [2] | Practically insoluble | 0.01 - 0.02 g / 100 g |
| 2-dodecanol [3] | Unknown | Unknown |
| 1-dodecanol [3] | 0.0004 g / 100 g | 3.0 g / 100 g |
| 1-undecanol [4] | 0.0015 g / 100 mL | 3.4 g / 100 g |
| 1-decanol [3] | 0.0037 g / 100 g | 3.6 g / 100 g |
| 1-nonanol [3] | 0.014 g / 100 g | 4.0 g / 100 g |
| 1-octanol [3] | 0.054 g / 100 g | 4.6 g / 100 g |
| 1-heptanol [3] | 0.174 g / 100 g | 5.4 g / 100 g |
| 1-hexanol [3] | 0.6 g / 100 g | 7.0 g / 100 g |
| Isopentanol [3] | 2.7 g / 100 g | 9.8 g / 100 g |
| 1-butanol [3] | 7.4 g / 100 g | 20.3 g / 100 g |
| Isopropanol | miscible | miscible |
| Ethanol | miscible | miscible |

**Table 2-8: Compounds were mixed at a 1:1 volume ratio.**

A “2” denotes phase separation into 2 distinct phases, whereas a “1” forms a single phase. VWB stands for Zymo Viral Wash Buffer, which contained 80% ethanol (v/v).

| | $H_2O$ | Shield | Lysis | Ethanol | VWB |
|---|---|---|---|---|---|
| FC-40 | 2 | 2 | 1 | 2 | 2 |
| Silicone oil | 2 | 2 | 1 | 2 | 2 |
| 2-dodecanol | 2 | 2 | 2 | 1 | 1 |
| 1-undecanol | 2 | 2 | 2 | 1 | 1 |
| 1-octanol | 2 | 2 | 2 | 1 | 1 |

*Evaluating a 3-step centrifugation extraction with TPW*

We wanted to see whether in some cases the TPW could be considered as an alternative to the ethanol wash for removing lysis buffer. Exchanging the ethanol wash for a TPW could be useful for applications in which the starting sample is already relatively pure. For this experiment, we used the Zymo ZR kit, which only has three centrifugation steps: lysis (sample, shield, lysis buffer), wash (ethanol-based viral wash buffer), and elution (water). We either followed the manufacturer protocol or replaced the viral wash buffer with a dry spin, ethanol, or TPW (**Figure 2.16**). We added 5 µL of the resulting eluent to 5 µL of LAMP reaction mix and amplified at 68C. Eluent from the manufacturer protocol amplified in 5.7 min. The dry spin did not amplify, which is expected because lysis buffer was not removed by any wash steps, and lysis buffer is very inhibitory for LAMP. A 100% ethanol wash performed slightly better (earlier TTP) than the viral wash buffer, and both 1-octanol and 2-dodecanol outperformed the wash buffer. Meanwhile, eluent from the silicone oil and FC-40 wash conditions did not amplify. A dPCR experiment on heavy dilutions of the eluent show similar recovery for all conditions, with a slight reduction for the silicone oil wash. This demonstrates that 1-octanol and 2-dodecanol remove lysis buffer from the column. The simplicity of a 3-step protocol (bind, wash, elute) is compatible with point-of-care devices (few steps), and could be useful for applications with relatively clean samples.

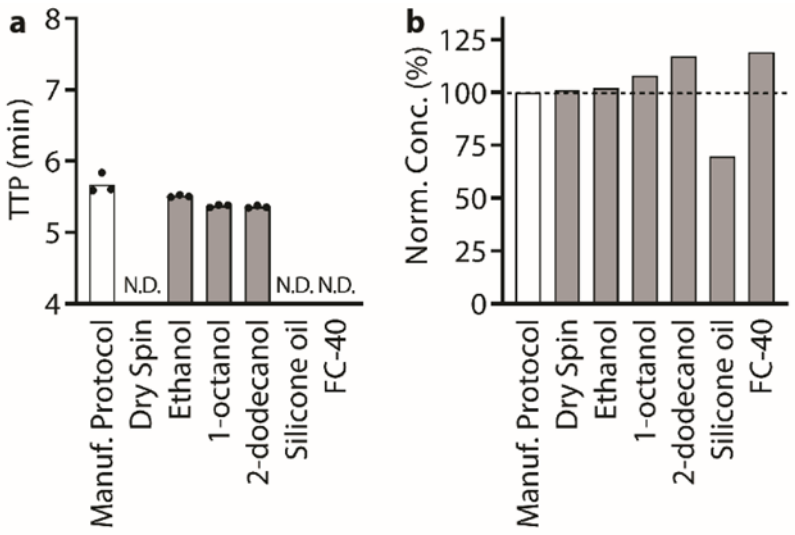


**Figure 2.16: Evaluation of TPW as a potential alternative to ethanol-based viral wash buffer in a Zymo ZR kit.**

(a) LAMP reaction with 2x dilution of eluent and (b) dPCR reaction with 100x dilution of eluent. Bars represent the average of technical LAMP triplicates or merged duplicate dPCR measurements. We ran 7 extractions (1 silica column x 7 conditions), and same eluent was used LAMP and dPCR reactions. No template controls (n=3) and samples marked N.D. were not detected within 40 min.

*Evaluating a low-carryover, high-yield MagBead protocol*

The manufacturer protocol for the Zymo Quick-DNA/RNA Viral MagBead Kit led to significant extraction buffer carryover (as shown in **Figure 2.7-8**). To improve NA yield with the added TPW, we performed the initial TPW aspiration, waited at least 1 min, and aspirated any remaining TPW. This second aspiration collected a few microliters of residual buffer that dripped down from the walls of the tube or from the magnetic beads. To reduce carryover of all buffers, we also applied this 1 min wait and secondary aspiration to all steps (lysis/binding buffer, wash buffers). We evaluated this modified protocol for different TPWs, and the results are shown in **Figure 2.17**. At high dilutions of eluent, there were no visible indicators of inhibition for any of the samples. Our modified protocol greatly reduced

carryover overall, such that qPCR began to work even at low dilutions (whereas when run using the standard manufacturer protocol, we saw inhibition). The addition of the TPW further improved LAMP at low dilutions. Finally, NA recovery improved to 75-100%, achieving our original goal.

When inhibitors are a major concern and time is not an issue, we recommend performing the MagBead protocol with secondary aspirations on each step, adding a 10-min dry step, and adding the TPW. For an approach balancing performance and assay time, we recommend following the manufacturer protocol, replacing the 10-min dry step with the TPW, and adding a secondary aspiration step just prior to the elution.

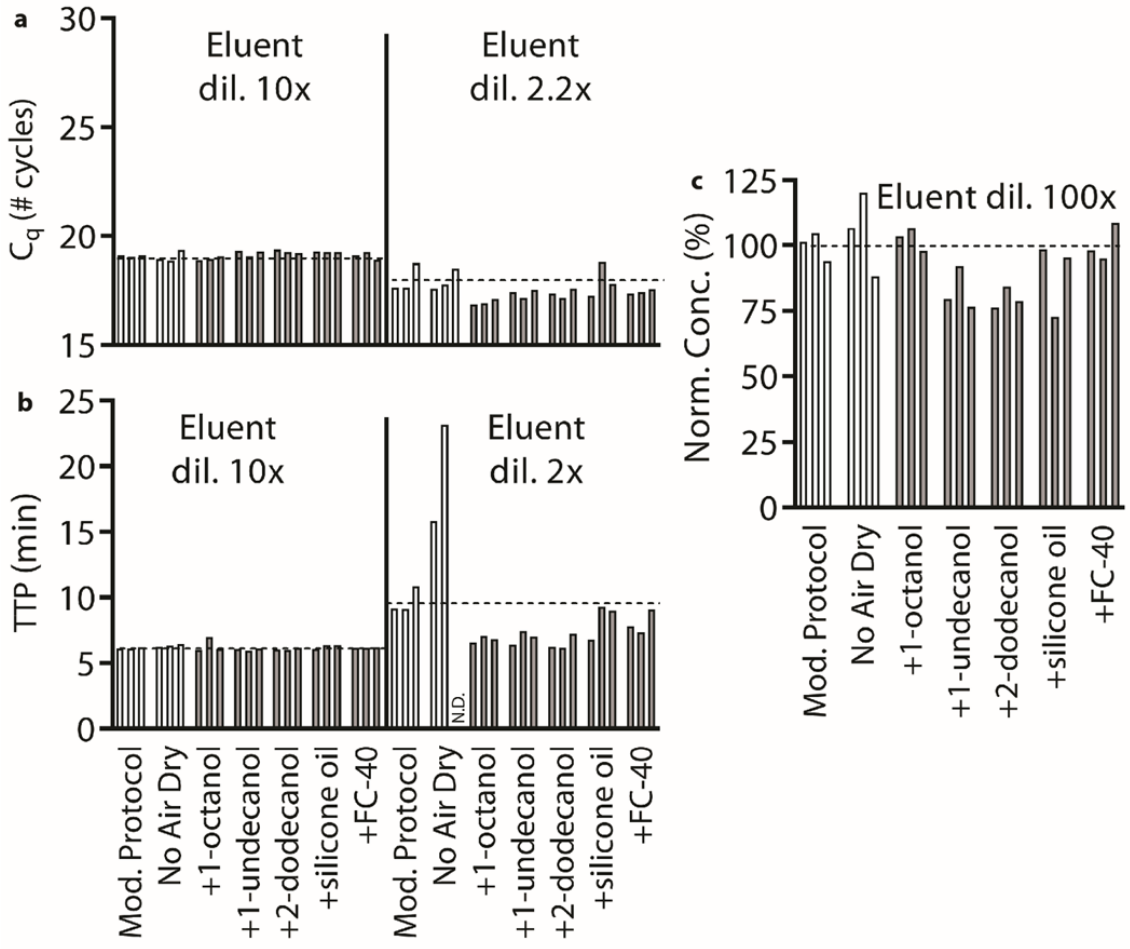


**Figure 2.17: Evaluation of a modified Zymo Quick-DNA/RNA Viral MagBead Kit for reduced carryover with and without TPW by (a) qPCR, (b) LAMP, or (c) dPCR.**

All conditions were performed with a modified protocol for high NA yield when combined with TPW. MagBead extractions were performed on 2.5 x $10^6$ λ phage DNA copies. Low and high eluent dilutions evaluated by qPCR and LAMP. A 100x eluent dilution into dPCR shows high yield with TPW. Bars represent single qPCR and LAMP reactions or merged duplicate dPCR measurements. We ran 21 extractions (3 magnetic-bead extractions x 7 conditions), and the same eluent was used in qPCR, LAMP, and dPCR analyses.

*Statistical analysis methods*

Confidence intervals were calculated assuming the populations to be normally distributed and using a t statistic. For buffer inhibition experiments, statistical analysis was performed by a 1-tailed unequal variance t-test (N=9) comparing the water condition (control) to each buffer concentration ($H_1$: the mean is delayed). For the subsequent experiments, we used a 2-tailed unequal variance t-test ($H_1$: the means are different). Non-detects were assigned the maximum possible $C_q$ measurement of 40 cycles or a TTP of 46.7 min to indicate the lack of amplification. Although this approach introduces some bias into the analysis, we believe this is the best representation for handling non-detects (other alternatives include excluding the non-detects or assigning non-detect values to the average of those that amplified).

There are many potential sources of experimental variation (e.g. column-to-column, day-to-day generation of master mix, buffer dilutions, and pipetting errors), and we tried to control for these by running triplicates for different variables (buffer/MM dilutions, columns, technical qPCR/LAMP assays). *A priori*, we would have assumed our independent variables to be differences in buffer dilutions or differences among columns, and we expected that our technical replicates would display a narrow distribution. Instead, we observed large variations among technical replicates (e.g. 2 out of 3 amplify). Because large variations appear at the level of the technical replicate, we treated each technical replicate as an independent sample in our statistical analysis.

Familywise error rate across the reported statistical analyses was not controlled (e.g. Bonferroni correction). All data have been made publicly available and, to strengthen the findings of this study, we encourage further replication and validation, as there are numerous different potential applications and variables to examine (e.g. sample matrices, extraction kits, sequencing, etc.).

**References**

1. 3M Fluorinert™ FC-40 Electronic Liquid. *MatWeb Material Property Data* http://www.matweb.com/search/DataSheet.aspx?MatGUID=2072a809f9ca4d529b1d136660736f81

2. Silicone Fluids: Stable, Inert Media. *Gelest, Inc* (2004).

3. Barton, Allan FM. Alcohols with Water in *Solubility Data Series Volume 15* (2013).

4. 1-Undecanol. *GESTIS Substance Database* http://www.dguv.de/ifa/gestis-database

*Chapter 3*

# COMMERCIAL STOCKS OF SARS-COV-2 RNA MAY REPORT LOW CONCENTRATION VALUES, LEADING TO ARTIFICIALLY INCREASED APPARENT SENSITIVITY OF DIAGNOSTIC ASSAYS

E. Jue and R.F. Ismagilov. 2020. *medRxiv*. pre-print. doi: 10.1101/2020.04.28.20077602

**Abstract**

In response to the rapidly evolving COVID-19 pandemic, the U.S. Food and Drug Administration (FDA) has rapidly issued 49 emergency use authorizations (EUAs) for SARS-CoV-2 in vitro diagnostic test-kits. A critical metric in the performance evaluation for a diagnostic test kit is the analytical sensitivity, which is measured by the limit of detection (LOD). Commercial RNA stocks with known titers are used to determine LOD. We identified a problem with the titer reported for the commercial stocks when examining the analytical sensitivity of the reverse transcription quantitative PCR (RT-qPCR) protocol that is recommended by the Centers for Disease Control and Prevention (CDC) using plasmid DNA from Integrated DNA Technologies (IDT), synthetic RNA from BEI Resources (BEI), and extracted genomic RNA from BEI. We detected 3/3 positives for reactions containing synthetic RNA at a concentration of 0.1 copies/reaction (based on the supplier's label concentration). The apparent better-than-single-molecule performance is a statistically highly unlikely event, indicating a potential inaccuracy in the supplier's quantification of the stock material. Using an ultrasensitive and precise assay, reverse transcription digital PCR (RT-dPCR), we independently quantified concentrations of commercial SARS-CoV-2 plasmid DNA and SARS-CoV-2 RNA stocks. For plasmid DNA, the actual concentration

measured by RT-dPCR was 11% of the nominal label concentration. For synthetic RNA, the actual concentration measured by RT-dPCR for one lot was 770% of the label concentration, and for a different lot was 57% of the label concentration. For genomic RNA, the concentration measured by RT-dPCR for one lot was 240% of the label concentration, and for a different lot it was 300% of the label concentration. This SARS-CoV-2 genomic RNA from BEI Resources has been used in at least 11 approved FDA Emergency Use Authorizations as of April 27, 2020. Such deviations of reported RNA or DNA stock concentrations from true concentrations can result in inaccurate quantification and calculation of LOD. Precise and accurate reporting of DNA and RNA stock concentrations by commercial suppliers will enable accurate quantification of assay performance, which is urgently needed to improve evaluation of different assays by diagnostic developers and regulatory bodies.

## Introduction

As of April 27, 2020, the COVID-19 pandemic has reached 185 countries/regions, with more than 3 million infected individuals, and more than 210,000 deaths.[1, 2] The rapid spread of SARS-CoV-2 (the virus that causes COVID-19) and the large proportion of asymptomatic infected individuals has led to widespread demand for diagnostic test kits. To meet the massive demand, on February 4, 2020, the U.S. Department of Health and Human Services (HSS) secretary declared that circumstances exist justifying the authorization of emergency use of *in vitro* diagnostics for detecting SARS-CoV-2.[3] Since then, the U.S. Food and Drug Administration (FDA) has fast-tracked 49 Emergency Use Authorizations (EUAs) for SARS-CoV-2 test-kit manufacturers and commercial laboratories.[4]

The application to receive an EUA requires a description of the assay and an evaluation of its performance.[5] A key metric in evaluating assay performance is the analytical sensitivity, which describes the ability of a test to detect very low concentrations of the target analyte. Analytical sensitivity is typically measured using the limit-of-detection (LOD), which is the

concentration of target analyte that can be consistently detected at least 95% of the time (19 of 20 replicates are positive). It is important for test kits to demonstrate a low LOD, which indicates good sensitivity of the test and the ability to detect samples containing very low viral RNA concentrations. Thus far, many diagnostic test kits for SARS-CoV-2 RNA have reported good LODs, with some reporting down to as low as 40 copies/mL.

We obtained SARS-nCoV-2 plasmid DNA from IDT, synthetic SARS-nCoV-2 RNA from BEI, and genomic RNA from SARS-nCoV-2, isolate USA-WA1/2020 from BEI. In a well-functioning assay (i.e., perfect transcription of RNA), we would expect to observe the same LOD for all 3 stocks. Instead, using the quantitative reverse transcription polymerase chain reaction (RT-qPCR) protocol recommended by the Centers for Disease Control and Prevention (CDC), we found substantial discrepancies, leading us to question the accuracy of the reported stock concentrations from the commercial suppliers.

In this manuscript, we aimed to resolve the discrepancies in the LODs obtained with the three SARS-CoV-2 NA stocks by performing our own quantification of each stock concentration using a highly sensitive digital quantification method, reverse transcription digital PCR (RT-dPCR).[6, 7]

## Results and Discussion

### *Half-log dilutions of NA stocks in RT-qPCR*

We first performed half-log dilutions on each SARS-CoV-2 NA stock (plasmid DNA from 10,000 to 3.16 nominal copies/reaction and synthetic RNA and genomic RNA from 100 to 0.0316 nominal copies/reaction) using the CDC-recommended RT-qPCR protocol (**Figure 3.1**). *A priori*, we expect all NA stocks to have similar LOD. We also expect that the RNA LOD may be slightly worse than the DNA LOD because RNA must be transcribed prior to amplification. Contrary to these expectations, we observed that both RNA stocks outperformed the DNA stock. The first non-detects (reactions failing to amplify) appeared at

3.16 copies/reaction for plasmid DNA (**Figure 3.1A**), at 0.0316 copies/reaction for synthetic RNA (**Figure 3.1B**), and at 0.316 copies/reaction for genomic RNA (**Figure 3.1C**). We also observed lower Cq values for synthetic RNA compared with genomic RNA at the same input dilution (using the supplier's label concentration).

Of particular interest, when quantifying the synthetic RNA, we detected 3/3 positives at a dilution of just 0.1 copies/reaction, indicating a virtually impossible better-than-single-molecule assay performance. An RT-qPCR reaction requires a minimum of 1 RNA copy as a template to exponentially amplify and generate a detectable signal. Better-than-single-molecule assay performance is highly unlikely based on statistics. Using the Poisson distribution,[8] which accounts for the stochasticity in loading a reaction well, when loading a solution into a well at an average target RNA concentration of 0.1 copies/reaction, there is a ~9.5% chance that a reaction well actually contains at least one RNA copy. If testing a set of 3 reaction wells, the probability that all 3 wells contains at least one RNA copy each drops to 0.086% (0.0953).

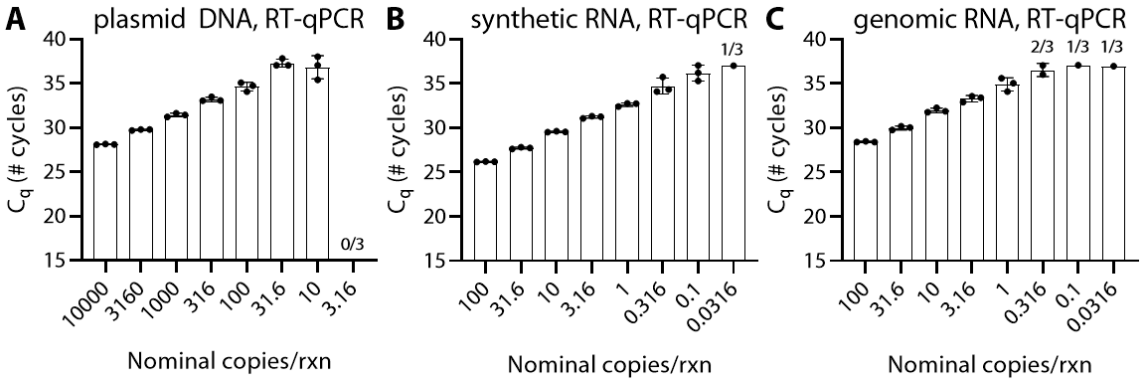


**Figure 3.1: Better-than-statistically-likely performance of reverse-transcription quantitative PCR (RT-qPCR) protocol recommended by the CDC using half-log dilution series of SARS-CoV-2 nucleic-acid targets.**

Plots show number of quantitation cycles (Cq) for half-log dilutions of (A) plasmid DNA lot 508728 from Integrated DNA Technologies (IDT), (B) synthetic RNA lot

70033953 from BEI Resources (BEI), and (C) genomic RNA lot 70033700 from BEI. No-template controls (n=24) did not amplify after 80 cycles.

*Re-quantification of NA stocks with RT-dPCR*

To resolve the differences in LOD and understand the apparent better-than-single-molecule performance of the CDC assay, we re-quantified the NA stocks using an RT-dPCR protocol (Bio-Rad dPCR EvaGreen Supermix with added WarmStart Rtx (NEB) (**Figure 3.2**). We first ran 16 no-template controls and measured an average background concentration of 1.9 ± 1.0 copies/µL. We defined the assay detection limit (99.7% confidence) as the background concentration plus 3 standard deviations of the background,[9] and calculated the assay detection limit of RT-dPCR to be 4.9 copies/µL. To quantify each stock concentration, we first diluted the NA stock down to a concentration within the digital quantification range (10 - 120,000 input copies of target) and measured with RT-dPCR.[10] We then took the concentration obtained from the RT-dPCR measurement, subtracted the background concentration, and multiplied the result by the dilution factor to calculate our RT-dPCR measured stock concentration.

We ran a dilution series for each SARS-CoV-2 NA stock. For plasmid DNA (IDT, lot 508528), we observed that all RT-dPCR quantifications were systematically lower than the concentration we expected from the supplier's label concentration, except when our measurements dropped below the assay detection limit (**Figure 3.2A**). To further validate our results, we performed 2 additional dilutions down to what should have been 633 copies/µL. Of the three measurements taken at 633 copies/µL, two were performed using RT-dPCR, and the third was performed using dPCR (no reverse transcription). The RT-dPCR measurements were 69 and 66 copies/ µL, and the dPCR measurement was 65 copies/µL. As expected for DNA, there was no difference in our measurements when using the dPCR assay with or without reverse transcription. To reduce the contributions of Poisson noise and background signal on our quantification, we used the highest concentration that we tested to quantify the stock concentration. Using the dilution for which we expected 2000

plasmid DNA copies/µL, we actually measured 220 copies/µL. From this measurement, we calculated a stock concentration of $2.2x10^4$ copies/µL, which is 11% of the supplier's label concentration of $2x10^5$ copies/µL.

For synthetic RNA (BEI, lot 70033953), we observed that all RT-dPCR quantifications were systematically higher than the supplier's label concentration of $5x10^5$ copies/µL (**Figure 3.2B**). We performed two additional dilutions (three in total) down to what should have been 6.33 copies/µL and observed that all three values were higher than expected (54, 67, and 66 copies/µL). In a separate experiment, we performed dPCR (no reverse transcriptase) and observed that the signal was below background levels, which is expected because no amplification should occur in an RNA sample in the absence of reverse transcriptase. Using the dilution for which we expected 2000 copies/µL (based on the label concentration), we actually measured 15,000 copies/µL. From this measurement, we calculated a stock concentration of $3.9x10^6$ copies/µL, which is 770% of the supplier's label concentration of $5x10^5$.

For genomic RNA (BEI, lot 70033700), we observed that all RT-dPCR quantifications were systematically higher than the supplier's label concentration of $5.5x10^4$ copies/µL (**Figure 3.2C**). We performed two additional dilutions (three in total) down to what should have been 6.33 copies/µL and observed that all three values were higher than expected (19, 15, and 23 copies/µL). The genomic RNA in a dPCR (no reverse transcription) experiment also measured below the background signal. Using the dilution for which we expected 63.3 copies/µL, we actually measured 155 copies/µL. From this measurement, we calculated a stock concentration of $1.3x10^5$ copies/µL, which is 240% of the supplier's label concentration of $5.5x10^4$.

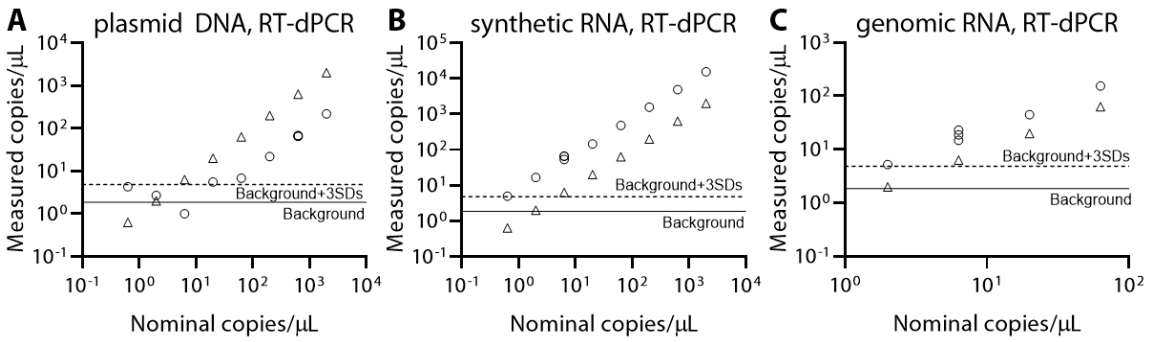


**Figure 3.2: Quantification of different SARS-CoV-2 nucleic acid targets using an RT-dPCR protocol.**

Plots show measured concentration (circles) for half-log dilutions of the label concentrations (triangles) based on supplier-reported values of (A) plasmid DNA (lot 508728 from IDT), (B) synthetic RNA (lot 70033953 from BEI), and (C) genomic RNA (lot 70033700 from BEI). Individual dilution series were repeated twice more for the 633 copies/µL dilution with plasmid DNA and the 6.33 copies/µL dilution for both RNA stocks. The background (solid line) was calculated by averaging no-template controls (n=16), and the assay detection limit (dashed line) was calculated as the background signal in no-template controls plus 3 standard deviations of the background signal (99.7% confidence).[9]

We next investigated potential differences among lots of stock SARS-CoV-2 RNA. We obtained an additional lot of synthetic RNA (lot 70034198) and an additional lot of genomic RNA (lot 70033320) from the same supplier (BEI). For each, we diluted the label concentration down to what should have been 63.3 copies/µL and measured the concentration with RT-dPCR (n=1). The synthetic RNA stock (lot 70034198) measured 38 copies/µL. From this, we calculated a concentration of $1.7 \times 10^5$ copies/µL, which is 57% of the label concentration of $2.9 \times 10^5$ copies/µL. We note that lot 70034198 was much closer (57%) to the label value as compared with lot 70033953 (770%). The genomic RNA stock (lot 70033320) measured 193 copies/µL. From this measurement, we calculated a concentration of $1.4 \times 10^5$ copies/µL, which is 300% of the label concentration of $4.8 \times 10^4$

copies/µL. We found that the RT-dPCR measurements for genomic RNA stocks were similarly higher (240% for lot 70033700, 300% for lot 70033320) than the supplier's label concentration.

*Dilutions of NA stocks in RT-qPCR with RT-dPCR correction*

Next, we selected concentrations near the LOD for each NA stock, and reran RT-qPCR with greater sample size (N=10 for each of three dilutions of each stock, **Table 3-1**). If we use the suppliers' label concentrations to understand the RT-qPCR results, we observed large deviations (orders of magnitude differences) from expected values. For example, 3 of 10 wells turned positive for a label concentration diluted to 0.0316 copies/reaction with synthetic RNA (lot 70033953), whereas we would expect (based on statistical calculations) for 3 out of 100 wells to be positive. We also note that only 7 of 10 wells turned positive for a label concentration diluted to 31.6 copies/reaction with plasmid DNA (lot 528728), whereas statistically we expect all 10 wells to turn positive (assuming single-molecule detection). By Poisson distribution, we would expect 1 out of every $5x10^{13}$ wells to be negative at this concentration.

If we instead use our RT-dPCR measured concentrations to understand our RT-qPCR results, the observed results are statistically more likely for all 3 NA stocks. The highest tested concentrations of plasmid DNA (lot 5208728), synthetic RNA (lot 70033953), and genomic RNA (lot 70033700) were measured by RT-dPCR to have concentrations of 3.45, 2.44, and 2.42 copies/reaction respectively. We observed 70%, 100%, and 90% positives for these conditions, which is a reasonable result considering that the Poisson distribution corresponding to 3 copies/reaction predicts an expected value (most likely) of 95% positives. For the tested concentrations measured by RT-dPCR to be near 1 copy/reaction with an expected value of 63% positives, we observed 30%, 80%, and 60% positives. Lastly, for the lowest tested concentrations measured by RT-dPCR to be near 0.3 copies/reaction with an expected value of 26% positives, we observed 20%, 30%, and 60% positives.

**Table 3-1: Analytical performance near the limit of detection (LOD) for different SARS-CoV-2 targets in the CDC-recommended RT-qPCR protocol.** Each nucleic acid stock was diluted, and we selected 3 different concentrations to spike into RT-qPCR reaction wells (10 replicates for each condition). Measured concentrations were used to convert the label concentrations based on the RT-dPCR measurements reported in **Figure 3.2**. Positives were counted as detected if they amplified within 40 cycles. No-template controls (N=6) did not amplify after 80 cycles.

| | Label concentration (copies/reaction) | RT-dPCR measured concentration (copies/reaction) |
|---|---|---|
| **plasmid DNA (IDT) lot 508728** | | |
| Detected 7 of 10 | 31.6 | 3.45 |
| Detected 3 of 10 | 10 | 1.09 |
| Detected 2 of 10 | 3.16 | 0.345 |
| **synthetic RNA (BEI) lot 70033953** | | |
| Detected 10 of 10 | 0.316 | 2.44 |
| Detected 8 of 10 | 0.1 | 0.772 |
| Detected 3 of 10 | 0.0316 | 0.244 |
| **genomic RNA (BEI) lot 70033700** | | |
| Detected 9 of 10 | 1 | 2.42 |
| Detected 6 of 10 | 0.316 | 0.765 |
| Detected 5 of 10 | 0.1 | 0.242 |

## Conclusions

In this chapter, we observed vast discrepancies in the analytical sensitivity of the CDC-recommended RT-qPCR protocol based on which commercial NA stock was used. Performing an ultrasensitive digital PCR method, RT-dPCR, revealed there are likely errors in the supplier-reported concentrations. Specifically, using RT-dPCR, the measured concentration of plasmid DNA (IDT, lot 508728) was 11% of the label concentration. For synthetic RNA (BEI), the measured concentration by RT-dPCR was 770% of the label concentration for lot 70033953, whereas it was 57% of the label concentration for lot 70034198. For genomic RNA (BEI), the measured concentration by RT-dPCR was 240% of

the label concentration for lot 70033700 and 300% of the label concentration for lot 70033320. An underreporting of the stock concentration could lead to an artificially improved LOD for a diagnostic assay. Such discrepancies in how NA suppliers quantify their stock can introduce significant biases and impair proper development and evaluation of *in vitro* diagnostics being considered for regulatory approvals and mass production.

The inaccurate quantification of the SARS-nCoV-2 genomic RNA concentration is concerning because our analysis of EUA documents indicated that this RNA stock (BEI, NR-52285) has been used in at least 11 EUAs: Lyra SARS-CoV-2 Assay, Abbott RealTime SARS-CoV-2 assay, AvellinoCoV2 test, NxTAG CoV Extended Panel Assay, NeuMoDx SARS-CoV-2 Assay, COV-19 IDx assay, BioGX SARS-CoV-2 Reagents for BD MAX System, ARIES SARS-CoV-2 Assay, Logix Smart Coronavirus Disease 2019 (COVID-19) Kit, Smart Detect SARS-CoV-2 rRT-PCR Kit, BD SARS-CoV-2Reagents for BD MAX System, and Curative-Korva SARS-Cov-2 Assay.[4] We note that the GeneFinder COVID-19 Plus RealAmp Kit and the STANDARD M nCoV Real-Time Detection Kit both report using genomic RNA, but we could not determine whether or not BEI was the supplier. Of the kits that used BEI genomic RNA, the majority did not report the lot or starting stock concentration (which could be used to deduce the lot number).

Discrepancies in stock quantification can be attributed to multiple factors, including differences in quantification method, reaction conditions, reverse transcriptase efficiency, polymerase efficiency, etc. We acknowledge that no assay is perfect (ours included), and it is virtually impossible to obtain a “true“ count of an underlying NA concentration. Nevertheless, it is possible to come close using an assay which yields the highest NA concentration, has low background, and produces statistically plausible results. For this, here we have successfully used ultrasensitive digital RT-dPCR. We suggest that RT-dPCR or a similarly improved methodology is implemented for quantification of all RNA stocks used for SARS-CoV-2 assays being submitted for emergency use authorization or equivalent regulatory approval. We also encourage independent evaluations of *in vitro* diagnostic assay performance using the same quantified standards by unbiased sources.[11]

## Materials and Methods

### Stocks and Dilutions

A DNA plasmid control (2019-nCoV, research-use only) was purchased from Integrated DNA Technologies (IDT; Coralville, Iowa, USA; Cat#148365270, Lot 0000508728; $2x10^5$ copies/µL). Quantitative Synthetic RNA from SARS-Related Coronavirus 2, NR-52358 (Lot 70033953, $5x10^5$ genome equivalents/µL; Lot 70034198, $2.9x10^5$ genome equivalents/µL) and Genomic RNA from SARS-Related Coronavirus 2, Isolate USA-WA1/2020, NR-52285 (Lot 70033700, $5.5x10^4$ genome equivalents/µL; Lot 70033320, $4.8x10^4$ genome equivalents/µL) were obtained from BEI Resources (Manassas, VA, USA). All stocks were aliquoted and stored at -80 C. For all dilution series, an aliquot was thawed and serially diluted in 1x TE buffer with 0.05% Tween-20 in 1.5 mL DNA LoBind Tubes (USA Scientific Incorporated; Ocala, FL, USA).

### RT-qPCR

qPCR was performed using protocol recommendation from the CDC's Real-Time RT-PCR Panel for Detection of 2019-Novel Coronavirus.[12] Briefly, 5 µL TaqPath 1-Step RT-qPCR Master Mix (ThermoFisher Scientific, Waltham, MA, USA) was added to 1.5 µL combined primer/probe mix (N1; Lot 0000509022 from IDT's 2019-nCoV CDC qPCR Probe Assay), and 8.5 µL nuclease-free water. Master-mix was added to a 96-well plate (thin-wall clear well, HSP9641, Bio-Rad), and 5 µL of template was mixed by pipette in individual wells. The 96-well plate was sealed (Microseal B, MSB1001, Bio-Rad) and spun briefly in a Mini Plate Spinner Centrifuge (14-100-141, Fisher Scientific) to bring down droplets. Thermocycling and real-time imaging were performed on the Bio-Rad CFX96 Touch Real-Time PCR Detection System (Bio-Rad Laboratories, Hercules, CA, USA) by heating to 25 °C for 2 min, 50 °C for 15 min, 95 °C for 2 min, and cycling 80 times between 95 °C for 3 s and 55 °C for 30 s.

**RT-dPCR**

RNA was quantified with reverse transcription droplet digital polymerase chain reaction (RT-dPCR). Reaction mix contained 1X Bio-Rad EvaGreen ddPCR Mix, 200 nM forward and backward COVID primers (N1 primers purchased from IDT, re-suspended in NF-H2O),[13] 1 U/µL Riboguard RNase inhibitor (Lucigen Corp., Madison, WI, USA), and 300 U/mL WarmStart RTx (New England Biolabs, NEB; Ipswich, MA, USA). Template was added at 10% of the reaction mix and the original concentration calculated from the dilution series. All samples were made to 50 µL, and duplicates were run by adding 22 µL to two sample wells in the DG8 Cartridge (1864008, Bio-Rad). Dilutions were quantified using the QX200 droplet digital PCR system (Bio-Rad), and droplet generation, droplet transfer, and foil sealing followed manufacturer's instructions. Thermocycling took place on a C1000 Touch Thermal Cycler (Bio-Rad) with an RT step at 55 °C for 10 min, pre-melt at 95 °C for 3 min, 40 cycles of 95 °C for 30 s, 60 °C for 30 s, and 68 °C for 30 s, and a stabilization at 4 °C for 5 min, 90 °C for 5 min, and a hold at 12 °C until droplet analysis. A temperature ramp rate of 2 °C/s was used for temperature transitions. Droplets were read according to manufacturer's instructions. Analysis thresholds were manually set to 10,000. Final concentrations were determined using the merge setting on the QuantaSoft analysis software (Bio-Rad). Measured stock concentrations were calculated by subtracting background (signal average of 16 no-template controls) and multiplying by the dilution factor.

**References**

1. CSSE. COVID-19 Dashboard by the Center for Systems Science and Engineering (CSSE) at Johns Hopkins University (JHU) 2020. Available from: https://gisanddata.maps.arcgis.com/apps/opsdashboard/index.html#/bda7594740fd40299423467b48e9ecf6.

2. Johns Hopkins Coronavirus Resource Center. COVID-19 Data Center. Available from: https://coronavirus.jhu.edu/.

3. Federal Register. Determination of Public Health Emergency: A notice by the Health and Human Services Department on 02/07/2020. 2020.

4. FDA. Emergency Use Authorization (EUA) information, and list of all current EUAs 2020. Available from: https://www.fda.gov/emergency-preparedness-and-response/mcm-legal-regulatory-and-policy-framework/emergency-use-authorization#2019-ncov.

5. FDA. Policy for Diagnostic Tests for Coronavirus Disease-2019 during the Public Health Emergency Immediately in Effect Guidance for Clinical Laboratories, Commercial Manufacturers, and Food and Drug Administration Staff. 2020.

6. Sanders R, Huggett JF, Bushell CA, Cowen S, Scott DJ, Foy CA. Evaluation of Digital PCR for Absolute DNA Quantification. Analytical chemistry. 2011;83(17):6474-84. doi: 10.1021/ac103230c.

7. Shen F, Du W, Kreutz JE, Fok A, Ismagilov RF. Digital PCR on a SlipChip. Lab on a chip. 2010;10(20):2666-72. Epub 2010/07/03. doi: 10.1039/c004521g.

8. Majumdar N, Wessel T, Marks J. Digital PCR modeling for maximal sensitivity, dynamic range and measurement precision. PloS one. 2015;10(3):e0118833-e. doi: 10.1371/journal.pone.0118833.

9. Analytical Methods C. Recommendations for the definition, estimation and use of the detection limit. Analyst. 1987;112(2):199-204. doi: 10.1039/AN9871200199.

10. Bio-Rad. Droplet Digital PCR Applications Guide 2014. Available from: http://www.bio-rad.com/webroot/web/pdf/lsr/literature/Bulletin_6407.pdf.

11. FIND. FIND Evaluation update: SARS-CoV-2 Molecular Diagnostics 2020. Available from: https://www.finddx.org/covid-19/sarscov2-eval-molecular/.

12. CDC. Real-Time RT-PCR Panel for Detection 2019-Novel Coronavirus. Centers for Disease Control and Prevention, Respiratory Viruses Branch, Division of Viral Diseases, 2020.

13. CDC. Research Use Only 2019-Novel Coronavirus (2019-nCoV) Real-time RT-PCR Primer and Probe Information 2020. Available from: https://www.cdc.gov/coronavirus/2019-ncov/lab/rt-pcr-panel-primer-probes.html.

*Chapter 4*

# EVALUATING 3D PRINTING TO SOLVE THE SAMPLE-TO-DEVICE INTERFACE FOR LRS AND POC DIAGNOSTICS: EXAMPLE OF AN INTERLOCK METER-MIX DEVICE FOR METERING AND LYSING CLINICAL URINE SAMPLES

E. Jue, N.G. Schoepp, D. Witters, and R.F. Ismagilov. 2016. *Lab on a Chip*. 16:1852-1860. doi:10.1039/c6lc00292g

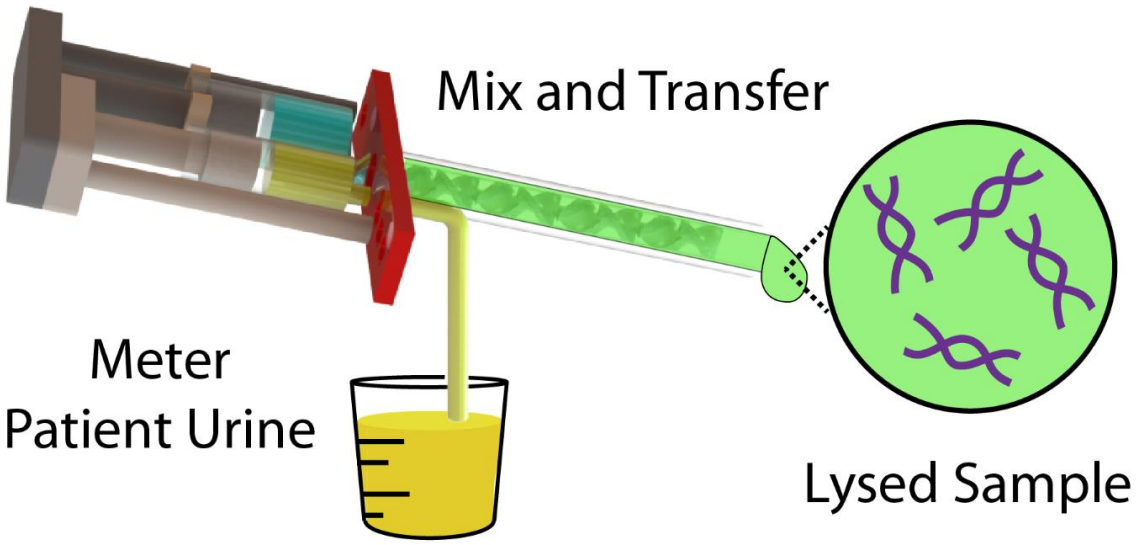


**Abstract**

This chapter evaluates the potential of 3D printing, a semi-automated additive prototyping technology, as a means to design and prototype a sample-to-device interface, amenable to diagnostics in limited-resource settings, where speed, accuracy, and user-friendly design are critical components. As a test case, we built and validated an interlock meter-mix device for

accurately metering and lysing human urine samples for use in downstream nucleic acid amplification. Two plungers and a multivalve generated and controlled fluid flow through the device and demonstrate the utility of 3D printing to create leak-free seals. Device operation consists of three simple steps that must be performed sequentially, eliminating manual pipetting and vortexing to provide rapid (5 to 10 s) and accurate metering and mixing. Bretherton's prediction was applied, using the Bond number to guide a design that prevents potentially biohazardous samples from leaking from the device. We employed multi-material 3D printing technology, which allows composites with rigid and elastomeric properties to be printed as a single part. To validate the meter-mix device with a clinically relevant sample, we used urine spiked with inactivated *Chlamydia Trachomatis* and *Neisseria gonorrhoeae*. A downstream nucleic acid amplification by quantitative PCR (qPCR) confirmed there was no statistically significant difference between samples metered and mixed using the standard protocol and those prepared with the meter-mix device, showing the 3D-printed device could accurately meter, mix, and dispense a human urine sample without loss of nucleic acids. Although there are some limitations to 3D printing capabilities (e.g. dimension limitations related to support material used in the printing process), the advantages of customizability, modularity and rapid prototyping illustrate the utility of 3D printing for developing sample-to-device interfaces for diagnostics.

## Introduction

We evaluate multi-material 3D printing for the design and prototyping of an interlock meter-mix device that meters and lyses human urine samples for a workflow compatible with limited-resource settings (LRS) and point of care (POC) diagnostic testing. 3D printing comprises a set of additive manufacturing techniques that allows the formation of complex 3D structures with minimal restrictions. The emerging technological capabilities of 3D printing bring exciting advancements in the fabrication of micro- and macrofluidic devices, enabling architectures that would be difficult with conventional fabrication techniques such as soft lithography.[1,2] A primary advantage of 3D printing is the ability to rapidly prototype

and iterate new designs, without needing to tool expensive molds.[3] 3D printing reduces the design and prototyping time from weeks and months down to hours and days, making prototyping more cost-effective and therefore more accessible—particularly for research labs where needs may change frequently. Because 3D printing is semi-automated, it minimizes assembly time, the requirements for labor, and reproducibility issues, therefore reducing many of the barriers that currently prevent some research labs from prototyping complex 3D parts.[2] The customizable design files generated in computer-aided design (CAD) software can be easily modified in coordination with experiments. 3D-printed materials also exhibit a wide range of properties, with varying levels of rigidity, surface roughness, optical clarity, and biocompatibility to fit a diverse range of device requirements.[4] In combination, all of these advantages make 3D printing attractive for prototyping fluidic devices relevant to lab-on-a-chip and diagnostics fields.

The sample-to-device interface for diagnostics is a critical component of nucleic acid amplification testing (NAAT) in LRS, and remains an unsolved challenge.[5,6] Many NAAT technologies are not amenable to LRS, because NAAT is an intrinsically multistep process involving sample metering, lysis, nucleic acid (NA) purification, amplification, and detection.[7] To be useful in clinical practice in POC or LRS, the entire NAAT workflow should be fully automated, user-friendly (without training or pipetting steps to meet CLIA-waiver), rapid, equipment-free, sensitive, and specific. To equip a portable device with complete sample-in to answer-out functionality requires the appropriate consideration of all upstream and downstream processes. While many efforts have been taken to automate nucleic acid (NA) purification and amplification, sample metering must always be addressed because a user in LRS or at the POC cannot be asked to pipette accurately. Furthermore, combining sample transfer with the step in which the sample is mixed with the lysis buffer is attractive, because it has the advantage of minimizing the cost and complexity of an integrated diagnostic device, and could benefit such devices being developed in research labs, including our own.[8-11] Precise metering is especially critical in NAAT testing of sexually transmitted diseases (STDs), such as *Chlamydia trachomatis* (CT) and *Neisseria gonorrhoeae* (NG).[12] In 2013, there were 1,401,906 and 333,004 reported cases of CT and

NG, respectively, in the United States, with many more cases unreported and undiagnosed.[13] The Centers for Disease Control and Prevention (CDC) estimates 20 million new STD infections per year in the US, accounting for $16 billion in healthcare costs.[13] The CDC now recommends NAAT for CT/NG diagnosis[14] because these tests are sensitive, accurate, and use non-invasive urine samples. Many of these tests need to be done under LRS or POC settings.

Currently, there is no standardized way to deliver a known amount of sample mixed with lysis buffer to an LRS- or POC-compatible NAAT diagnostic device. A method for doing so is subject to the following constraints: (i) meter a precise volume of urine with <5% coefficient of variation (CV), (ii) mix urine with premeasured, preloaded lysis buffer at a specific ratio (as determined by the extraction chemistry), (iii) transfer the lysed urine without dripping potentially infectious solution, (iv) perform these operations quickly, in a user-friendly, equipment-free manner that minimizes potential user errors, and (v) maintain the sensitivity and specificity of the overall assay (no loss of nucleic acids to 3D-printed surfaces, contamination, or leachates).

Here, we evaluate the capabilities of multi-material 3D printing to design and prototype a single-use disposable macrofluidic device that meets the above constraints. We also discuss the advantages and disadvantages of 3D printing as a research tool for device development. Multi-material printing, wherein different materials are combined into a single printed part, offer expanded capabilities, so we chose to specifically investigate multi-material 3D printing as a tool for building sample-to-device interfaces. We have previously demonstrated the utility of multi-material printing in the development of a pumping lid for interfacing with microfluidic devices,[15] however, the pumping lid we developed was only used to compress air, and did not contact fluids directly. Here, we expand on the ability to use multi-material printed parts to generate sealed fluid cavities through the development of a multivalve and plungers used within our device.

## Results and Discussion

*Interlock design and meter-mix device operation*

To operate the meter-mix device (see ESI† video), the user performs three simple steps: 1. insert urine suction tube into patient sample and pull urine plunger; 2. remove from patient sample and slide multivalve; and 3. push lysis buffer plunger to eject the mixed solution. The device can then be easily disposed in biohazardous waste. Furthermore, the user of the device cannot accidentally perform these three operations out of order due to the presence of interlock features attached to the plungers. In the initial position, the urine plunger interlock blocks the sliding of the multivalve, and the multivalve blocks the movement of the lysis buffer plunger (**Figure 4.1A**). When the user pulls up on the urine plunger, urine is aspirated through the suction tube, through the valve, and into the urine chamber. Pulling up on the urine plunger also releases the interlock that was blocking the multivalve (**Figure 4.1B-C**). The user then slides the multivalve, which disconnects the urine suction tube inlet while generating two new outlets to a static mixer, one outlet urine and the other for lysis buffer which has been pre-stored on the device. By pre-storing the lysis buffer on device, we eliminate many manual pipetting steps and reduce user error.[16] The sliding of the multivalve also creates openings for the urine plunger interlock and the lysis buffer plunger interlock (**Figure 4.1C**). In the final step, the user pushes down on the lysis buffer plunger, which also pushes the urine plunger, ejecting both urine and lysis buffer through the static mixer (**Figure 4.1D**). The total user operating time is between 5 and 10 s.

The meter-mix device is composed of eight assembled parts: 1. main enclosure, 2. lysis buffer plunger, 3. urines plunger, 4. two plunger stoppers, 5. multivalve, 6. urine suction tube, 7. static mixer elements, and 8. static mixer case (**Figure 4.2**). All parts were designed using 3D CAD software (Solidworks 2015 Education Edition) and fabricated using an Objet 260 multi-material 3D printer (Stratasys, Eden Prairie, MN, USA). We judiciously selected two semi-transparent photopolymer materials, Veroclear and TangoPlus, corresponding to a rigid plastic, analogous to poly(methyl methacrylate) (PMMA), and a soft, elastomeric material, analogous to rubber, respectively. By utilizing translucent materials, fluids are

visible as they are transported among chambers of the device, providing visual feedback during operation. All of the parts were composed of Veroclear, providing a strong structure. The plunger heads, stoppers, and the multivalve were printed with a combination of Veroclear and TangoPlus, which enabled us to design sliding surfaces and generate seals. With the exception of the plunger stoppers, each part underwent between seven and 25 unique design iterations. In the **Figure 4.2** demonstration, which shows the entire device assembly and operation, 1150 µL 0.05% (v/v) Sky blue Ateco dye (August Thomson Corp., Glencove, NY, USA) was preloaded into the lysis buffer chamber and 0.1% Lemon yellow Ateco dye was manually loaded into the urine chamber. These two dye solutions were run through the device and combined to form a green mixed solution (**Figure 4.2D**).

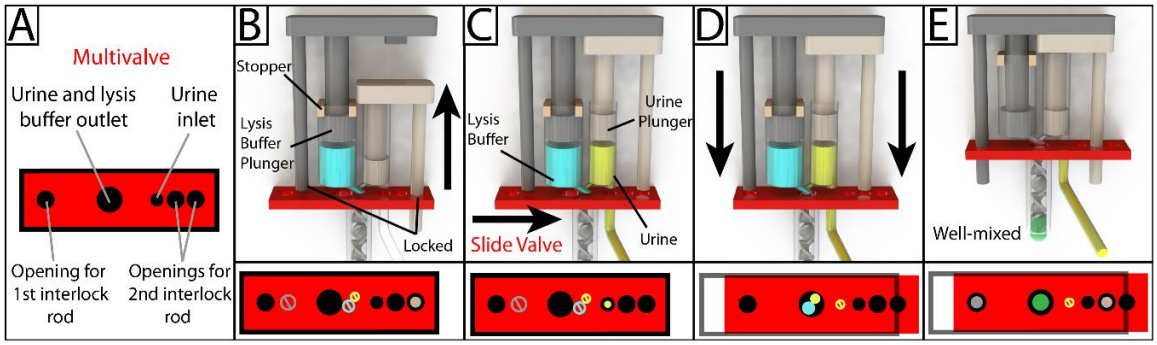


**Figure 4.1: Schematic overview of the design and operation of the 3D-printed interlock meter-mix device for metering and mixing a urine sample with lysis buffer.**

(A) The multivalve has 5 holes which are labeled accordingly. (B) Lysis buffer (blue) is preloaded into the lysis buffer chamber, where the topmost position of the lysis buffer plunger (left, grey) is pre-determined by stoppers (tan). The urine plunger interlock rod (right, beige) is positioned within the multivalve, preventing the valve from sliding and simultaneously blocking the lysis buffer plunger interlock rod. The user pulls up on the urine plunger (C) until it contacts and is stopped by the lysis buffer plunger, aspirating urine and simultaneously removing the urine plunger interlock rod from the multivalve. The user slides the multivalve (D), closing off the urine suction tube, opening the lysis buffer and urine outlets to the mixer, and

providing openings for both interlock rods. In the final step, the user pushes down on the lysis buffer plunger (E), ejecting urine and lysis buffer through a static mixer, wherein the solutions are well mixed before finally being ejected from the tip of the mixer. Red blocks at the bottom of each panel show a top-down view of the multivalve. Black circles and rings indicate holes in the multivalve. Slashed circles indicate the presence of a feature that is blocked by the multivalve. Colored circles indicate the presence of an interlock rod or an open channel for the flow of a solution.

*Designing and prototyping leak-proof connections*

To ensure reliable device operation, all of the seals on the device need to be hermetically sealed. We accomplish this using the capability of Multi-jet 3D printing to generate materials jointly composed of hard plastic (Veroclear) and soft rubber-like material (TangoPlus). We used multi-material printing for fabricating both plungers and the multivalve. The challenge with creating leak-proof connections is determining the appropriate dimensions, overlap, and the ratio of soft:hard material to create a strong leak-proof connection that is still easy to move by hand. We took advantage of the rapid prototyping capabilities of 3D printing to quickly converge on functional designs. For the urine chamber, we found a good fit using an 8 mm diameter hole and an 8 mm diameter plunger head, where the inner diameter of the plunger head consisted of 7.2 mm Veroclear surrounded by a 0.4 mm (5%) thick layer of TangoPlus. For the lysis buffer chamber, we found good fit using an 11.31 mm diameter hole and an 11.31 mm diameter plunger head (surrounded by a 5% TangoPlus layer). These parameters made hermetically sealed connections capable of generating and holding a vacuum. We selected the dimensions of the chambers in the main enclosure to provide the desired air volumes and mixing ratios (see Accurate Dispensing). To generate the multivalve seal, an open cavity was designed through the side of the main enclosure, with raised ridges around each hole for the inlets and outlets. The multivalve was 2.7 mm thick, with 0.54 mm TangoPlus (20%) layered on the top and 0.54 mm on the bottom. At the points of contact between the multivalve and the inlet/outlet ridges, there was a 0.2 mm overlap where the

ridge pushed into the TangoPlus layer (by 3D CAD design). To assist sealing and sliding, we applied silicone oil to lubricate all contact points at movable interfaces (plunger heads, chambers, and the multivalve).

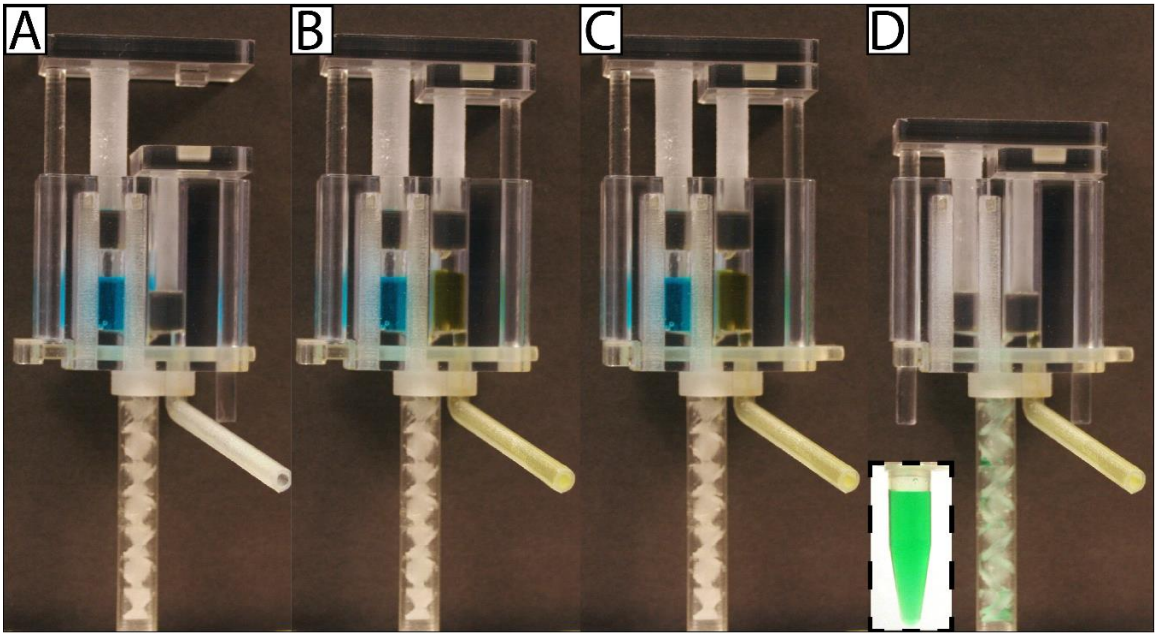


**Figure 4.2: Photographs of the device at different stages of operation.**
(A) In the initial position, blue dye representing lysis buffer is preloaded and the urine plunger is down. (B) In the second position, the urine plunger contacts the lysis buffer plunger and a specific volume of yellow dye representing urine is metered. (C) In the third position, the multivalve was slid 5 mm to the right, simultaneously closing and opening new connections. (D) In the final position, both plungers are down, dispensing a green solution out through the static mixer (inset).

*Plunger system and accurate metering*

To accurately meter urine, we designed a plunger system with predetermined start and stop positions. During device operation, the urine plunger is pulled up until it contacts the underside of the lysis buffer plunger. The volume displaced by the plunger was calculated in

CAD software, providing an estimate for the volume of urine aspirated into the device. To precisely calibrate metering, the working design was iterated by testing prototypes of the device by aspirating deionized water, weighing the device, and modifying the height of the plunger stoppers to adjust the volume displaced by the plunger. To accurately meter lysis buffer, we use a pipettor to preload the meter-mix device. When the device is set to the initial configuration, lysis buffer is sealed on both sides by the lysis buffer plunger and multivalve. This is advantageous for a disposable LRS and POC device because the filling step can be performed during manufacturing and assembly. In this way, the end-user does not need to consider handling of the lysis buffer during device operation.

With diagnostic devices, it is important to minimize dead volumes to avoid wasting reagents, losing sample, or introducing a source of variability. One strength of 3D printing is that potential sources of dead volume can be identified and reduced during the design process. During our design process, we identified four potential sources of dead-volume: urine lost in the suction tube, urine lost in the urine chamber, lysis buffer lost in the lysis buffer chamber, and mixed solution remaining in the static mixer. We recognize that patient urine is abundant, and that it is acceptable for the meter-mix device to overfill urine; however, the final volume of urine ejected from the device must be consistent between runs. To ensure accurate, consistent ejected volumes, the dead-volume of the urine suction tube was taken into account while modifying the positions of the plunger stoppers. It should be noted that dead-volume can be reduced by changing the design of the suction tube as required. For our meter-mix device, we were concerned with dead volumes of urine remaining in the urine chamber and the static mixer, which could contribute to differences in the volumes of urine ejected between runs. In particular, a user who sees liquids trapped in the static mixer may be inclined to shake the meter-mix device, introducing error which affects the accuracy of downstream quantitative processes. To remove this dead volume, we leave a pocket of air that sits above the lysis buffer within the lysis buffer chamber. After urine is aspirated into the device, we designed the system so that the heights of the pocket of air are roughly equal (the air initially residing in the suction tube is incorporated into the device during the aspiration step). These

two pockets of air produce a blow-out volume of air which removes the dead volumes of urine and lysis buffer that would otherwise remain in the chambers and static mixers.

We wanted to ensure that after urine is aspirated into the urine chamber, urine is unable to leak out through the tip of the urine suction tube. Bretherton previously examined this problem, and found the dimensionless bond number, Bo (which relates gravity to surface tension), to be a guiding parameter.[17] The bond number is related to the density difference between the liquid and air, the diameter of the tube, and the surface tension of the liquid. He predicted that for a vertical tube that is sealed at one end, a bubble contained within will not rise if $Bo < 0.842$.[17] Thus, in our meter-mix device, if the bond number is low, and a bubble enters the urine suction tube, the bubble will be immobile, preventing solution from dripping out through the tip of the urine suction tube. Bretherton's prediction suggests that we want to minimize the bond number, which we can do simply by reducing the diameter of the 3D-printed urine suction tube. We would not, however, want to make the diameter so small that it generates a high resistance to flow, as this would generate a noticeable delay in the filling time and negatively affect the user experience. Tube diameter is constrained with our 3D printing methods because as tube diameter decreases, it becomes increasingly difficult to remove the support material and clean inside the tube. For our device, we limited our testing to >1.5 mm diameter sized suction tubes. At the millimeter scale, there was no noticeable delay between pulling up on the urine plunger and filling of the urine chamber.

We tested the Bretherton prediction using 3D-printed parts. A simple plunger system was designed along with suction tubes of varying diameters. In multi-material 3D printing, the printing of support material can be avoided for some geometries and configurations. We printed straight suction tubes in the vertical configuration, which does not print support within the suction tube and therefore does not require support cleaning. While some support can be avoided, one limitation of our multi-material printer is that it always prints support material for the bottom layer in contact with the 3D printer's build plate. When one side of the model is printed in contact with support and the other parts of the model are located on the exterior sides of the device, there may be minor differences between dimensions and

surface roughness. For example, we found that when printing straight tubes upright, the diameter on the side of the tube in contact with the 3D printer's build plate was slightly smaller than the opposite opening. A discrepancy between parts of the model in contact with the build plate and open to air is not an exclusively multi-material 3D printing characteristic, but is common to many types of 3D printers. Care was taken to always use the side of the tube in contact with the build plate for the connection to the body of the plunger system.

**Table 4-1: Bretherton's prediction tested using 3D-printed tubes of varying diameter.**

| Fluid | Diameter (mm) | Bo | Observed behavior |
|---|---|---|---|
| Water | 2 | 0.136 | No drip |
| | 2.5 | 0.212 | No drip |
| | 3 | 0.306 | No drip |
| | 3.5 | 0.416 | No drip |
| | 4 | 0.544 | Bubble sticks |
| | 4.5 | 0.688 | Bubble sticks |
| | 5 | 0.850 | Bubble sticks/bubble rises |
| | 5.5 | 1.028 | Bubbles rises |
| Ethanol | 2 | 0.345 | Bubble sticks |
| | 2.5 | 0.539 | Bubble sticks |
| | 3 | 0.776 | Bubble sticks/bubble rises |
| | 3.5 | 1.056 | Bubble rises |
| | 4 | 1.379 | Bubble rises |
| | 4.5 | 1.746 | Bubble rises |
| | 5 | 2.155 | Liquid spills as air column rises |
| | 5.5 | 2.608 | Liquid spills as air column rises |

To test the prediction, we used the opposite side of the suction tube to aspirate solution into the tube. The suction tube was manually disturbed through tapping the tip in order to introduce bubbles, mimicking a real-world user experience where the user bumps the device. We found that there was general agreement between bond number and the Bretherton prediction (**Table 4-1**). Using water, for bond number <= 0.416, no bubbles entered the device and no fluid dripped from the tip. For bond numbers between 0.544 and 0.688, a

bubble entered the tube releasing some drops, but the bubble did not rise and the liquid-air interface at the tip regained stability. Close to the Bretherton prediction at Bo = 0.850, bubbles entered the tube and both rise and no rise of the bubble were observed, which seemed to depend on the size of the bubble incorporated. Finally, for a large bond number (1.028), drops were released when the bubble initially entered the tube, the liquid-air interface at the tip regained stability, and we saw bubble rise as predicted by Bretherton. The experiment was repeated using ethanol with similar results. We also observed that for very large bond numbers (Bo >/= 2.155), once the ethanol-air interface at the tip was disturbed, a column of air entered the suction tube, spilling all of the solution out of the tip. Accounting for Bretherton's prediction, the limitations of cleaning support material, and accounting for the pocket of air for blow-out, we selected a suction tube diameter of 2.3 mm in the final design. The surface tension of urine from healthy patients ranges from 48–70 mN/m.[18] Using the low value of surface tension at 48 mN/m, a density of 1.01, and a 2.3 mm diameter gives a Bo = 0.272.

*Accurate dispensing*

The flow rate of each solution is determined by the design of the device chambers, plungers, and outlets. We designed each chamber of the device to undergo the same driving pressures over the entire dispensing operation. We can accomplish this by matching the solution height, air pocket height, and plunger heights in both chambers. For example, a 2:1 volume ratio can be obtained by making the area of one chamber twice the area of the second chamber. The cross-sectional area of the channels and outlet valves should also be maintained at the 2:1 ratio to obtain the flow resistance and corresponding volumetric flow rate. Our device was designed with a 2:1 volume ratio between lysis buffer and urine, but we were cognizant of the potential for flow irregularities near the beginning and end of the flow regime. If slight inaccuracies during filling cause urine to enter the static mixer prematurely or after all of the lysis buffer has gone through, this could leave some urine unmixed and unlysed. This could lead to inaccuracies during downstream quantification, and unlysed bacteria are a biohazard.

To address these concerns, we slightly overfilled the lysis buffer compartment leading to a final lysis buffer to urine volume ratio of 2.2:1.

We evaluated the dispensing accuracy of our device using water, green dye, spectrophometer measurements, and a balance. To examine inter-device variability, we tested three different device prototypes each run in triplicate (**Table 4-2**). There was no significant difference among devices for aspiration volume ($P = 0.46$) or the volume expelled ($P = 0.44$). Sample aspiration was found to accurately meter ~790 µL (<1% CV). As previously described, the blow-out volume of air is responsible for ejecting the final volumes of urine and lysis buffer remaining in the chambers and the static mixer. We found that pushing the plunger down over the course of 1–2 s led to relatively little error in the final ejection volume (<2% CV). However, pushing the plunger down faster (in <1 s) pushed bubbles through the static mixer and greater volumes of liquid remained in the device, resulting in reduced ejection volumes (~1350 µL). In real-world applications, it is important to minimize differences resulting from user operation. Future designs can address the issue of plunger speed affecting dead volume by reducing the diameter of the outlets to prevent bubbles from escaping before the fluid. The ratio of solution ejected from the lysis buffer chamber and the urine chamber was calculated by measuring the absorbance of the final ejected solution and comparing it to the green dye loaded into the lysis buffer chamber. We found that dispensed volumes out of the lysis buffer chamber and urine chamber were similar, with percent deviations of 2.5% and 6.6%.

**Table 4-2: Evaluation of metering and dispensing accuracy of the meter-mix device.**

| Device | Trial | Aspiration volume (μL) | Ejection volume (μL) | Calc. volume from lysis chamber (μL) | Calc. volume from urine chamber (μL) |
|---|---|---|---|---|---|
| 1 | 1 | 782 | 1591 | 1067 | 524 |
| | 2 | 784 | 1613 | 1121 | 492 |
| | 3 | 798 | 1660 | 1135 | 525 |
| 2 | 1 | 796 | 1619 | 1150 | 469 |
| | 2 | 799 | 1630 | 1065 | 565 |
| | 3 | 791 | 1577 | 1120 | 457 |
| 3 | 1 | 788 | 1611 | 1134 | 477 |
| | 2 | 787 | 1586 | 1106 | 480 |
| | 3 | 799 | 1572 | 1099 | 473 |
| AVG | | 792 | 1607 | 1111 | 496 |
| STD | | 6 | 27 | 28 | 33 |
| CV | | 0.8% | 1.7% | 2.5% | 6.7% |

*Static mixer design and mixing evaluation*

To simplify user experience and eliminate mixing by pipetting or vortexing, we designed an on-device Kenics static mixer (KMS), a common mixer used for a variety of industrial applications.[19] We had previously designed the flow rates of urine and lysis buffer to exit the outlets at a consistent flow rate. We predicted that a KMS mixer placed after the lysis buffer and urine outlets would be an efficient way to mix the two streams. The static mixer is composed of alternating left- and right-hand 180° helical twists with 90° offsets between elements. This immobile structure encased within a tube guides the flow of solutions from the center of the tube to the wall of the tube and from the wall to the center. Each element splits and recombines streams of flow, rapidly homogenizing the fluid, similar to mixing by

chaotic advection in moving plugs.[14,20,21] We designed a KMS static mixer composed of eight elements, with a diameter of 5 mm, and a length:diameter ratio of 1.25:1. Limited by the requirements of removing support material from 3D-printed parts, it was not feasible to print the entire mixer and tube enclosure as a single unit. Instead, we used a modular approach, printing the mixer elements and the mixer case as separate pieces. Both parts were printed in the upright configuration.

When static mixer elements were printed with the glossy finish setting, only the topmost element was glossy and had different surface roughness and dimensions than the other elements (remaining parts had the matte finish because they were printed in contact with supporting material). To address this issue, we printed the static mixer elements with the matte finish (**Figure 4.3A**). The static mixer elements and the static mixer case were cleaned separately and assembled carefully because the static mixer elements were very prone to breaking (**Figure 4.3B–D**).

To evaluate mixing quality, a starch iodine-thiosulfate decolorization was used. The decolorization reaction is a preferred method to evaluate mixing because any pockets of unmixed regions will be visible.[22] The initial decolorization reaction occurs quickly in a 1:1 iodine:thiosulfate ratio, although a secondary reaction leads to the reappearance of color so higher ratios of iodine:thiosulfate (e.g. 1:1.2 or 1:1.4) can be used.[23-25] For the meter-mix device, we used a 1:1.05 ratio because the design enables rapid mixing within the timescale of the device operation. The starch iodine solution was loaded into the urine chamber through the suction tube, and the sodium thiosulfate was preloaded into the lysis buffer chamber. The device mixed the two solutions within the first three to four elements (**Figure 4.3G**). As a control, to confirm that the loss of color is due to mixing and not an artifact of the chemical or optical properties of the 3D-printed part, we also show the static mixer element fully filled and while mixing with a solution that does not cause decolorization. We ran the meter-mix device with starch iodine indicator loaded into both chambers (**Figure 4.3E**) and in a separate experiment with starch iodine loaded into the urine chamber and water loaded into the lysis buffer chamber (**Figure 4.3F**).

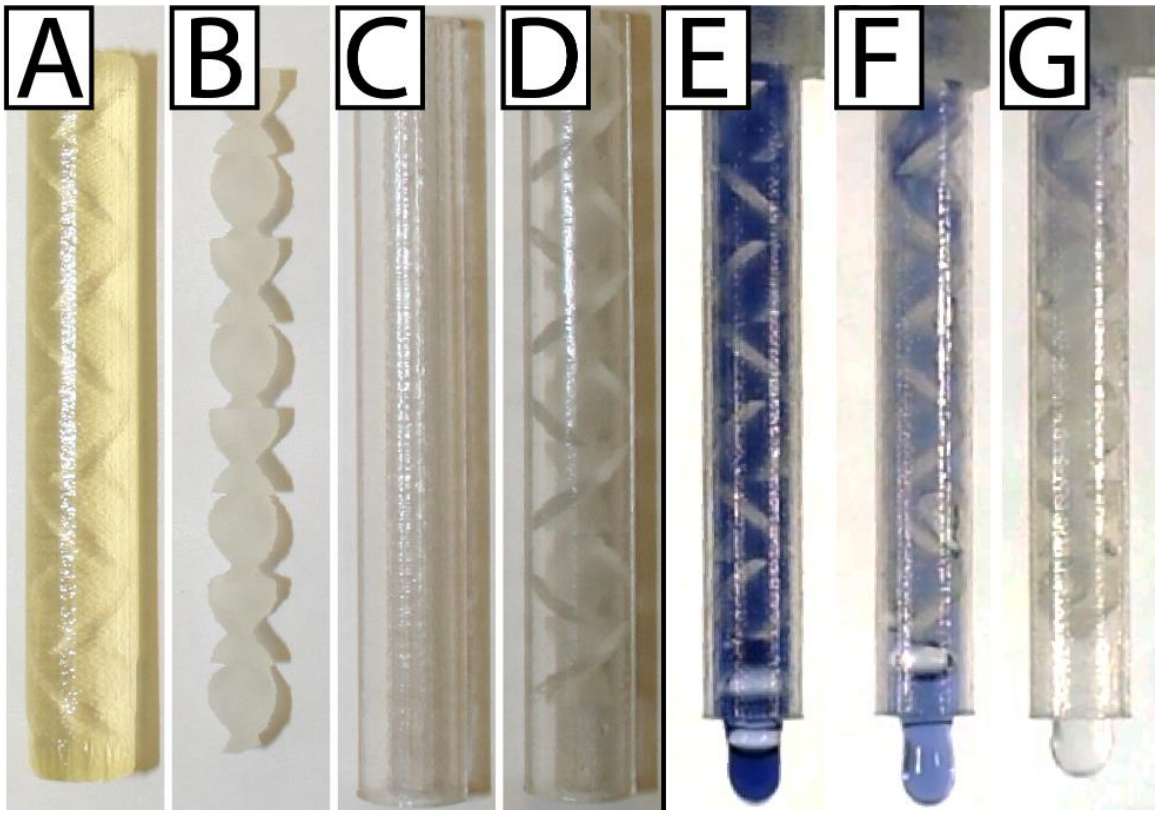


**Figure 4.3: Assembly of the static mixer (A–D) and a demonstration of its use in the meter-mix device (E–G).**

(A) Freshly printed static mixer elements before cleaning. (B) Static mixer elements after a 15 min cleaning step to remove support material. (C) Static mixer case. (D) Assembled static mixer with elements inserted into case. (E) Iodine– starch indicator loaded into both chambers and ejected through the static mixer. (F) Iodine–starch indicator mixing with water to show a dilution. (G) Iodine–thiosulfate de-colorization reaction demonstrating rapid mixing within the first few static mixer elements.

*Function and biocompatibility*

We evaluated the meter-mix device for compatibility with a routine nucleic acid extraction kit by comparing the metering and mixing steps performed by the device with standard approaches for metering and mixing (manual pipetting and vortexing). Two concerns are the

potential for nucleic acids to bind to 3D-printed surfaces, and the potential for compounds from 3D-printed materials to leach into the solutions, both of which can negatively affect downstream analysis of nucleic acids. We preloaded the device with 1150 µL lysis buffer and aspirated urine spiked with $10^4$ cells/mL of either *C. trachomatis* (CT) or *N. gonorrhoeae* (NG) through the suction tube. The multivalve was slid, and the plungers were pushed manually, ejecting the solutions through the static mixer and into a 2 mL polypropylene tube. An off-device sample was tested in parallel, with 1100 µL lysis buffer and 500 µL spiked urine (see **Table 4-2**) metered by a pipettor and the solution mixed by vortex. We also ran no-template controls containing clean urine for both on and off-device conditions. After mixing, all samples were processed in parallel according to the manufacturer's instructions using the QIAamp Viral RNA Mini kit (recommended for purification of bacterial DNA from urine). Following extraction, nucleic acid concentrations were compared using routine quantitative polymerase chain reaction (qPCR) with primers previously evaluated for the detection of *C. trachomatis*[26] or *N. gonorrhoeae*.[27] The threshold cycle for vortex and device-mixed samples were not statistically different, indicating that there was no significant loss of nucleic acids and or material leaching that inhibited downstream analysis. No-template negative controls showed no amplification after 35 cycles.

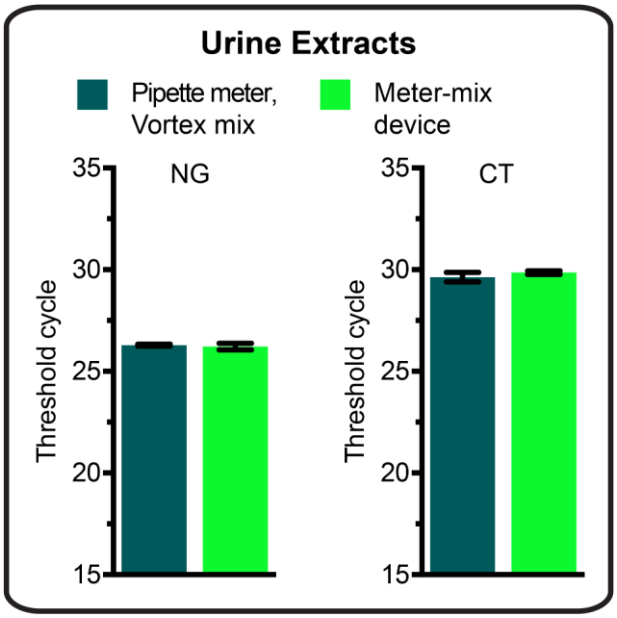


**Figure 4.4: qPCR threshold cycles on DNA extracted from urine spiked with either inactivated Chlamydia trachomatis (CT) or Neisseria gonorrhoeae (NG).** Sample metering and mixing with lysis buffer was performed with either the meter-mix device (light green bars) or standard pipette and vortex (dark green bars). The remainder of the extraction protocol was identical for both conditions.

## Experimental

*Meter-mix device cleaning and assembly*

Printed parts were cleaned using pipette tips or copper wire and rinsed with water. The urine plunger, lysis buffer plunger, multivalve, and both chambers of the main enclosure chambers were lubricated with viscous silicone oil (Dimethylpolysiloxane 12,500 cSt, Sigma Aldrich, St. Louis, MO, USA). To assemble, first the urine plunger was inserted into the urine chamber of the main enclosure followed by the lysis buffer plunger into the lysis buffer chamber. The two plunger stoppers were then inserted, locking the topmost position of the lysis buffer plunger. The multivalve was inserted into the main enclosure from the side, and pushed into its final position to preload 1150 uL lysis buffer through the outlet. The

multivalve was then moved into its starting position, the urine plunger pushed to the bottom of the chamber, and the urine suction tube and static mixer were attached. For these joints, the outer diameter of the static mixer case (8 mm) and the outer diameter of the urine suction tube (4.5 mm) sized exactly to the diameter of adapters on the main enclosure. After cleaning, a thin layer of support material remains at the junctions of the main enclosure. Because this support material is shed from the joints during device use, we used silicone oil to enhance the seal.

*Characterization of metering and dispensing*

To evaluate metering and dispensing, we loaded into the lysis buffer chamber 1150 µL 0.5% (v/v) green food color dye (The Kroger Co., Cincinnati, OH, USA) diluted in deionized water was aspirated into the urine chamber through the urine suction tube, and mass measured to obtain the aspirated volume (using water density of 1 g/mL). The multivalve was pressed and the solution ejected into a pre-tared conical tube to obtain the mass of the solution ejected from the device. The resulting solutions were well-mixed through vortexing. The original 0.5% (v/v) green dye and each resulting solution was diluted by 20x, loaded into a cuvette, and measured with a UV-vis spectrophotometer (Nanodrop 2000c, Thermo Scientific, Wilmington, DE, USA). Measurements were taken at the wavelength where the absorbance was maximal (630 nm), and the ratio was used to determine the volume of solutions ejected from each chamber.

*Iodine-thiosulfate decolorization reaction*

Iodine, starch indicator, and sodium thiosulfate solutions were prepared according to the *Handbook of Industrial Mixing*.[22] Briefly, 1150 µL sodium thiosulfate nonahydrate (0.5 mM, ThermoFisher Scientific, Waltham, MA, USA) was loaded into the the lysis buffer chamber. Starch indicator was prepared by adding 100 mg starch, soluble potato, powder (J.T. Baker,

Center Valley, PA, U.S.) and 20 g potassium iodide to 10 mL deionized water. 50 µL of this starch solution was added to a 1 mL solution of iodine (1 mM, Alfa Aesar, Ward Hill, MA, USA), coloring the solution dark bluish-purple. The final ratio of iodine:thiosulfate was 0.95:1. A video was taken using the Samsung Galaxy S4 camera, and frames extracted during device operation when the flow fully filled the static mixer (**Figure 4.3E-G**).

*Qiagen extraction and qPCR experiment*

In order to test device compatibility with biological samples and ensure that downstream nucleic acid analysis was not negatively affected, we compared samples that were metered and mixed on-device against traditional vortex mixing using a commercial nucleic acid extraction kit (QIAamp Viral RNA Mini Kit, 52904). Lysis buffer was loaded with 2 ng/µL carrier DNA (salmon sperm DNA, Thermo Fisher AM9680). Non-infectious CT and NG samples were obtained from ZeptoMetrix Corp. (NATNG-ERCM, NATCT(434)-ERCM, Buffalo, NY, USA). Quantitative PCR was performed on a Roche LightCyler 96. PCR reactions consisted of 5 µL SsoFast EvaGreen Supermix (BioRad cat no. 1725200), 2.0 µL of template (extracted spiked urine), 0.5 µL of 20X primer stocks, and 2.5 µL nuclease-free water. The primers used[26,27] were previously evaluated for the detection of either CT or NG. Final primer concentration in the reaction was 500 nM. Thermal cycling consisted of a 3 min initial denaturation step at 95 ˚C, followed by 40 cycles of 20 s at 95 ˚C, 20 s at 62 ˚C, and 20 s at 72 ˚C. Melt analysis confirmed specific product for all reactions.

## Conclusions

We showed that multi-material 3D printing can be used to prototype a disposable interlock meter-mix device that accurately meters urine and completely mixes it with lysis buffer in a format that meets the requirements for a downstream NAAT compatible with LRS and POC settings. The 3D-printed device accurately aspirated predetermined volumes into a urine

chamber with a coefficient of variation of 0.8%. Urine and lysis buffer were dispensed through a KMS static mixer at a 2.2:1 mixing ratio. Printing with translucent materials enabled visual confirmation of fluid movement and showed that mixing occurred within the first few elements of the static mixer, with homogenization and lysis later verified by qPCR. Printing with a multi-material 3D printer enabled us to use a combination of composites to create airtight seals that slide without leaking or losing vacuum pressure. Using a 3D printer also helped address the potential for sample dripping, a biohazardous concern when working with bodily fluids and potentially dangerous solutions, as we were able to test Bretherton's prediction for bubble rising through several prototype iterations and identify optimal tube dimensions that ensured the sample did not drip.

The 3D-printed device was designed to optimize the user's experience: operation is simple (three steps); interlock features protect against user error; neither pipetting nor vortexing are required; and the entire device operation is completed within 5 to 10 s (see ESI† video). We validated our device by lysing urine samples spiked with CT/NG and performed downstream processes to quantify nucleic acids through qPCR. These results confirmed that the 3D-printing materials (Veroclear and TangoPlus) were biocompatible; we observed no loss of nucleic acids and devices performed equally well compared with the standard protocol of pipettor metering and vortex mixing in a polypropylene tube. Finally, we demonstrated that the performance of the meter-mix device matched the performance of standard laboratory protocols for metering and mixing, with a substantially shorter time period for device operation.

The meter-mix device described here is not limited to mixing urine with lysis buffer. A common operation in biology, chemistry, and medicine is to mix two solutions of known volume. Due to the customizability of 3D printing and CAD design, it is easy to adapt the meter-mix device to different volumes or configurations. In some applications, it may be desirable to meter two different solutions at the time of use. In this example, the meter-mix device could be reconfigured with an additional suction tube appended to the lysis buffer chamber. Given the versatility of the meter-mix device, it may be useful in a variety of

applications such as sequencing, dilutions, or chemical syntheses. Because the meter-mix device simplifies and accelerates workflow, protects against user error, and provides a user-friendly experience, we foresee its future application in research labs and limited-resource settings. For example, time-sensitive laboratory measurements may require metering and mixing on the timescale of single digit seconds rather than the tens of seconds required for pipetting. In commercial applications, an important advantage of a single-use disposable device is that it can be assembled and pre-loaded with lysis buffer before it is shipped, eliminating a pipetting step for the end user.

Throughout the course of device development, the 3D printing workflow was a major advantage over analogous forms of prototyping, such as soft lithography. Prototyping with 3D printing was rapid, enabling us to design, test, redesign, and reprint a prototype in the period of a single day. For small parts that can be printed in less than a few hours, it is possible to iterate multiple designs within in a single day. The ease with which parts can be modified after having developed the initial design allowed us to print multiple variations of the meter-mix device at once and determine the optimal architecture of each part in a single experiment. This was useful for determining the diameter of the suction tube, setting the parameters for the static mixer, and adjusting the fit for the seals. Another advantage with 3D printing is that the 3D CAD models which are developed during the design stage can also be utilized and adapted for injection molding. This is important in commercial applications when large quantities are required, since injection molding has higher start-up costs but lower costs per part than 3D printing. We also found modularity to be an important advantage with 3D printing. Parts can be built as separate components and later reassembled, reducing build time (which relies heavily on z-axis height). It is also easier, and less expensive, to validate and iterate with individual components than to redesign and reprint an entire device. Of course, the final cost of producing these devices using standard manufacturing methods (injection molding) will be even lower than prototyping costs.

The greatest limitation we faced with multi-material 3D printing pertained to the support material. We faced three specific issues: (i) wherever support material is printed in contact

with the model, the printer produces a matte finish with different surface characteristics and dimensions compared with the glossy finish of parts that do not contact the support material; (ii) it can be difficult to remove the support material for some geometries, so care needs to be taken during the design to account for cleaning; and (iii) removal of the support material takes time, requiring ~45 min to clean all of the components for a single device. As new support material is developed, this limitation will diminish. For example, some companies have developed new dissolvable support materials that can be removed in a soak-and-rinse process, however, these processes are still diffusion-limited and may be difficult to implement when cleaning long, narrow channels relevant to microfluidic devices. Despite some limitations, we conclude that 3D printing is an attractive prototyping technology with great potential for solving the sample-to-device interface problem in diagnostics, especially in resource-limited settings.

**References**


1. C. M. B. Ho, S. H. Ng, K. H. H. Li and Y.-J. Yoon, *Lab Chip*, 2015, **15**, 3627-3637.

2. B. C. Gross, J. L. Erkal, S. Y. Lockwood, C. Chen and D. M. Spence, *Anal. Chem.*, 2014, **86**, 3240-3253.

3. A. Waldbaur, H. Rapp, K. Lange and B. E. Rapp, *Anal. Methods*, 2011, **3**, 2681-2716.

4. A. Pilipović, P. Raos and M. Šercer, *Int. J. Adv. Manuf. Tech.*, 2007, **40**, 105-115.

5. A. Niemz, T. M. Ferguson and D. S. Boyle, *Trends. Biotechnol.*, 2011, **29**, 240-250.

6. P. Craw and W. Balachandran, *Lab Chip*, 2012, **12**, 2469-2486.

7. R. W. Peeling, K. K. Holmes, D. Mabey and A. Ronald, *Sex. Transm. Infect.*, 2006, **82 Suppl 5**, v1-6.

8. D. Lee, Y. T. Kim, J. W. Lee, D. H. Kim and T. S. Seo, *Biosens. Bioelectron.*, 2016, **79**, 273-279.

9. Q. Tian, Y. Mu, Y. Xu, Q. Song, B. Yu, C. Ma, W. Jin and Q. Jin, *Anal. Biochem.*, 2015, **491**, 55-57.

10. R. C. den Dulk, K. A. Schmidt, G. Sabatte, S. Liebana and M. W. Prins, *Lab Chip*, 2013, **13**, 106-118.

11. A. V. Govindarajan, S. Ramachandran, G. D. Vigil, P. Yager and K. F. Bohringer, *Lab Chip*, 2012, **12**, 174-181.

12. W. Huang, C. A. Gaydos, M. R. Barnes, M. Jett-Goheen and D. R. Blake, *Sex. Transm. Infect.*, 2013, **89**, 108-114.

13. CDC, *Reported STDs in the United States. 2012 National Data for Chlamydia, Gonorrhea and Syphilis*, 2014.

14. J. R. Papp, J. Schachter, C. A. Gaydos and B. Van Der Pol, *Recommendations for the Laboratory-Based Detection of Chlamydia trachomatis and Neisseria gonorrhoeae — 2014*, 2014, **63**, 1-19.

15. S. Begolo, D. V. Zhukov, D. A. Selck, L. Li and R. F. Ismagilov, *Lab Chip*, 2014, **14**, 4616-4628.

16. S. Makwana, B. Basu, Y. Makasana and A. Dharamsi, *Int. J. Pharm. Investig.*, 2011, **1**, 200-206.

17. F. P. Bretherton, *J. Fluid. Mech.*, 1961, **10**, 166-188.

18. C. O. Mills, E. Elias, G. H. Martin, M. T. Woo and A. F. Winder, *J. Clin. Chem. Clin. Biochem.*, 1988, **26**, 187-194.

19. A. W. Etchells and C. F. Meyer, in *Handbook of Industrial Mixing*, John Wiley & Sons, Inc., 2004, DOI: 10.1002/0471451452.ch7, pp. 169, 391-477.

20. H. Song, D. L. Chen and R. F. Ismagilov, *Angew. Chem., Int. Ed.*, 2006, **45**, 7336-7356.

21. H. Song, M. R. Bringer, J. D. Tice, C. J. Gerdts and R. F. Ismagilov, *Appl. Phys. Lett.*, 2003, **83**, 4664-4666.

22. D. A. R. Brown, P. N. Jones, J. C. Middleton, G. Papadopoulos and E. B. Arik, in *Handbook of Industrial Mixing*, John Wiley & Sons, Inc., 2004, DOI: 10.1002/0471451452.ch4, pp. 145-256.

23. A. D. Awtrey and R. E. Connick, *J. Am. Chem. Soc.*, 1951, **73**, 1341-1348.

24. S. Hashimoto, Y. Chikamochi and Y. Inoue, *Chem. Eng. Sci.*, 2012, **80**, 30-38.

25. P. J. Carreau, I. Patterson and C. Y. Yap, *Can. J. Chem. Eng.*, 1976, **54**, 135-142.

26. J. B. Mahony, K. E. Luinstra, J. W. Sellors and M. A. Chernesky, *J. Clin. Microbiol.*, 1993, **31**, 1753-1758.

27. B. S. Ho, W. G. Feng, B. K. Wong and S. I. Egglestone, *J. Clin. Pathol.*, 1992, **45**, 439-442.

*Chapter 5*

# READING OUT SINGLE-MOLECULE DIGITAL RNA AND DNA ISOTHERMAL AMPLIFICATION IN NANOLITER VOLUMES WITH UNMODIFIED CAMERA PHONES

*J. Rodriguez-Manzano,*M.A. Karymov, S. Begolo, D.A. Selck, D.V. Zhukov, E. Jue, and R.F. Ismagilov. 2016 *ACS NANO*. 10(3):3102-3113. doi:10.1021/acsnano.5b07338

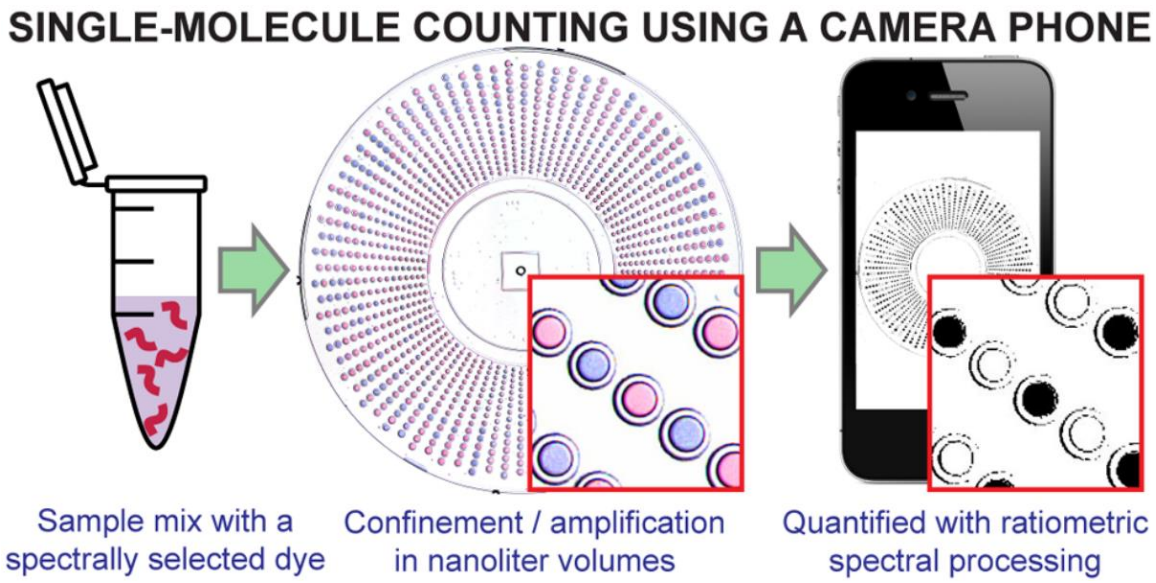


**Abstract**

Digital single-molecule technologies are expanding diagnostic capabilities—enabling the ultrasensitive quantification of targets, such as viral load in HIV and hepatitis C infections, by directly counting single molecules. Replacing fluorescent readout with a robust visual

readout that can be captured by any unmodified cell phone camera will facilitate the global distribution of diagnostic tests, including into limited-resource settings where the need is greatest. This chapter describes a methodology for developing a visual readout system for digital single-molecule amplification of RNA and DNA by: (i) selecting colorimetric amplification-indicator dyes that are compatible with the spectral sensitivity of standard mobile phones, and (ii) identifying an optimal ratiometric image-process for a selected dye to achieve a readout that is robust to lighting conditions and camera hardware and provides unambiguous quantitative results—even for colorblind users. We also include an analysis of the limitations of this methodology, and provide a microfluidic approach that can be applied to expand dynamic range and improve reaction performance, allowing ultrasensitive, quantitative measurements at volumes as low as 5 nanoliters. We validate this methodology using SlipChip-based digital single-molecule isothermal amplification with lambda DNA as a model and hepatitis C viral RNA as a clinically relevant target. The innovative combination of isothermal amplification chemistry in the presence of a judiciously chosen indicator dye and ratiometric image processing with SlipChip technology allowed the sequence-specific visual readout of single nucleic acid molecules in nanoliter volumes with an unmodified cell phone camera. When paired with devices that integrate sample preparation and nucleic acid amplification, this hardware-agnostic approach will increase the affordability and the distribution of quantitative diagnostic and environmental tests.

## Introduction

This chapter shows that single nucleic acid molecules confined in nanoliter volumes in microfluidic devices can be detected and counted by an unmodified cell phone camera, in combination with isothermal amplification chemistry, a judiciously chosen indicator dye and ratiometric image processing. We describe a novel methodology that can be used to develop a visual readout for digital single-molecule amplification of sequence-specific RNA and DNA that can be used with any camera phone—without modifications or attachments. Single-molecule visual readout has never been achieved before. Diagnostic tests that

incorporate such a visual readout will greatly expand the applicability of emerging digital single-molecule technologies, including into limited resource settings (LRS). Ultrasensitive and quantitative detection of nucleic acid molecules is of particular interest for infectious disease diagnosis in LRS, such as the quantification of viral load for human immunodeficiency virus (HIV) and hepatitis C virus (HCV),[1-3] as many of these infections occur far from centralized laboratories where diagnostic tests are routine. Increasing diagnoses in these locations will lead to faster and more appropriate treatment and have a major impact on disease burden[4,5] Most point of care (POC) tests are not amenable to LRS because they don't meet the World Health Organization's ASSURED criteria of being affordable, sensitive, specific, user-friendly, rapid, robust, equipment-free, and deliverable.[5] The tests that do meet the requirements for LRS (*e.g.* immunochromatography to detect antigens or antibodies in a dipstick or lateral-flow format; or the visualization of antigen-antibody lattice formation) have poor reported sensitivities and thus are unable to detect and quantify analytes at low concentrations.[4,6] Nucleic acid amplification tests (NAATs), such as PCR, have the desired high sensitivity and target specificity, providing accurate quantification, but these technologies are costly, time-consuming, and require skilled technicians and laboratory settings.[7]

Of the NAATs, isothermal amplification methods (*e.g.* loop-mediated isothermal amplification, LAMP) are among the most attractive for LRS because they do not require thermocycling or capital equipment and can be run in water baths, using simple heaters or with exothermic chemical heating that does not require electricity.[8-11] Still, acquiring quantitative and ultrasensitive measurements outside of the lab remains challenging because the methods are not robust to variability in reaction conditions, and readouts rely on precise measures of fluorescence intensity. Running isothermal amplification chemistries in a digital, single-molecule format maintains the high sensitivity and quantification capabilities typically achieved only in lab settings.[12-15] In digital single-molecule isothermal amplification, single, stochastically confined DNA or RNA molecules are randomly distributed among discrete nanoliter or picoliter volumes and amplified under controlled conditions.[16-18] This creates relatively high local concentrations of target DNA or RNA,

making digital amplification more efficient and robust compared to bulk reactions with the same number of starting target molecules. Nucleic acid amplification of even a single target molecule produces a clear fluorescent signal, and the results of digital amplification can be read by a modified cell phone (e.g. a phone camera with an optical filter) under dim lighting.[14]

Microfluidic technology has been an instrumental tool in developing single nucleic acid molecule capabilities,[19-27] and the integration of sample-preparation modules into portable microfluidic devices will further enable their use by untrained users in any setting.[28-30] To bring these emerging technological capabilities to LRS, however, such devices capable of ultrasensitive, quantitative measurements should provide a rapid, visual readout that can be captured easily—*e.g.* by any mobile phone without modifications or attachments. Cell phone cameras provide a convenient, nearly universal tool to pair with emerging diagnostic technologies to transform global healthcare as ~7 billion mobile cellular subscribers exist worldwide and 70% of users live in developing countries.[31] Mobile devices are emerging as a powerful platform to create cost-effective alternatives for molecular diagnostics in LRS[32-42] and colorimetric diagnostics based on unmodified cell phones have been used before,[38,43-46] but not in a digital format, where the short path lengths and nanoliter volumes have constrained visual-based methods. Here, we describe an approach that enables visual readout of single nucleic acid molecule amplification by (i) selecting an appropriate colorimetric indicator dye based on spectral properties that align well with the RGB sensitivities of common cell phone camera sensors and (ii) identifying the optimal ratiometric image-processing for the selected dye to achieve a readout that is robust to lighting conditions and camera hardware. Using this approach, after sequence-specific single-molecule isothermal amplification, a visual readout is captured by an unmodified camera phone, and the resulting image is analyzed using a ratiometric approach, wherein the measured intensities of two of the three RGB color channels are divided to provide a binary result (a positive or negative reaction) for each well. The automation of this ratiometric analysis provides a clear, reliable digital readout without requiring the user to differentiate color change by eye or manipulate lighting (**Figure 5.1a**). We further show how limitations related to reaction inhibition by the

readout dye can be solved with SlipChip microfluidics technology to decouple the amplification and readout steps. We validated our visual readout method with SlipChip-based digital single-molecule isothermal amplification reactions using phage lambda DNA as a model and HCV RNA as a clinically relevant target, in reaction volumes as low as 5 nL, using a variety of common cell phones and a range of illumination conditions.

## Results and discussion

### *Selecting an indicator dye*

To eliminate the need for a fluorescent readout in single-molecule amplification and produce a readout that can be imaged by any cell phone camera under various illumination conditions, one can use a nucleic acid amplification-indicator dye that changes color in response to amplification. A robust colorimetric readout balances two opposing requirements: the indicator dye must be sufficiently concentrated (or present in a large enough volume) to provide readable absorbance (*i.e.* smaller volumes and shorter path lengths require greater concentrations of dye for sufficient absorbance to be detected), but not so concentrated that the dye interferes with the amplification reaction. To optimize a visual readout system for single-molecule counting with an unmodified cell phone camera, we first identified the factors that contribute to hypothetical limitations of a visual readout system, including the range of reaction volumes (or path lengths) at which a particular indicator could be used to monitor amplification and the range of indicator concentrations that would not interfere with the amplification reaction. Where these ranges overlap are the optimal volumes and dye concentrations at which a reaction is not inhibited and can provide a change in absorbance that is sufficient for readout with an unmodified camera phone (dotted green region of **Figure 5.1b**).

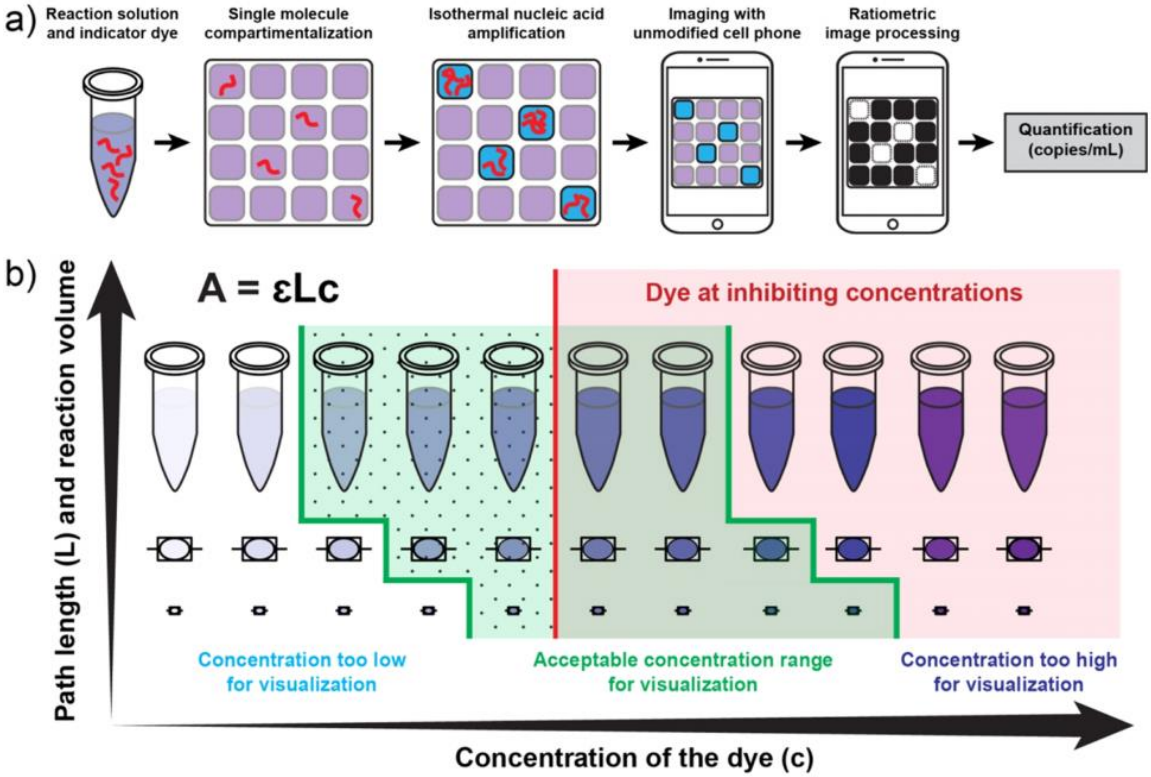


**Figure 5.1: A visual readout approach for digital single-molecule isothermal amplification for use with an unmodified cell phone camera.**

(a) A workflow for visual readout of digital single-molecule amplification. Single nucleic acid molecules and indicator dye are compartmentalized on a microfluidic device and followed by isothermal nucleic acid amplification. Positive reaction solutions are blue; negative reactions are purple. After ratiometric image processing, positive reactions become white and negative reactions become black—an unambiguous binary result. The number of positive wells is then used to quantify the concentration of the input target. (b) A diagram for delineating the optimal range of dye concentrations as a factor of path length (reaction volume) and the threshold for reaction inhibition. The green-shaded region indicates the range of acceptable dye concentrations for visualization with an unmodified cell phone camera. Concentrations to the left of the green region are too low for visualization; concentrations to the right of the green region are too high. Within this green region, the dotted area indicates dye concentrations that both enable readout with an

unmodified cell phone camera and do not inhibit the amplification reaction. The area to the right of the red line indicates dye concentrations that interfere with amplification making accurate quantification based on real-time data challenging.

We validated this visual readout approach using loop-mediated isothermal amplification (LAMP)[47,48] (Supporting Information **Table 5-1**, **Table 5-2**) because this method has been well characterized and validated previously for single-molecule analyses.[12,14-17,49] LAMP chemistry is based on an auto-cycling strand displacement reaction performed at a constant temperature to synthesize large amounts of amplified product; a LAMP reaction generates more than $10^9$ copies of template within 1 h of incubation at 60–65 °C.[48] We used a cubic reaction volume of 8 nL (200 x 200 x 200 $\mu m^3$), which is in the range of volumes used in digital experiments.[12,14,15,17,49] We assume that an appropriate indicator of an amplification reaction will have a change in absorbance that equates to a change of extinction coefficient of ~25,000 L $mol^{-1}$ $cm^{-1}$ upon reaction (this number approaches the maximum achievable change in absorbance for small-molecule dyes). We use the Beer-Lambert law ($A = \varepsilon(A)$, which describes the relevant parameters to consider for visualization, wherein A = absorbance (the percentage of light absorbed); $\varepsilon$ = extinction coefficient (L $mol^{-1}$ $cm^{-1}$); L = length of the light's path through the solution (cm); c = concentration of absorbing species (mol/L). At a path length of 0.2 mm, an estimated ~2 mM concentration of the dye is required to reach a change of absorbance of 1 unit. Given these parameters, to obtain a readout that can be captured by an unmodified mobile phone, we predicted that an appropriate indicator dye would be one that responds to each nucleotide incorporation (present in mM concentrations), as opposed to responding only to the number of produced molecules (amplicons), which would not exceed primer concentration (present in the µM range).

Colorimetric approaches to visual detection of nucleic acid amplification typically measure absolute changes in color intensity,[50-54] however distinguishing color change—*e.g.* purple *vs.* blue—is difficult and therefore not an appropriate way to quantify readout under variable conditions, such as in LRS. Ratiometric measurements, which take the ratio of two

independent measurements under the same conditions, improve the robustness of a colorimetric approach, converting results to a yes/no binary outcome, eliminating the need for the user to differentiate colors. We hypothesized that a cell phone camera's sensor, which reads in three color channels (red, green, and blue, RGB) could provide suitable information for using a ratiometric approach to read amplification reactions at the single molecule level. The example we considered here is the back-illuminated Exmor R CMOS image sensor[55] used on popular cell phones such as the Samsung Galaxy 4, iPhone 4S, and iPhone 5, which has a sensitivity maxima of ~520 nm (green), ~459 nm (blue), and ~597 nm (red) (**Table 5-2a**).

To illustrate our methodology for a hardware-agnostic visual readout with a ratiometric approach, we selected eriochrome black T (EBT), a magnesium ion indicator that meets the aforementioned dye specifications and has been used previously for visualization of LAMP products.[56,57] During an isothermal amplification reaction, as nucleotides are incorporated, protons and bi-product pyrophosphate ions ($P_2O_7^{4-}$) are produced, and these ions can strongly bind metal ions (*e.g.* $Mg^{2+}$ ions) and form insoluble salts, decreasing the concentration of metal ions in the reaction solution. Before the amplification reaction, EBT is bound to magnesium ions and the reaction solution is purple. As a LAMP reaction proceeds in the presence of target nucleic acid, it is suggested that EBT is deprived of $Mg^{2+}$ by newly generated pyrophosphate ions, and the reaction solution turns blue.

We hypothesized that EBT would be amenable to colorimetric analysis with a cell phone camera because, in RGB terms, in a positive LAMP reaction containing EBT dye, there is higher transmittance in the blue channel (blue LAMP reaction solution), while in a negative LAMP reaction transmittance remains high in the blue and red channels (purple LAMP reaction solution) (**Figure 5.2a**). These observed changes in transmittance between positive and negative reactions can be captured by the Exmor R optical sensor (**Figure 5.2a**), which match well with the observed differences between positive and negative transmittance profiles of LAMP reactions containing EBT (**Figure 5.2a**).

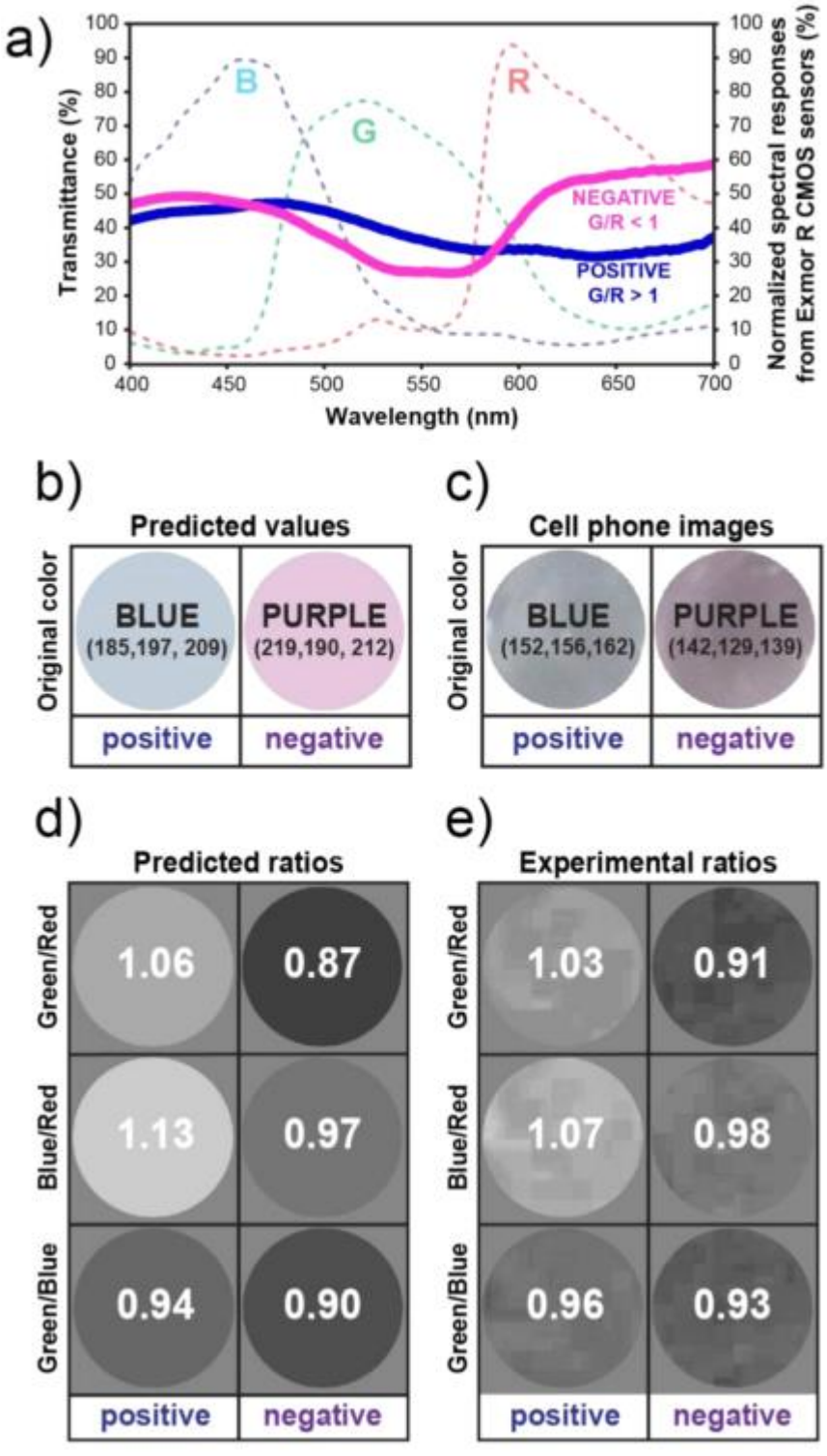
a)
Transmittance (%)
Normalized spectral responses from Exmor R CMOS sensors (%)
Wavelength (nm)
B
G
R
NEGATIVE
G/R < 1
POSITIVE
G/R > 1
b)
Predicted values
Original color
BLUE
(185,197, 209)
PURPLE
(219,190, 212)
positive
negative
c)
Cell phone images
Original color
BLUE
(152,156,162)
PURPLE
(142,129,139)
positive
negative
d)
Predicted ratios
Green/Red
Blue/Red
Green/Blue
1.06
0.87
1.13
0.97
0.94
0.90
positive
negative
e)
Experimental ratios
Green/Red
Blue/Red
Green/Blue
1.03
0.91
1.07
0.98
0.96
0.93
positive
negative

**Figure 5.2: Predicted values and experimental validation of the first step of the ratiometric approach.**

(a) Measured spectral transmittance (%) in the range of visible light (400−700 nm) for positive (solid blue line) and negative (solid purple line) RT-LAMP reaction solutions, each containing 0.7 mM of eriochrome black T (EBT) as the amplification indicator dye. Dashed lines correspond to normalized spectral responses for red (R), green (G), and blue (B) channels of an Exmor R CMOS sensor, a common sensor in cell phone cameras. (b−e) Analysis of the three possible RGB ratiometric combinations for positive and negative RT-LAMP reaction solutions. (b) The predicted RGB values and corresponding colors for positive and negative LAMP amplification reactions obtained by convoluting the transmittance spectrum and Exmor R spectral responses described in panel a. (c) The cropped and enlarged color images collected with an Apple iPhone 4S for positive and negative RT-LAMP reaction solutions containing 90 μM of EBT dye. (d) Predicted images and ratiometric values for positive and negative amplification reactions processed for each ratiometric combination, G/R, B/R, and G/B. (e) Experimental images and ratiometric values for positive and negative amplification reactions for each combination: G/R, B/R, and G/ B. All experiments were performed with HCV RNA as template.

*Selecting the optimal ratiometric approach*

We tested whether the suitability of an indicator dye can be evaluated for a ratiometric approach prior to experimental validation by predicting the RGB values read by a cell phone camera for a positive and a negative reaction. First, we took the transmittance spectra for positive and negative amplification reactions containing EBT and convoluted them with the normalized spectral responses for each of the RGB channels in an Exmor R CMOS sensor[58] providing six curves (a positive and negative for each of the three color channels). Next, we calculated the area under each curve and took its square root (to correct for the standard

square-root scaling that occurs when an image data is compressed to be stored in the memory card of a cell phone), providing the predicted RGB values (**Figure 5.2b**) for positive (R=185, G=197 and B=209) and negative (R=219, G=190 and B=212) RT-LAMP reaction solutions in the presence of EBT at this particular concentration. These values can then be evaluated to select the optimal ratiometric approach for this particular indicator dye. In an RGB color scheme, there are three possible combinations for ratiometric analysis: G/R, B/R, or G/B. The predicted RGB values for a positive and a negative reaction are used to calculate the ratios for each channel combination (**Figure 5.2d**); the ratio with the greatest difference between positive and negative outcomes (G/R in this example) is predicted to be the most robust ratiometric analysis.

Using the approach described above, we predicted the RGB ratios for a positive and negative RT-LAMP reaction in the presence of two additional indicator dyes: hydroxynaphthol blue (HNB) and calmagite. HNB is being reported increasingly in the literature for LAMP visualization,[50,59-62] and calmagite is an analogue of EBT dye with the nitro group absent (more stable version).[63] A side-by-side comparison showed that the greatest predicted difference between positive and negative RT-LAMP reactions, as captured by an unmodified cell phone camera, would be achieved using EBT as the indicator dye and G/R as the ratiometric combination (**Figure 5.17**). Based on these predicted ratios, we decided to validate our methodology using EBT as the indicator dye. We confirmed the storage stability of the EBT dye stock solution in the dried state (**Figure 5.19**), as this is a critical requirement for the use of a dye in real point-of-need diagnostic applications. EBT serves as our validation dye in this paper, however our methodology is designed to be applicable to alternative dyes.

To experimentally validate this approach to predicting an optimal ratiometric combination, we performed an RT-LAMP reaction for HCV RNA containing EBT as the indicator dye and captured an image of the readout with an unmodified camera phone (iPhone 4S) (**Figure 5.2c**). We processed the readout image; color channels of the original image were split, and all three channel ratios (G/R, B/R, G/B) were calculated to derive a ratiometric image for each ratiometric combination. These experimental ratios obtained with an unmodified cell

phone camera (**Figure 5.2e**) matched well with the predicted values (**Figure 5.2d**) for each of the three ratiometric combinations, confirming the predictive power of this approach. The G/B ratio was identified as less appropriate for distinguishing positive and negative reactions because the values for positive and negative reactions were similar; G/R and B/R ratios were identified as suitable because there was sufficient contrast between the values for positive and negative reactions. For the G/R combination, the ratio obtained after a negative reaction was 0.91, and the ratio from a positive reaction was 1.03—a difference of 0.12 (**Figure 5.2e**). For the B/R combination, the ratios for negative and positive reactions were 0.98 and 1.07—a difference of 0.09 (**Figure 5.2e**). Therefore, we selected the G/R combination for our subsequent validation experiments. Counting positives is a more intuitive approach, so the B/R ratio (where the positive ratio had the greatest difference from the background) can be a useful and attractive method. However, it is generally more desirable to select a ratio that includes the green channel because most single-chip digital image sensors used in digital cameras, including cell phones, utilize a Bayer filter mosaic pattern that is composed of 50% green, 25% red, and 25% blue pixels.[64]

To test the robustness of our approach to different hardware and illumination conditions, we used HCV RNA amplified by RT-LAMP at two-fold increasing concentrations of indicator dye ranging from 10.9 µM to 1.4 mM (for a total of eight dye concentrations). After RT-LAMP amplification, 50 µL of each reaction solution were transferred to 96-well plates (path length of ~1.5 mm), and the readout was imaged with cameras from four common cell phone models: Apple iPhone 4S (**Figure 5.3a**), HTC inspire 4G (**Figure 5.3b**), Motorola Moto G (**Figure 5.3c**), and Nokia 808 PureView (**Figure 5.3d**). Under fluorescent light and using the G/R ratiometric process (green channel divided by red channel followed by a threshold adjustment to generate a binarized black and white image), we determined that EBT concentrations lower than 0.175 mM provided an insufficient color change for detection with a cell phone camera (**Figure 5.3, region I, white background**), while concentrations of 1.4 mM inhibited the amplification reaction (**Figure 5.3, region III, red background**). For this particular indicator dye, the range of concentrations at which color change could be detected by an unmodified cell phone camera and no inhibition was observed at the endpoint of the

reaction (Supporting information, **Figure 5.7**) was identified as 0.175 mM to 0.7 mM (**Figure 5.3, region II, green background**). Some cell phone cameras were more sensitive (*e.g.* HTC inspire 4G was able to distinguish a positive result at EBT concentrations as low as 0.0875 mM) (**Figure 5.3b**), but all four cell phone models distinguished a positive reaction at concentrations between 0.175–0.7 mM (**Figure 5.3, region II, green background**). We then chose one cell phone with the most representative performance (Apple iPhone 4S) to test the robustness of the G/R approach to different lighting conditions. Under all conditions tested: incandescent light (**Figure 5.3e**), direct sunlight (**Figure 5.3f**), and indirect sunlight (**Figure 5.3g**), the optimal EBT concentration range that we identified under fluorescent light (0.175–0.7 mM) could be read clearly, confirming the robustness of the ratiometric approach to variations in illumination.

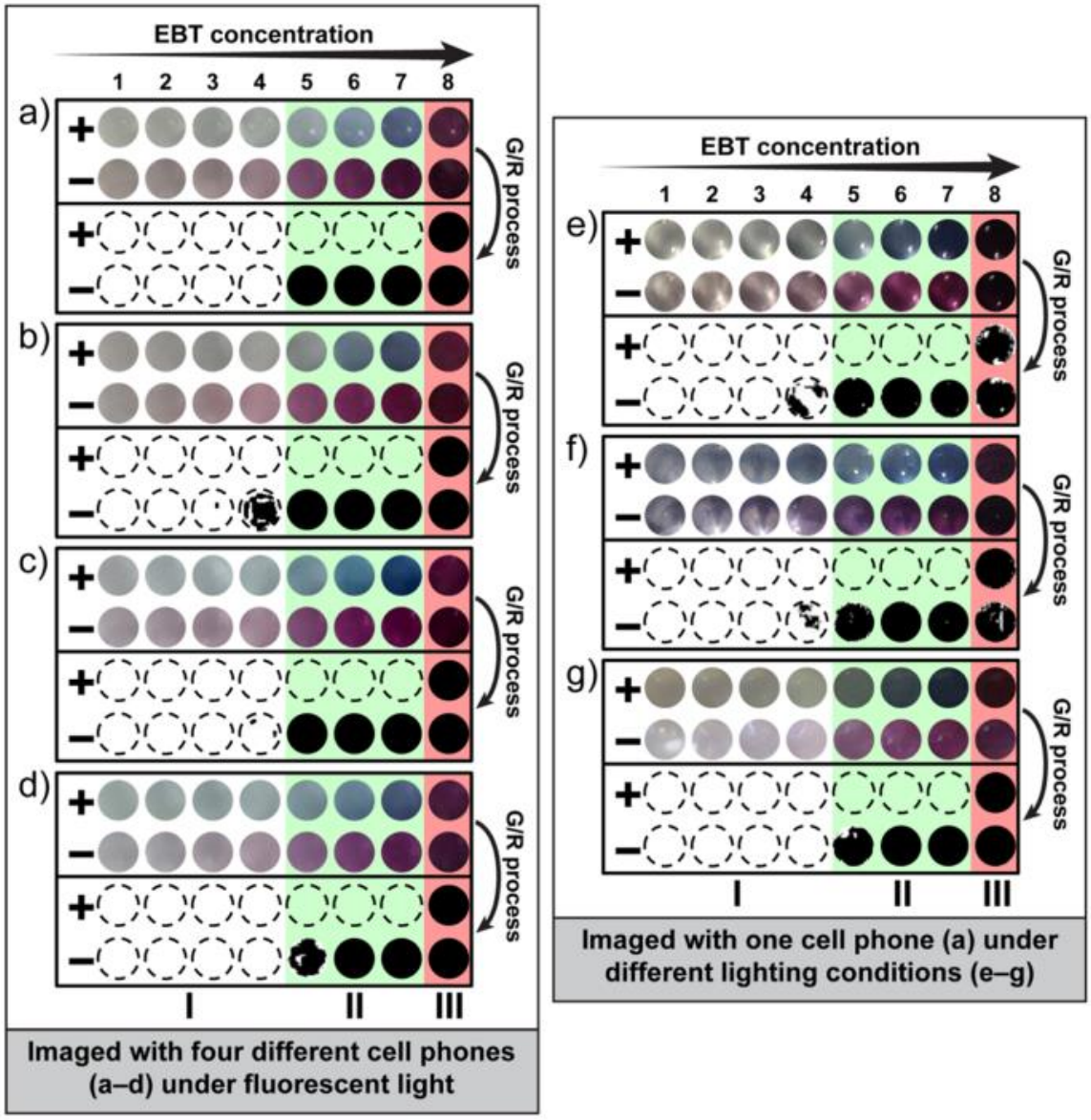


**Figure 5.3: Validation of the robustness of the G/R ratiometric approach to different hardware (cell phone cameras) and lighting conditions.**

(a−g) Enlarged and cropped color images (top two rows of each individual panel) captured by an unmodified cell phone camera from positive (+) and negative (−) RT-LAMP reactions at 2-fold increases in EBT concentration from 10.9 μM to 1.4 mM (1 = 0.011 mM; 2 = 0.022 mM; 3 = 0.044 mM, 4 = 0.088 mM, 5 = 0.175 mM; 6 = 0.35 mM; 7 = 0.7 mM; 8 = 1.4 mM). Positive wells are blue and negative wells are

purple. After G/R ratiometric processing (bottom two rows of each individual panel), negative wells are black. Regions I, II, III in each panel indicate the effect of dye concentration: (II) acceptable concentration range for visualization (green regions); (I) concentrations too low for visualization (white regions); and (III) concentrations too high for visualization (red regions). (a−d) Images captured by four common cell phones under fluorescent light: (a) Apple iPhone 4S, (b) HTC inspire 4G, (c) Motorola Moto G, and (d) Nokia 808 PureView. (e−g) Images captured by an Apple iPhone 4S under three additional light conditions: (e) incandescent light, (f) direct sunlight, and (g) indirect sunlight. All experiments were performed with HCV RNA as a clinically relevant target. All images were acquired with unmodified cell phone cameras. Detailed information for the G/R ratiometric process (**Figure 5.8**) and additional cell phone camera images (**Figure 5.9**) are provided in the Supporting Information.

*One-step method for digital visual readout*

Microfluidic devices enable ultrasensitive digital quantification. Small well volumes are valuable because they enable faster reactions (because concentrations are high in single wells), minimize the effects of inhibitory materials (due to their isolation into wells), and expand the upper limit of the dynamic range (because single molecules can be confined from samples containing high template concentrations).[18,65,66] However, as well volumes (and path lengths) decrease, color visualization becomes challenging for a mobile phone. To compensate, the concentration of the indicator dye can be increased, however high concentrations of some dyes inhibit amplification reactions. Thus, there are inherent physical limits to a colorimetric approach. To validate that this visual readout approach could be applied to single-molecule amplification at nanoliter volumes, we used digital LAMP (dLAMP) and phage lambda DNA (λDNA) as a target. We specifically aimed to resolve three questions: (i) Can we obtain a visual readout for amplified single molecules that can be

captured by an unmodified cell phone camera? (ii) Is volume a factor in achieving a digital visual readout? (iii) Does ratiometric processing work for small volumes?

To answer these questions, we designed a multivolume rotational SlipChip device containing 1,240 wells of eight volumes ranging from 15 nL to 50 nL (**Figure 5.10-11**). We loaded these devices with LAMP reaction solution containing an appropriate target concentration in the middle of the device's dynamic range, a fluorescent DNA-detecting intercalation dye (Syto 9), and EBT dye at 0.7 mM (the highest non-inhibiting concentration identified in **Figure 5.3**). We imaged this device with a house-built real-time fluorescence imager, with a Leica stereoscope (optimal imaging conditions), and with an Apple iPhone 4S. The number of positive counts based on fluorescence was 261, while 260 positives were counted using the indicator dye and G/R process both with the stereoscope and the cell phone (**Figure 5.4**). This experiment showed that the G/R method could be used in place of fluorescence readout to count amplified single molecules and that the readout capture and G/R processing performed on an unmodified cell phone matched the results obtained under optimal lighting conditions (stereoscope). Additionally, using a device containing 800 wells of 27 nL, we observed excellent correlation among positive counts obtained from the stereoscope, fluorescence imager, and cell phone camera (**Figure 5.12**).

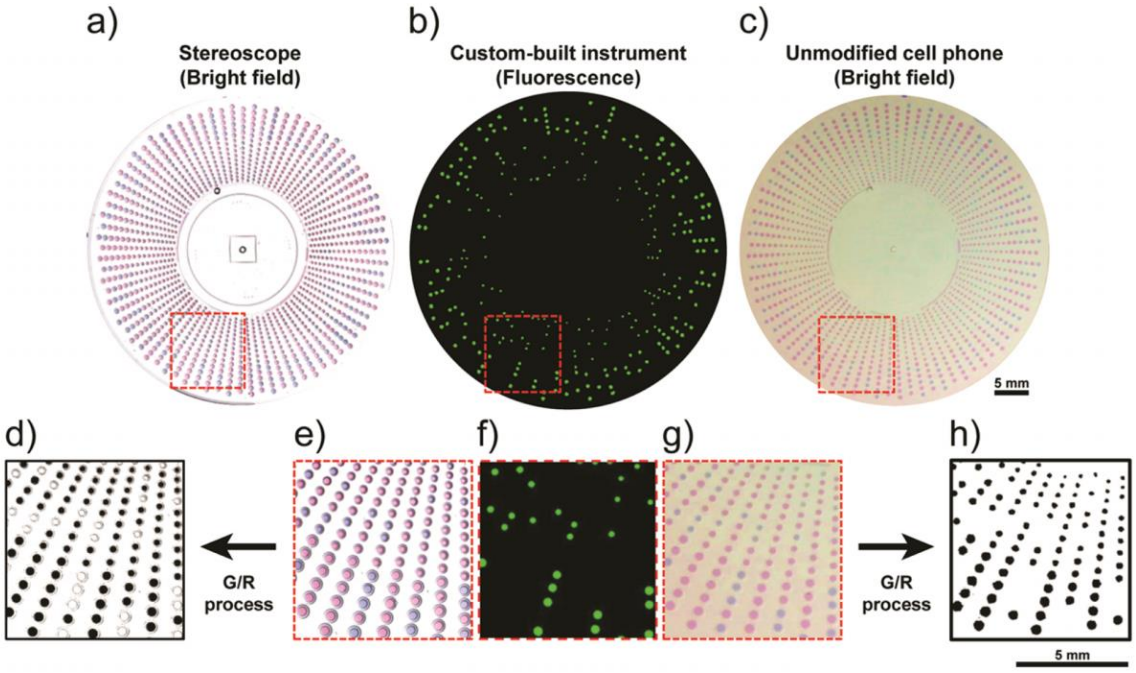


**Figure 5.4: Readout from single-molecule digital LAMP reactions performed with λ DNA on a multivolume rotational SlipChip device imaged by (a) a stereoscope, (b) a fluorescence microscope, and (c) an unmodified cell phone camera.**

(e−g) Callouts are magnified to show visual correlation among the three imaging methods. (d) The results of the ratiometric processing for the stereoscope G/R-processed image and (h) the cell phone G/R-processed image. Colors were enhanced in these figures for clarity of publication; raw images were used in all ratiometric analyses. These devices contained 1240 wells of eight volumes ranging from 15 to 50 nL.

While investigating the limits that reaction volume may impose on visual readout, we observed that the estimated template concentration determined from each of the eight well volumes produced similar Most Probable Numbers (MPN) of molecules (mean 8,500 ± 1,500 copies/mL) (**Figure 5.5a**) (estimated concentration from all volumes are within 95% confidence interval at each volume, detailed in **Figure 5.13**). In addition, all SlipChip

devices, analyzed independently, gave similar target concentrations (8,400 ± 500 copies/mL) (**Figure 5.5b**), suggesting that the selected indicator dye did not impair quantification of single molecules in well sizes 15–50 nL and that these well volumes can be imaged reliably with either a stereoscope or an unmodified cell phone camera. However, the cell phone camera images of well volumes of 15 nL were less clear than those obtained from the stereoscope, suggesting that volumes of ~15 nL may approach the limit of colorimetric imaging with current camera phone sensors, although as higher quality sensors are integrated into commercial cell phones, this limit would change.

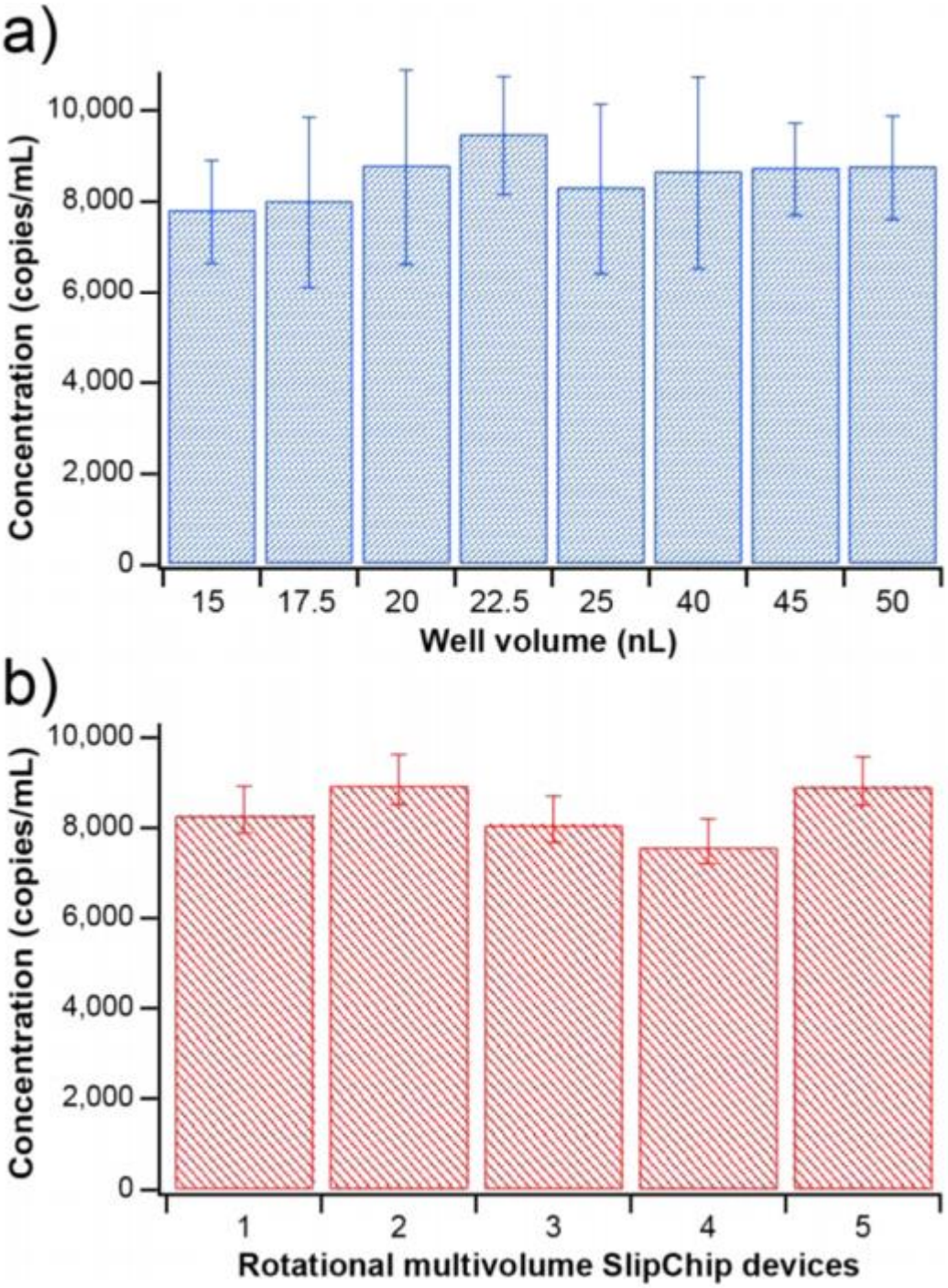


**Figure 5.5: Robustness of digital visual readout at different well volumes.**
Concentration of lambda DNA was estimated by digital LAMP using five multivolume rotational SlipChip devices, each of which contained eight well

volumes ranging from 15–50 nL. (a) Measured template concentration for each well volume averaged over five devices. (b) Mean template concentration for each of five rotational SlipChip devices. Concentrations were calculated using MPN theory,[65] and error bars represent standard deviation. Images were captured by a stereoscope and processed with the ratiometric approach (G/R process).

*Two-step method for digital visual readout*

We next developed a method to apply the visual readout approach to digital devices that contain smaller well volumes. To be able to image at small volumes (*e.g.* 5 nL) on a microfluidic device, one must balance the need for greater indicator color intensity for visualization with the need to keep dye concentrations below the level of inhibition (**Figure 5.3 region III**) for an amplification reaction. High concentrations of indicator dye can completely halt an amplification reaction, and we knew from performing real-time bulk experiments that even when reactions are positive, an indicator dye can still interfere to some extent with isothermal nucleic acid amplification—for both RNA and DNA we observed delays in the time-to-positive, and this delay increased at greater concentrations of the indicator dye, even though reactions were positive (**Figure 5.14**). We hypothesized that we could prevent inhibition completely by decoupling the amplification step from the readout step. To do this, we designed a two-step SlipChip device (based on previous SlipChip designs)[13] (**Figure 5.15-16**) in which the amplification solution and the detection solution are loaded into separate wells (**Figure 5.6a**). We validated this two-step protocol with a clinically relevant target, purified HCV RNA, using digital reverse transcription-LAMP (dRT-LAMP). First, we performed digital isothermal amplification in the set of small (5 nL) amplification wells (in the absence of the indicator dye) (**Figure 5.6a (i)**). After amplification, a "slip" was performed and the amplification wells came into contact with a second set of larger (9.5 nL) wells, which contained the indicator dye—for a total well volume of 14.5 nL (**Figure 5.6a (ii)**). After mixing, negative wells lacking target molecules stayed purple and wells containing positive reactions turned blue (**Figure 5.6a (iii)**). Counts

obtained by a house-built real-time imaging instrument (to read fluorescence), and counts obtained by G/R processing from an image captured by an unmodified cell phone camera were significantly correlated (Pearson's Corr = 0.9998; $R^2$ = 0.9996) (**Figure 6h**), showing that this two-step SlipChip-based protocol provides a suitable visual readout for digital single-molecule amplification for devices containing wells of small volumes.

Devices shown in this manuscript were not designed to achieve clinically relevant concentrations in the lower detection limit of quantification (LDL) because larger well volumes do not represent a challenge when imaging with a mobile phone. Instead, we studied the performance of our approach with wells of small volumes to ensure that this method meets the ULQ required for clinical relevance. The upper limit of quantification (ULQ) is determined by the total number of wells with the smallest volume. As an example, for SlipChip devices with 800 wells of 5 nL the ULQ is 1,162,413 copies/mL, while a SlipChip device with 10,000 wells of 5 nL the ULQ is 1,622,660 (calculations performed according to Kruetz, *et al.* 2011.[65]

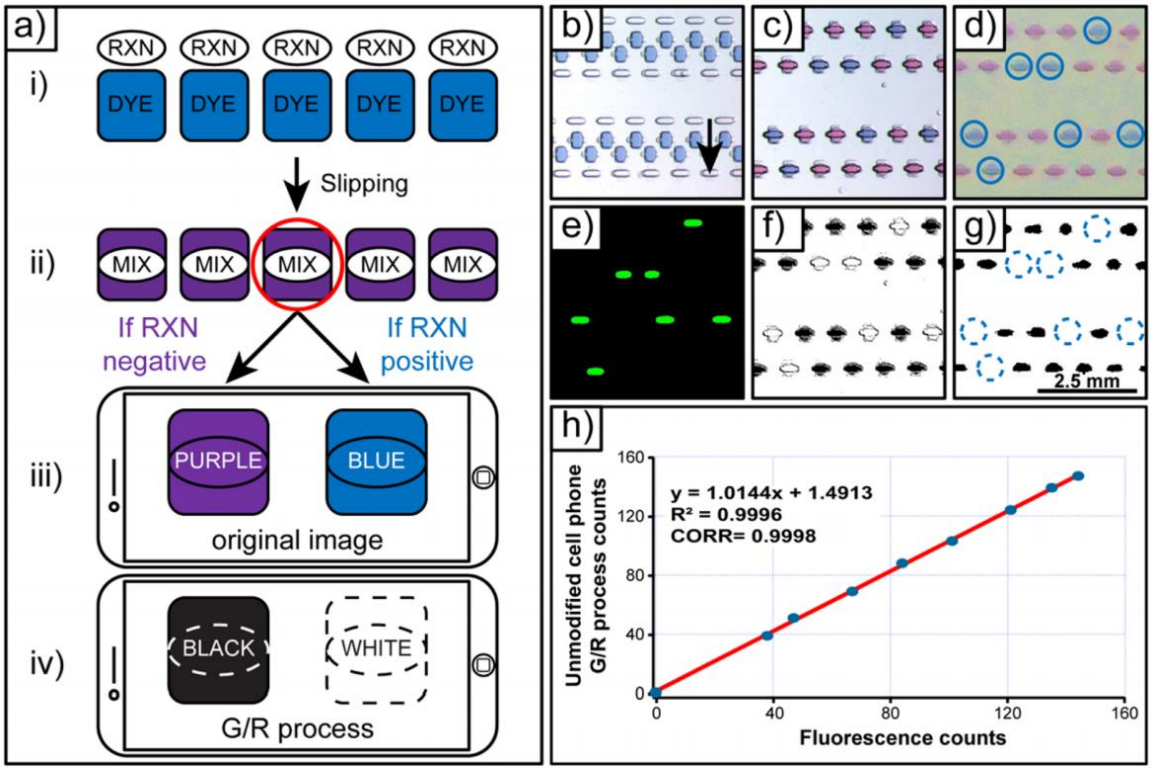


**Figure 5.6: Experimental validation of two-step SlipChip devices for single molecule counting with an unmodified cell phone camera.**

(a) A flow-chart of detection of single molecules in two-step SlipChip: (i) 5 nL amplification wells are loaded with amplification reaction solution (RXN), and 9.5 nL detection wells are loaded with indicator dye (DYE). (ii) After amplification, a slip is performed and the RXN and DYE wells are combined. (iii) Immediately after mixing, positive reaction solutions become blue, while negative reactions remain purple. The readout is imaged by an unmodified cell phone camera. (iv) Ratiometric image processing (G/R process) provides a single binary result (positive or negative). (b) Stereoscope and (c) fluorescence images of the device before the amplification and readout wells are merged (arrow designates direction of slip). (d) Stereoscope and (f) cell phone camera images after the device is slipped and the wells are merged. (e) Stereoscope and (g) cell phone camera images after G/R image processing. (h) Correlation between fluorescence counts and cell phone (G/R processed) counts. Colors were enhanced in figure panels (b, c, d, and f) for clarity of publication; raw

images were used in all ratiometric analyses. In these experiments, HCV RNA was amplified by dRT-LAMP.

## Conclusions

Here we show that single nucleic acid molecules can be detected and counted with an unmodified cell phone camera by employing microfluidic technology, sequence-specific isothermal amplification, and a judiciously chosen amplification-indicator dye. We further show that ratiometric processing of the cell phone image enables robust quantification without the need for a user to differentiate colors. The general methodology we developed can be used as a guideline to enable others to develop their own cell phone based single-molecule counting approach. The methodology includes the following steps: First, an appropriate amplification indicator should be selected. Indicators should respond optically to each nucleotide incorporation event (as opposed to responding to number of produced molecules) resulting in a change in the transmittance profile in the wavelength range of visible light (400–700 nm). The indicator dye should have a change in absorbance matched to the spectral sensitivity of the image sensor in an unmodified cell phone; for ratiometric processing, the solution should have a large relative change in transmittance in color channels for which the camera's image sensor is most sensitive. Second, the color ratio used in the ratiometric approach is chosen based on the spectral sensitivity of the image sensor in an unmodified cell phone. This step can be done *in silico* to identify the dye with the ratio that provides an unambiguous binary readout of positive and negative reactions that is robust to illumination and hardware conditions. We hope others will use this algorithm to identify even better dyes that will move this field forward. Third, the selected dye and ratiometric approach should be validated using the desired amplification chemistry. Experiments should be performed to establish the range of dye concentrations and well volumes at which an amplification reaction is not inhibited and at which imaging can be done with an unmodified cell phone. For some indicator dyes, the range of suitable well volumes and concentrations will be too narrow. In such situations, an alternative approach is to use a two-step device that

separates the amplification and readout steps. Processing can be done directly on a cell phone or uploaded wirelessly to a cloud server to swiftly communicate results, as we have shown previously.[14] We anticipate that the capabilities of visual readout for counting single molecules will extend further as cell phone camera technology advances, as additional indicators are available (*e.g.* metal ions, pH indicators) and as additional types of amplification reactions are developed. Devices that integrate sample preparation, nucleic acid amplification, and a visual digital readout that can be captured easily will be a critical breakthrough toward bringing quantitative, ultrasensitive measurements outside of central laboratories—a key step for *in vitro* diagnostics, pandemic surveillance and environmental monitoring. We hope this work will stimulate regulatory agencies such as the FDA to consider the use of cell phones as valuable diagnostic components.

## Materials and Methods

*Chemicals and materials.*

All chemicals were purchased from commercial sources. The LoopAmp® RNA amplification kit (Eiken Chemical Co., Ltd., Japan) was purchased from SA Scientific (San Antonio, TX, USA). The LoopAmp® RNA amplification kit contains 2X Reaction Mix (RM) (40 mM Tris-HCl pH 8.8, 20 mM KCl, 16 mM MgSO4, 20 mM (NH4)2SO4, 0.2% Tween20, 1.6 M Betaine and dNTPs 2.8 mM each), Enzyme Mix (EM) (mixture of Bst DNA polymerase and AMV reverse transcriptase), and distilled water (DW). Bovine serum albumin (BSA) was purchased from Roche Diagnostics (Indianapolis, IN, USA). Phage lambda DNA (500 μg), SUPERase In RNase Inhibitor (20 U/μL), Eriochrome Black T (EBT) dye, mineral oil (DNase, RNase, and Protease free), tetradecane, Costar™ Clear Polystyrene 96-Well Plates, Corning® Universal Optical Microplate Sealing Tape, and DEPC-treated nuclease-free water were purchased from Thermo Fisher Scientific (Hanover Park, IL, USA). Chelex® 100 resin was purchased from Bio-Rad (Hercules, CA, USA). Trehalose Solution (1 M) was purchased from Amersham Life Science (Cleveland, Ohio,

USA). Tris-HCl buffer stock solution (1 M, pH 8.0) was purchased from Affymetrix (Santa Clara, CA, USA). All primers were produced by Integrated DNA Technologies (Coralville, IA, USA). Dichlorodimethylsilane was purchased from Sigma-Aldrich (St. Louis, MO, USA). SYTO® 9 Stain and AcroMetrix® HCV High Control were purchased from Life Technologies (Grand Island, NY, USA). Nucleic acid extraction kit QIAamp Viral RNA Mini kit was purchased from QIAGEN Inc. (Valencia, CA, USA). Eppendorf Mastercycler Gradient PCR Themal Cycler was purchased from Eppendorf (Hamburg, Germany). POLARstar Omega microplate reader was purchased from BMG Labtech (Durham, NC, USA). Leica MZ Fl III stereoscope with PLAN 0.5x lens was purchased from Leica Microsystems (Bannockburn, IL, USA). Photomasks were designed in AutoCAD 2013 and ordered from CAD/Art Services, Inc. (Bandon, OR, USA). Soda-lime glass plates coated with layers of chromium and photoresist were ordered from the Telic Company (Valencia, CA, USA).

*SlipChip device design.*

The multivolume rotational SlipChip device design was used to demonstrate the one-step method for digital visual readout; this device was composed of 1,240 microfluidic wells, with the following volumes: 160 wells x 15 nL, 160 x 17.5 nL, 160 x 20 nL, 160 x 22.5 nL, 160 x 25 nL, 160 x 40 nL, 160 x 45 nL, 120 x 50 nL (**Figure 5.10**). The total combined volume of all wells was 35.6 µL. For loading, one inlet hole (in the middle ring structure) and four oil escape holes (in the outer ring structure) were drilled in the top plate. The two-step SlipChip device was used to demonstrate a two-step method for digital visual readout; this device was based on previously published SlipChip designs.[13] For the two-step SlipChip design used in this study, the device was modified in the following ways: (i) the number of each type of well was reduced to 800; (ii) space was added between the arrays to allow for the incubation conformation; (iii) the sequence of well loading was reversed (the smaller 5 nL wells are loaded before the larger 9.5 nL wells). See **Figure 5.15** for more details.

SlipChip multivolume designs for HCV and HIV viral load quantification at clinically relevant dynamic ranges[67-69] is provided in the SI (**Table 5-3**).

*SlipChip device fabrication.*

The procedure for fabricating the multivolume rotational SlipChip and two-step SlipChip devices was based on previous work.[70] The device features were etched to a depth of ~100 μm for the multivolume rotational SlipChip devices and ~67 μm for the two-step SlipChip devices. After etching and drilling access holes, both devices were subjected to the same glass silanization process, previously described,[66] where the glass plates were first thoroughly cleaned with piranha mix,dried sequentially with 200-proof ethanol and nitrogen gas, then oxidized in a plasma cleaner for 2 min, and immediately transferred into a vacuum desiccator for 1.5 h for silanization with dimethyldichlorosilane. After silanization, the devices were rinsed thoroughly with chloroform, acetone, and ethanol, and dried with nitrogen gas before use. When a glass SlipChip device needed to be reused, it was first cleaned with acid Piranha Solution and then subjected to the same silanization and rinsing procedure described above.

*Assembling and loading SlipChips.*

The SlipChips used for both the dLAMP and the dRT-LAMP reactions were assembled under degassed oil (mineral oil: tetradecane 1:4 v/v). Both top and bottom plates were immersed in the oil phase and placed face to face. The two plates were aligned under a stereoscope (Leica, Germany) and stabilized using binder clips. Through-holes were drilled into the top plate to serve as fluid inlets and oil outlets in dead-end filling. The reagent solutions were loaded through the inlets by pipetting.

*HCV viral RNA purification from AcroMetrix® HCV High Control.*

200 µL plasma containing HCV RNA (viral load estimate provided by the company: 1.1 IU/mL – 3.5 IU/mL) was extracted using the QIAamp Viral RNA Mini Kit (QIAGEN Inc, Valencia, CA, USA) according to the manufacturer's instructions. The elution volume was 60 µL. The purified HCV viral RNA was analyzed immediately or stored at -80 °C until further analysis.

*Preparation of EBT solution.*

The EBT stock solutions were prepared by dissolving EBT dye in deionized water. The aqueous solution was sonicated for 10–20 min, and the free volume was filled with argon gas and mixed on a rotator at 65 °C for 1 h. To remove any potential impurities from the EBT dye, Chelex® 100 ion exchange resin was added to the resulting solution (5% w/v) and placed on rotator for 1 h. Resin was centrifuged at 3,000 rpm for 5 min, and the top fraction was collected in a Falcon tube, flushed with argon, and stored at room temperature for no more than 2 days. A comparison of EBT, HNB, and calmagite indicator dye stock solutions before and after treatment with Chelex® 100 is provided in the SI (**Figure 5.18**).

*Storage stability of amplification indicator dyes by drying in the presence of stabilizer trehalose*

EBT, HNB, and calmagite stock solutions at 0.7 mM were prepared by dissolving the dyes in 20 mM Tris-HCl buffer (pH 8.8) and adding 30 mM of trehalose. The solutions were sonicated for 10 min and mixed on a rotator at room temperature for 1 h. Chelex® 100 ion exchange resin was added (5% w/v) and placed on rotator for 1 h. Resin was centrifuged at 3,000 rpm for 5 min and the top fraction was collected in a Falcon tube. The resulting stock solutions were transferred to a Costar™ Clear Polystyrene 96-Well Plate (40 µL per well)

and sealed with Corning® Universal Optical Microplate Sealing Tape before spectrophotometric analysis (time 0 h). Immediately after analysis, the sealing cover was removed and the plate was placed in a desiccator under vacuum overnight until the dye stock solutions were completely dry. Then, at 24-hour time points over the next 120 h (for a total of 5 time points), three wells of each dried amplification indicator solution were resuspended with 40 μL of deionized water and spectrophotometric analyses were performed. After each measurement, the plate was sealed again (to prevent hydration of the dried solutions in the other wells) and kept in the dark at room temperature. The absorption spectra analyses were performed by using the POLARstar Omega microplate reader with Omega Data analysis software. Absorbance in the range of 400–700 nm was recorded at 2-nm intervals. Blank solutions (20 mM Tris-HCl buffer with 30 mM Trehalose) were also loaded at time 0 h, desiccated after the first measurement, and treated as the rest of the solutions. The measured spectral absorbance from these control solutions was subtracted at each time point from the plotted data (**Figure 5.19**).

*RT-LAMP amplification of HCV RNA in-tube*

The purified HCV RNA described above was used for in-tube RT-LAMP amplification. The RT-LAMP mix contained the following: 20 μL of RM, 2μL of EM, 2 μL of SYTO® 9 Stain from a 40 μM stock, 4 μL of LAMP primer mixture (20 μM BIP/FIP, 10 μM LB/LF, and 2.5 μM B3/F3), 1 μL of SUPERase In RNase Inhibitor (20 U/L), EBT solutions of various concentrations and with various amounts of RNA template solution, and enough nuclease-free water to bring the volume to 40 μL. The solution was loaded into 0.2 mL PCR tubes and heated at 63 °C for 50 min and 85 °C for 5 min (heat inactivation) on an Eppendorf Mastercycler Gradient PCR Themal Cycler.

*Spectrophotometric analysis for positive and negative RT-LAMP reactions*

Fifty-µL of positive and negative RT-LAMP reaction solutions containing 0.7 mM of EBT, HNB, and calmagite dyes were transferred to a Costar™ Clear Polystyrene 96-Well Plates, the plate was sealed with a Corning® Universal Optical Microplate Sealing Tape and then used for spectrophotometric analysis. An absorption spectra analysis was performed by using the POLARstar Omega microplate reader with Omega Data analysis software. The instrument was first set to zero at 700 nm for distilled water, and absorbance in the range of 400 nm to 700 nm was recorded at 2-nm intervals. Transmittance was calculated from absorbance values using the following equation: $T = 10^{(2-A)}$.

*Prediction of RGB values*

Predicted RGB values for a positive and negative LAMP amplification reaction containing EBT were calculated as follows: (i) The spectral response curves for a Exmor R CMOS image sensor were available only in a graphical format, so data was extracted using Plot Digitizer (ver. 2.6.6) and new plots were generated. (ii) The area under the curve for each of the three color channel spectra was normalized (selecting 1,000 arbitrary values under each curve). Uniform white-balanced light source was assumed. (iii) Convolution of the spectral transmittance spectral profiles of the indicator dye for a positive and a negative LAMP reaction solution (experimentally obtained) with the normalized spectral responses from the Exmor R CMOS image sensor was performed. We ignored the light scattering caused by pyrophosphate release during the amplification reaction. As a result, six curves were generated (a positive and negative for each of the three color channels). (iv) The area under each curve was calculated and its square root taken, providing the predicted RGB values for positive and negative RT-LAMP reaction solutions in the presence of EBT at this particular concentration.

*dLAMP amplification of phage lambda DNA on multivolume rotational SlipChip devices*

To amplify lambda phage DNA using dLAMP method, the LAMP mix contained the following: 20 μL of RM, 2 μL of EM, 2 μL of SYTO® 9 Stain from 40 μM stock, 4 μL of primer mixture (20 μM BIP/FIP, 10 μM LB/LF, and 2.5 μM B3/F3), 2 μL of BSA (20 mg/mL), various amounts of DNA template solution, 4.7 μL of 6 mM EBT dye (0.7 mM final concentration), and enough nuclease-free water to bring the volume to 40 μL. The solution was loaded onto a multivolume rotational SlipChip device and heated at 63 °C for 50 min on flat block PCR machine (Eppendorf Mastercycler). Five minutes of heating at 85 °C was used to stop the reaction.

*Real-time dRT-LAMP of HCV RNA on two-step SlipChip devices*

To amplify HCV viral RNA using dRT-LAMP method on house-built real-time instrument, the RT-LAMP mix contained the following: 20 μL of RM, 2 μL of EM, 2 μL of SYTO® 9 Stain from 40 μM stock, 4 μL of primer mixture (20 μM BIP/FIP, 10 μM LB/LF, and 2.5 μM B3/F3), 2 μL of BSA (20 mg/mL), 1 μL of SUPERase In RNAase inhibitor, various amounts of RNA template solution, and enough nuclease-free water to bring the volume to 40 μL. The solution was loaded into the 5 nL wells of two-step SlipChip devices. Other set of wells (9.5 nL) were loaded with 2.4 mM solution of EBT solution (1.57 mM final concentration). SlipChips were heated at 63 °C for 50 min on a house-built real-time instrument; reactions were stopped by heating to 85°C for 5 min.

*House-built real-time instrument imaging*

Experiments were performed on a Bio-Rad PTC-200 thermocycler with a custom machined block. The block contains a flat 3” x 3” portion onto which the devices are placed ensuring optimal thermal contact. The excitation light source used was a Philips Luxeon S (LXS8-PW30) 1315 lumen LED module with a Semrock filter (FF02-475). Image acquisition was performed with a VX-29MG camera and a Zeiss Macro Planar T F2-100mm lens. A Semrock

filter (FF01-540) was used as an emission filter. Images acquired were analyzed using LabVIEW software.

*House-built real-time instrument data analysis*

Fluorescent images were analyzed using self-developed Labview software. The data were analyzed by first creating a binary mask that defined the location of each reaction volume within the image. The masked spots were then overlaid on the stack of images collected over the course of the experiment, and the average intensity of each individual masked spot was tracked over the course of the stack. Background subtraction of the real-time trace was performed by creating a least mean square fit of each individual trace. Threshold was then manually set at the half height of the averaged maximum intensity, and the time-to-positive of each reaction was then determined as the point at which the real-time curve crossed the defined threshold.

*Bright-field image acquisition*

A mobile phone was used to capture the readout under standard fluorescent light, using the camera's default autofocus and autoexposure settings. Photographs of the 96-well plate were also taken using alternate commercial cell phones and under different lighting conditions (**Figure 5.3** and **Figure 5.9**). Stereoscope imaging was done using Leica MZ Fl III stereoscope with a PLAN 0.5x lens. The stereoscope was equipped with a Diagnostic Instruments color mosaic model 11.2 megapixel camera, and images were acquired using Spot imaging software. An automatic white-balance adjustment was done for each image using Spot software. Multiple images were acquired to capture all wells in the device, and assembled to form a complete image of the device to compare with the image acquired from the cell phone camera by using the freeware Image Composite Editor (ver. 2.0).

*Bright field image processing and data analysis*

Images acquired with cell phone and stereoscope were processed using open source Image J software (ver.1.49) according to the standard procedure. Briefly: (i) white balance was corrected as needed, (ii) color channels of the original image were split and, (iii) one channel was divided by a second channel (*e.g.*, green channel divided by the red channel in the G/R approach) to derive a ratiometric image; and (iv), automatic thresholding was applied to make a binary (black and white) image. Semi-automatic counting on the two-step Slipchip images was accomplished using a freeware Fiji image processing. Acquired bright field images for the multivolume rotational SlipChips were counted manually.

**References**

1. Calmy, A., Ford, N., Hirschel, B., Reynolds, S.J., Lynen, L., Goemaere, E., de la Vega, F.G., Perrin, L. and Rodriguez, W. HIV Viral Load Monitoring in Resource-Limited Regions: Optional or Necessary? *Clin. Infect. Dis.* **2007** *44*, 128-134.

2. Johannessen, A. Where We Are with Point-of-Care Testing. *J. Viral Hepatitis* **2015** *22*, 362-365.

3. Wang, S., Xu, F. and Demirci, U. Advances in Developing HIV-1 Viral Load Assays for Resource-Limited Settings. *Biotechnol. Adv.* **2010** *28*, 770-781.

4. Yager, P., Edwards, T., Fu, E., Helton, K., Nelson, K., Tam, M.R. and Weigl, B.H. Microfluidic Diagnostic Technologies for Global Public Health. *Nature* **2006** *442*, 412-418.

5. Peeling, R.W., Holmes, K.K., Mabey, D. and Ronald, A. Rapid Tests for Sexually Transmitted Infections (STIs): The Way Forward. *Sex. Transm. Infect.* **2006** *82 Suppl 5*, 1-6.

6. Yager, P., Domingo, G.J. and Gerdes, J. Point-of-Care Diagnostics for Global Health. *Annu. Rev. Biomed. Eng.* **2008** *10*, 107-144.

7. Niemz, A., Ferguson, T.M. and Boyle, D.S. Point-of-Care Nucleic Acid Testing for Infectious Diseases. *Trends Biotechnol.* **2011** *29*, 240-250.

8. Thom, N.K., Yeung, K., Pillion, M.B. and Phillips, S.T. "Fluidic Batteries" as Low-Cost Sources of Power in Paper-Based Microfluidic Devices. *Lab Chip* **2012** *12*, 1768-1770.

9. Labarre, P., Gerlach, J., Wilmoth, J., Beddoe, A., Singleton, J. and Weigl, B. **2010**, *Conf. Proc. IEEE Eng. Med. Biol. Soc*. 2010/11/26 ed, Vol. 2010, pp. 1097-1099.

10. Curtis, K.A., Rudolph, D.L., Nejad, I., Singleton, J., Beddoe, A., Weigl, B., LaBarre, P. and Owen, S.M. Isothermal Amplification Using a Chemical Heating Device for Point-of-Care Detection of HIV-1. *PLoS One* **2012** *7*, e31432.

11. Liu, C., Mauk, M.G., Hart, R., Qiu, X. and Bau, H.H. A Self-Heating Cartridge for Molecular Diagnostics. *Lab Chip* **2011** *11*, 2686-2692.

12. Sun, B., Shen, F., McCalla, S.E., Kreutz, J.E., Karymov, M.A. and Ismagilov, R.F. Mechanistic Evaluation of the Pros and Cons of Digital RT-LAMP for HIV-1 Viral Load Quantification on a Microfluidic Device and Improved Efficiency *Via* a Two-Step Digital Protocol. *Anal. Chem.* **2013** *85*, 1540-1546.

13. Shen, F., Davydova, E.K., Du, W.B., Kreutz, J.E., Piepenburg, O. and Ismagilov, R.F. Digital Isothermal Quantification of Nucleic Acids *Via* Simultaneous Chemical

Initiation of Recombinase Polymerase Amplification Reactions on SlipChip. *Anal. Chem.* **2011** *83*, 3533-3540.

14. Selck, D.A., Karymov, M.A., Sun, B. and Ismagilov, R.F. Increased Robustness of Single-Molecule Counting with Microfluidics, Digital Isothermal Amplification, and a Mobile Phone *Versus* Real-Time Kinetic Measurements. *Anal. Chem.* **2013** *85*, 11129-11136.

15. Sun, B., Rodriguez-Manzano, J., Selck, D.A., Khorosheva, E., Karymov, M.A. and Ismagilov, R.F. Measuring Fate and Rate of Single-Molecule Competition of Amplification and Restriction Digestion, and Its Use for Rapid Genotyping Tested with Hepatitis C Viral RNA. *Angew. Chem. Int. Edit.* **2014** *53*, 8088-8092.

16. Zhu, Q.Y., Gao, Y.B., Yu, B.W., Ren, H., Qiu, L., Han, S.H., Jin, W., Jin, Q.H. and Mu, Y. Self-Priming Compartmentalization Digital LAMP for Point-of-Care. *Lab Chip* **2012** *12*, 4755-4763.

17. Gansen, A., Herrick, A.M., Dimov, I.K., Lee, L.P. and Chiu, D.T. Digital LAMP in a Sample Self-Digitization (Sd) Chip. *Lab Chip* **2012** *12*, 2247-2254.

18. Witters, D., Sun, B., Begolo, S., Rodriguez-Manzano, J., Robles, W. and Ismagilov, R.F. Digital Biology and Chemistry. *Lab Chip* **2014** *14*, 3225-3232.

19. Sidorova, J.M., Li, N., Schwartz, D.C., Folch, A. and Monnat, R.J., Jr. Microfluidic-Assisted Analysis of Replicating DNA Molecules. *Nat. Protoc.* **2009** *4*, 849-861.

20. Chou, H.P., Spence, C., Scherer, A. and Quake, S. A Microfabricated Device for Sizing and Sorting DNA Molecules. *Proc. Natl. Acad. Sci. U. S. A.* **1999** *96*, 11-13.

21. Marcus, J.S., Anderson, W.F. and Quake, S.R. Microfluidic Single-Cell mRNA Isolation and Analysis. *Anal. Chem.* **2006** *78*, 3084-3089.

22. Ottesen, E.A., Hong, J.W., Quake, S.R. and Leadbetter, J.R. Microfluidic Digital PCR Enables Multigene Analysis of Individual Environmental Bacteria. *Science* **2006** *314*, 1464-1467.

23. Beer, N.R., Hindson, B.J., Wheeler, E.K., Hall, S.B., Rose, K.A., Kennedy, I.M. and Colston, B.W. On-Chip, Real-Time, Single-Copy Polymerase Chain Reaction in Picoliter Droplets. *Anal. Chem.* **2007** *79*, 8471-8475.

24. Kiss, M.M., Ortoleva-Donnelly, L., Beer, N.R., Warner, J., Bailey, C.G., Colston, B.W., Rothberg, J.M., Link, D.R. and Leamon, J.H. High-Throughput Quantitative Polymerase Chain Reaction in Picoliter Droplets. *Anal. Chem.* **2008** *80*, 8975-8981.

25. Sundberg, S.O., Wittwer, C.T., Gao, C. and Gale, B.K. Spinning Disk Platform for Microfluidic Digital Polymerase Chain Reaction. *Anal. Chem.* **2010** *82*, 1546-1550.

26. Lagally, E.T., Medintz, I. and Mathies, R.A. Single-Molecule DNA Amplification and Analysis in an Integrated Microfluidic Device. *Anal. Chem.* **2001** *73*, 565-570.

27. Shen, F., Du, W., Kreutz, J.E., Fok, A. and Ismagilov, R.F. Digital PCR on a Slipchip. *Lab Chip* **2010** *10*, 2666-2672.

28. Chin, C.D., Linder, V. and Sia, S.K. Lab-on-a-Chip Devices for Global Health: Past Studies and Future Opportunities. *Lab Chip* **2007** *7*, 41-57.

29. Chin, C.D., Laksanasopin, T., Cheung, Y.K., Steinmiller, D., Linder, V., Parsa, H., Wang, J., Moore, H., Rouse, R., Umviligihozo, G., Karita, E., Mwambarangwe, L., Braunstein, S.L., van de Wijgert, J., Sahabo, R., Justman, J.E., El-Sadr, W. and Sia, S.K. Microfluidics-Based Diagnostics of Infectious Diseases in the Developing World. *Nat. Med.* **2011** *17*, 1015-1019.

30. Chin, C.D., Linder, V. and Sia, S.K. Commercialization of Microfluidic Point-of-Care Diagnostic Devices. *Lab Chip* **2012** *12*, 2118-2134.

31. International Telecommunication Union. **2015** ICT Facts and Figures--the World in 2015. http://www.itu.int/en/ITU-D/Statistics/Pages/facts/default.aspx.

32. Whitesides, G.M. A Glimpse into the Future of Diagnostics. *Clin. Chem.* **2013** *59*, 589-591.

33. Berg, B., Cortazar, B., Tseng, D., Ozkan, H., Feng, S., Wei, Q.S., Chan, R.Y.L., Burbano, J., Farooqui, Q., Lewinski, M., Di Carlo, D., Garner, O.B. and Ozcan, A. Cellphone-Based Hand-Held Microplate Reader for Point-of-Care Testing of Enzyme-Linked Immunosorbent Assays. *ACS Nano* **2015** *9*, 7857-7866.

34. Wei, Q., Luo, W., Chiang, S., Kappel, T., Mejia, C., Tseng, D., Chan, R.Y., Yan, E., Qi, H., Shabbir, F., Ozkan, H., Feng, S. and Ozcan, A. Imaging and Sizing of Single DNA Molecules on a Mobile Phone. *ACS nano* **2014** *8*, 12725-12733.

35. Laksanasopin, T., Guo, T.W., Nayak, S., Sridhara, A.A., Xie, S., Olowookere, O.O., Cadinu, P., Meng, F., Chee, N.H., Kim, J., Chin, C.D., Munyazesa, E., Mugwaneza, P., Rai, A.J., Mugisha, V., Castro, A.R., Steinmiller, D., Linder, V., Justman, J.E., Nsanzimana, S. *et al.* A Smartphone Dongle for Diagnosis of Infectious Diseases at the Point of Care. *Sci. Transl. Med.* **2015** *7*, 273re271.

36. Yetisen, A.K., Akram, M.S. and Lowe, C.R. Paper-Based Microfluidic Point-of-Care Diagnostic Devices. *Lab Chip* **2013** *13*, 2210-2251.

37. Besant, J.D., Das, J., Burgess, I.B., Liu, W., Sargent, E.H. and Kelley, S.O. Ultrasensitive Visual Read-out of Nucleic Acids Using Electrocatalytic Fluid Displacement. *Nat. Commun.* **2015** *6*, 6978.

38. Martinez, A.W., Phillips, S.T., Carrilho, E., Thomas, S.W., Sindi, H. and Whitesides, G.M. Simple Telemedicine for Developing Regions: Camera Phones and Paper-Based Microfluidic Devices for Real-Time, Off-Site Diagnosis. *Anal. Chem.* **2008** *80*, 3699-3707.

39. Martinez, A.W., Phillips, S.T., Whitesides, G.M. and Carrilho, E. Diagnostics for the Developing World: Microfluidic Paper-Based Analytical Devices. *Anal. Chem.* **2010** *82*, 3-10.

40. Park, T.S., Li, W.Y., McCracken, K.E. and Yoon, J.Y. Smartphone Quantifies Salmonella from Paper Microfluidics. *Lab Chip* **2013** *13*, 4832-4840.

41. Vashist, S.K., Mudanyali, O., Schneider, E.M., Zengerle, R. and Ozcan, A. Cellphone-Based Devices for Bioanalytical Sciences. *Anal. Bioanal. Chem.* **2014** *406*, 3263-3277.

42. You, D.J., Park, T.S. and Yoon, J.Y. Cell-Phone-Based Measurement of TSH Using Mie Scatter Optimized Lateral Flow Assays. *Biosens. Bioelectron.* **2013** *40*, 180-185.

43. Shen, L., Hagen, J.A. and Papautsky, I. Point-of-Care Colorimetric Detection with a Smartphone. *Lab Chip* **2012** *12*, 4240-4243.

44. Tyburski, E.A., Gillespie, S.E., Stoy, W.A., Mannino, R.G., Weiss, A.J., Siu, A.F., Bulloch, R.H., Thota, K., Cardenas, A., Session, W., Khoury, H.J., O'Connor, S., Bunting, S.T., Boudreaux, J., Forest, C.R., Gaddh, M., Leong, T., Lyon, L.A. and Lam, W.A. Disposable Platform Provides Visual and Color-Based Point-of-Care Anemia Self-Testing. *J. Clin. Invest.* **2014** *124*, 4387-4394.

45. Garcia, A., Erenas, M.M., Marinetto, E.D., Abad, C.A., de Orbe-Paya, I., Palma, A.J. and Capitan-Vallvey, L.F. Mobile Phone Platform as Portable Chemical Analyzer. *Sens. Actuator B-Chem.* **2011** *156*, 350-359.

46. Wang, S.Q., Zhao, X.H., Khimji, I., Akbas, R., Qiu, W.L., Edwards, D., Cramer, D.W., Ye, B. and Demirci, U. Integration of Cell Phone Imaging with Microchip ELISA to Detect Ovarian Cancer HE4 Biomarker in Urine at the Point-of-Care. *Lab Chip* **2011** *11*, 3411-3418.

47. Nagamine, K., Hase, T. and Notomi, T. Accelerated Reaction by Loop-Mediated Isothermal Amplification Using Loop Primers. *Mol. Cell. Probes* **2002** *16*, 223-229.

48. Notomi, T., Okayama, H., Masubuchi, H., Yonekawa, T., Watanabe, K., Amino, N. and Hase, T. Loop-Mediated Isothermal Amplification of DNA. *Nucleic Acids Res.* **2000** *28*.

49. Nixon, G., Garson, J.A., Grant, P., Nastouli, E., Foy, C.A. and Huggett, J.F. Comparative Study of Sensitivity, Linearity, and Resistance to Inhibition of Digital and Nondigital Polymerase Chain Reaction and Loop Mediated Isothermal Amplification Assays for Quantification of Human Cytomegalovirus. *Anal. Chem.* **2014** *86*, 4387-4394.

50. Goto, M., Honda, E., Ogura, A., Nomoto, A. and Hanaki, K.I. Colorimetric Detection of Loop-Mediated Isothermal Amplification Reaction by Using Hydroxy Naphthol Blue. *Biotechniques* **2009** *46*, 167-+.

51. Tanner, N.A., Zhang, Y. and Evans, T.C., Jr. Visual Detection of Isothermal Nucleic Acid Amplification Using pH-Sensitive Dyes. *Biotechniques* **2015** *58*, 59-68.

52. Wang, D.G. **2014**, Visual Detection of *Mycobacterium Tuberculosis* Complex with Loop-Mediated Isothermal Amplification and Eriochrome Black T. *Proceedings in Materials, Machines and Development of Technologies for Industrial Production*, Vol. 618, pp. 264-267.

53. Yetisen, A.K., Martinez-Hurtado, J.L., Garcia-Melendrez, A., Vasconcellos, F.D. and Lowe, C.R. A Smartphone Algorithm with Inter-Phone Repeatability for the Analysis of Colorimetric Tests. *Sens. Actuator B-Chem.* **2014** *196*, 156-160.

54. Safavieh, M., Ahmed, M.U., Sokullu, E., Ng, A., Braescu, L. and Zourob, M. A Simple Cassette as Point-of-Care Diagnostic Device for Naked-Eye Colorimetric Bacteria Detection. *Analyst* **2014** *139*, 482-487.

55. Sony Corp. **2010** Sony "Exmor R" Cmos Image Sensors Achieve a Dramatic Increase in Performance. *CX-News Archives, Vol. 59,* http://www.sony.net/Products/SC-HP/cx_news_archives/img/pdf/vol_59/featuring_Exmorr.pdf.

56. Oh, S.J., Park, B.H., Jung, J.H., Choi, G., Lee, D.C., Kim do, H. and Seo, T.S. Centrifugal Loop-Mediated Isothermal Amplification Microdevice for Rapid, Multiplex and Colorimetric Foodborne Pathogen Detection. *Biosens. Bioelectron.* **2016** *75*, 293-300.

57. Wang, D.G. Visual Detection of *Mycobacterium Tuberculosis* Complex with Loop-Mediated Isothermal Amplification and Eriochrome Black T. *Appl. Mech. Mater.* **2014** *618*, 264-267.

58. Sony Corp. **2011** High Picture Quality Cellular Phone CMOS Image Sensors Feature Full HD Video. *CX-News Archives, Vol. 65,* http://www.sony.net/Products/SC-HP/cx_news_archives/img/pdf/vol_65/imx081_091_111pq.pdf.

59. Ma, X.J., Shu, Y.L., Nie, K., Qin, M., Wang, D.Y., Gao, R.B., Wang, M., Wen, L.Y., Han, F., Zhou, S.M., Zhao, X., Cheng, Y.H., Li, D.X. and Dong, X.P. Visual Detection of Pandemic Influenza a H1N1 Virus 2009 by Reverse-Transcription Loop-Mediated Isothermal Amplification with Hydroxynaphthol Blue Dye. *J. Virol. Meth.* **2010** *167*, 214-217.

60. Nie, K., Zhao, X., Ding, X., Li, X.D., Zou, S.M., Guo, J.F., Wang, D.Y., Gao, R.B., Li, X.Y., Huang, W.J., Shu, Y.L. and Ma, X.J. Visual Detection of Human Infection with Influenza a (H7n9) Virus by Subtype-Specific Reverse Transcription Loop-Mediated Isothermal Amplification with Hydroxynaphthol Blue Dye. *Clin. Microbiol. Infect.* **2013** *19*, E372-375.

61. Duan, Y.B., Ge, C.Y., Zhang, X.K., Wang, J.X. and Zhou, M.G. Development and Evaluation of a Novel and Rapid Detection Assay for *Botrytis Cinerea* Based on Loop-Mediated Isothermal Amplification. *PLoS One* **2014** *9*, e111094.

62. Yang, B.Y., Liu, X.L., Wei, Y.M., Wang, J.Q., He, X.Q., Jin, Y. and Wang, Z.J. Rapid and Sensitive Detection of Human Astrovirus in Water Samples by Loop-Mediated Isothermal Amplification with Hydroxynaphthol Blue Dye. *BMC Microbiol.* **2014** *14*, 38.

63. Lindstrom, F. and Diehl, H. Indicator for the Titration of Calcium Plus Magnesium with (Ethylenedinitrilo)Tetraacetate. *Anal. Chem.* **1960** *32*, 1123-1127.

64. Bayer, B.E. **1976** Color Imaging Array US 05/555,477.

65. Kreutz, J.E., Munson, T., Huynh, T., Shen, F., Du, W.B. and Ismagilov, R.F. Theoretical Design and Analysis of Multivolume Digital Assays with Wide Dynamic Range Validated Experimentally with Microfluidic Digital PCR. *Anal. Chem.* **2011** *83*, 8158-8168.

66. Shen, F., Sun, B., Kreutz, J.E., Davydova, E.K., Du, W.B., Reddy, P.L., Joseph, L.J. and Ismagilov, R.F. Multiplexed Quantification of Nucleic Acids with Large Dynamic Range Using Multivolume Digital RT-PCR on a Rotational Slipchip Tested with HIV and Hepatitis C Viral Load. *J. Am. Chem. Soc.* **2011** *133*, 17705-17712.

67. Arnedo, M., Alonso, E., Eisenberg, N., Ibanez, L., Ferreyra, C., Jaen, A., Flevaud, L., Khamadi, S., Roddy, P., Gatell, J.M. and Dalmau, D. Monitoring HIV Viral Load in Resource Limited Settings: Still a Matter of Debate? *PLoS One* **2012** *7*, e47391.

68. Feeney, E.R. and Chung, R.T. Antiviral Treatment of Hepatitis C. *BMJ* **2014** *348*, g3308.

69. Cobb, B., Pockros, P.J., Vilchez, R.A. and Vierling, J.M. HCV RNA Viral Load Assessments in the Era of Direct-Acting Antivirals. *Am. J. Gastroenterol.* **2013** *108*, 471-475.

70. Du, W.B., Li, L., Nichols, K.P. and Ismagilov, R.F. Slipchip. *Lab Chip* **2009** *9*, 2286-2292.

**Supporting Information**

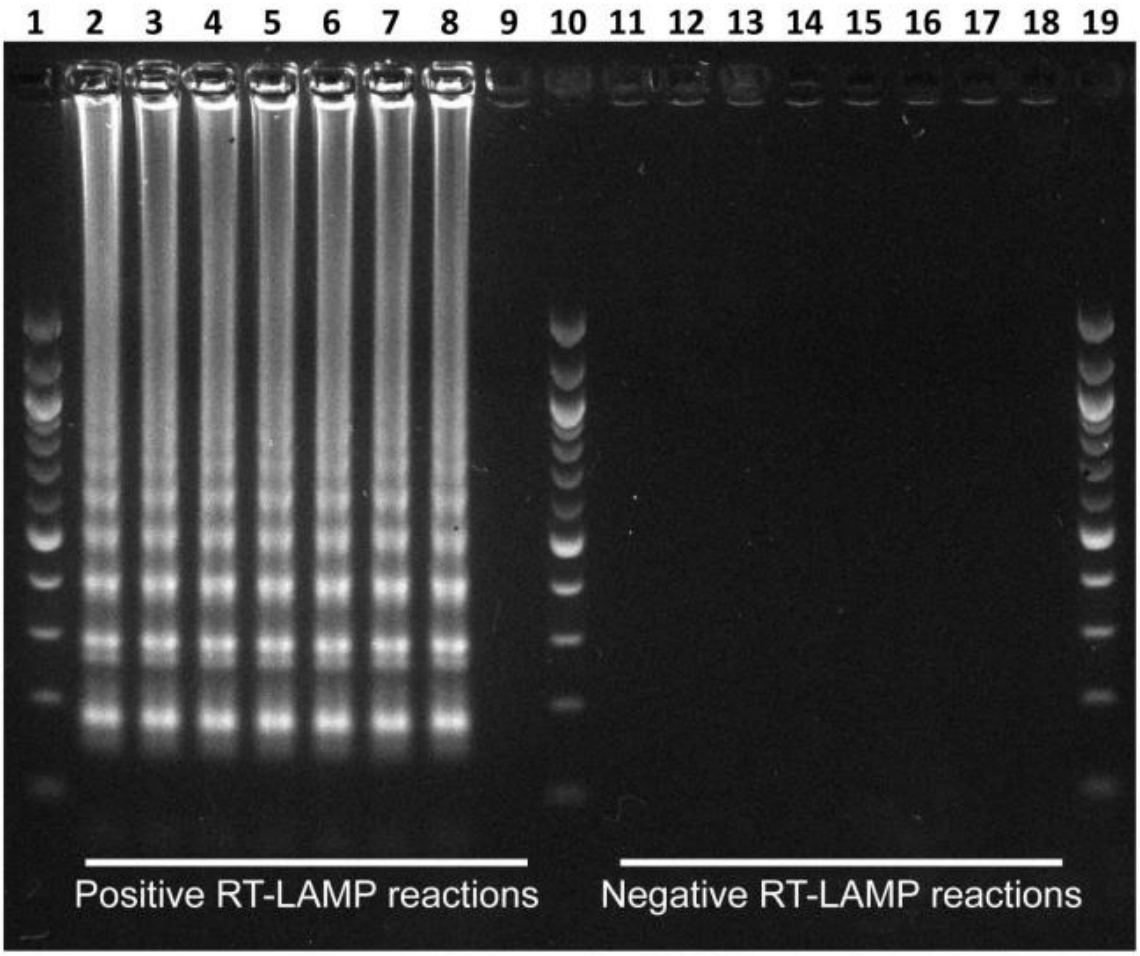


**Figure 5.7: DNA gel electrophoresis for RT-LAMP product.**

Lanes 1, 10, and 19 are 100 bp DNA ladders. Lanes 2–9 are positive (HCV RNA) RT-LAMP reactions at two-fold increased EBT solution concentration (from 0.011 to 1.4 mM). Lanes 11–18 are negative RT-LAMP reactions at two-fold increased EBT solution concentration (from 0.011 to 1.4 mM). Lane 9 shows an inhibited RT-LAMP reaction in the presence of 1.4 mM EBT solution.

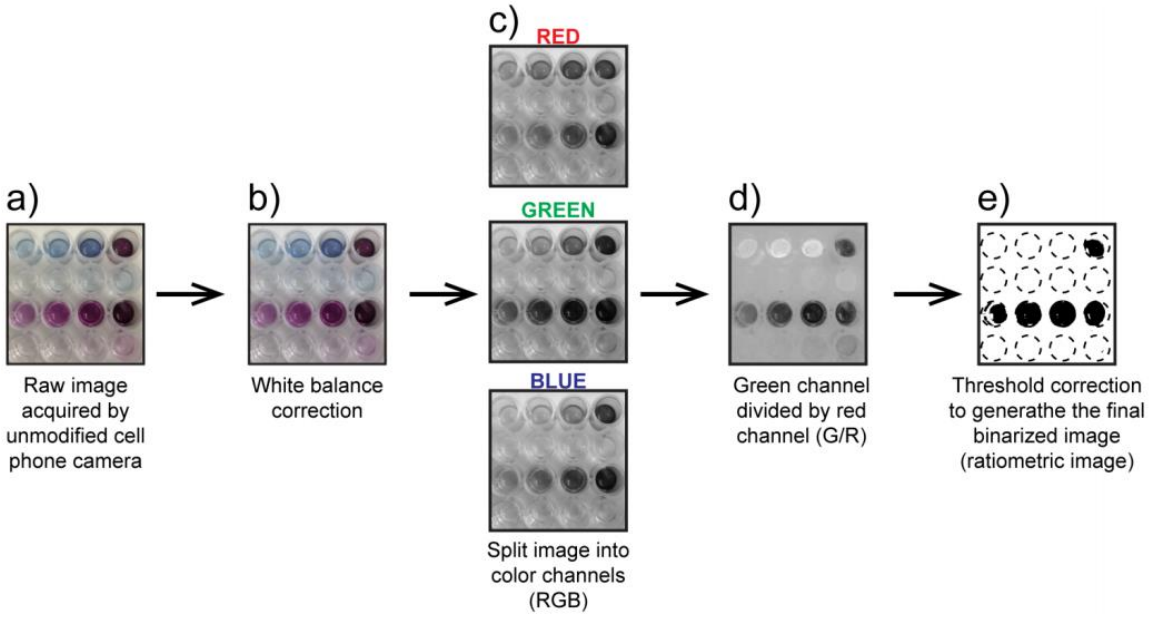


**Figure 5.8: Each step of the G/R process algorithm.**

This experiment was performed with HCV RNA as a clinically relevant target, and the raw image was acquired with an Apple iPhone 4S under fluorescent light. The top row of each panel (eight wells) shows a positive RT-LAMP reaction containing EBT solution at two-fold increasing concentrations from 10.9 µM to 1.4 mM (from left to right). The bottom row of each panel (eight wells) shows negative RT-LAMP reactions containing EBT solution at two-fold increasing concentrations from 10.9 µM to 1.4 mM. a). A raw image acquired by a cell phone camera. b) The same image after white balance correction. c) Red, green, and blue color channels separated. d) Resulting image after green channel is divided by red channel. e) The binary image after a threshold correction. Positive reactions (originally blue) are white and negative reactions (originally purple) are black. Image processing was performed with Image J (ver. 1.49).

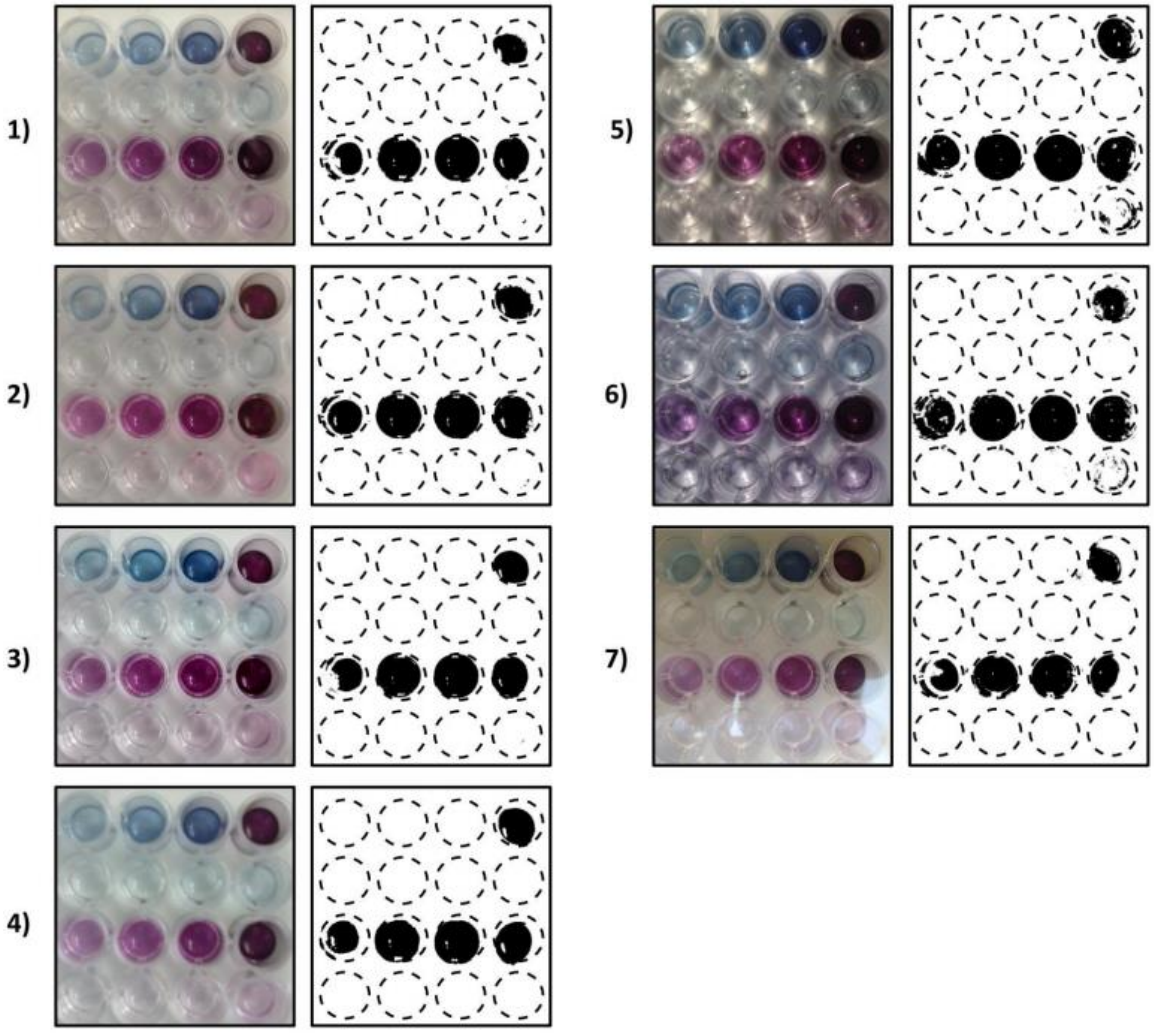


**Figure 5.9: Original and G/R-processed images acquired with unmodified cell phone cameras.**

Original color images show negative (bottom two rows) and positive (top two rows) RT-LAMP reactions. From left to right, EBT concentration is increased in two-fold increments between 10.9 µM to .088mM (bottom row) and .175mM to 1.4mM (second row from the bottom). Positives contained HCV RNA, and the same EBT concentration pattern was repeated. Negative wells are purple and positive wells are blue. Ratiometric G/R-processed images show the binary result in which the negative wells become black and the positive wells become white. (1–4) Images collected with four common cell phones under fluorescent light: (1) Apple iPhone 4S, (2) HTC

inspire 4G, (3) Motorola Moto G, and (4) Nokia 808 PureView. (5–7) Images collected with Apple iPhone 4S under different light conditions: (5) incandescent light, (6) direct sunlight, and (7) indirect sunlight. Image processing was performed with ImageJ (ver. 1.49).

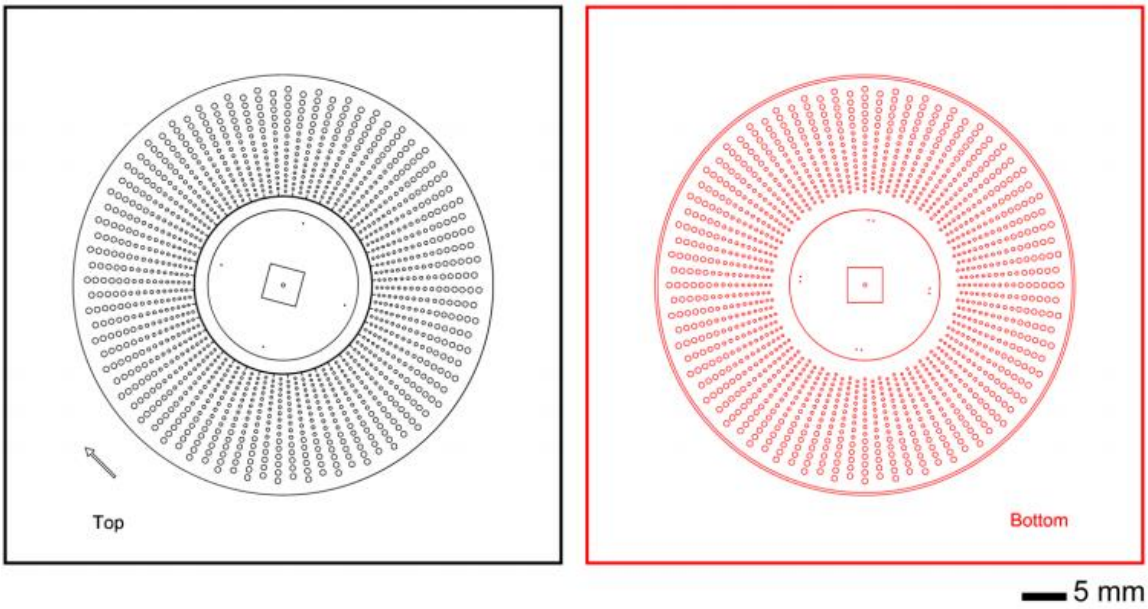


**Figure 5.10: Schematic of the top (left) and bottom (right) plates of the multivolume rotational SlipChip device used in the one-step digital LAMP experiments before being assembled.**

The top plate shows the direction of the rotational 4.5° slip.

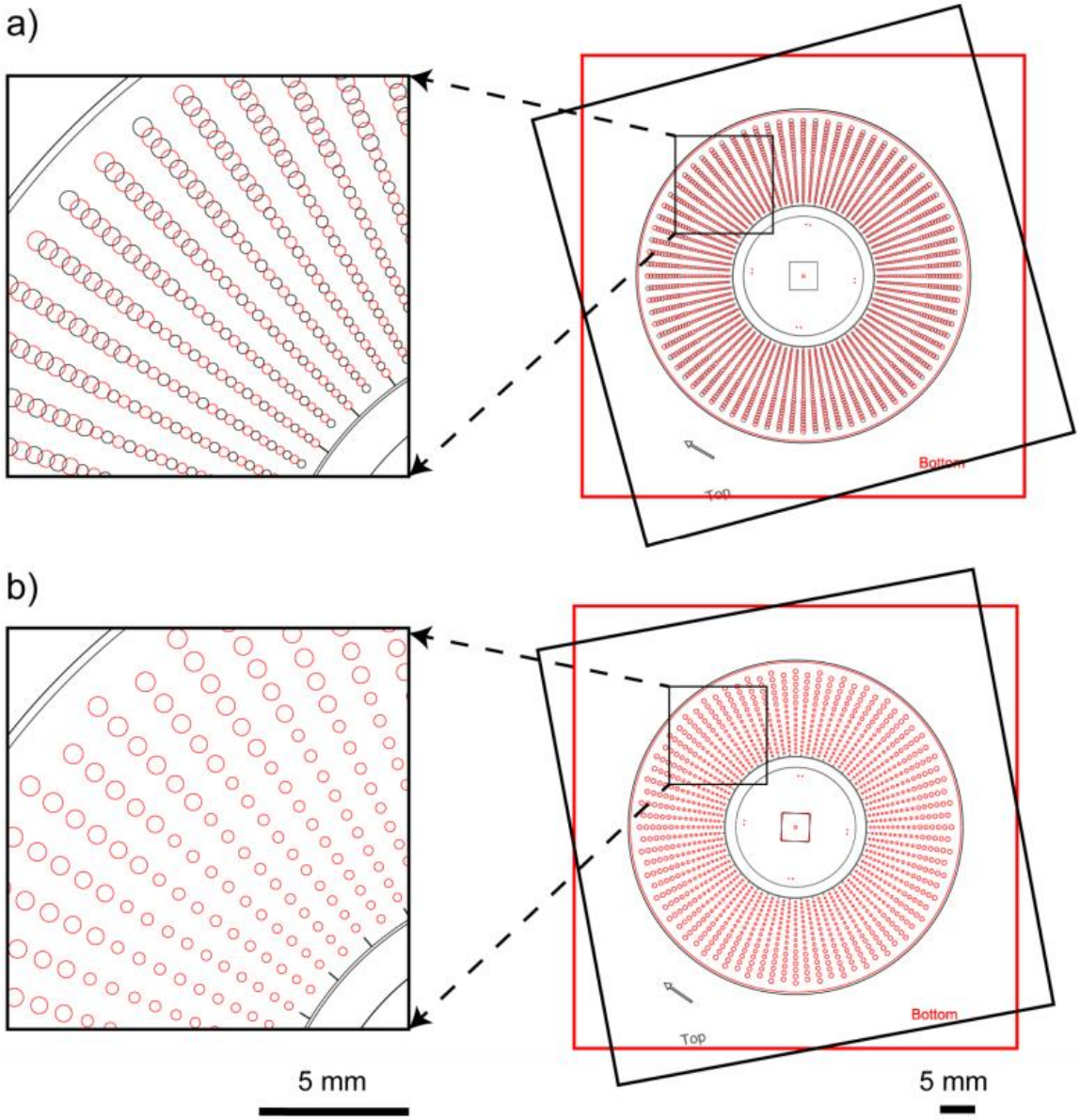


**Figure 5.11: Schematic of the multivolume rotational SlipChip device used for one-step digital LAMP experiments after being assembled.**

Drawing shows the layout of top and bottom piece of the entire device on the right and a zoomed-in region (black box) on the left. a) Relative position of the two pieces when they are aligned to allow loading of solution through the channel, and b) the relative position of the two pieces when they are slipped (top slide rotated 4.5°) to

separate droplets from one another and form compartments. Features shown are before isotropic glass etching.

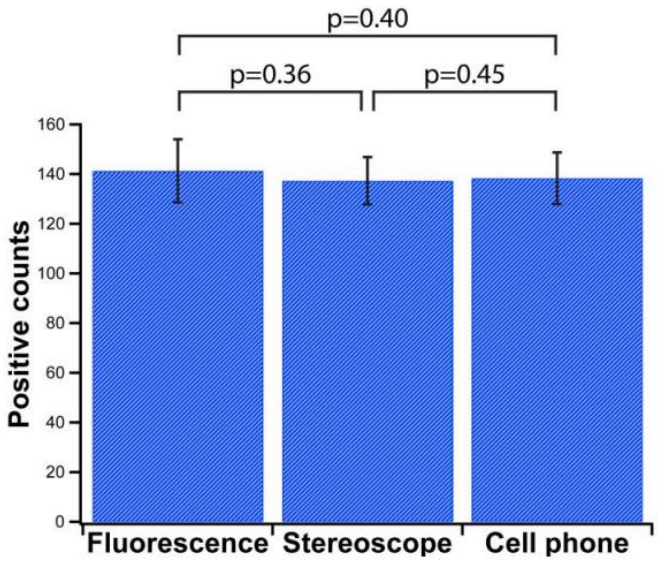


**Figure 5.12: Positive counts obtained from single-molecule digital LAMP reactions performed with lambda DNA on a one-step SlipChip device imaged by a house-built real-time fluorescence microscope, a Leica MZ Fl III stereoscope, and an unmodified cell phone camera (Apple iPhone 4S) under fluorescent light.**

One-step visual readout was performed on SlipChip devices composed of 800 wells of 27 nL volumes. LAMP amplification mix contained 0.7 mM eriochrome black T dye solution, SYTO® 9 Stain, and phage lambda DNA. Automated counting was performed by self-developed Labview software for fluorescent images and freeware Fiji image processing for bright field G/R processed images. Data are mean positive counts and error bars are S.D. (N = 3). Student's t-tests were used for statistical comparisons, showing no significant differences among counts obtained by the three imaging methods (*P* values > 0.05).

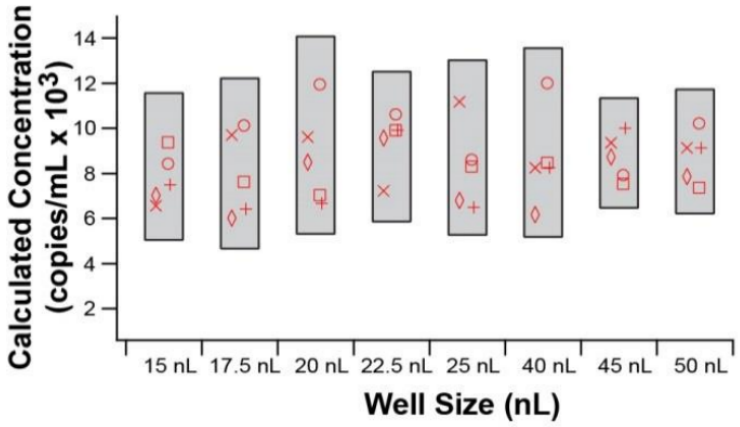


**Figure 5.13: Five multivolume experiments were performed, and the concentration of each volume was calculated based on the methods of Kreutz *et al.***

Gray boxes denote the 95% confidence interval for the set of experiments at each volume. Concentrations calculated at each volume are consistent, and there is no bias based on the volume in which the reaction is performed.

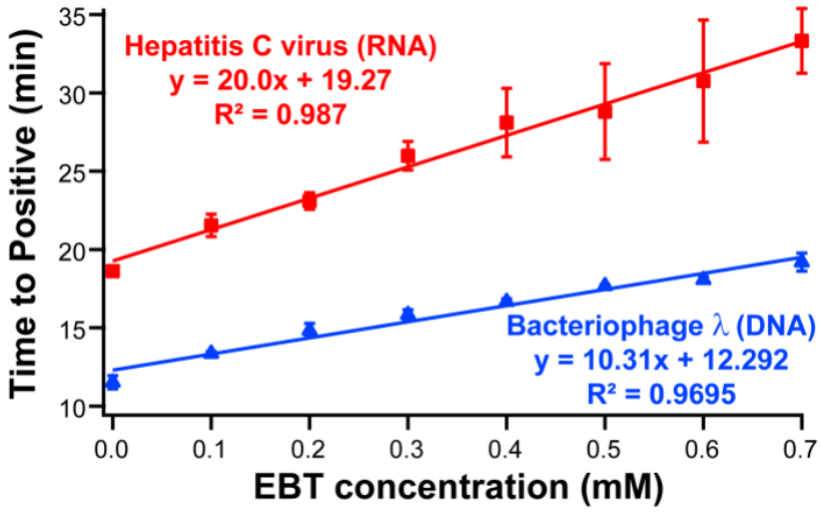


**Figure 5.14: Performance of bulk LAMP reactions at increasing concentrations of the amplification indicator dye eriochrome black T (EBT).**

All reactions performed in 10 μL volumes with concentrations of EBT solution ranging from 0.0 to 0.7 mM, SYTO® 9 Stain and either 1,000 copies of HCV RNA (red) or 1,000 copies of phage lambda DNA (blue). All reactions were run in triplicate.

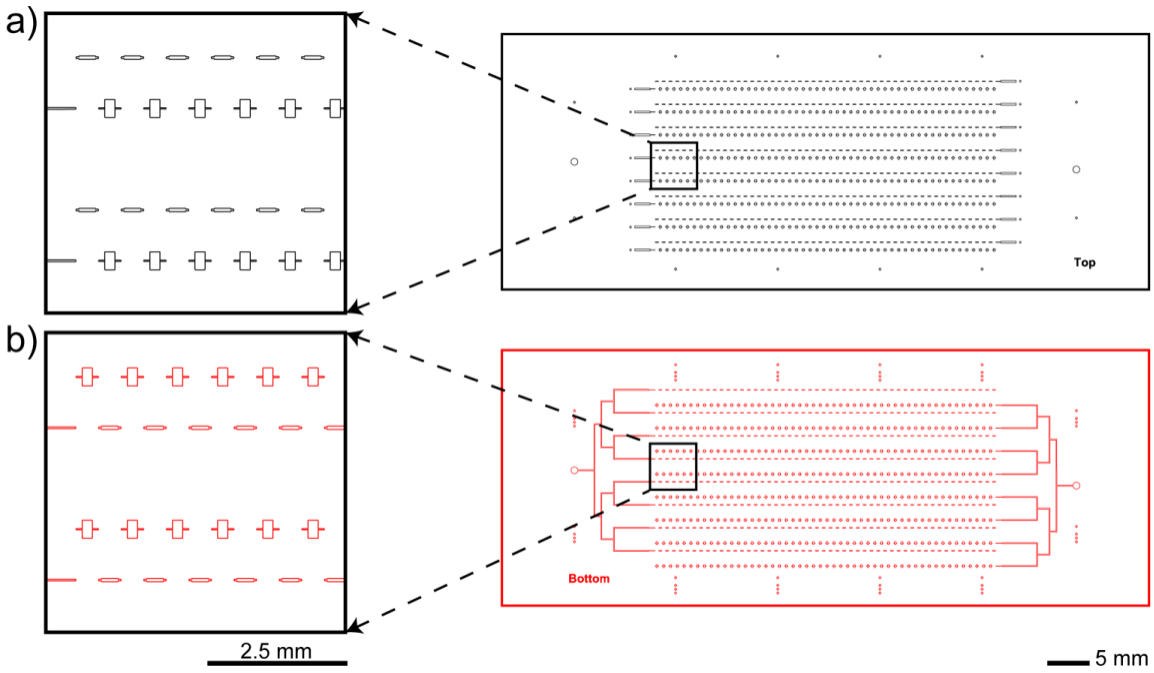


**Figure 5.15: Schematic of the two-step SlipChip device before assembly.** Drawings show the top (a) and bottom (b) device plates with a selected region (black box) magnified on the left to show locations of the 5 nL and 9.5 nL wells. Features are shown before isotropic glass etching. The design of the two-step SlipChip device was based on previously published SlipChip designs.[13]

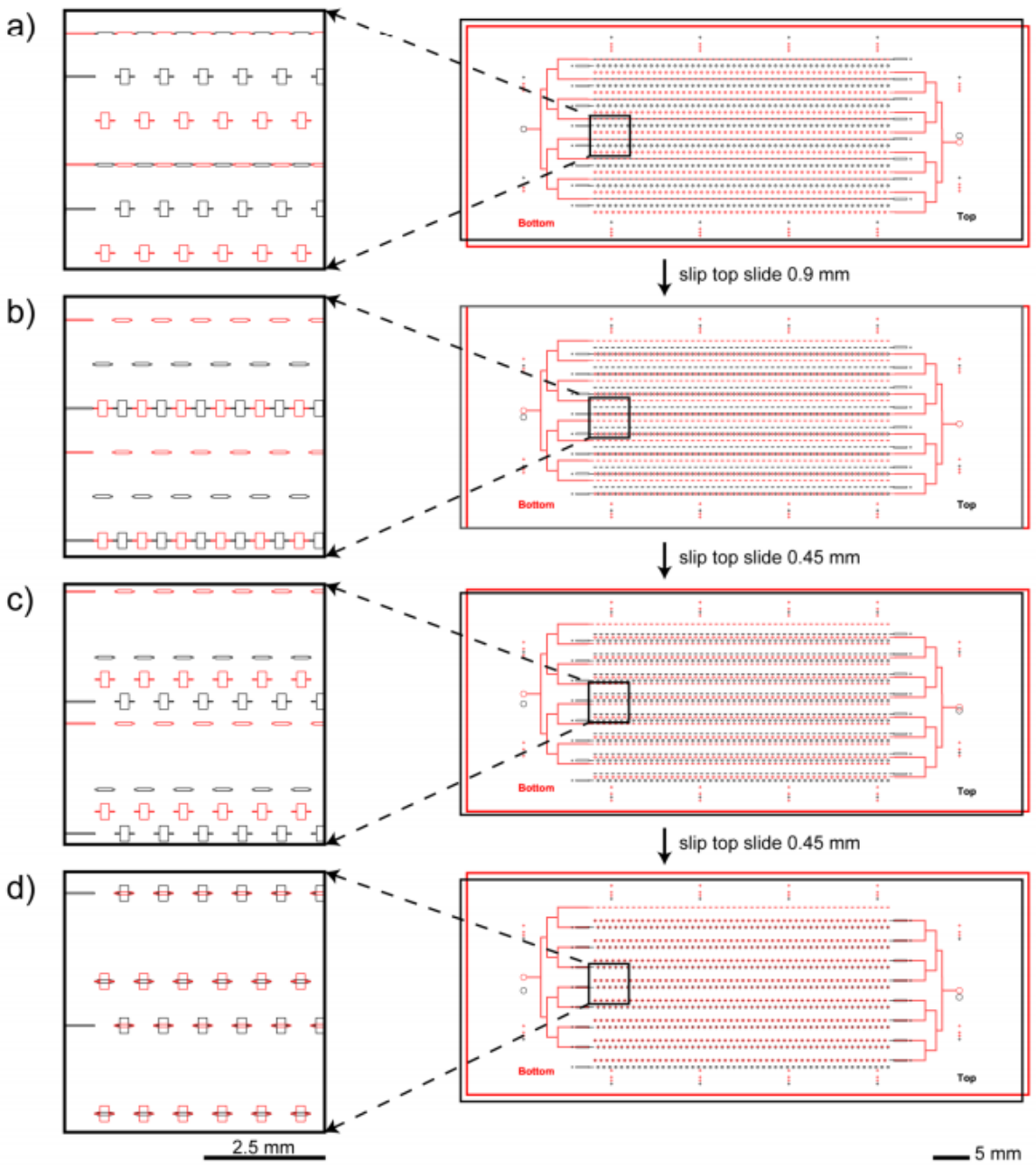


**Figure 5.16: Schematic of the two-step SlipChip device after assembly and its operation.**

Drawings show the layout of the top and bottom plates on the right and a magnified region (black box) on the left. (a) Loading conformation for the first set of wells (5 nL each). (b) Loading conformation for the second set of wells (9.5 nL each). (c)

Incubation conformation. (d) Final mixing conformation ready for imaging with a cell phone camera. Features are shown before isotropic glass etching.

**Table 5-1: Sequence of primers used in RT-LAMP experiments for detection of hepatitis C RNA.[15]**

| primer | sequence (5'-3') |
|---|---|
| F3 | CCTCCCGGGAGAGCCATAG |
| FIP | TCCAAGAAAGGACCCIGTCTTTTTCTGCGGAACCGGTGAGTAC |
| LF | TTICCGGIAATTCCGGT |
| B3 | CCACTCCCAACCACCITATC |
| BIP | TTGGGCGTGCCCCCGCIAGATTTTTCAGTACCACAAGGCCITTCGCIACC |
| LB | CTGCTAGCCGAGTAGIGTTG |

**Table 5-2: Sequence of primers used in LAMP experiments for detection of lambda phage DNA.[17]**

| primer | sequence (5'-3') |
|---|---|
| F3 | GAATGCCCGTTCTGCGAG |
| FIP | CAGCATCCCTTTCGGCATACCAGGTGGCAAGGGTAATGAGG |
| LF | GGCGGCAGAGTCATAAAGCA |
| B3 | TTCAGTTCCTGTGCGTCG |
| BIP | GGAGGTTGAAGAACTGCGGCAGTCGATGGCGTTCGTACTC |
| LB | GGCAGATCTCCAGCCAGGAACTA |

**Table 5-3: Multivolume device designs for viral load quantification.**

| Volumetric step | Number of well volumes | Well volume range (nL) | Number of wells per device | LDL – ULQ (copies/mL) | DR (log) |
|---|---|---|---|---|---|
| 2 | 6 | 5 – 160 | 2,700 | 500 – 1,000,000 | 3.3 |
| 2 | 6 | 5 – 160 | 2,700 | 50 – 1,000,000 | 4.3 |
| 5 | 3 | 5 – 125 | 1,350 | 500 – 1,000,000 | 3.3 |
| 5 | 3 | 5 – 125 | 1,350 | 50 – 1,000,000 | 4.3 |
| 25 | 2 | 5 – 125 | 900 | 500 – 1,000,000 | 3.3 |
| 25 | 2 | 5 – 125 | 940 | 50 – 1,000,000 | 4.3 |

The lower detection limit (LDL) is defined as the concentration which would have a 95% probability of generating at least one positive well. The upper limit of quantification (ULQ) is defined as the concentration where the probability of all wells being positive is 5%. DR: dynamic range. Calculations were performed according to the equations and algorithms found in *Kreutz JE, Munson T, Huynh T, Shen F, Du W, Ismagilov RF. "Theoretical design and analysis of multivolume digital assays with wide dynamic range validated experimentally with microfluidic digital PCR." Anal Chem. 2011 83(21):8158-68.*

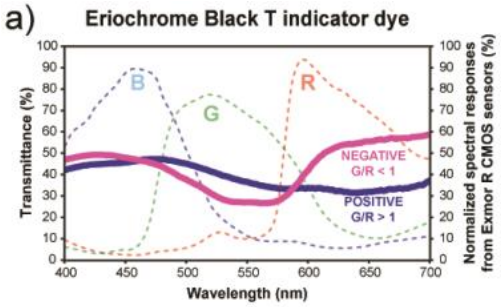


b)

Predicted ratiometric values and difference between positive and negative LAMP reactions in the presence of Eriochrome Black T indicator dye

| Process | positive | negative | positive-negative (%) |
|---|---|---|---|
| Green/Red | 1.06 | 0.87 | 0.19 (17.9) |
| Blue/Red | 1.13 | 0.97 | 0.16 (14.2) |
| Green/Blue | 0.94 | 0.90 | 0.04 (4.3) |

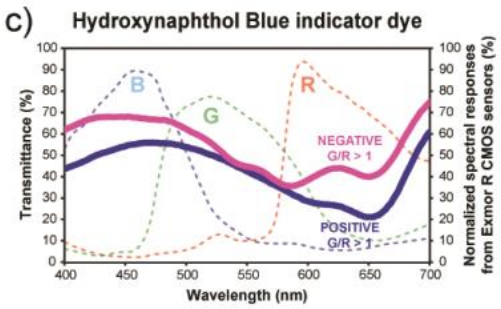


d)

Predicted ratiometric values and difference between positive and negative LAMP reactions in the presence of Hydroxynaphthol Blue indicator dye

| Process | positive | negative | positive-negative (%) |
|---|---|---|---|
| Green/Red | 1.17 | 1.06 | 0.11 (9.4) |
| Blue/Red | 1.25 | 1.17 | 0.08 (6.4) |
| Green/Blue | 0.94 | 0.90 | 0.04 (4.3) |

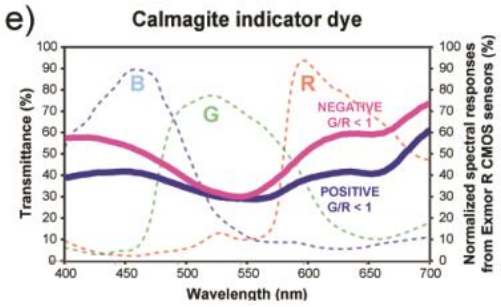


f)

Predicted ratiometric values and difference between positive and negative LAMP reactions in the presence of Calmagite indicator dye

| Process | positive | negative | positive-negative (%) |
|---|---|---|---|
| Green/Red | 0.92 | 0.86 | 0.06 (6.5) |
| Blue/Red | 0.98 | 0.95 | 0.03 (3.1) |
| Green/Blue | 0.94 | 0.91 | 0.03 (3.2) |

**Figure 5.17: (a, c and e) Measured spectral transmittance (%) in the range of visible light (400–700 nm) for positive (solid purple line) and negative (solid blue**

**line) RT-LAMP reaction solutions, each containing 0.7 mM of eriochrome black T, hydroxynaphthol blue or calmagite as the amplification indicator dye.**

Dashed lines correspond to normalized spectral responses for red (R), green (G), and blue (B) channels of an Exmor R CMOS sensor, a common sensor in cell phone cameras. (b, d, and f) Predicted ratiometric values for positive and negative LAMP amplification reactions processed for each ratiometric combination, Green/Red, Blue/Red, and Green/Blue. Tables show absolute differences (positive – negative), and the relative difference (in %) between positive and negative ratiometric values are shown. All experiments were performed with HCV RNA as a template. Dye stock solutions were prepared as described in the Methods section, "Preparation of EBT solution."

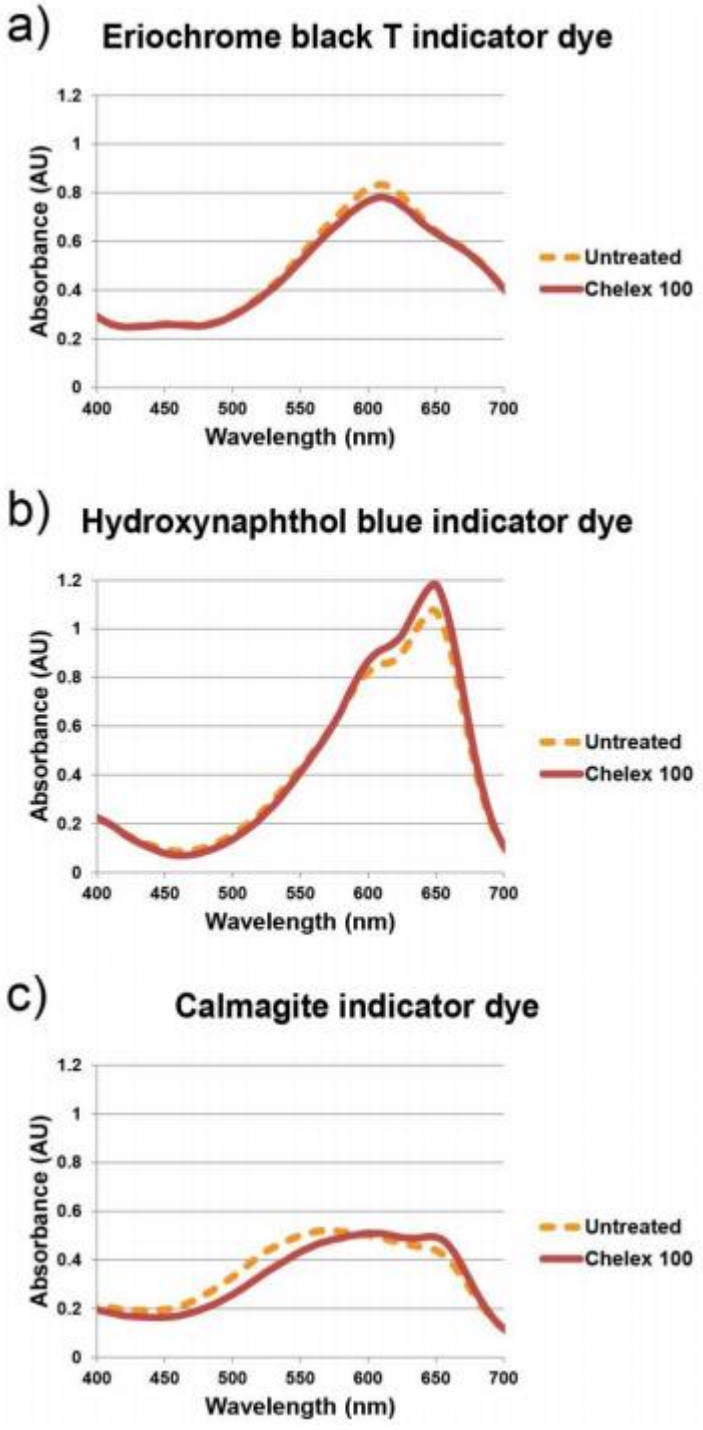


**Figure 5.18: Comparison of the spectral absorbance (Absorbance Units) of untreated indicator dye stock solutions (dashed orange lines) and solutions**

**treated with Chelex® 100 resin (solid red lines) for (a) eriochrome black T (EBT), (b) hydroxynaphthol blue (HNB) and (c) calmagite indicator dyes.**

The EBT, HNB, and calmagite stock solutions were prepared by dissolving the dyes in 20 mM Tris-HCl buffer (pH 8.8) at 0.7 mM. The solutions were sonicated for 10 min and mixed on a rotator at room temperature for 1 h. The solutions were split into two equal volumes for the comparison; one volume was treated with Chelex® 100 ion exchange resin (5% w/v).

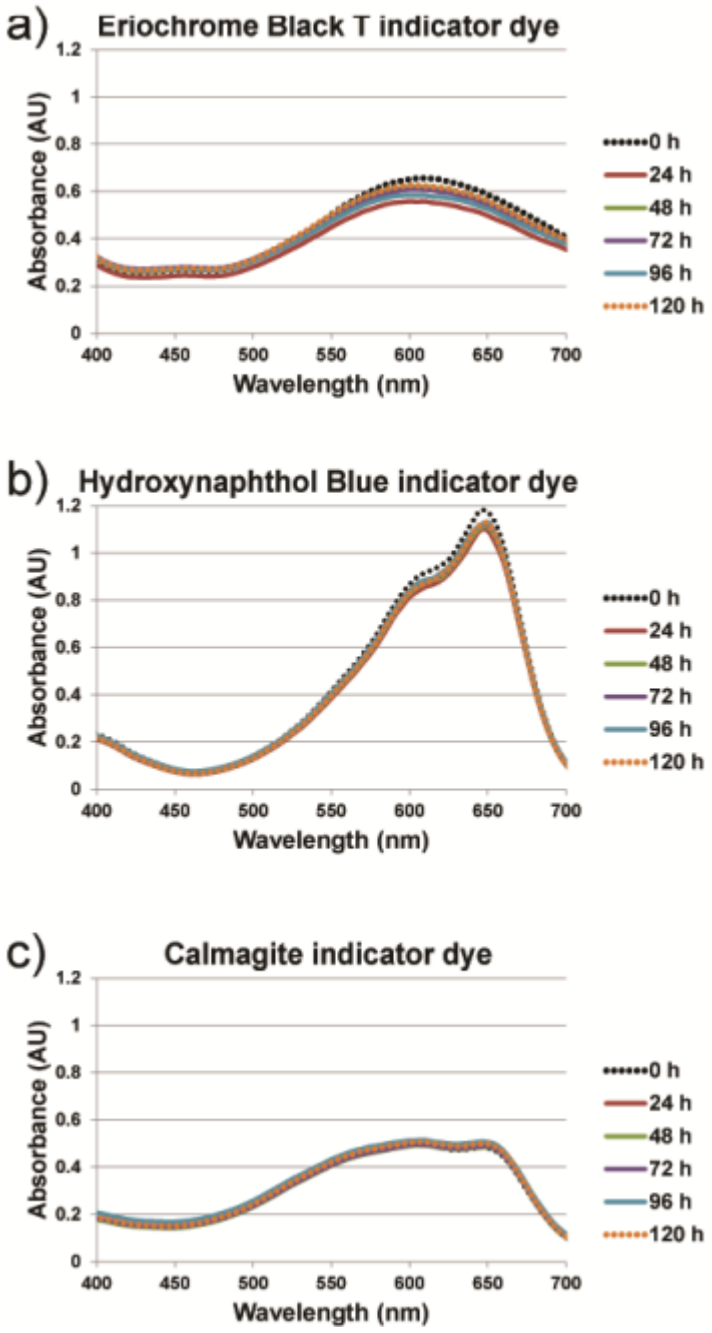


**Figure 5.19: Storage stability of amplification indicator dyes by drying the stock solutions in the presence of stabilizer trehalose.**

Measured spectral absorbance (Absorbance Units) in the range of visible light (400–700 nm) for (a) eriochrome black T (EBT), (b) hydroxynaphthol blue (HNB), and (c) calmagite indicator dyes solutions. Time "0 h" is the spectral absorbance of the dye

stock solution prior to drying in a dessiccator under vacuum. The following time points correspond to the length of time the dye stock solution was maintained in its dried state before being resuspended in distilled water. Full protocol is in the Methods section, “Storage stability of amplification indicator dyes by drying in the presence of stabilizer trehalose.”

*Chapter 6*

# REAL-TIME, DIGITAL LAMP WITH COMMERCIAL MICROFLUIDIC CHIPS REVEALS THE INTERPLAY OF EFFICIENCY, SPEED, AND BACKGROUND AMPLIFICATION AS A FUNCTION OF REACTION TEMPERATURE AND TIME

J.C. Rolando, E. Jue, N.G. Schoepp, and R.F. Ismagilov. 2018. *Analytical Chemistry*. 91(1):1034–1042. doi:10.1021/acs.analchem.8b04324

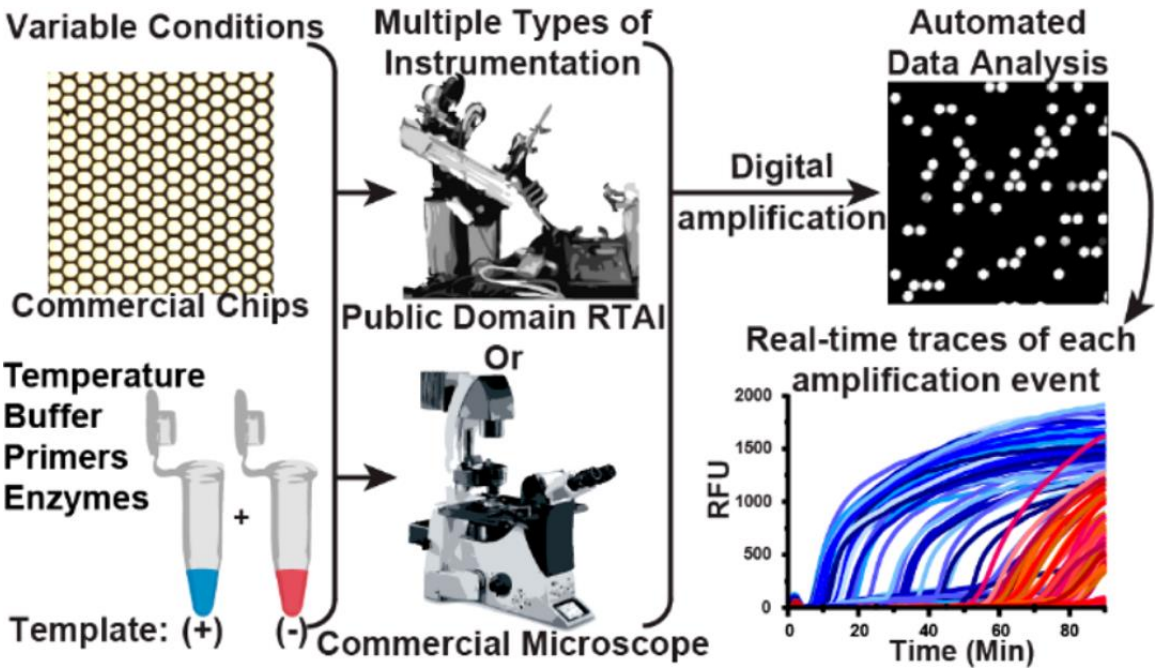


**Abstract**

Real-time, isothermal, digital nucleic acid amplification is emerging as an attractive approach for a multitude of applications including diagnostics, mechanistic studies, and assay optimization. Unfortunately, there is no commercially available and affordable real-time, digital instrument validated for isothermal amplification; thus, most researchers have not been able to apply digital, real-time approaches to isothermal amplification. Here, we generate an approach to real-time digital loop-mediated isothermal amplification (LAMP) using commercially available microfluidic chips and reagents, and open-source components. We demonstrate this approach by testing variables that influence LAMP reaction speed and the probability of detection. By analyzing the interplay of amplification efficiency, background, and speed of amplification, this real-time digital method enabled us to test enzymatic performance over a range of temperatures, generating high-precision kinetic and endpoint measurements. We were able to identify the unique optimal temperature for two polymerase enzymes, while accounting for amplification efficiency, non-specific background, and time to threshold. We validated this digital LAMP assay and pipeline by performing a phenotypic antibiotic susceptibility test on 17 archived clinical urine samples from patients diagnosed with urinary tract infections. We provide all the necessary workflows to perform digital LAMP using standard laboratory equipment and commercially available materials. This real-time digital approach will be useful to others in the future to understand the fundamentals of isothermal chemistries—including which components determine amplification fate, reaction speed, and enzymatic performance. Researchers can also adapt this pipeline, which uses only standard equipment and commercial components, to quickly study and optimize assays using precise, real-time, digital quantification—accelerating development of critically needed diagnostics.

## Introduction

In this chapter, we describe a methodology to use commercially available chips, reagents, and microscopes to perform real-time digital LAMP. We use this methodology to perform a

mechanistic study of digital isothermal amplification, and apply the lessons learned to perform a phenotypic antibiotic susceptibility test (AST).

Microfluidics-based diagnostics for infectious diseases are advancing as a result of using nucleic acid testing—making them amenable to the point of care (POC) and limited-resource settings where they will have clinical impact. Isothermal amplification methods in particular show promise for simplifying nucleic-acid-based POC diagnostics by circumventing the stringent thermal cycling requirements of PCR.[1] One isothermal method that is being actively pursued in bioanalytical chemistry and the field of diagnostics is loop-mediated isothermal amplification (LAMP).[2-6]

LAMP and other isothermal technologies are fast and sensitive, but when performed in a bulk format in microliter volumes (e.g. in a tube), they provide only semi-quantitative (log-scale) resolution or presence/absence measurements.[7-15] As a result, when optimizing an assay, it is difficult to quantify how small changes in assay conditions (e.g. in primers, reagents, or temperature) impact the reaction's speed and analytical sensitivity. To reliably understand these effects with high precision would require hundreds of bulk experiments per condition.[16] For the field to be able to take full advantage of the capabilities of LAMP, researchers need to be able to optimize reaction conditions by understanding and testing the variables that may influence reaction speed and probability of detection. Furthermore, the semi-quantitative measurements yielded by bulk isothermal methods are insufficient for analyses requiring precise quantification, such as phenotypic antibiotic susceptibility testing.[17,18]

These problems can be solved using "digital" approaches, which partition single target molecules in large numbers of compartments and give a binary (presence/absence) readout for each compartment. These "digital" approaches thus allow determination of the efficiency of the amplification reaction[19] and provide absolute quantification with high resolution. Digital isothermal measurements have been used to quantify viral load for HCV,[16,20,21] HIV,[19,20] and influenza,[22] perform bacterial enumeration,[23-25] optimize primers,[16] and test for phenotypic antibiotic susceptibility[18] using LAMP[18-28] and RPA.[29]

Real-time digital formats are especially valuable for examining the variables that mostly affect non-specific amplification and the speed of amplification. Many excellent approaches for end-point[19,20,22-28] and real-time[16,18,21] digital LAMP (dLAMP) have been published. Despite the value that real-time dLAMP can bring to diagnostics, this method is difficult to implement—especially for those without a background in micro-electro-mechanical systems or microfluidics—because there is no commercial system for real-time, digital isothermal amplification. To achieve statistical significance, a meaningful study might require dozens of experiments; such studies are difficult to perform without a commercial source of chips. Consequently, the few LAMP mechanistic studies that have been performed were not done with high precision. Further, those who would most benefit from optimized digital isothermal reactions (e.g. those working on POC diagnostics) cannot efficiently improve them.

Here, we demonstrate how to generate high-precision kinetic and endpoint measurements using a real-time dLAMP assay that is performed completely with commercially available and open-source components (**Figure 6.1**). We use this real-time information to investigate dLAMP reactions mechanistically, including the interplay of efficiency, speed, and background amplification as a function of reaction temperature and time on two enzymes. To illustrate one application of using real-time dLAMP to improve a clinically relevant assay, we optimized the assay conditions for a phenotypic AST using the real-time dLAMP pipeline and used the optimized protocol to compare our AST of 17 clinical urine samples to the gold-standard method.

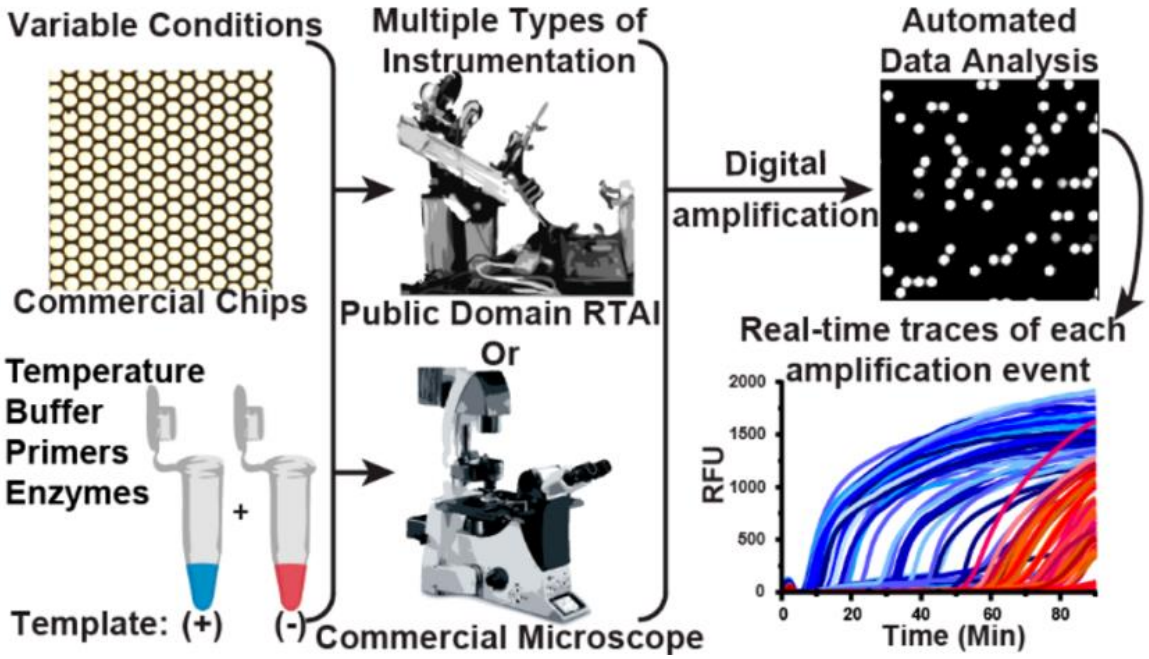


**Figure 6.1: A schematic of the pipeline for performing multiplexed, real-time, digital loop-mediated isothermal amplification (LAMP) using only commercially available and/or open source components.**

Microfluidic chips and reagents (e.g. primers, enzymes, buffer composition) can be purchased commercially. Multiple instrument configurations can be used to capture results. e.g. a customized real-time instrument (instructions for building publicly available[30]) or any commercial microscope. Data analysis is automated using a MATLAB script (Supporting Information, S-I).

## Experimental

Microfluidic chips used in this paper were sourced from Applied Biosystems, Foster City, CA, USA) Ref A26316, "QuantStudio 3D Digital PCR 20k Chip Kit V2."

*LAMP reagents*

Our amplification target was the *E. coli* 23S ribosomal gene, which we used previously as a target to perform rapid AST on clinical samples.[18] Primers were purchased through Integrated DNA Technologies (San Diego, CA, USA) and were described previously.[18] Final primer concentrations were identical for all experiments: 1.6 μM FIP/BIP, 0.2 μM FOP/BOP, and 0.4 μM LoopF/LoopB.

LAMP experiments using *Bst* 3.0 (**Figure 6.2; Figure 6.3b d, e, f, h-j; Figure 6.4**) contained the following final concentrations, optimized previously18: 1x Isothermal Amplification Buffer II (New England BioLabs (NEB), Ipswich, MA, USA; Ref. B0374S; containing 20 mM Tris-HCl 10 mM (NH4)2SO4 150 mM KCl, 2 mM MgSO4, 0.1% Tween 20 pH 8.8 at 25 °C), 4 mM additional MgSO4 (beyond 2 mM from buffer), 1.4 mM Deoxynucleotide Solution Mix, primers: 1.6 μM FIP/BIP, 0.2 μM FOP/BOP, and 0.4 μM LoopF/LoopB, 1 mg/mL BSA (New England BioLabs, Ref B90005), 320 U/mL *Bst* 3.0, Ambion RNAse cocktail (ThermoFisher, Waltham, MA, USA; Ref AM2286, 5 U/mL RNase A, 400 U/mL TNase T1), 2 μM SYTO 9 (ThermoFisher, Reference S34854), and approximately 660 copies/μL template in Ambion nuclease-free water (ThermoFisher, Ref AM9932).

LAMP experiments using *Bst* 2.0 (**Figure 6.3a, c, e, g)** contained the following final concentrations, optimized as shown in **Figure 6.7**: 1x Isothermal Amplification Buffer (New England BioLabs, Ref. B0537S; containing 20 mM Tris-HCl 10 mM (NH4)2SO4, 50 mM KCl 2 mM MgSO4 0.1% Tween 20 pH 8.8 at 25 °C), additional 6 mM MgSO4 (New England BioLabs, Ref. B1003S), 1.4 mM Deoxynucleotide Solution Mix (New England BioLabs, Ref N0447S), primers: 1.6 μM FIP/BIP, 0.2 μM FOP/BOP, and 0.4 μM LoopF/LoopB, 1 mg/mL BSA (New England BioLabs, Ref B90005), 320 U/mL *Bst* 2.0 (New England BioLabs, Ref M0537S), Ambion RNAse cocktail (ThermoFisher, Ref AM2286, 5 U/mL RNase A, 400 U/mL TNase T1), 2 μM SYTO 9 (ThermoFisher, Ref S34854), and approximately 660 copies/μL template in Ambion nuclease-free water (ThermoFisher, Ref AM9932).

Template *E. coli* DNA was extracted from exponential-phase cultures grown in BBL Brain-Heart Infusion media (BD, Franklin Lakes, NJ, USA; Ref. 221813) using QuickExtract DNA

Extraction Solution (Lucigen, Middleton, WI, USA; Ref. QE09050) as described previously.18 Serial 10-fold dilutions were prepared in Tris-EDTA buffer (5 mM Tris-HCl, 0.5 mM EDTA, pH 8.0) containing 2 U/mL RNase A and 80 U/mL RNase T1 (ThermoFisher, Ref AM2286). DNA dilutions were quantified as described previously[18] using the QX200 Droplet Digital PCR (ddPCR) system (Bio-Rad Laboratories, Hercules, CA, USA).

*Phenotypic antibiotic susceptibility testing (AST) on clinical samples*

For the phenotypic AST, we adopted a workflow described previously,[17,18] and used archived nucleic-acid extractions from a previous study.[18] Briefly, clinical urine samples from patients with urinary tract infections (UTI) were split and diluted into equal volumes of media with or without the presence of an antibiotic. Samples were incubated for 15 min at 37 °C, a nucleic-acid extraction was performed, and these samples were archived at -80 °C until use. LAMP was performed on the archived samples to quantify the number of copies of the *E. coli* 23S ribosomal gene.

We tested our optimized assay on 17 archived clinical UTI samples containing $\geq 5 \times 10^4$ CFU/ml *E. coli* that had been categorized previously using the gold-standard broth microdilution AST (5 ciprofloxacin-susceptible, 5 ciprofloxacin-resistant, 4 nitrofurantoin-susceptible, and 3 nitrofurantoin-resistant).

We assessed samples as phenotypically “resistant” or “susceptible” by calculating the ratio of the concentration of 23S in the control and antibiotic-treated sample, which we call the control:treated (C:T) ratio. The C:T ratio was calculated 10 min after beginning to heat the LAMP reaction. A threshold of 1.1 was established previously,[17,18] so samples with C:T ratios >1.1 indicated that there was DNA replication in the untreated (control) group but not in the antibiotic-treated samples; these samples were identified as susceptible to the antibiotic. Samples with C:T ratios of <1.1 indicated that DNA replication occurred in both

the control and antibiotic-treated samples; these samples were identified as resistant to the antibiotic.

## Results and discussion

*Workflow summary of real-time digital LAMP*

To evaluate a pipeline for real-time dLAMP experiments, we chose commercially sourced microfluidic chips sold for endpoint digital PCR applications. The chips consist of an array of 20,000 uniform partitions (**Figure 6.1**), each 60 μm in diameter and an estimated 0.75 nL internal volume, which is similar to the volumes typically used in dLAMP.[16,18,20-23,25,26,28] These chips are loaded by pipetting the sample mixture (in our case containing the LAMP reagents: buffer components, enzymes, template, and primers) into the plastic "blade" provided with the chips, and dragging the blade at a 70–80° angle to the chip to load the sample mixture by capillarity. This is followed by drying and evaporation of the surface layer for 20 sec at 40 °C, and application of the immersion fluid. Manual loading requires some skill, though a machine can be purchased to perform the task; typically, we were able to load ~18,000 out of the 20,000 partitions. We performed our evaluation using two different enzyme mixtures, *Bst* 2.0 and *Bst* 3.0. Our amplification target (**Figure 6.1**) was the *E. coli* 23S ribosomal gene that we previously used as a target to perform rapid AST on clinical samples.[18]

The instrumentation requirements for real-time isothermal capabilities include a heater that can hold a stable temperature, and optical components with high spatial resolution that are capable of imaging the fluorescence intensity of the 20,000 individual partitions of the chip over time (**Figure 6.2a**). Here, we investigated two approaches: using a standard laboratory microscope (Leicia DMI-6000B), and using the RTAI,[30] which is composed of a thermocycler, optical components, a camera, and a light source.

We generated a custom MATLAB script to analyze the digital real-time data (details in **Supporting Information, S-I**). The software follows the change in fluorescence in individual partitions over time. From these data, we extract each partition's time to a fluorescence intensity threshold and calculate the bulk template concentration. In our demonstration, we loaded the acquired images into FIJI31 as a time-stack series and manually separated the images of the individual chips to be analyzed separately. To process each chip's image stack, we used the custom MATLAB script that tracks the mean intensity of each partition over the course of each experiment. This script could be run with only minor modifications with images obtained from different instruments.

To calculate the bulk template concentration over time, we (1) identified the partitions that did or did not contain reaction solution, (2) tracked the partitions that met a minimum fluorescence intensity, and (3) used the previous information to calculate the concentration of template in the bulk solution.

A summary of the script is as follows: (i) load the images into memory, (ii) count the total number of partitions before heating, (iii) identify positive partitions after the conclusion of the experiment, (iv) track the intensity of positive partitions for each image frame, (v) apply Gaussian smoothing and baseline subtraction, (vi) save the data, and (vii) repeat for each image stack. The output of the script contains: the raw traces of individual partitions over time, baseline corrected traces of individual partitions over time (**Figure 6.2b**), the number of partitions exceeding the manually defined minimum fluorescence intensity threshold with time (**Figure 6.2f**), and the maximum relative rate in RFU per 30 sec for individual partitions (**Figure 6.2d**). These data provide all the necessary information to conduct the analyses detailed in **Figure 6.2**.

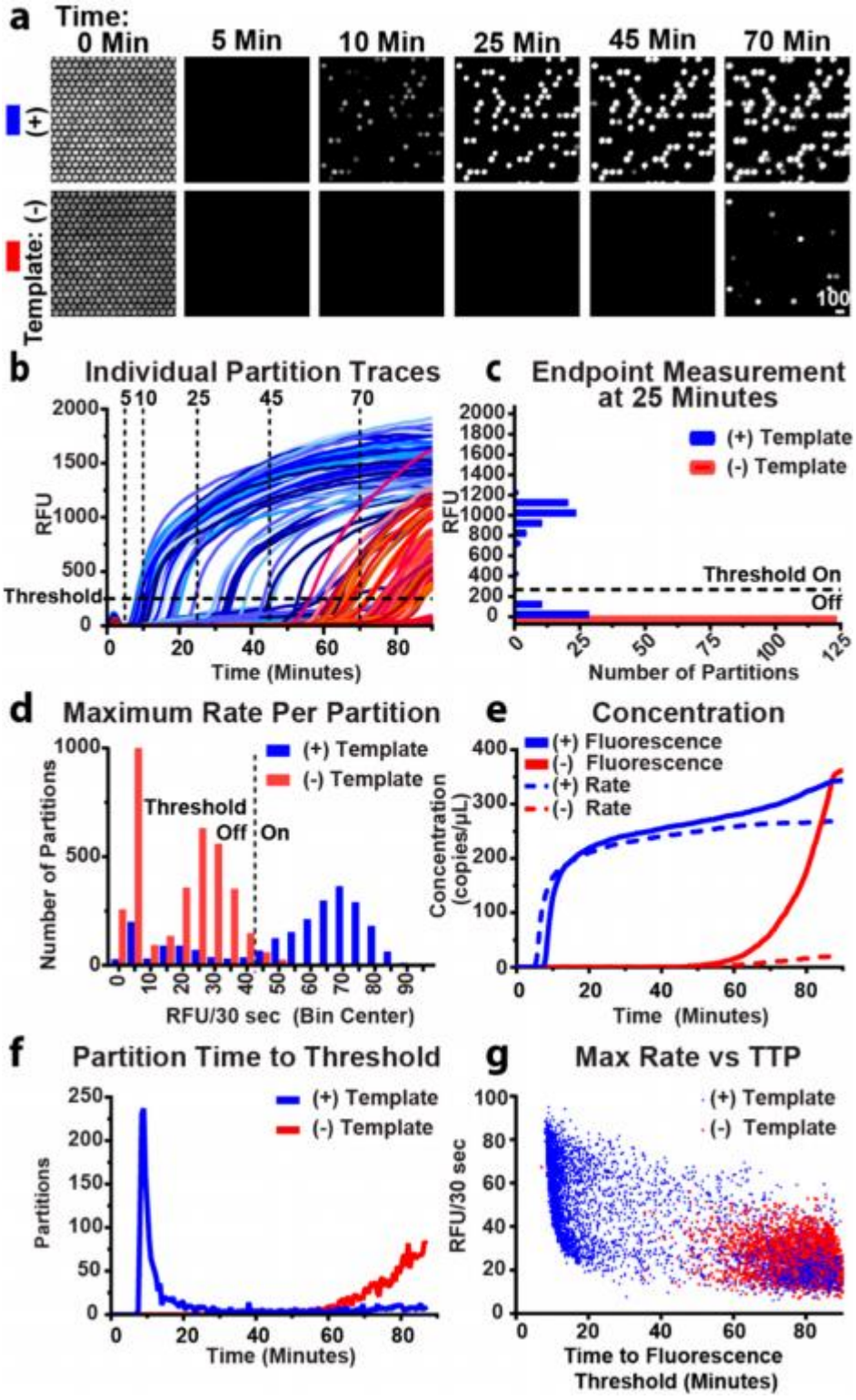
a
Time:
0 Min
5 Min
10 Min
25 Min
45 Min
70 Min
(+)
Template: (-)
100
b
Individual Partition Traces
5 10 25 45 70
RFU
Threshold
Time (Minutes)
c
Endpoint Measurement at 25 Minutes
(+) Template
(-) Template
RFU
Threshold On
Off
Number of Partitions
d
Maximum Rate Per Partition
(+) Template
(-) Template
Threshold
Off
On
Number of Partitions
RFU/30 sec (Bin Center)
e
Concentration
(+) Fluorescence
(-) Fluorescence
(+) Rate
(-) Rate
Concentration (copies/µL)
Time (Minutes)
f
Partition Time to Threshold
(+) Template
(-) Template
Partitions
Time (Minutes)
g
Max Rate vs TTP
(+) Template
(-) Template
RFU/30 sec
Time to Fluorescence Threshold (Minutes)

**Figure 6.2: Experimental demonstration of the real-time digital LAMP (dLAMP) approach using the commercially available enzyme *Bst* 3.0. Experiments were run at 70 °C and imaged using a commercial microscope.**
(a) A time course of fluorescence images from a subset of 350 partitions out of 20,000 partitions undergoing dLAMP reactions. (Intensity range 920-1705 RFU). (b) Fluorescence intensity for a subset of partitions over time. Blue traces indicate partitions containing template; red traces indicate fluorescence in the absence of template (i.e. non-specific amplification). Partitions turn "on" at the time point when the curve passes the threshold at 250 RFU. Vertical traces correspond to time points illustrated in panel (a) and generate endpoint measurements. (c) An "endpoint" measurement taken on a subset of partitions at 25 min. Bin width is 100 RFU. Fluorescence threshold is 250 RFU. (d) A histogram of the maximum observed change in fluorescence of individual partitions using the full chip. Rate threshold is 45 RFU/30 sec. (e) Change in observed bulk concentration over time from the full chip using fluorescence intensity as threshold (solid lines) and rate (dashed lines). (f) Time at which individual partitions in panel (b) cross the fluorescence intensity threshold. (g) Maximum rate per partition plotted by time to fluorescence intensity threshold.

*Digital, real-time experiments to quantify LAMP performance*

We next sought to experimentally evaluate this pipeline (**Figure 6.1**). First, we established whether the fluorescence from LAMP reactions could be reliably measured from individual partitions over time (**Figure 6.2a**). We used LAMP reagents for *Bst* 3.0, commercial chips, a resistive heater held at 70 °C, and a commercial microscope. Although the microscope is capable of collecting all 20,000 partitions on one chip in a single image, for simplicity, in **Figure 6.2a**, we cropped the image to include only 350 of the 20,000 partitions. Before turning on the heater (t = 0), we measured the autofluorescence from SYTO 9 to quantify the total number of partitions loaded with reaction solution. (To calculate template concentration

using the Poisson distribution,[32,33] we must know the total number of partitions containing the reaction mixture.) Autofluorescence from SYTO 9 decreases as the chip is heated and is completely eliminated within 3 min. The heater used on the microscope reaches reaction temperature within 120 sec. In less than 10 min, an increase in fluorescence was observed within some of the individual partitions, indicating amplification of individual template molecules inside those partitions. Due to the stochastic nature of amplification initiation, some of the partitions fluoresced later.

In the negative-control (no template) partitions, fluorescence was not observed for the first 45 min. However, we began to observe non-specific amplification after ~60 min. In these experiments, the negative control contains only 0.05x Tris-EDTA buffer in place of template and represents a best-case scenario. We attribute amplification in the absence of template to primer dimers and other non-specific LAMP products.

Second, we asked if the signal from non-specific amplification was sufficiently delayed to differentiate it from the signal arising from specific amplification in the presence of template. To answer this question, we generated real-time fluorescence curves by plotting the change in fluorescence of individual partitions as a function of time (**Figure 6.2b**). We observed specific amplification (blue curves) beginning to initiate at ~7 min and non-specific amplification beginning to initiate at ~50 min (red curves) and concluded that we could discriminate specific and non-specific amplification by time.

Third, we asked whether enzymatic heterogeneity[16,21,34] of specific amplification can be quantified to differentiate specific from non-specific amplification. We plotted the maximum change of fluorescence achieved by each partition of the full chip per 30-sec interval (**Figure 6.2d)**. For the negative-control sample (red bars), we observed non-specific amplification following a bimodal distribution of rates, with a first peak with little to no rate of fluorescence increase and a second peak at ~25 RFU per 30 sec. For the sample containing template (blue bars), rates for specific amplification were heterogeneous and centered around a rate of 70 RFU/30 sec. We note that in PCR, which is gated by temperature cycling, there is no equivalent concept of "rate" as long as replication of DNA occurs faster that the duration of

each elongation step. We found in our dLAMP experiments that the rate of specific amplification was greater than non-specific amplification. Hence, tracking amplification in real-time made it possible to distinguish true positives from false positives (non-specific amplification).

Fourth, we asked if the distribution in time to fluorescence threshold is sufficiently narrow to discriminate specific and non-specific amplification. By plotting the number of "on" partitions (i.e. partitions that crossed the fluorescence intensity threshold defined in **Figure 6.2b)** against time, we generated a distribution curve (**Figure 6.2f**) that illustrates the number of partitions that turn on per time point. This is related to the derivative of the change in concentration over time. This plot contains the time to threshold of all partitions within the entire chip, rather than a subset, to minimize sampling bias**.** In the sample containing template (blue curve), most partitions reached the threshold in 7–20 min, whereas the negative-control sample (red curve) had little non-specific amplification until approximately 60 min.

Graphing time to threshold illustrates the overall reaction's speed (defined as the location of the peak or mode time to threshold) and efficiency (proportional to the area under the curve and illustrated in **Figure 6.2f** as the calculated concentration). In our experiment, the peak of the sample containing template was narrow and well separated from the non-specific amplification of the negative control (**Figure 6.2f**), indicating sufficiently low heterogeneity in amplification rate and time to initiation of the reaction.

Fifth, we asked how the calculated bulk concentration changes over time. To answer this question, we generated endpoint-style measurements for each 30-sec time point, and calculated how the concentration changed over time. To demonstrate how to generate a single endpoint-style measurement, we selected one time point (25 min) and plotted RFU as a factor of the number of partitions (**Figure 6.2c**). Partitions were classified as either "on" (>250 RFU threshold) or "off" (<250 RFU threshold). Partitions that are defined as having turned "on" contain a template molecule that amplified, whereas partitions that are "off" either lack a template molecule or have not yet begun amplification. The sum of the partitions passing the threshold out of the total number of partitions with solution was used to determine a

precise bulk concentration of template in the sample using the Poisson equation, as has been documented elsewhere.[32,33] We plotted the calculated concentration as it changed over time in **Figure 6.2e** (solid lines).

When the aim is to determine a precise concentration, we need to determine the best time at which to stop the assay. Deciding the best time to end the assay is complicated because each reaction initiates stochastically,[16,21] causing the calculated concentration to asymptotically approach the true concentration (**Figure 6.2e**). It would be ideal for the calculated concentration to rapidly rise to the true bulk concentration and plateau near the true concentration; however, the reaction should be stopped before the rise in non-specific amplification (observed in our example starting at 60 min; red curves, **Figure 6.2e–f**). We tested whether there is heterogeneity in amplification rate (i.e. whether partitions with slow amplification rates take longer to reach the fluorescence intensity threshold than partitions with fast amplification rates) and found that initiation time was stochastic, but the reaction rates for true and false positives were consistent (**Figure 6.2g**). Hence, two molecules could have the same TTP, yet initiate at different moments, resulting in variable amplification rates.

Combining information about the concentration of template (**Figure 6.2e**) and the time it takes for partitions to turn "on" (**Figure 6.2f**) can be used to inform the choice of an optimal assay length for endpoint measurements, for situations where real-time quantification is not feasible. For example, in **Figure 6.2**, the optimal assay length for an endpoint readout would be ~45 min. This approach allows one to balance stochastic initiation of amplification, overcome enzymatic heterogeneity, and reduce the incidence of false positives caused by non-specific amplification.

However, in cases where real-time measurements are desirable, thresholding by rate may be used to separate specific and non-specific amplification. For example, to correct for the observed increase in non-specific amplification (after 45 min), we implemented a threshold (**Figure 6.2d**) on the maximum rate per partition, thus eliminating some of the non-specific amplification in both the presence and absence of template (compare solid and dashed lines in **Figure 6.2e).** For example, the measured value at 60 min is 280 copies per μL (solid line),

and the corrected value is 258 copies per μL (dashed line). In the no-template control, at 60 min, the measured value is 16 copies per μL (solid line), whereas the corrected value is 3 copies per μL (dashed line). The correction is more pronounced at 80 min where non-specific amplification is greater. At 80 min, the measured value in the presence of template is 325 copies per μL and the corrected value 266 copies per μL, indicating that almost 20% of the signal could arise from non-specific amplification. In the absence of template, the uncorrected value at 80 min is 187 copies per μL, however if rate is accounted for, then the value can be corrected to 16 copies per μL, thus eliminating the majority of the false positives.

Finally, we note that although we calculated template concentration, the value is precise but could be inaccurate if not all target molecules loaded into the chip undergo amplification (in other words, if efficiency of amplification is not 100%). Thus, we next sought to measure the absolute likelihood of detecting a molecule as a function of reaction condition.

*Evaluation of the effect of temperature on dLAMP with two different enzymes to analyze the interplay of amplification efficiency, background, and speed of amplification*

After establishing a protocol for generating real-time, digital measurements, we evaluated the absolute amplification efficiency of LAMP as a function of temperature for two different enzymes. We selected two commercial polymerases that worked well for us previously. Both enzymes are *in silico* homologues on the *Bacillus stearothermophilus* DNA Polymerase I and Large Fragment. NEB describes *Bst* 3.0 as an improvement of *Bst* 2.0 by adding reverse transcriptase activity, increased amplification speed, and increased thermostability. We sought to understand the differences in performance between these two enzymes at the single template level. For this experiment, we used the previously described RTAI.30 The field of view for this instrument is larger than a microscope, allowing up to six samples to be observed concurrently. Hence, both the positive and negative controls could be collected in triplicate simultaneously. We expect some differences in measurements made on different

instruments as a result of differing camera sensitivities and differences in the heating mechanism. Indeed, when we ran a single-concentration amplification reaction under identical conditions and compared measurements from the microscope and the RTAI, we found that there was significant difference ($P = 0.03$) in amplification efficiency between the two instruments (**Figure 6.6**), with the RTAI generating higher amplification efficiency. Hence, we performed all enzyme-performance comparisons on a single instrument.

*Amplification efficiency*

First, we sought to establish the amplification efficiency of dLAMP, i.e. the fraction of template copies loaded that are detected (**Figure 6.3a-b**). We calculated the bulk concentration of template molecules from the digital measurement and plotted the observed template concentration as a fraction of template molecules loaded. To calculate the amplification efficiency, we determined template concentration using ddPCR and assumed all template molecules amplified. Using the real-time component of our measurements, we plotted the percent of copies detected over time compared with ddPCR.

We next asked how temperature impacts amplification efficiency. In general, we observed greater amplification efficiency at longer amplification times, which aligned with our previous observation (**Figure 6.2d–e)**. Second, when observing at a fixed time, increasing temperature increased amplification efficiency to an optimum (green box in **Figure 6.3a-b**) before activity decreased.

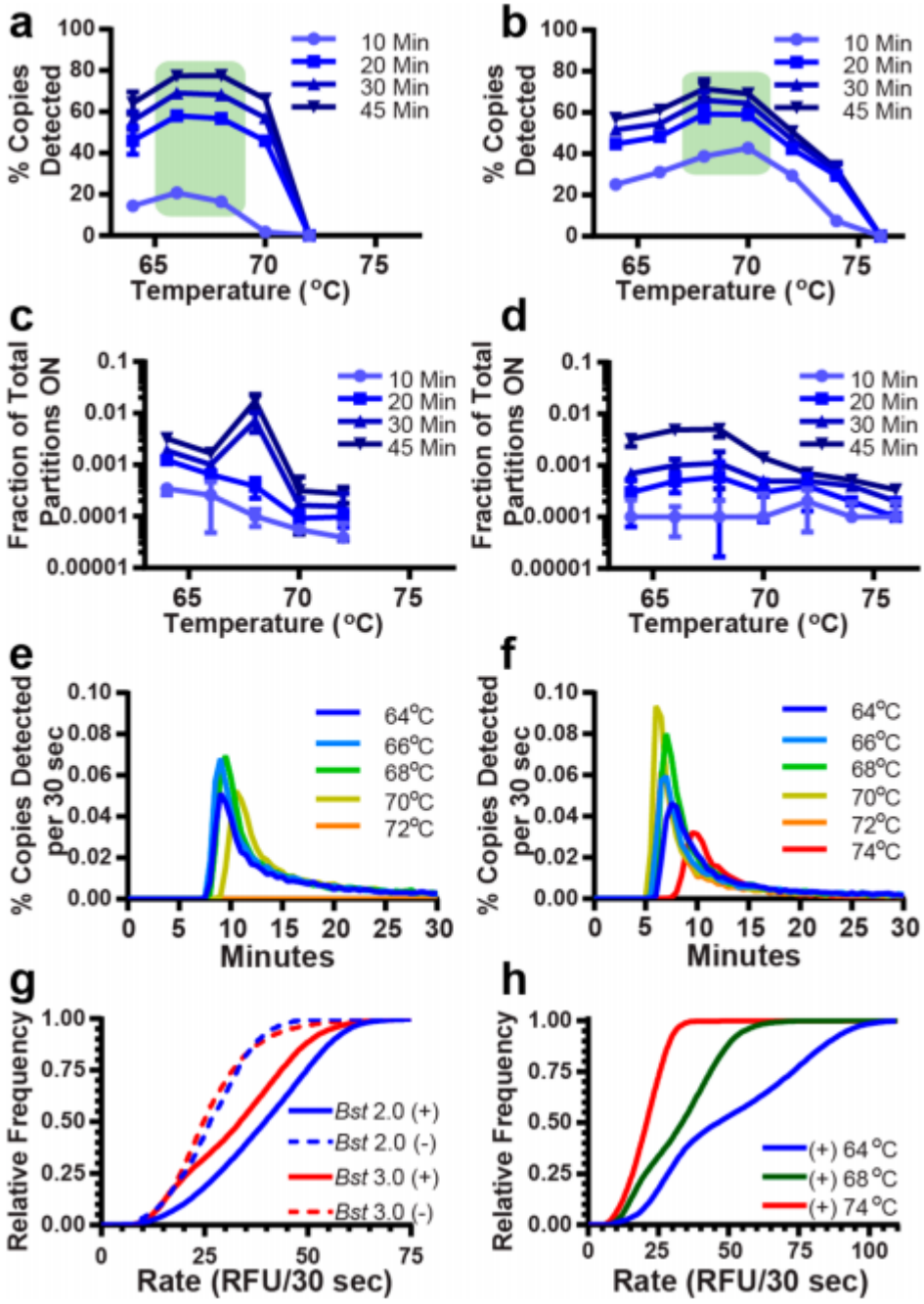


**Figure 6.3: Evaluation of reaction conditions (enzymes and temperature) using real-time digital LAMP.**

(a,b) Amplification efficiency (percent template copies detected out of copies loaded) of Bst 2.0 (a) and Bst 3.0 (b) as a function of temperature. Green boxes indicate the optimal temperature range for the greatest probability of template detection. (c,d)

Nonspecific amplification in template-free buffer samples using Bst 2.0 (c) and Bst 3.0 (d) for conditions matching (a) and (b). (e,f) Distribution of time to fluorescence threshold using Bst 2.0 (e) and Bst 3.0 (f). (g) The fractional cumulative distribution function (CDF) compares the enzymes at their optimal temperatures (68 °C). (h) Fractional CDF plots of Bst 3.0 rate at three temperatures. Error bars are SD. For all data sets, N = 3 chips (technical replicates). CDF plots are the sum of three technical replicates.

Several observations can be made by comparing the results from *Bst* 2.0 and *Bst* 3.0 (**Figure 6.3a-b**). Although *Bst* 2.0 and *Bst* 3.0 have an identical reported optimal incubation temperature in bulk (65°C), we observed they had different optimal temperature ranges for amplification efficiency (*Bst* 2.0 at 66–68 °C; *Bst* 3.0 at 68–70 °C). We detected lower amplification efficiency at higher temperatures with *Bst* 2.0 compared with *Bst* 3.0. *Bst* 2.0 failed to amplify at 72 °C, whereas *Bst* 3.0 continued amplifying until 76 oC. At short amplification times, (such as 10 min), *Bst* 3.0 had greater amplification efficiency than *Bst* 2.0 (42.8% vs 20.8%, respectively). In contrast, at longer amplification times, such as 30 or 45 min, efficiency for the enzymes was similar (77.6% vs 71.5% at 45 min, respectively), though *Bst* 2.0 had slightly greater amplification efficiency than *Bst* 3.0.

We hypothesize that increased temperature improved amplification efficiency (presumably by increasing the breathing of dsDNA and facilitating primer annealing) until, at higher temperatures, a combination of enzyme denaturation or failure of the primers to anneal occurred. Our primers had melting temperatures ranging from 56–61 °C, when excluding the secondary FIP and BIP anealing regions, as calculated using OligoCalc.35 We found that chip-to-chip variability was extremely low. Relative error for *Bst* 2.0 at optimal temperature (68 °C) and 45 min of amplification was ~2% (**Figure 6.2a**), whereas the predicted Poisson noise for a single chip is 0.7%. Achieving such high precision using bulk measurements would require hundreds of experiments. The low variability among these measurements

indicates that we were correctly determining whether a partition contained solution and whether it amplified.

*Non-specific background amplification*

Next, we quantified the amount of non-specific amplification (**Figure 6.3c-d)** as a function of time and temperature. We plotted the number of wells that turned "on" in the absence of template relative to the total number of wells filled with LAMP solution. As previously stated, these non-specific amplification reactions included buffer in place of template and represent a best-case scenario. We concluded that at least for these idealized conditions, non-specific amplification in dLAMP was extremely low. For example, a fraction of 0.001 could correspond to 20 partitions turning on from among a total of 20,000 possible partitions. For both enzymes, we found the maximum fraction of non-specific amplification per total partitions was 0.0012 for times 20 min or less. The highest fraction of non-specific amplification observed was 0.017 at 45 min, corresponding to fewer than 350 non-specific partitions of the 20,000 total (**Figure 6.3c-d**). Furthermore, we observed higher temperatures resulted in lower non-specific amplification (**Figure 6.3c-d**). Finally, at extremely long amplification times (e.g. 60 min amplification, data not shown) *Bst* 2.0 had lower background than *Bst* 3.0.

*Variation in speed and amplification efficiency*

Third, we quantified the variation in speed and amplification efficiency across partitions in the time to reach fluorescence intensity threshold (**Figure 6.3e-f**). We first plotted the percent copies detected as a function of time for each temperature. As described previously, these curves represent the distribution in the time to threshold across all partitions and thus illustrate the interplay of (i) detecting a molecule (area under the curve from zero to a given time corresponding to the values plotted in **Figure 6.3a-b**), (ii) the speed of the reaction (the

time at which the peak reaches a maxima), and (iii) several parameters of peak width summarized in **Table 6-1**. We hypothesize peak width is related to both the enzyme amplification rate, overall amplification efficiency, and the time at which the reaction initiates. Next, we plotted the peak time to threshold (**Figure 6.5)**. Images were collected in 30-sec intervals and we report the average of three trials. In some cases, the difference in time to threshold was less than the imaging time interval. For each time point, if fewer than 15 partitions (0.075% of total partitions) were "on," that time point was not included in the calculation of the mode. For these measurements, at the start of the reaction, the heat block was at 25 °C, and the time to threshold included the time for the heat block to come to reaction temperature (~70 sec). Hence, there will be minor differences (seconds) in the time for each reaction to reach the fixed temperature. We do not see evidence that this difference manifests in the mode time to positive (TTP) measurements.

In reactions with *Bst* 2.0, below 68 °C, mode TTP was narrowly clustered around 9.5 min. At 70 °C, mode TTP increased, and the reaction failed to amplify beyond 72 °C. In reactions with *Bst* 3.0, the mode TTP decreased from 8.2 ± 0.3 (mode ± S.D.) min at 64 °C to 6.6 ± 0.3 min at 70 °C, then increased with increasing temperature until amplification failed for all partitions at temperatures ≥76 °C. In the negative controls for both enzymes (**Figure 6.5**), amplification either failed or started after 75 min.

Several observations can be made by comparing the results from **Figure 6.3e-f.** We found that the optimal temperature for time to threshold corresponded with the optimal temperature for amplification efficiency (**Figure 6.3a-b)**, and that the optimal temperatures also had the smallest tailing factors, Full Width at Half Maximum (FWHM) and asymmetric factor (i.e. narrowest peak widths) **(Figure 6.3e-f; Table 6-1)**. At optimal efficiency, *Bst 3*.0 was approximately 2 min faster in mode TTP, had much narrower FWHM, smaller tailing factor, and lower asymmetry than *Bst* 2.0. Finally, as efficiency decreases, measurements of peak shape and width increase. To the best of our knowledge, this is the first published quantification that explicitly tests and quantifies the time dependence of LAMP efficiency using these enzymes. Real-time digital enables us to identify the time point at which the

observed concentration most closely approximates the true concentration thus optimizing the assay duration.

*Rates of amplification (specific and non-specific)*

Fourth, we compared the rates of specific and non-specific amplification between *Bst* 2.0 and *Bst* 3.0. The data shown represent the combined rates of three separate trials. We found that non-specific amplification rates were similar for the two enzymes (**Figure 6.3g**, dashed lines), whereas in the presence of template, amplification rates were faster for *Bst* 2.0 than *Bst* 3.0 (**Figure 6.3g**, solid lines), despite lower efficiency at short times. Differences in camera sensitivity between the microscope (used for real-time images in **Figure 6.2**) and the RTAI (used for **Figure 6.3**) result in different apparent amplification rates.

We also examined the relationship between temperature, efficiency, and maximum rate. In the case of *Bst* 3.0, maximum reaction amplification rate does not correspond with optimal efficiency (**Figure 6.3h**). 64 °C had the fastest amplification rates, but suboptimal efficiency (57.3% at 45 min). Optimal amplification efficiency occurs at 68 °C (71.5% at 45 min), but slightly slower amplification rate than 64 °C. At 74 °C, we observed both poor efficiency (32.7% at 45 min) and slowest reaction rate. We attribute this to a combination of decreased enzymatic velocity and decreased primer annealing. Additionally, we note that different thresholds for amplification rate would be needed for each temperature. This is expected given changes in enzymatic velocity.

*Application of the pipeline to a phenotypic antibiotic susceptibility test (AST) using clinical samples*

We next asked whether we could apply the output of this digital real-time pipeline to perform a rapid phenotypic AST. Specifically, we aimed to categorically sort clinical samples as

phenotypically “susceptible” or “resistant” to an antibiotic in agreement with the gold-standard reference method. This study was constructed as a demonstration of the capability of the microfluidic chips and the value gained from using this digital real-time pipeline to optimize reaction conditions — it was not an assessment of the digital AST (dAST) methodology established previously.[17,18] We selected the optimal dLAMP conditions for *Bst* 3.0 based on the measurements of mode TTP and amplification efficiency established in the previous experiments (**Figure 6.3b**) — 70 °C and a reaction time of 10 min. We used archived clinical urine samples from patients diagnosed with urinary tract infections (UTI) containing *E. coli.* These samples had been categorized as phenotypically susceptible or resistant to the antibiotics ciprofloxacin or nitrofurantoin using the gold-standard (broth microdilution) method.[18] We tested exactly 17 samples and observed 100% categorical agreement with the gold-standard method (0 major errors; 0 minor errors). We conclude that the pipeline presented in this paper performs well and could be used, among other applications, to optimize reaction conditions for speed and sensitivity and apply those conditions to a determination of phenotypic antibiotic susceptibility in clinical samples.

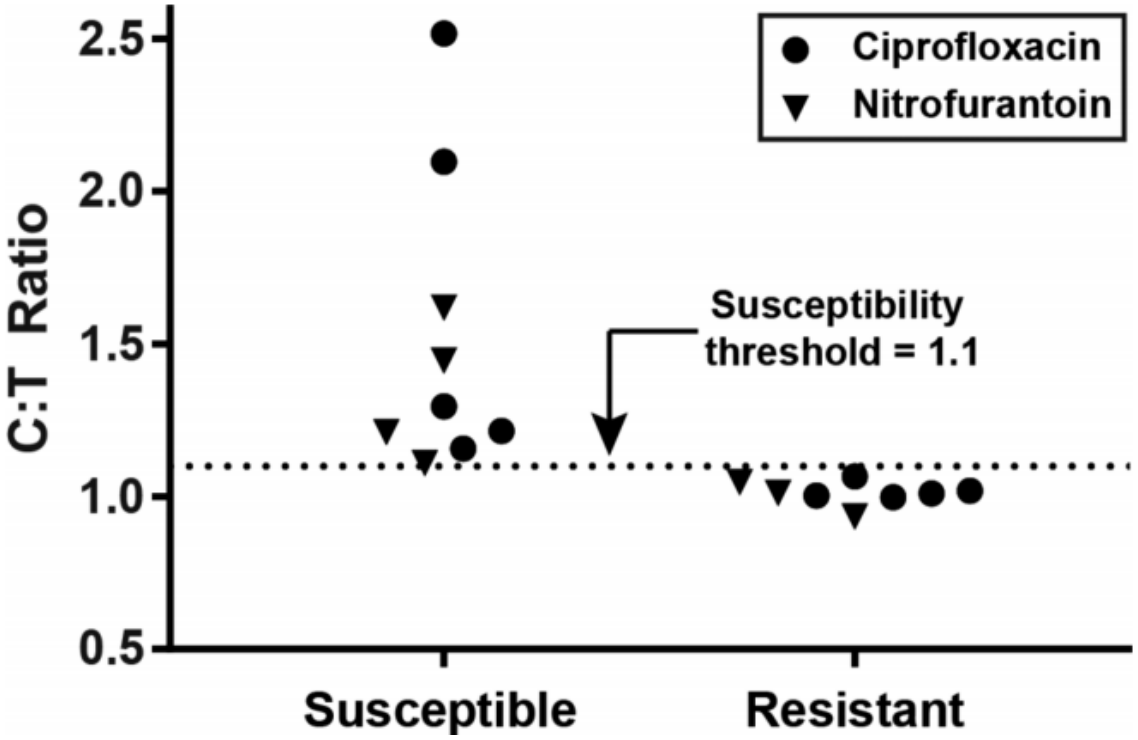


**Figure 6.4: Phenotypic antibiotic susceptibility tests of 17 clinical urine samples from patients infected with a urinary tract infection containing *E. coli*.**
Susceptibility to the antibiotics nitrofurantoin and ciprofloxacin were tested using dLAMP conditions optimized using digital real-time experiments (**Figure 6.3**). Urine samples were exposed to media without antibiotic (control) or media with an antibiotic (treated) for 15 min and then concentrations of nucleic acids were quantified to calculate a control:treated (C:T) ratio. Samples were categorized by dLAMP as susceptible (above the susceptibility threshold) or resistant (below the threshold). All samples were categorized in agreement with the clinical gold-standard method.

## Conclusions

We have presented a pipeline to generate real-time, digital isothermal amplification measurements using only commercial and open-source components. We used this pipeline to examine how small changes in reaction conditions influence the interplay of LAMP

efficiency, speed, and background by performing 124 real-time dLAMP experiments. As one practical application of this approach, we determined the optimal reaction conditions for a phenotypic test of antibiotic susceptibility using 17 clinical urine samples from patients diagnosed with urinary tract infections. In all cases, the results of the optimized dLAMP assays were in agreement with the clinical gold-standard AST.

These experiments validate that real-time digital measurements enable tests of enzymatic performance in dLAMP. Generally, we found that each enzyme had a unique optimal temperature for amplification efficiency (probability of detecting a target molecule) and for eliminating non-specific amplification. This "optimal" temperature produced the fastest mode TTP and the narrowest, most symmetrical distribution curves; interestingly, the optimal temperature did not necessarily yield the fastest amplification rate. Together, these data suggest that amplification efficiency is an interplay of enzymatic rate, diffusive transport, and DNA breathing. When reactions are performed away from optimal temperature, the distribution curves broaden and decrease in total area, resulting in reduced overall amplification efficiency and slower mode TTP; whereas amplification rate decreases with increasing temperature. With regard to the specific enzymes in this study, although efficiency was similar at long amplification times (> 20 min), *Bst* 3.0 had a faster mode TTP than *Bst* 2.0 by approximately 2 min, and more narrow and symmetrical distribution curves. However, *Bst* 2.0 had faster amplification rates than *Bst* 3.0, so reactions with *Bst* 2.0 took longer to initiate, but proceeded more rapidly. For both polymerases, non-specific amplification in buffer was extremely low.

In the future, this pipeline can be used to understand the fundamental pieces of LAMP. The field of diagnostics would benefit from a thorough mechanistic study of LAMP asking which components determine amplification fate, and how components, such as primers and heating rate (**Figure 6.6**), impact reaction and enzymatic speed. This pipeline makes such a mechanistic study possible. For example, in this study we corrected the observed concentration by separating true positives from background amplification using rate and fluorescence, but we did not explore the origins of non-specific amplicons—which deserves

its own study and development of more precise tools for studies of non-specific amplification. Finally, this pipeline can be extended to optimize other isothermal amplification chemistries that could be suited to other types of diagnostic assays.

Ultimately, this pipeline will make digital real-time measurements more accessible to researchers, even those who lack microfluidic expertise or specialized equipment. The commercially available chips and reagents used here could be coupled with many combinations of standard laboratory or field equipment, such as a hot plate and a fluorescent stereoscope, or a chemical heater and a cell phone camera. While we believe the general trends found in this manuscript will extend to other primer sets, we hope this pipeline will enable others to study other primer sets and conditions of interest to them.

**References**


1. Heid, C. A.; Stevens, J.; Livak, K. J.; Williams, P. M. *Genet. Res.* **1996**, *6*, 986-994.

2. Tanner, N. A.; Zhang, Y.; Evans, T. C. *BioTechniques* **2012**, *53*, 81-89.

3. Tanner, N. A.; Zhang, Y.; Evans, T. C. *BioTechniques* **2015**, *58*, 59-68.

4. Notomi, T.; Okayama, H.; Masubuchi, H.; Yonekawa, T.; Watanabe, K.; Amino, N.; Hase, T. *Nucleic Acids Res.* **2000**, *28*, e63-e63.

5. Tanner, N. A.; Evans, T. C. *Curr. Protoc. Mol. Biol.* **2014**, *105*, 15.14.11-15.14.14.

6. Becherer, L.; Bakheit, M.; Frischmann, S.; Stinco, S.; Borst, N.; Zengerle, R.; von Stetten, F. *Anal. Chem.* **2018**, *90*, 4741-4748.

7. Aoi, Y.; Hosogai, M.; Tsuneda, S. *J. Biotechnol.* **2006**, *125*, 484-491.

8. Drame, P. M.; Fink, D. L.; Kamgno, J.; Herrick, J. A.; Nutman, T. B. *J. Clin. Microbiol.* **2014**, *52*, 2071-2077.

9. Mori, Y.; Kitao, M.; Tomita, N.; Notomi, T. *J. Biochem. Bioph. Meth.* **2004**, *59*, 145-157.

10. Ball, C. S.; Light, Y. K.; Koh, C.-Y.; Wheeler, S. S.; Coffey, L. L.; Meagher, R. J. *Anal. Chem.* **2016**, *88*, 3562-3568.

11. Calvert, A. E.; Biggerstaff, B. J.; Tanner, N. A.; Lauterbach, M.; Lanciotti, R. S. *PLOS One* **2017**, *12*, e0185340.

12. Poole, C. B.; Ettwiller, L.; Tanner, N. A.; Evans, T. C., Jr.; Wanji, S.; Carlow, C. K. S. *PLOS One* **2015**, *10*, e0139286.

13. Poole, C. B.; Tanner, N. A.; Zhang, Y.; Evans, T. C., Jr.; Carlow, C. K. S. *PLOS Neglect. Trop. D.* **2012**, *6*, e1948.

14. Wheeler, S. S.; Ball, C. S.; Langevin, S. A.; Fang, Y.; Coffey, L. L.; Meagher, R. J. *PLOS One* **2016**, *11*, e0147962.

15. Bhadra, S.; Jiang, Y. S.; Kumar, M. R.; Johnson, R. F.; Hensley, L. E.; Ellington, A. D. *PLoS One* **2015**, *10*, e0123126.

16. Khorosheva, E. M.; Karymov, M. A.; Selck, D. A.; Ismagilov, R. F. *Nucleic Acids Res.* **2016**, *44*, e10.

17. Schoepp, N. G.; Khorosheva, E. M.; Schlappi, T. S.; Curtis, M. S.; Humphries, R. M.; Hindler, J. A.; Ismagilov, R. F. *Angew. Chem. Int. Edit.* **2016**, 9557-9561.

18. Schoepp, N. G.; Schlappi, T. S.; Curtis, M. S.; Butkovich, S. S.; Miller, S.; Humphries, R. M.; Ismagilov, R. F. *Sci. Trans. Med.* **2017**, *9*, eaal3693.

19. Sun, B.; Shen, F.; McCalla, S. E.; Kreutz, J. E.; Karymov, M. A.; Ismagilov, R. F. *Anal. Chem.* **2013**, *85*, 1540-1546.

20. Rodriguez-Manzano, J.; Karymov, M. A.; Begolo, S.; Selck, D. A.; Zhukov, D. V.; Jue, E.; Ismagilov, R. F. *ACS Nano* **2016**, *10*, 3102-3113.

21. Sun, B.; Rodriguez-Manzano, J.; Selck, D. A.; Khorosheva, E.; Karymov, M. A.; Ismagilov, R. F. *Angew. Chem. Int. Edit.* **2014**, *53*, 8088-8092.

22. Hu, Y.; Xu, P.; Luo, J.; He, H.; Du, W. *Anal. Chem.* **2017**, *89*, 745-750.

23. Ma, Y.-D.; Chang, W.-H.; Luo, K.; Wang, C.-H.; Liu, S.-Y.; Yen, W.-H.; Lee, G.-B. *Biosens. Bioelectron.* **2018**, *99*, 547-554.

24. Ma, Y.-D.; Luo, K.; Chang, W.-H.; Lee, G.-B. *Lab Chip* **2018**, *18*, 296-303.

25. Schuler, F.; Siber, C.; Hin, S.; Wadle, S.; Paust, N.; Zengerle, R.; von Stetten, F. *Anal. Methods-UK* **2016**, *8*, 2750-2755.

26. Gansen, A.; Herrick, A. M.; Dimov, I. K.; Lee, L. P.; Chiu, D. T. *Lab Chip* **2012**, *12*, 2247-2254.

27. Rane, T. D.; Chen, L.; Zec, H. C.; Wang, T.-H. *Lab Chip* **2015**, *15*, 776-782.

28. Zhu, Q.; Gao, Y.; Yu, B.; Ren, H.; Qiu, L.; Han, S.; Jin, W.; Jin, Q.; Mu, Y. *Lab Chip* **2012**, *12*, 4755-4763.

29. Shen, F.; Davydova, E. K.; Du, W.; Kreutz, J. E.; Piepenburg, O.; Ismagilov, R. F. *Anal. Chem.* **2011**, *83*, 3533-3540.

30. Selck, D. A.; Ismagilov, R. F. *PLOS One* **2016**, *11*, e0163060.

31. Schindelin, J.; Arganda-Carreras, I.; Frise, E.; Kaynig, V.; Longair, M.; Pietzsch, T.; Preibisch, S.; Rueden, C.; Saalfeld, S.; Schmid, B.; Tinevez, J.-Y.; White, D. J.; Hartenstein, V.; Eliceiri, K.; Tomancak, P.; Cardona, A. *Nat. Methods* **2012**, *9*, 676.

32. Kreutz, J. E.; Munson, T.; Huynh, T.; Shen, F.; Du, W.; Ismagilov, R. F. *Anal. Chem.* **2011**, *83*, 8158-8168.

33. Rissin, D. M.; Walt, D. R. *Nano Lett.* **2006**, *6*, 520-523.

34. Rojek, M. J.; Walt, D. R. *PLOS One* **2014**, *9*, e86224.

35. Kibbe, W. A. *Nucleic Acids Res.* **2007**, *35*, W43-W46.

**Supporting Information**

*Summary of MATLAB script functions*

In order to quantify the reactions on chips using the Poisson distribution, we needed to know the number of partitions that contained solution and the number of partitions that were empty. (It would be naïve to assume that all 20,000 partitions were loaded with solution; visual inspection shows that was rare.) We counted the total number of partitions with solution using the image of the autofluorescence of SYTO 9 dye before heating at time 0 (**Figure 6.2a**). SYTO 9 had uniform autofluorescence independent of template presence, making it easy to count all partitions loaded with solution.

To track the mean fluorescence intensity of each partition over time, we solved two challenges. First, when the microfluidic chip was heated (especially during the first 2 min), the chip moved. As the chip heated, it lost the initial autofluorescence from SYTO 9. Consequently, it was not possible to track this movement with the fluorescence of a single fluorophore. We solved this challenge by creating a mask (using image segmentation) that outlined each detectable partition at the chip's final position using a frame at the end of

amplification. An advantage to using only the detectable partitions that met a minimum fluorescence intensity (out of a total of 20,000 partitions per chip) reduced overall computation time because only a fraction of the total partitions were tracked in real-time.

A second challenge when tracking mean fluorescence intensity of each partition over time using only the detectable partitions is that partitions can appear to be different sizes because of differences in fluorescence intensity (dark partitions can appear artificially smaller and bright partitions can appear artificially larger). To counteract the effect of each partition having a different average intensity, we performed multi-level thresholding with tight restrictions for the area and major axis filters. We set a minimum fluorescence intensity (threshold) for each pixel at a given time and used this information to segment (define the perimeter) each individual partition. This threshold was combined with selection criteria for the area and major axis. The area filter defined the smallest and largest partitions while the major axis filter ensured that detected regions were circular. We repeated this for different threshold values and merged the resulting partitions. This technique restricted partitions to a specific size and shape while enabling detection over many intensity values.

Finally, we used the information from quantifying the number of partitions containing solution and tracking mean fluorescence of each partition over time to calculate the concentration of template in the bulk solution. To smooth the traces and reduce the noise, we first applied a Gaussian-weighted moving average filter with window length 10 frames to each intensity curve. To ensure all partitions start at zero intensity, we determined the baseline intensity by calculating the average partition intensity for selected frames after heating but prior to detectable amplification (between 2.5 min and 5 min). The baseline intensity was subtracted from all frames. Finally, we manually defined a threshold to determine whether a partition would be counted as a “positive” or “negative.” Using the adjusted traces, threshold, and the total number of partitions, we determined the fraction of partitions that were “on” for any given time. Using the fraction of partitions that were “off,” we calculated via the Poisson distribution the concentration of template detected in the bulk solution for any given time point. From this measurement of concentration, we can calculate

the amplification efficiency by dividing the measured concentration by the known (true) concentration.

The MATLAB script described here has been deposited in the open-access online repository GitHub and may be accessed using the following direct link: https://github.com/IsmagilovLab/Digital_NAAT_Analyzer

*Acquiring real-time data using microscopy*

Images were acquired in 30-sec intervals on a Leica DMI-6000B (Leica, Buffalo Grove, IL, USA) with a 1.25x 0.04NA HCX PL FLUOTAR Objective (506215) and 0.55x coupler (Leica C-mount 11541544) using a 1-sec exposure through the L5 (GFP) Nomarski prism and a Hamamatsu ORCA-ER CCD camera (Hamamatsu Photonics K.K., Hamamatsu City, Shizuoka, Japan; Ref. C4742-80-12AG). Heating was performed using an integrated circuit (IC) board prototype for temperature control developed by Green Domain Design (San Diego, CA, USA). The IC board was connected to a DC power supply (Model 3670; Electro Industries, Monticello, MN, USA), a Nichrome wire (12 ohm) attached to a 5 x 25 x 25 mm aluminum block. A thermistor was mounted within the block to measure the temperature of the heating block. When the temperature of the heating block was lower than the set-point temperature, the IC board supplied current to the Nichrome wire resistive heater. With this setup, heating was achieved to 70.0 ± 2 °C within 2 min. Images obtained on the microscope were processed with our MATLAB script (**Supporting Information, S-I**) using the following parameters: Area Bound [5 40] pixels, Major Axis [2 9] pixels, Threshold [250] Relative Fluorescence Units (RFU), Baseline Smoothing Frames [6 11], Masking Image Frame [175].

*Acquiring data using a custom large-format real-time amplification instrument (RTAI)*

Images were acquired in 30-sec intervals on a custom-built, public-domain real-time amplification instrument (RTAI), described previously,[30] using the FAM channel with a 15-sec exposure at *f*/5.6. Heating was achieved using the built-in PCT-200 thermocycler, which heats to 70.0 ± 0.3 °C within 70 sec. The temperature of the thermocycler block was held at 25 °C to start all reactions, with the exception of an experiment where the block was preheated to the optimal temperature (**Figure 6.2, Figure 6.6b**). We equipped the thermocycler with an aluminum block with two sloped planes (each set at 11°—an angle defined by the microfluidic chip manufacturer's requirements) to segregate bubbles formed during the reaction to a specifically designed bubble trap. It was advantageous to use this instrument to analyze up to six chips in parallel in a single field of view and under a uniform temperature. By running multiple chips on a real-time instrument we achieved "multiplexed" assays (wherein multiple measurements are made simultaneously). Images obtained on the RTAI were processed through our MATLAB script (**Supporting Information, S-I**) using the following parameters: Area Bound [4 12] pixels, Major Axis [2 5] pixels, Threshold [100] RFU, Baseline Smoothing frames [6 11], Masking Image Frame [175].

*Limitations of chips used*

A limitation of chips that discretize by capillary action is that solution can spread among the partitions. For example, during dLAMP quantification of extractions for three of the clinical samples, we observed spreading of one positive partition to its adjacent partitions. We attribute this spreading to liquid bridges forming among adjacent wells, resulting in transfer of the amplicon among compartments. These bridges could arise from defects in surface coatings of commercial chips or from an excess of surface active molecules present in some clinical samples. To test whether spreading was due to surface active impurities in the samples, samples were diluted in Tris-EDTA (TE) buffer and in the subsequent test, spreading was eliminated for one sample. For the remaining samples, dilution reduced the spreading enough that quantification at 10 min was not hindered, although some spreading

was observed at later times. Quantification of the C:T ratio remained consistent (and the susceptibility call the same) because we use a ratiometric calculation.

*Calculation of peak width metrics*

The average distribution curve (averaged over three trials) was calculated for each temperature and all values normalized to the peak prominence. Time resolution was estimated to the nearest 15 sec interval. Calculations were based on: John V. Hinshaw. "How Do Your Peaks Measure Up?" Oct 01, 2013, LCGC Europe, Volume 26, Issue 10, pg 575–582.

Full Width at Half Maximum was calculated at the time difference between the leading at tailing edges at 50% peak prominence.

Asymmetric factor was calculated by dividing the time between the peak prominence and the tailing edge ("*b0.1*") by the time between the peak prominence and the leading edge at 10% peak height ("*f0.1*").

**Equation 6-1**

$$Asymmetric\ Factor = \frac{b_{0.1}}{f_{0.1}}$$

Tailing factor was calculated as the total peak width at 5% of the prominence (or the distance from the leading edge to the time of peak prominence ("*f0.05*") plus the distance from the time of peak prominence to the tailing edge ("*b0.05*")) divided by twice the distance from the leading edge to the time of peak prominence.

**Equation 6-2**

$$Tailing\ Factor = \frac{f_{0.05} + b_{0.05}}{2f_{0.05}}$$

**Table 6-1: Tabular quantification of the time to threshold distribution curves.**

| *Bst* 2.0 | | | | | | *Bst* 3.0 | | | | | |
|---|---|---|---|---|---|---|---|---|---|---|---|
| Temp (°C) | Efficiency at 45 min (%) | Mode TTP (min) | FWHM (min) | Asymmetric Factor | Tailing Factor | Temp (°C) | Efficiency at 45 min (%) | Mode TTP (min) | FWHM (min) | Asymmetric Factor | Tailing Factor |
| 64.0 | 64±8 | 9.5±0.0 | 2.5 | 10.2 | 14.8 | 64.0 | 57±2 | 8.2±0.3 | 3.0 | 8.0 | 14.2 |
| 66.0 | 78±2 | 9.3±0.3 | 2.3 | 7.6 | 11.7 | 66.0 | 61±2 | 7.3±0.3 | 2.3 | 5.6 | 11.4 |
| 68.0 | 78±2 | 9.8±0.3 | 2.3 | 7.2 | 14.3 | 68.0 | 71±6 | 7.6±0.3 | 2.3 | 6.0 | 9.2 |
| 70.0 | 66±1 | 11.0±0.0 | 2.8 | 8.8 | 9.1 | 70.0 | 69±3 | 6.7±0.3 | 1.5 | 7.3 | 3.7 |
| | | | | | | 72.0 | 51±3 | 7.2±0.3 | 2.0 | 8.3 | 4.3 |
| | | | | | | 74.0 | 33±9 | 10.2±0.6 | 2.8 | 5.7 | 13.1 |

*Time to mode positive*

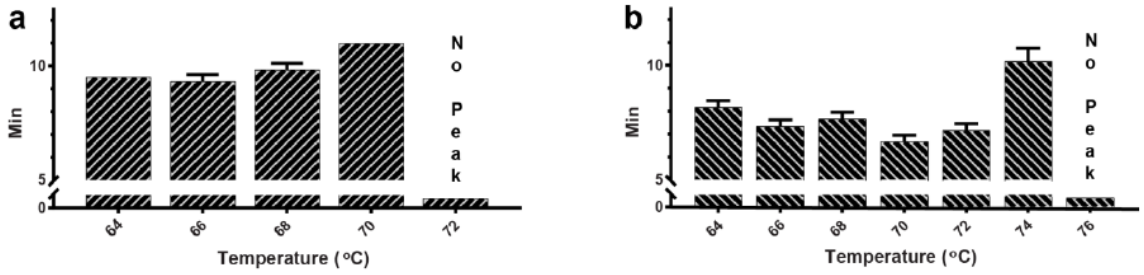


**Figure 6.5: Bar graphs of the time location of the peak of the distribution curve (time to mode positive) using *Bst* 2.0 (a) and *Bst* 3.0 (b).**

We required 15 or greater partitions turn on at a given time (0.075% of total partitions), to include the time point for the mode. Data are summarized in **Table 6-1**.

*Hardware and pre-heating condition*

We asked if multiple instrumentation formats could be used to collect the data and if hardware format impacted the amplification efficiency. We used the optimal conditions for *Bst* 3.0. First, we compared the performance of the large-format real-time amplification instrument (RTAI) to a wide-field microscope fitted with a heat block—a set-up that would be accessible to most laboratories. We found that the heater ramp rate was slower on the microscope than the RTAI (120 sec versus 70 sec) resulting in 9.0 ±1.0 min time to mode positive (**Figure 6.6a)**.

Next, we looked at the effect of pre-heating using the RTAI. We compared the optimal conditions using *Bst* 3.0 and starting from 25 °C (green curve) with the same instrument and heating block already at the optimal reaction temperature of 70 °C (orange curve). When the block is preheated, we observed the mode time to threshold reduced from 6.7 ±0.3 min to 6.0 ±0.0 min (**Figure 6.6a**).

Next, we asked if differences in hardware configuration and the heating rates between the instruments would also correspond to differences in probability of detection. We observed significant variation in amplification efficiency (RTAI vs RTAI with preheating $P = 0.002$; RTAI vs microscope with heater $P = 0.031$, RTAI with preheating vs microscope with heater $P < 0.001$) and concluded that heating rate may impact probability of amplification (**Figure 6.6b**). Hence, all comparisons made in this study were instrument specific. Though it remains to be tested, we suspect more precise hardware, with improved heating control, could improve device performance.

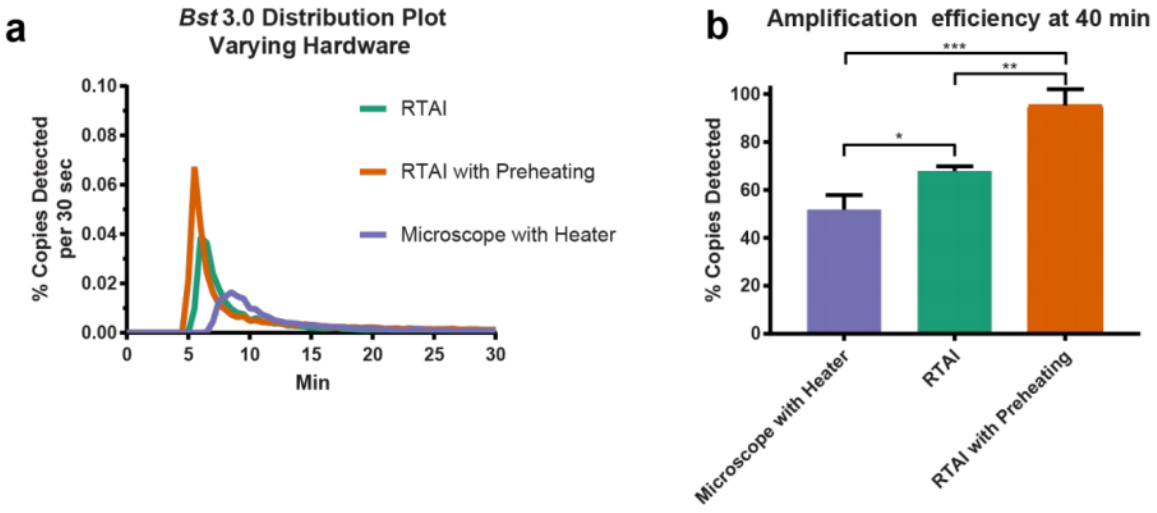


**Figure 6.6: Effect of hardware and heating on (a) the distribution in time to fluorescence threshold and (b) quantification of amplification efficiency (mean percentage copies detected ± S.D.) at 40 min.**

*Optimization of Bst 2.0 buffer composition*

Following the protocol described previously,[18] buffer conditions for *Bst* 2.0 were optimized in bulk at 713 copies/µL (e.g. ~4,280 or 0 copies per 6 µL reaction). Optimal buffer composition was selected based on fastest bulk time to positive.

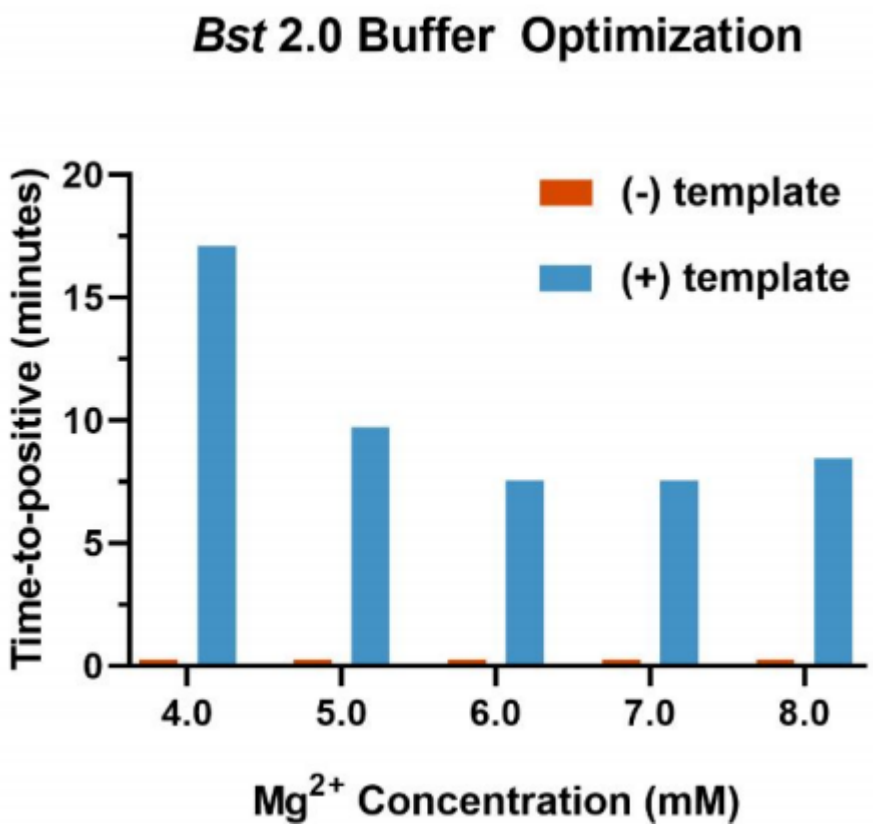


**Figure 6.7: Magnesium optimization for *Bst* 2.0.**

A value of 0.25 indicates that no amplification was observed. Amplification was performed at 67.5° C. N=1 for all TTP values.

*Chapter 7*

# REAL-TIME KINETICS AND HIGH-RESOLUTION MELT CURVES IN SINGLE-MOLECULE DIGITAL LAMP TO DIFFERENTIATE AND STUDY SPECIFIC AND NONSPECIFIC AMPLIFICATION

J.C. Rolando, E. Jue, J. Barlow, and R.F. Ismagilov. 2020. *Nucleic Acids Research.* 48(1):42. doi:10.1093/nar/gkaa099

**Abstract**

Isothermal amplification assays, such as loop-mediated isothermal amplification (LAMP), show great utility for the development of rapid diagnostics for infectious diseases because they have high sensitivity, pathogen-specificity, and potential for implementation at the point of care. However, elimination of nonspecific amplification remains a key challenge for the optimization of LAMP assays. Here, using chlamydia DNA as a clinically relevant target and high throughput sequencing as an analytical tool, we investigate a potential mechanism of nonspecific amplification. We then develop a real-time digital LAMP (dLAMP) with high-resolution melting temperature (HRM) analysis and use this single-molecule approach to analyze approximately 1.2 million amplification events. We show that single-molecule HRM provides insight into specific and nonspecific amplification in LAMP that are difficult to deduce from bulk measurements. We use real-time dLAMP with HRM to evaluate differences between polymerase enzymes, the impact of assay parameters (e.g., time, rate, or florescence intensity), and the effect background human DNA. By differentiating true and false positives, HRM enables determination of the optimal assay and analysis parameters that leads to the lowest limit of detection (LOD) in a digital isothermal amplification assay.

## Introduction

Isothermal methods, such as loop-mediated isothermal amplification (LAMP), are attractive for nucleic acid amplification tests (NAATs) in point-of-care and limited-resource settings (1,2). LAMP in particular shows promise as a NAAT with fewer hardware requirements compared with PCR (3). Despite advancements, the ability to optimize LAMP NAATs for a specific target sequence and primer set (specific to a target organism) remains constrained by a limited understanding of how amplification is affected by myriad factors, including polymerase choice, primer design, temperature, time, and ion concentrations. In particular, addressing nonspecific amplification remains a core problem as it constrains an assay's limit of detection (LOD). In reactions containing template target molecules, both specific and nonspecific amplification reactions may occur. Unlike PCR, LAMP lacks a temperature-gating mechanism, so nonspecific reactions consume reagents and compete with specific amplification impacting its kinetics. The presence of nonspecific amplicons therefore adversely impacts both the assay's analytical sensitivity (the fewest template molecules that can be detected) and its analytical specificity (ability to detect the target template in the presence of competing reactions). Classifying reactions as either specific or nonspecific amplification would therefore be invaluable both during assay optimization and assay deployment in clinical diagnostics.

Substantial research is focused on using isothermal amplification chemistries for diagnosis of infectious disease. For example, chlamydia (caused by the pathogen *Chlamydia trachomatis,* CT) is the most common sexually transmitted infection worldwide, with more than 110 million cases reported annually (4). Diagnosis of CT infections is challenged by a lack of standard symptoms (many infections are asymptomatic) (5) and the presence of mixed flora (particularly in the female reproductive tract) (6). Thus, rapid NAATs with high sensitivity and specificity are critically needed, especially NAATs that can deal with the high levels of host or background DNA likely to be present in clinical samples such as urine samples and swabs (7,8).

Optimizing LAMP for CT and other infectious pathogens requires addressing and reducing nonspecific amplification or a method for separating nonspecific reactions from specific amplification. Reactions run in bulk (i.e., in a tube) in the absence of template can be informative to provide information on performance of nonspecific amplification. Another method to identify nonspecific amplification includes mathematical modeling in conjunction with electrophoresis to distinguish between nonspecific and specific banding patterns(9). However, in the presence of template, although specific and nonspecific reactions occur simultaneously, they cannot be monitored simultaneously. Thus, bulk reactions have three important limitations with regard to assay optimization: (i) differences in the kinetics of specific and nonspecific reactions cannot be separated; (ii) rare but significant events, such as early but infrequent nonspecific amplification, cannot be easily characterized; and (iii) testing the full design space requires many hundreds of replicates to obtain statistically significant data. To improve an assay's analytical specificity and sensitivity, one strategy is to eliminate the detection of nonspecific amplification. In bulk LAMP experiments, nonspecific amplification can be excluded from detection by using probes, beacons, FRET, or reporter-quencher schemes that show only specific amplification of the target (10-19). Although these methods improve the assay, they do not capture nonspecific reactions and thus cannot give insights into the origin of nonspecific amplification or the conditions that led to nonspecific amplicons. Moreover, probes and beacons do not eliminate nonspecific amplification; nonspecific amplification still competes for reagents and can limit the extent of the signal generated by specific amplification events (20). Hence, it is highly desirable to distinguish specific from nonspecific amplification.

In this study, we combined sequencing and digital single-molecule LAMP (dLAMP) with high-resolution melting temperature (HRM) to probe the fundamental mechanics of amplification reactions. We used dLAMP to extract real-time kinetic information to identify the digital threshold data-processing parameters that minimize nonspecific amplification events and elucidate how an interfering molecule impacts amplification. Digital single-molecule methods separating individual amplification events into discrete compartments, eliminating interference among individual amplification events (21,22). Furthermore, digital

experiments consist of thousands of reactions that run in parallel and thus provide valuable statistical information (21-23). We used real-time imaging to monitor the kinetics of 20,000 dLAMP reactions per experiment and observe ~ 1.2 x $10^6$ reactions in total. We hypothesized that high-resolution melting analysis (HRM) could be a tool for separating specific from nonspecific amplification events and for identifying the optimal digital threshold data-processing parameters to distinguish specific and nonspecific amplification events (even when an assay is deployed without HRM). To test this hypothesis, we used a dLAMP assay with CT DNA as the target (combined with sequencing to identify the products of bulk reactions) to analyze both specific and nonspecific amplification under conditions that include clinically relevant concentrations of background human DNA.

## Materials and Methods

### *LAMP reagents*

IsoAmp I (#B0537S), IsoAmp II (#B0374S), $MgSO_4$ (#B1003S), deoxynucleotide solution (#N0447S), Bovine Serum Albumen (BSA, #B9000S0), *Bst* 2.0 (8,000 U/mL, #M0537S), and *Bst* 3.0 (8,000 U/mL, #M0374S) were purchased from New England Biolabs (Ipswich, MA, USA). Ambion RNase Cocktail (#AM2286), Ambion nuclease-free water (#AM9932), Invitrogen SYTO 9 (S34854), and Invitrogen ROX Reference Dye (#12223012) were purchased from Thermo Fisher Scientific (Waltham, MA, USA). We found it important to use SYTO 9 dilutions within one week of preparation.

Primers sequences were targeted against the *Chlamydia trachomatis* 23S ribosomal gene using Primer Explorer V5 (Eiken Chemical, Tokyo, Japan) and checked in SnapGene (GSL Biotech, Chicago, IL, USA) to ensure the sequences were in a mutation-free region from the available Genebank sequences of CT. Primers were purchased from Integrated DNA Technologies (San Diego, CA, USA) and suspended in nuclease-free water. For all experiments, the final concentrations of primers were 1.6 µM FIP/BIP, 0.2 µM FOP/BOP,

and 0.4 µM LoopF/LoopB. Primer sequences are listed in Supplementary Materials and Methods.

LAMP experiments using *Bst* 2.0 were amplified at 68 °C in nuclease-free water, with final concentrations of: 1x IsoAmp I Buffer, 7mM total $MgSO_4$ (5 mM additional), 1.4 mM each dNTP, 1.25 uM ROX Reference Dye, 1 mg/mL BSA, 320 U/mL *Bst* 2.0, 1x Ambion RNase Cocktail, and 2 uM SYTO 9.

LAMP experiments using *Bst* 3.0 were amplified at 69 °C in nuclease-free water, with final concentrations of: 1x IsoAmp II Buffer, 8mM total $MgSO_4$ (6 mM additional), 1.4 mM each dNTP, 1.25 uM ROX Reference Dye, 1 mg/mL BSA, 320 U/mL *Bst* 2.0, 1x Ambion RNase Cocktail, and 2 uM SYTO 9.

For both enzymes, after 90 min of amplification, reactions were ramped to 95°C at maximum output and held for 30 sec to inactivate the enzymes. Chips were cooling to 55°C and the melt performed at a ramp rate of 1 °C per image from 55–90 °C, and a ramp rate of 0.5 °C per image from 90–95 °C.

*Extraction of spiked* Chlamydia trachomatis *(CT) from a relevant clinical matrix*

A frozen stock of live CT (D-UW3, Z054, Zeptometrix, Buffalo, NY, USA) was re-suspended in pre-warmed (37 °C) SPG buffer (219 mM sucrose, 3.7 mM KH2PO4, 8.5 mM NA2HPO4, and 4.9 mM L-glutamate) to 1E8 IFU/mL. It was then diluted 10-fold into a freshly donated urine sample to $1x10^7$ IFU/mL. Urine from a healthy human donor (>18 years of age) was acquired and used in accordance with approved Caltech Institutional Review Board (IRB) protocol 15-0566. Written informed consent was obtained from all participants, donations were never tied to personal identifiers, and all research was performed in accordance with relevant institutional biosafety regulations. A 250 µL aliquot from this CT-spiked urine sample was then extracted following the ZR Viral DNA/RNA Kit protocol (#D7020, Zymo Research, Irvine, CA, USA). Briefly, 250 µL of CT-spiked urine was mixed

with 250 µL DNA/RNA shield and 1000 µL DNA/RNA Viral Buffer. 1500 µL (750 µL x 2) was added to the column and centrifuged at 16,000 xg for 1 min. Then, 500 µL Viral Wash buffer was added to the column and centrifuged at 16,000 xg for 2 min. Lastly, 60 µL DNAse/RNAse-free water was added directly to the column and centrifuged at 16,000 xg for 30 s. The eluent was treated by adding 2.5 µL Ambion RNAse Cocktail (#AM2286, Thermo Fisher Scientific) to 47.5 µL template. Stocks were prepared in 0.5x TE buffer and dilutions quantified using the QX200 droplet digital PCR system (Bio-Rad Laboratories, Hercules, CA, USA), outer primers at 500 nM each, and 1x EvaGreen Supermix (Bio-Rad).

*Fabrication of thermoelectric unit and mount*

A Thermoelectric Module (VT-127-1.4-1.5-72), Thermister (MP-3022), Controller (TC-720), and 12V Power Supply (PS-12-8.4; TE Tech, Traverse City, MI, USA) were wired according to the manufacturer's instructions.

While the Peltier can be used out of the box, we manufactured a heat plate and sink to improve the efficiency in the cooling mode. Instructions for fabrication can be found in the Supplementary Materials and Methods, "Fabrication of thermoelectric unit mount." The ability of the embedded thermocouple to accurately assess temperature of the aluminum block was verified with an independent K-type mini-thermcouple read through a General IRT659K [IR] Thermometer.

*Shearing of genomic DNA*

Human genomic DNA from buffy coat leukocytes (Roche (via Sigma Aldrich), Reference 11691112001) was fragmented using a Covaris Focused Ultrasonicator M220 (Woburn, MA, USA) equipped with 130 µL microTUBE AFA Fiber Snap-Cap at 50W peak power, 5% duty factor, 200 cycles per burst, for 80 sec. Fragment concentration was determined

using a Qbit 3 Fluorimiter (Thermo Fisher, Ref # Q33216) with dsDNA HS assay kit (ThermoFisher, Ref #Q32851), and mean fragment size determined as 365 bp using an Agilent 4200 TapeStation (#G2991AA, Agilent, Santa Clara, CA, USA) and High Sensitivity D5000 ScreenTape (#5067-5592) with ladder (#5190-7747), and D100 ScreenTape (#5067-5584) with High Sensitivity D1000 Reagents (#5067-5585). Dilutions were prepared with a final concentration of 0.5x TE buffer.

*Microfluidic chips*

Microfluidic chips for dLAMP (#A26316; Applied Biosystems, Foster City, CA, USA) were loaded as we have described previously (23) at a concentration where ~40% of partitions would fluoresce (corresponding to the Poisson maximum single template per partition loading of 660 cp/µL). We estimated the volume of each partition to be 750 pL. To achieve this concentration of template molecules, we diluted template stocks from storage in 0.5x TE to ~0.03x TE for all experiments. Genomic DNA (gDNA) stocks, also stored in 0.5x TE, were diluted to a final concentration of 0.077x. Thus, the total final concentration of TE for all experiments of was approximately 0.1081x TE buffer.

*Microscopy data collection*

Data were collected in 30-sec intervals using a DMI-6000B microscope (Leica, Buffalo Grove, IL, USA) equipped with a 1.25x 0.04NA HCX PL FLUOTAR Objective and 0.55x coupler (Leica C-mount 11541544). The response from SYTO 9 was recorded using a 1.5-sec exposure through an L5 (GFP) Nomarski prism, while the ROX Reference Dye was collected using a 1-sec exposure through a Texas Red prism. Images were collected using a Hamamatsu ORCA-ER CCD camera (Hamamatsu Photonics K.K., Hamamatsu City, Japan) at 100 gain. Temperature was recoded using the built-in features of the TC-720 Controller in approximately one second intervals and correlated to the images via image metadata.

In these experiments, we chose to use a microscope, instead of the custom real-time amplification instrument we used previously (23,24), because the microscope has superior optical properties (greater pixels per partition and lower exposure time requirements) to access higher temporal resolution and enhanced kinetic measurements.

*MATLAB script processing*

The MATLAB script processes a .txt file with temperature-time data generated from the TE Tech Controller and a TIF stack containing 2-channel images of the LAMP and melt curve from the LEICA microscope. Partitions are identified using a custom iterative thresholding algorithm, and labels are propagated throughout the TIF stack using a custom labeling algorithm. Average well intensity is tracked over time to generate LAMP curves and plotted against temperature to generate the melt curves. Complete details of the script are in the Supplementary Materials and Methods, "MATLAB script."

Bulk LAMP reactions were conducted in 10 µL volumes within a well plate on a CFX96 Real-time Thermocycler (Bio-Rad) at buffer conditions and temperatures matching the dLAMP reactions.

Enzymatic digestions of bulk LAMP products were conducted using CAC8I (Ref #R0579S), Hpy166II (Ref #R0616S), ACCI (Ref #R0161S), AciI (Ref #SR0551S), MseI (Ref #R0525S), and HpyCH4III (Ref #R0618S) purchased from New England Biolabs and were conducted in 50 µl reaction volumes containing 1 µL enzyme, 1 µg DNA, in 1 x Cut Smart Buffer, and incubated for 1 h at 37 °C. Samples were inactivated for 1 h at 80 °C and diluted to 1 ng/µL (~1:300) to run on an Agilent 4200 TapeStation using High Sensitivity D5000 ScreenTape (#5067-5592) with ladder (#5190-7747), and D100 ScreenTape (#5067-5584) with High Sensitivity D1000 Reagents (#5067-5585).

*Library preparation and sequencing*

300-500 ng of amplified DNA products were fragmented to the average size of 200 bp with Qsonica Q800R sonicator (power: 20%; pulse: 15 sec on/15 sec off; sonication time: 12 min), and libraries were constructed using NEBNext Ultra™ II DNA Library Prep Kit (NEB, #E7645) following manufacturer's instructions. Briefly, fragmented DNA was end-repaired, dA tailed, and ligated to NEBNext hairpin adaptors (NEB, #E7335). After ligation, adapters were converted to the "Y" shape by treating with USER enzyme and DNA fragments were size selected using Agencourt AMPure XP beads (Beckman Coulter, Ref #A63880) to generate fragment sizes between 250 and 350 bp. Adaptor-ligated DNA was PCR amplified with 5 cycles followed by AMPure XP bead clean up. Libraries were quantified with Qubit dsDNA HS Kit (ThermoFisher Scientific, #Q32854), and the size distribution was confirmed with High Sensitivity DNA Kit for Bioanalyzer (Agilent Technologies, #5067). Libraries were sequenced on Illumina HiSeq2500 in single-read mode with the read length of 50 nt to the sequencing depth of 10 million reads per sample, following manufacturer's instructions. Base calls were performed with RTA 1.18.64 followed by conversion to FASTQ with bcl2fastq 1.8.4.

*Sequencing analysis*

Raw FASTQ files were first analyzed with FastQC v0.11.8. Overrepresented sequences were compared with input primer sequences to find reads consisting of potential products from the LAMP reactions. To verify that all adjoining products were accounted for, the FASTQ files were aligned to the predicted products using Bowtie2 v2.3.4.3 with global very-sensitive settings. Unaligned reads were checked for any remaining possible amplification products. All regions consisting of sequences from multiple primers were tallied by counting the reads with a substring of n=11 from the end of each primer. One adjoining region between primers contained a random insertion of nucleotides and was analyzed by first extracting all reads

containing the primer before and after the random nucleotides. The length and sequence distribution of random inserts was then analyzed from the extracted reads.

## Results and Discussion

*Bulk LAMP studies reveal nonspecific products with high melting temperature (Tm)*

We first wished to test whether melting temperature (Tm) could be used to separate specific and nonspecific amplification in a LAMP assay run in bulk. To start, we selected a concentration near the LOD where we might observe both specific and nonspecific amplification. We used extracted CT genomic DNA in the presence of two commercially available polymerases, *Bst* 2.0 and *Bst* 3.0, with CT 23S as the amplification target. At target molecule concentrations of 10 copies per µL (cp/µL), amplification using *Bst* 2.0 polymerase began between 10-11 min (**Figure 7.1A**) and had uniform Tm (**Figure 7.1B**). Amplification using *Bst* 3.0 polymerase (**Figure 7.1C**), also yielded amplification from 10-11 min; however, we also observed a nonspecific amplification at 15 min, defined as having a different Tm than the specific amplification events (**Figure 7.1D**). This indicated *Bst* 3.0 could be a useful model for studying nonspecific amplification. We observed that early amplifying products corresponded to specific amplification events, and the later products corresponded to nonspecific amplification, supporting our prediction that we could use Tm as a proxy for sequence identity, as is common with PCR, and has been used previously in LAMP (25-29).

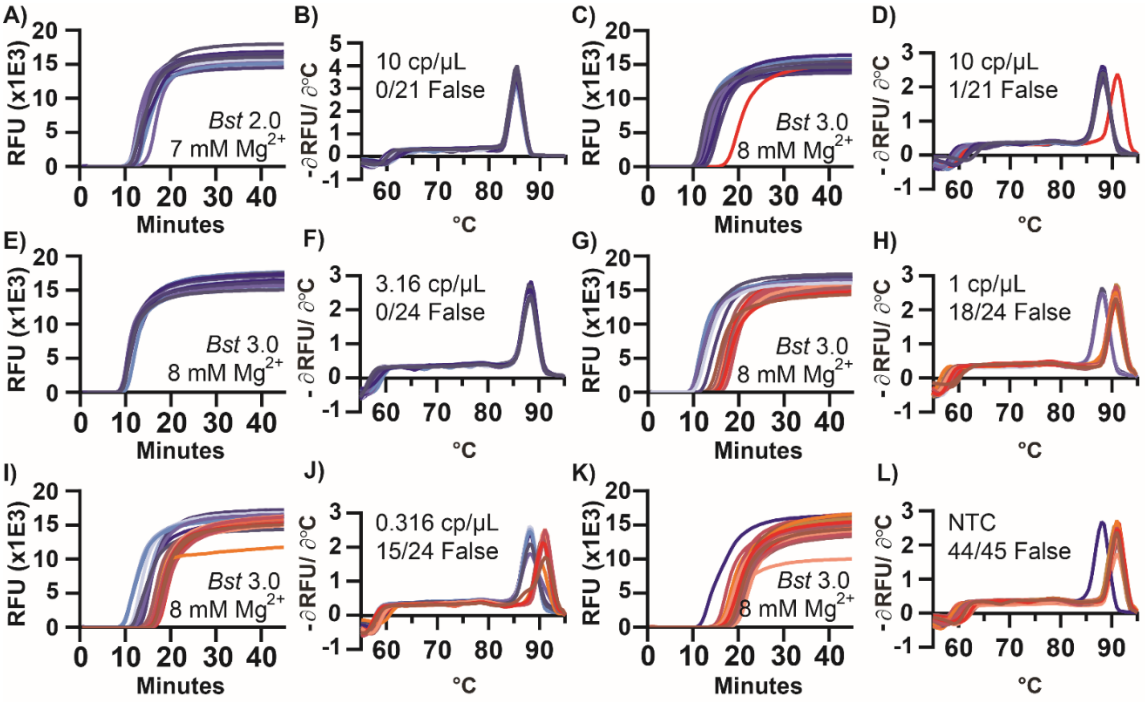


**Figure 7.1: Amplification and melting temperature (Tm) curves of *Chlamydia trachomatis* in a bulk reaction show nonspecific amplification products with high Tm.**

Plots of fluorescence as a function of time during a LAMP reaction (A,C,E,G,I,K) and the derivative plot of fluorescence as a function of temperature for the corresponding melting curves (B,D,F,H,I,J). Reactions using *Bst* 2.0 at 10 copies per microliter (cp/µL) (A,B), and using *Bst 3.0* at 10 cp/µL (C,D), 3.16 cp/µL (E,F), 1 cp/µL (G,H), 0.316 cp/µL (I,J), and without template (K,L). Reactions of specific amplification are different shades of blue; nonspecific amplification is different shades of red. The number of false-positive reactions is reported within each panel as $N/N_{reaction}$ False. $N_{Total}$ for all conditions = 159 reactions.

Using *Bst* 3.0 at low concentrations of target is a useful system to study nonspecific amplification. To investigate the role of the concentration of the target on the incidence of nonspecific amplification, we performed half-log dilutions of template from 10 to 0.316

cp/µL. At 3.16 cp/µL (**Figure 7.1E-F**), only specific amplification occurred (24 replicate wells/plate). However, once template concentrations reached 1 cp/µL (**Figure 7.1G-H**), nonspecific amplification occurred with greater frequency than specific amplification (18 of the 24 replicates generated false positives). Similarly, for 0.316 cp/µL (**Figure 7.1I-J**) 15 of the 24 replicates generated false positives. We next ran the same assay in the absence of template (no-template control, NTC) (**Figure 7.1K-L**). Even though we did not expect amplification, we observed all reactions amplified. 44 of 45 replicates amplified at a Tm of 91 °C, consistent with the Tm of nonspecific amplification in the presence of template. Although it is possible for a reaction to generate multiple different nonspecific amplification products, even ones with Tm matching to the specific products, the single amplicon observed at 88 °C in the NTC was a contaminant that appeared to have the same sequence as the specific products (**Figure 7.2A [well F8]**). In general, when the specific target was present, it amplified sooner and outcompeted the nonspecific amplification, thereby reducing the number of observations of nonspecific amplification. To determine if the nonspecific amplification was inherent to the polymerase or a consequence of buffer selection, we conducted additional studies using both Bst polymerases (**Supplementary Figure 7.11 and Table 7-1**).

To better understand nonspecific amplification in LAMP, we investigated the sequence identity of the nonspecific products with high Tm using sequencing and gel analysis and compared them with the specific products. The Tm of specific amplification differed between the two polymerases tested. Specific amplification for *Bst* 2.0 had a Tm of 85.5 °C, whereas specific amplification using *Bst* 3.0 had a Tm of 88 °C, and demonstrated nonspecific amplification at Tm of 91 °C. The nonspecific amplification had identical Tm to amplification in absence of template (**Figure 7.1K,L**). Despite the specific amplification products of *Bst* 2.0 and *Bst* 3.0 producing similar gel banding patterns (**Figure 7.3**) and the same sequencing results (see **Figure 7.2B**), they had different Tm (**Figure 7.1B,D** respectively). We determined the difference in Tm was due to differences in buffer conditions (**Supplementary Figure 7.11 and Table 7-1**).

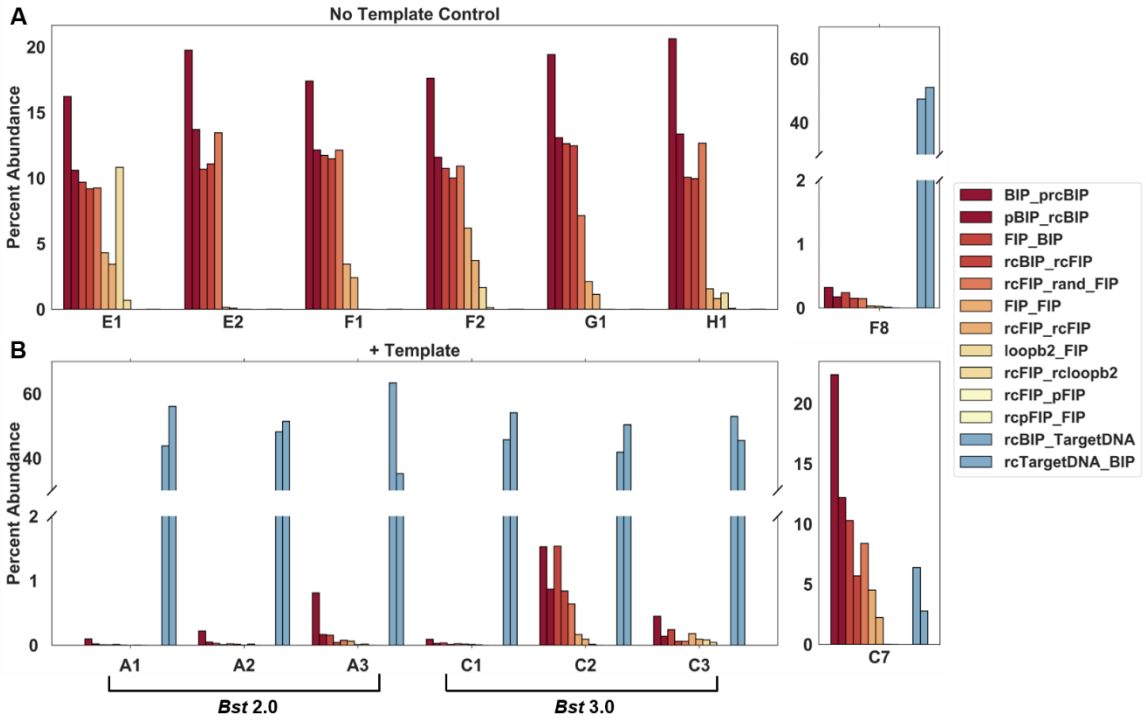


**Figure 7.2: Quantification of junctions using next-generation sequencing of select *Chlamydia trachomatis* amplification products from bulk reactions.**

Nonspecific amplification from the no-template control using *Bst* 3.0 (A), including amplification of a specific target contamination (well F8) corresponding to **Figure 7.1**K,L. Amplification in the presence of 10 cp/µL template (B), using *Bst* 2.0 (wells A1-A3) corresponding to **Figure 7.1A,B**, and *Bst* 3.0 (wells C1-C3) corresponding to **Figure 7.1C,D**. Nonspecific amplification in the presence of 10 cp/µL template and *Bst* 3.0 (well C7) corresponding to **Figure 7.1C,D**. For a complete list of abbreviations used in this figure, see Supplementary **Table 7-2**.

In all bulk reactions, we observed nonspecific products with high Tm. This was surprising because in PCR, primer dimers have low Tm; moreover, in previous demonstrations of LAMP, Tm was lower for nonspecific compared with specific products (27). Thus, we

investigated the sequence identity of the nonspecific product with high Tm. We ran the LAMP products on a gel and observed that the characteristic pattern of the specific amplification products differed substantially from the banding pattern seen in the high-Tm nonspecific products (**Figure 7.3**). Interestingly, the high-Tm nonspecific product had a ladder pattern resembling that of specific LAMP products.

To determine the identity of the high-Tm nonspecific products, we performed next generation sequencing (NGS). We observed that the nonspecific products lacked the corresponding target sequence and identified the product as a mixture of full-length FIP, BIP, and their complements, as well as fragments of BIP (**Figure 7.2A**).

To confirm the sequence identity of the amplicon, we targeted the FIP and BIP regions using several restriction endonucleases. Digestion of the specific and nonspecific products resulted in different banding patterns than the undigested samples, and was consistent with the presence of both FIP and BIP endonuclease recognition sites within the sequence (**Supplementary Figure 7.12**). Specific amplification products were 47% GC; nonspecific amplification products were 53% GC.

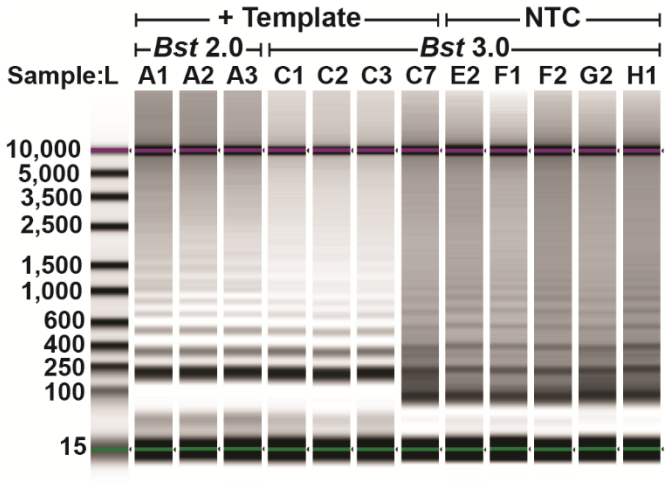


**Figure 7.3: Composite image of select *Chlamydia trachomatis* amplification products from a bulk reaction.**

Products were collected using D5000 tape on Agilent TapeStation. Amplification in the presence of 10 cp/µL template using *Bst* 2.0 (lanes A1-A3) corresponding to **Figure 7.1A,B**, and *Bst* 3.0 (lanes C1-C3, C7) corresponding to **Figure 7.1C,D**. Nonspecific amplification in the no-template control (NTC; lanes E2-H1) corresponds to **Figure 7.1K,L**. Contrast was determined using the automatic "scale to sample" feature in the Agilent TapeStation analysis software.

*A proposed mechanism for formation of nonspecific product*

We hypothesize a mechanism for the formation of the nonspecific product with high Tm originating as a consequence of interactions of the *Bst* polymerase and LAMP inner primers. Other potential mechanisms include LIMA (30) and UIMA (31), but are inconsistent with our sequencing results, which observe nearly equal reads of the forward and reverse strand as measured by counting the complementary sequences between each junction. Our proposed mechanism requires properties that have been observed with *Bst* enzymes: a strand-displacing polymerase lacking 3'-5' exonuclease activity—common to polymerases from thermophilic bacteria (32,33), template switching ability to allow synthesis across a

discontinuous template (33), terminal transferase activity, or the ability to perform non-templated synthesis (32,34,35). Briefly, the nonspecific product likely arises from extension of a low probability homo-dimerization of the Backward Inner Primer (BIP), followed by elongation across a discontinuous junction ("template switching") to form a double-stranded product incorporating Forward Inner Primer (FIP). Through breathing of the molecule, the 3' of one strand may form a second hairpin and amplify. Some of these amplification events incorporate several random nucleotides via terminal nucleotidyl transferase activity resulting in a pool of hairpins with 3' randomers. Sequences with complementary randomers are selected *in vitro* to amplify. The double-stranded product of this amplification can, through intramolecular hydrogen bonding, form two dumbbell-like structures and amplify in a fashion similar to the standard LAMP mechanism, but primed by BIP. Repetitive cycles of self-priming and hairpin priming by BIP result in numerous sequences with complementarity and the possibility of multiple replication loci within a single molecule. This process can give rise to very long amplicons, and even a branched, mesh-like network from the multimeric sequences annealing to their neighbors or in a self-complementary fashion. A simplified version of this mechanism, annotated with sequencing data, can be found in **Supplementary Figure 7.13**.

In more detail, a potential mechanism of formation of nonspecific products is as follows: Initially, a double-stranded amplicon is generated by homo-dimerization of BIP, and 3' extension of the homodimer to produce a partial reverse complement of BIP (prcBIP) (**Figure 7.4-1**). *Bst* polymerase is highly prone to mismatched extension (36), and the two base pairs of CG provide a sufficient anchoring in the 3' to start elongation. Multiple Primer Analyzer (ThermoFisher) does not identify the BIP homodimer, unless maximum sensitivity is used. Alternatively, BIP-prcBIP product may arise from a single stranded BIP-hairpin, as has been observed by others (37), although UNAfold (IDT) does not predict the formation of the hairpin for this primer. These structures may not need to be abundant at equilibrium, but as long as they are extended by the polymerase, the product will be stabilized and will accumulate.

Upon accumulation of the BIP-prcBIP construct, the reverse complement of FIP (rcFIP) is incorporated by template switching (**Figure 7.4-2**). The 3' of FIP is within spatial proximity of the homo-BIP sequence due to microhomology of to 5' end of the double-stranded sequence coupled with rapid breathing of two base pairs of TA. This allows temporary insertion and hybridization of FIP with the double-stranded BIP-prcBIP sequence (**Figure 7.4-3**). When the polymerase is also in proximity of this reaction, FIP slips out of the junction, and the polymerase elongates across the 3' discontinuous junction (33,35) templated by FIP (**Figure 7.4-4**). We confirmed the interaction of FIP and BIP produced the high-Tm nonspecific amplification, and that elimination of 3' microhomology could significantly reduce high-Tm nonspecific amplification (**Supplementary Figure 7.14-16, Table 7-3, Table 7-4**). After elongation, the FIP which has served as template, is poised to prime in the opposite direction (**Figure 7.4-5**). This either displaces the initial BIP mispairing (BIP*) or opens the hairpin, resulting in a double-stranded BIP-prcBIP-FIP product (**Figure 7.4-6**). This three-part junction is observed as a complete product in NGS data. Breathing of double-stranded BIP-prcBIP-FIP is prone to formation of an intramolecular self-priming hairpin of rcBIP-pBIP (**Figure 7.4-7**). Elongation of the 3' hairpin results in a double-stranded FIP-pBIP-rcBIP-rcFIP hairpin (**Figure 7.4-8**) and displacement of a BIP-prcBIP-rcFIP hairpin (**Figure 7.4-9**), which may be primed by FIP to restart this cycle (**Figure 7.4-10**). With each amplification, and re-prime by FIP, a single product is generated. This process of hairpin accumulation would cause the linear "rinsing" baseline observed by other researchers (37).

Within this pool of linear amplifying products, the *Bst* enzyme will randomly incorporate additional nucleotides at the 3' end of FIP-pBIP-rcBIP-rcFIP via terminal transferase activity (**Figure 7.4-11**). Our sequencing methods are unable to observe a FIP-randomer hairpin because adapter ligation requires double-stranded products. This pool of hairpins with random sequences will accumulate until LAMP selects for sequences that amplify by sharing complementary 3' "toe holds" (**Figure 7.4-12**). Much like *in vitro* evolution, those sequences with the highest probability of amplification are selected (32). The lack of a thermal gating mechanism in LAMP and lack of 3'–5' exonuclease activity makes the amplification reaction

especially prone to *in vitro* evolution of self-amplifying products. When considered in this light, it is unsurprising that nonspecific amplification could arise from mechanisms similar to the specific products. Within a given bulk reaction, variation in randomer sequence length and identity was low. However, between different samples, randomer sequences of multiple lengths and identities were observed. These two results further suggest that in bulk reactions amplification occurs from one or a few sequences (**Supplementary Table 7-5, Table 7-6, Table 7-7**).

Elongation from the randomer overhang results in a double-stranded products, leading to dumbbell structures, and LAMP-like amplification. First, elongation of hairpins with complementary randomer toe holds produces a dimer of FIP-BIP-prcBIP-rcFIP coupled through the randomer (**Figure 7.4-13**). Breathing of the molecule can result in formation of intramolecular hairpins, and eventual disassociation into two separate self-priming, dumbbell shaped hairpins (**Figure 7.4-15 and -16**). The products of elongation from self-priming amplification doubles the amount of dsDNA present and forms sequences with internal hairpins capable of priming by BIP (**Figure 7.4-17**). Elongation from BIP priming creates a new double-stranded product and reveals a self-priming 3' hairpin of the original strand (**Figure 7.4-18**), which upon elongation, displaces the sequence primed by BIP (**Figure 7.4-19**) while transforming the trimer of FIP-BIP-prcBIP-rcFIP to a pentamer (more than tripling the amount of ds products from structures 15 and 16). The pentamer still contains an rcBIP hairpin, and may amplify in a functionally similar method as previously (**Figure 7.4-17**). The displaced product **Figure 7.4-19** is similar to **Figure 7.4-16** but missing 5'-FIP. However, much as with **Figure 7.4-16**, this products is self-priming and produces a structure with an internal rcBIP hairpin (**Figure 7.4-20**). A second priming of the hairpin by BIP of the rcBIP-pBIP hairpin and subsequent elongation, creates a new double-stranded product and reveals a self-priming 3' hairpin of the original strand (**Figure 7.4-21**). As previously, upon elongation, the sequence primed by BIP is displaced (**Figure 7.4-22**). Simultaneously, the self-priming event turns the FIP-BIP-prcBIP trimer to a pentamer, which may continue to be amplified by BIP. The released sequence (**Figure 7.4-22**) is again self-priming, and its product is equivalent to **Figure 7.4-20** to restarts the cycle. Further, amplified hairpins may,

in addition to BIP priming of the hairpin, duplicate through self-priming by breathing and formation of a 3' rcBIP-pBIP hairpin (**Figure 7.4-23**).

The products of these reactions are capable of forming a branched, mesh-like network resulting in the observed high temperature melting. Products may experience random internal priming by through hairpin formation (e.g. **Figure 7.4-13,-17,-20**), or 3' self-priming (**Figure 7.4-23**). Consequently, multiple replication loci may exist within a single strand, and products may have internal stem loop structures (**Figure 7.4-24**). Furthermore, in addition to intramolecular bonding, the highly repetitive nature of these products allows for melting of fragment, which reanneals to self in a different conformation, or a neighboring strand.

Though the initial steps of generating a double-stranded hairpin will be unique to our particular primer set, once a seed is generated, the processes of template switching and terminal transferase activity should be a general phenomenon associated with nonspecific amplification of thermophilic polymerase resulting in exponential amplification. As evidenced, when the mechanism of seed formation is disrupted through elimination of the microhomology, amplicons with high Tm still occur, albeit with lower frequency and delayed occurrence (**Supplementary Figure 7.14-16, Table 7-3, Table 7-4**). Template switching and non-template synthesis are 100x slower than template extension (33). However, once the self-amplifying products are selected, the reaction follows standard exponential LAMP enrichment. Thus, accumulation of a sufficient pool of randomers may take time, but still result in a delayed bulk exponential amplification event. Furthermore, should a hairpin with attached randomer form, it is possible that the rising baseline, attributed to hairpin formation (37), may also be *in vitro* selection of the products, leading to and resulting in spontaneous exponential amplification.

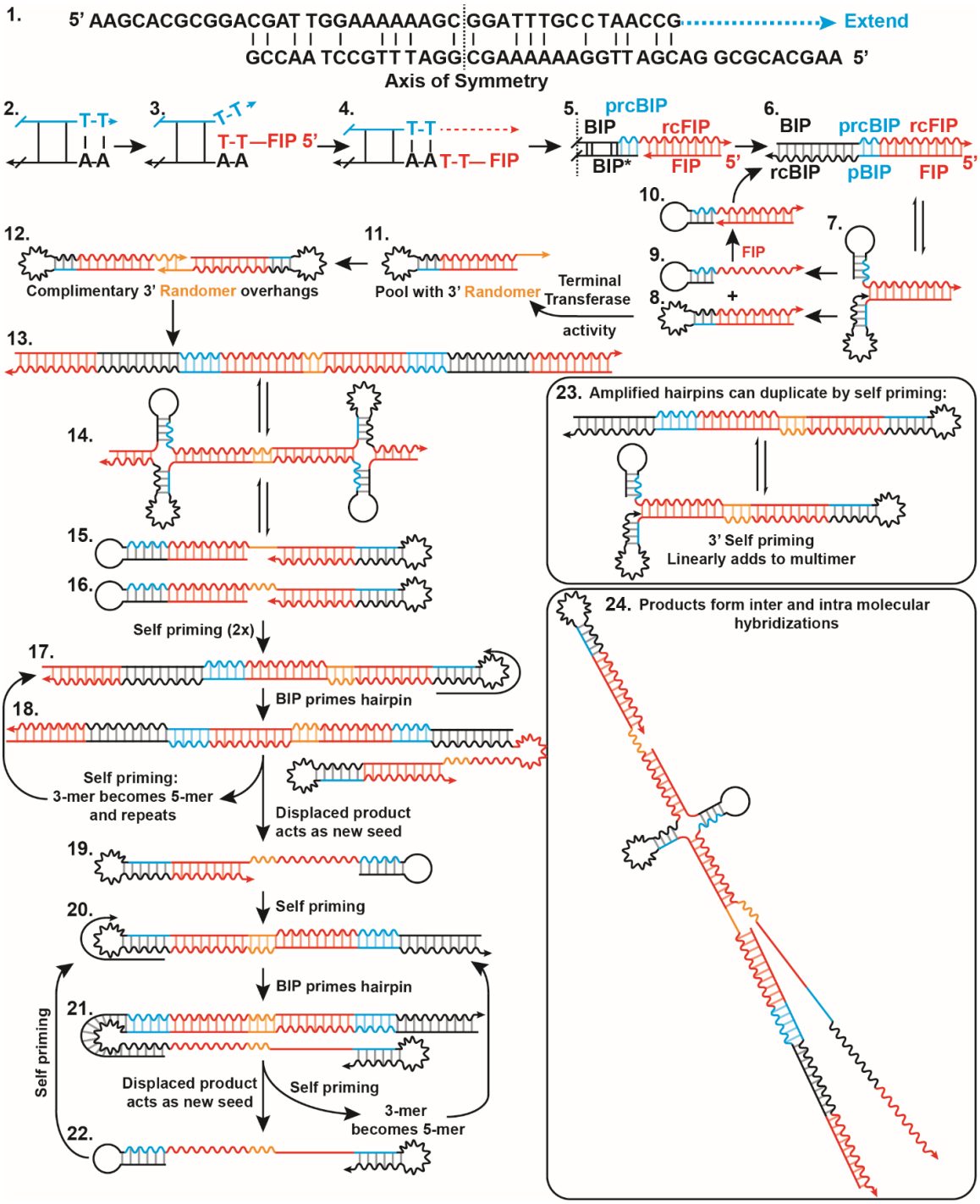


**Figure 7.4: Illustration of a mechanism for formation of nonspecific amplification products in LAMP reactions.**

Putative structures and intermediates are labeled with numbers. Forward sequences are illustrated as a straight line, and the reverse compliment as a wavy line of matching color. Abbreviations used in this figure: BIP, Backward Inner Primer; rcBIP, Reverse compliment of BIP; FIP, Forward Inner Primer; rc FIP, Reverse Compliment of FIP; prcFIP, Partial Reverse Compliment of FIP.

*Melting temperature differentiates specific and nonspecific reactions in dLAMP*

To study specific and nonspecific amplification events at the digital single-molecule level, we developed a new approach that enabled HRM analysis (obtaining "melt curves") to be performed on each partition. We used a commercially available microfluidic chip with 20,000 partitions and a previously published open-source dLAMP method accessible to most standard laboratories (23) with the following improvements: incorporation of an off-the-shelf thermoelectric unit to both heat and cool the chips, and an enhanced MATLAB script to allow for multicolor tracking. We used the temperature-independent fluorophore ROX to track each partition's location and the dsDNA intercalating fluorophore SYTO 9 to follow amplification and hybridization status. This two-channel approach is required to follow a partition through both amplification and the entirety of the HRM when fluorescence from SYTO 9 is lost.

As an illustration of the capabilities of our approach, we first used real-time dLAMP to study the kinetic parameters of individual reactions, and we used Tm to classify reaction outcome (**Figure 7.5**). Using real-time dLAMP, we followed individual partitions as they amplified as a function of time (**Figure 7.5A**) and then by temperature as they went through HRM (**Figure 7.5B**). Real-time imaging of individual partitions enables us to reconstruct the standard amplification curves of intensity for each partition as a function of time (**Figure 7.5C**), and plotting the fluorescence intensity as a function of temperature yields an HRM trace (**Figure 7.5D**); the negative derivative plot (**Figure 7.5E**) of this melt trace is the standard melt curve. Analogous to bulk measurements, the standard melt curve is used to

classify reactions as specific or nonspecific. We used these classifications to identify important patterns in the kinetics of each type of amplification (**Figure 7.5F-H**).

We next used real-time dLAMP with HRM to determine whether differences in time to positive (TTP) were due to a difference in amplification initiation or in rate. We expect this information would be valuable for elucidating whether the molecules that lead to bulk amplification are the ones that are first to initiate or the ones that initiate with the fastest rates. We found that TTP can be heterogeneous while Tm is constant (28.6±8.9 min with 87.5±0.2 °C), indicating that the same product may initiate at different times (**Figure 7.5F**). This is consistent with our knowledge of the stochastic initiation of LAMP (23,38,39). Further, we observed some variability in the maximum rate despite similar Tm (23.7±6.8 RFU/30 sec, with 87.5±0.2 °C Tm), which indicates the same product may amplify at different velocities. (**Figure 7.5G**). In general, we observed that maximum rate often corresponds to the point when the reaction first began to amplify. Finally, by plotting rate as a function of TTP (**Figure 7.5H**), we observed little fluctuation in rate across a range of different TTPs (23.7±6.8 RFU/30 sec with 28.6±8.9 min), indicating that the differences in TTP are mostly delays in the initiation of amplification rather than differences in the rate of amplification.

The use of real-time data revealed heterogeneity in the timing of amplification initiation and the amplification rate, but homogeneity in Tm, indicating stochasticity in initiation of amplification. In some cases, outlier data points for rate occurred. To determine whether removing these outliers impacted the distribution of enzymatic rates, we performed a non-parametric test (**Supplementary Figure 7.17**) and found no significant differences in enzymatic rates when these outliers were excluded.

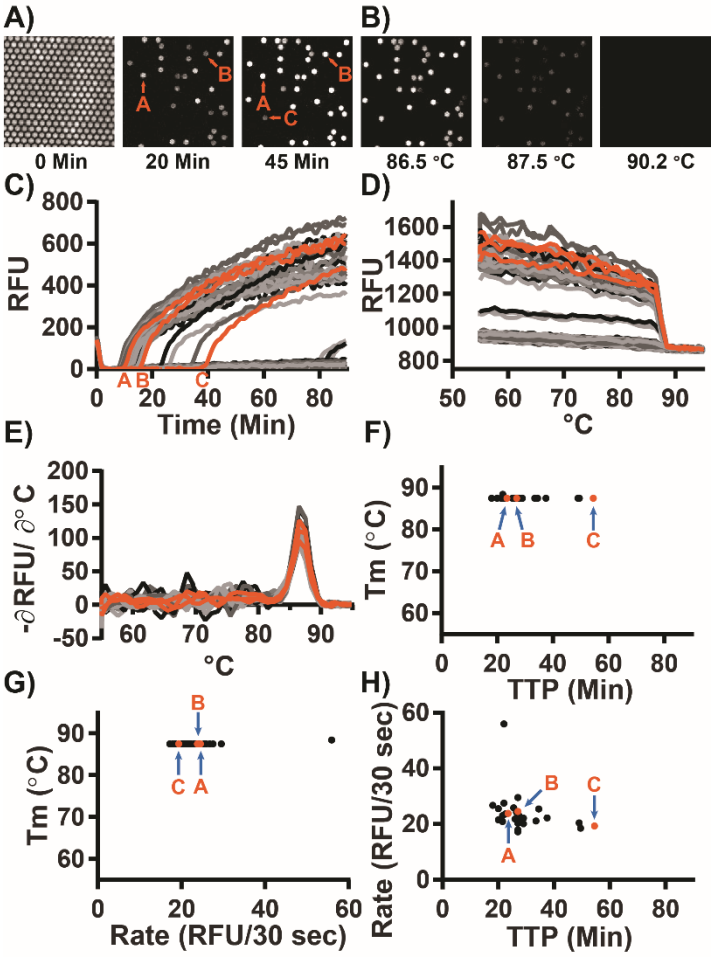


**Figure 7.5: Specific amplification in digital single-molecule experiments using *Bst* 2.0. (A) Fluorescence micrographs of individual partitions are traced over time.**

For simplicity, we illustrate a subset of 250 of 20,000 possible partitions at three time points (0, 20, and 45 min). Of the 250 partitions in this micrograph, 30 partitions amplified. Partitions A and B are visible at 20 min; partition C becomes visible at 45 min. (B) Fluorescence micrographs of individual partitions are traced across temperatures during an HRM experiment. As the double-stranded DNA in each partition de-hybridizes, the intercalating dye is released and fluorescence decreases. (C) Plotting the fluorescence intensity as function of time generates the standard amplification traces of individual partitions generated during a 90-min LAMP

experiment. Orange curves correspond to partitions A–C from panel A. (D) Traces of fluorescence intensity as a function of temperature for individual partitions during melting experiments. By quantifying real-time intensity of individual partitions as temperature increases, melting traces are obtained. Temperature resolution is 1 °C from 55–90 °C, and 0.5 °C from 90–95 °C. (E) The derivative plot of panel d generates the standard melting curve. The temperature at which the derivative maximum occurs corresponds to the "melting point" of the LAMP products in the individual partition. (F) The time each partition reached a fluorescence intensity of 250 RFU (TTP) as a function of temperature. (G) Maximum rate as a function of Tm for each partition. (H) TTP as a function of maximum rate for each partition.

We next asked whether we could observe in dLAMP the same pattern of high-Tm nonspecific amplification and low-Tm specific amplification that we observed in bulk. We performed dLAMP using three chips containing template, and three chips lacking template (NTC), and observed ~55,000 partitions for each condition. Although 60,000 partitions are possible, not all partitions filled nor can all partitions be tracked for the full duration of an experiment. For the melt curve, fluorescence readings were taken at 1 °C increments from 55-90 °C; and at 0.5 °C increments from 90–95 °C to give higher resolution. Due to slight differences in the timing between the heating element and the image collection, some chips were observed at slightly different temperatures (<0.5 °C).

Our approach enabled us to differentiate specific and nonspecific amplification events using HRM. When using the polymerase *Bst* 2.0 and template (**Figure 7.6A**, blue points), we observed a large band of amplification in the temperature range 88.5–90.3 °C, in agreement with the Tm observed when performing the reaction in bulk (**Figure 7.1**). In contrast, the NTC (**Figure 7.6A**, red points) had very few amplification events in that temperature range (68 out of 51,279 partitions). Hence, we defined events that occurred in the Tm range 88.5–90.3°C as true positives (specific amplification events), and we defined those that occurred

outside this range (in both the NTC and in the presence of template) as false positives (nonspecific amplification events). When using the polymerase *Bst* 3.0, we observed a large band of amplification from 91.25–92.75 °C in the presence of template (**Figure 7.6B**, blue points) that did not correspond with amplification in the NTC (**Figure 7.6B**, red points), so we defined these as specific amplification events. As with bulk measurements, we determined the difference in Tm between specific amplification events between *Bst* 2.0 and *Bst* 3.0 was due to the difference in buffer composition (**Supplementary Figure 7.11, Table 7-1**).

During these experiments, we observed two common patterns. First, the Tm for specific amplification events was 3–5 °C lower in digital compared with bulk measurements. We attribute this difference to temperature calibration; the thermocycler is calibrated to the liquid temperature, whereas the thermoelectric element measures the temperature of the heating element. Second, false positives in the NTC had predominantly high Tm, which we attribute to the nonspecific product we identified in the bulk reactions. We also observed differences in total amplification events between the two polymerases. Assays with *Bst* 3.0 resulted in substantially more nonspecific amplification than those with *Bst* 2.0 and confirmed this was not an issue with buffer selection (**Supplementary Figure 7.11, Table 7-1**). After 90 min, *Bst* 3.0 yielded 15,200 nonspecific events (out of 54,337 observed paritions) in the NTC, whereas *Bst* 2.0 yielded only 74 nonspecific events (out of 51,279) in the NTC. Occasionally, outliers occurred in the NTC and would be misidentified as positives by fluorescence and Tm. For *Bst* 3.0 this occurred in 29 partitions; for *Bst* 2.0, it occurred in only 3 out of ~55,000 partitions.

Next, we tested whether TTP is different for specific and nonspecific amplification. Because LAMP follows a "winner-takes-all" format, frequent and early nonspecific amplification events may dominate bulk amplification. In general, for both *Bst* 2.0 and *Bst* 3.0, specific amplification had earlier TTP than nonspecific amplification, although there was some overlap, mostly >90.5 °C (**Figure 7.6A-B).** We were able to distinguish the clustering of high-Tm nonspecific products separately from specific amplification using a threshold of

88.5–90.3 °C (**Figure 7.6C and Supplementary Figure 7.18A).** We illustrate each partition with only partial opacity so that when false positives in the NTC (red) overlap with false positives in the template-containing sample (blue), the overlap of multiple colors appears purple (**Figure 7.6D)**. Color intensity indicates the abundance of paritions at a given TTP and temperature. To further illustrate how this approach can be used to differentiate specific and nonspecific amplification, we next selected a region where both specific and nonspecific products were observed**.** For *Bst* 3.0, we were able to distinguish the clustering of high-Tm nonspecific products separately from specific amplification using the threshold of 91.25–92.75 °C **(Figure 7.6E)**, and we observed better separation of specific and nonspecific amplification than with *Bst* 2.0 **(Figure 7.6F and Supplementary Figure 7.18B).** Both enzymes had highly variable TTP, which we have observed previously (23), and attribute to stochastic initiation of LAMP. *Bst* 2.0 had both earlier specific amplification and later nonspecific amplification than *Bst* 3.0. *Bst* 2.0 reactions containing template generally started at 10 min, whereas nonspecific amplification began at ~40 min. In contrast, *Bst* 3.0 reactions containing template began at 11.5 min, and nonspecific amplification began at ~20 min.

Next we asked whether there is a difference between the maximum rates of specific and nonspecific amplification. Previously, we demonstrated that rate could be used to correct for some nonspecific amplification using *E. coli* 23S primers (23), so we wished to test whether we could use maximum rate as a way to differentiate specific and nonspecific amplification. Generally, specific and nonspecific amplification reactions did not have the same maximum rate. For *Bst* 2.0, nonspecific amplification tended to have a slower max rate than specific amplification, although there was some overlap **(Figure 7.6G)**. At high Tm, the clustering of nonspecific amplification in both the presence of template and in the NTC were observed at >90.5 °C and below approximatley 50 RFU/30 sec **(Figure 7.6H)**. For *Bst* 3.0, although there was substantial overlap, we again observed that nonspecific amplification tended to have slower maximum rate than specific amplification **(Figure 7.6I)**. Examining the high-Tm amplification events, nonspecific amplification collects above 92.75 °C and has maximum rate extending out to 75 RFU/30 sec **(Figure 7.6J)**. For both enzymes, overlap

between specific and nonspecific amplification was similar, and specific amplification tended to be faster. However, the maximum rate of specific amplification between the two enzymes differed; *Bst* 2.0 had a maxium rate of 150 RFU/30 sec, whereas *Bst* 3.0 did not exceed 100 RFU/30 sec. *Bst* 2.0 performing faster than *Bst* 3.0 is consistent with our previous observations using an *E. Coli* 23S primer set (23). Additionally, the maximum rate of nonspecific amplification in *Bst* 2.0 tended to be lower than nonspecific amplification in *Bst* 3.0 (50 and 75 RFU/30 sec, respectively). Consequently, the extent of overlap of specific and nonspecific amplificaiton was greater for *Bst* 3.0 than *Bst* 2.0.

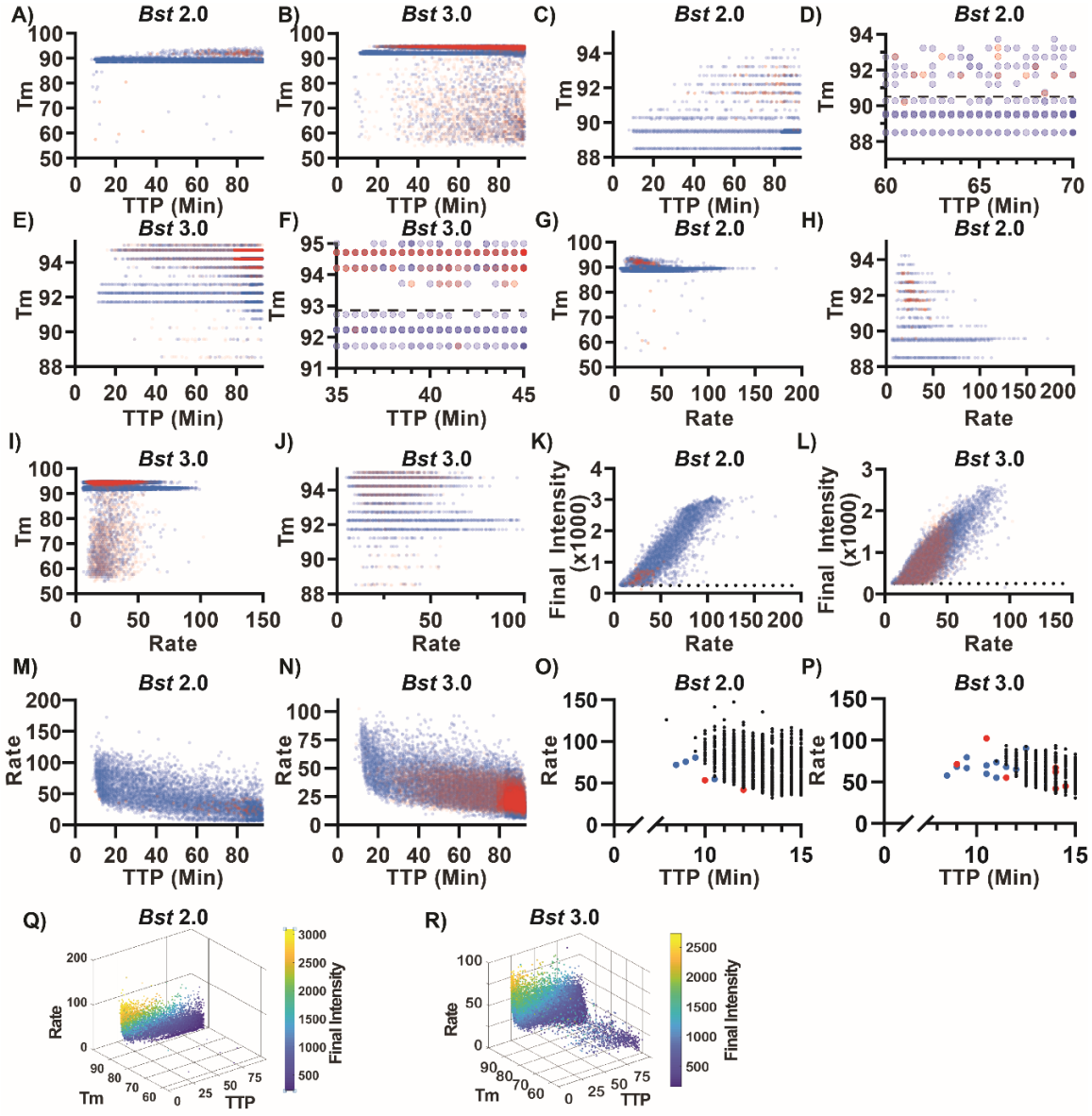


**Figure 7.6: Properties of specific and nonspecific amplification using real-time kinetics and Tm.**

Blue indicates amplification events in the presence of template, red indicates amplification in the absence of template (NTC). Among these amplification events, true positives were identified using Tm (88.5–90.3 °C for *Bst* 2.0 and 91.25–92.75 °C using *Bst* 3.0). Color intensity indicates the abundance of paritions at a given TTP and temperature (partitions in panels A,C,D,G,H,K,M using *Bst* 2.0 are rendered at

20% opacity in the NTC and in the presence of template; panels B,E,F,I,J,L,N using *Bst* 3.0 are rendered at 5% opacity in the NTC and 20% in the presence of template. (A) Tm of individual amplification events as a function of TTP using *Bst* 2.0. (B) Tm of individual amplification events as a function of TTP using *Bst* 3.0. (C) Individual partitions with Tm between 88 and 95°C as a function of TTP using *Bst* 2.0. (D) Individual partitions with Tm between 88 and 95°C and TTP between 60 and 70 min using *Bst* 2.0. Dashed line at 90.3 °C indicates the upper threshold separating specific and nonspecific amplification. (E) Individual partitions with Tm between 91 and 95°C as a function of TTP using *Bst* 3.0. (F) Individual partitions with Tm between 91 and 95°C and TTP between 35 and 45 min using *Bst* 3.0. Dashed line at 92.75 °C indicates the upper threshold separating specific and nonspecific amplification. (G) Tm of individual amplification events as a function of maximum rate using *Bst* 2.0. (H) Tm of individual amplification events between 88 and 95°C as a function of maximum rate using *Bst* 2.0. (I) Tm of individual amplification events as a function of maximum rate using *Bst* 3.0. (J) Tm of individual amplification events between 88 and 95°C as a function of maximum rate using *Bst* 3.0. (K) The final intensity of individual amplification events as a function of maximum rate using *Bst* 2.0. (L) The final intensity of individual amplification events as a function of maximum rate using *Bst* 3.0. (K-L) Partitions with a final intensity less than 250 RFU (dotted line) were excluded from analyses. (M) The maximum rate of individual amplification events as a function of TTP using *Bst* 2 and (N) using *Bst* 3.0. (O) Plot of maximum rate from false-positive amplifications in NTC (red), false positives amplifications in the presence of template (blue) and true-positive amplifications by Tm (black) as a function of TTP using *Bst* 2.0 and (P) using *Bst* 3.0. (Q) 3D plot comparing maximum rate, Tm, TTP, and final intensity of individual partitions using *Bst* 2.0 and (R) using *Bst 3*.0.

We observed an unexpected relationship between the final intensity of each partition and the maximum rate of that partition. After 90 min of amplification, a partition should theoretically

reach a fluorescence maximum whereby all reagents are consumed, amplification plateaus, and thus the final intensity would be independent of the maximum rate of amplification. However, surprisingly, we observed a general scaling between the maximum rate and the final intensity of the partition. For *Bst* 2.0, all amplification in the NTC has final intensity less than 1017 RFU and maximum rate less than 53.4 RFU/30 sec. In the presence of template, 79.7% of nonspecific amplification and 52.3% of specific amplification had final intensity and maximum rate less than these thresholds. For *Bst* 3.0, 87.7% of amplification in the NTC has final intensity less than 1017 RFU and maximum rate less than 53.4 RFU/30 sec. In the presence of template, 89.0% of nonspecific amplification but only 45.6% of specific amplification fell within these thresholds using Bst 3.0. Thus, false positives were generally dimmer and had slower maximum rates than most true-positive events. When examining the brightest partitions, *Bst* 2.0 (**Figure 7.6K**) and *Bst* 3.0 (**Figure 7.6L**) exhibit a similar maximal final intensity near 3000 RFU. These maxima are also surprising, considering our 12-bit camera is capable of imaging up to 4096 RFU (the detector was not at saturation). We suspect that this maxima corresponds to consumption of one of the reagents; while scaling between maximum rate and final intensity occurs when stochastically initiated reactions have not completely amplified, resulting in partitions dimmer than the maxima and proportional to their rate of amplification.

During these dLAMP experiments, we also observed a relationship between maximum rate and TTP. In bulk reactions, the first and fastest amplification event determines the reaction outcome by consuming all of the reagents. Thus, we hypothesized that reaction conditions that promote fast and early amplification in the NTC would lead to a high false-positive rate in bulk and thus misidentification of amplification. In both *Bst* 2.0 (**Figure 7.6M**) and *Bst* 3.0 (**Figure 7.6N**) we observed a general trend of fast amplification events occurring earlier, and slow events occurring later. In *Bst* 2.0, we observed greater heterogeneity in TTP and rate than in *Bst* 3.0. Furthermore, nonspecific amplicons in the NTC tended to produce slower and later amplification events. Occasional outliers occurred at both fast and early times.

Next, to explicitly test whether fast and early events correspond to specific amplification, we analyzed the relationship between a partition's TTP, its maximum rate, and Tm. In the first 12 min of amplification, we observed six nonspecific amplification events in *Bst* 2.0 (four in the presence of template; two in the NTC; **Figure 7.6O**), and we observed 13 nonspecific events in *Bst* 3.0 (10 in the presence of template; three in the NTC; **Figure 7.6P**). For both polymerases, we were able to distinguish the rare, fast, and early nonspecific amplicons from true positives. For *Bst* 2.0, these nonspecific amplifications were slower than the fastest true positives, and occurred at similar times. In contrast, for *Bst* 3.0, the earliest amplification events were false positives and tended to have similar rates to the true positives. We hypothesize that in bulk reactions, the fast and early nonspecific amplification events (as seen in *Bst* 3.0 **Figure 7.6P**) lead to nonspecific measurements, whereas nonspecific amplification that coincides with specific amplification, but proceeds at a slower rate (as seen in *Bst* 2.0 **Figure 7.6O**), would still produce specific amplification in bulk. This hypothesis is corroborated by sequencing of bulk LAMP reactions (**Figure 7.2**). Though individual bulk reactions may be assigned a homogeneous label as "true positive" or "false positive" by Tm, sequencing identifies multiple products within each reaction, and the Tm is determined by the dominant product. For example, we observed a "false positive" by Tm (**Figure 7.1C-D)**, despite the presence of template. The sequencing of this product, contained nonspecific product sequences, similar to those observed in the NTC, at high prevalence, as well as the specific target sequences in low abundance (**Figure 7.2 [well C7])**. Similarly, though "true positive" is assigned to other bulk reactions in the presence of template, the nonspecific products are still observed at low abundance (**Figure 7.2 [well F8]**). Further, a greater number of nonspecific partitions in digital using *Bst* 3.0 as compared to *Bst* 2.0, is correlated with a greater number of nonspecific reads despite the presence of template in the sequencing data (Comparing **Figure 7.6A-B** and **Figure 7.2B group A vs C)**. We hypothesize that the combination of real-time parameters (such as rate and TTP), combined with the ability of digital assays to yield probabilities and to assign reaction identity through HRM, may ultimately help researchers optimize bulk reaction conditions.

*A complex interplay exists among TTP, max rate, final intensity, and Tm*

To better visualize how TTP, max rate, final intensity, and Tm data are interrelated, we next plotted these data in a four-dimensional (4D) space (**Figure 7.6Q-R, Supplementary Videos S1 and S2 available online**). We observed that among all partitions, regarless of if the product was specific or nonspecific amplificiation, fluorescence was brighter when amplification occurred earlier and faster. This was true for both polymerases. Additionally, we observed two types of nonspecific amplification. The first type of nonspecific was the traditional "primer-dimer" cloud, which is characterized by a low Tm, low final fluorescence intensity, a slow max rate, and a generally late TTP. The second type of nonspecific cloud matches only in its high Tm, and spans a wide range of rates, TTP, and final intensities. The high-Tm nonspecific amplification occurs with greater frequency than the low-Tm nonspecific amplification. The major differences between the polymerases can also be resolved with this visualization. The number of nonspecific amplification events is much fewer for *Bst* 2.0 than for *Bst* 3.0. Further, these nonspecific events in *Bst* 2.0 never achieve same fluorescene intensity or maximum rate as with *Bst* 3.0. We include the 4D representation as part of our MATLAB code, and as videos in the SI.

*Classification of true or false positives enables optimal analysis parameter selection*

We next asked whether using a combination of digital real-time parameters, in conjunction with Tm, could be used to improve the performance (LOD) of a dLAMP assay. For any given assay, there is a large combination of possible parameters (e.g. amplification rate, TTP, fluorescence intensity) that are used to determine when a digital partition is "on" or "off." Use of these parameters and selection of thresholds will influence assay performance (analytical specificity and sensitivity). Assay performance is affected by amplification time and the combination of choices of parameters used to process the data impacting LOD, the probability of detecting a molecule (efficiency), and the clinical sensitivity and specificity. Having established that there is a direct relationship between Tm, sequence identity, and

structure, we determined that Tm allows us to explicitly differentiate specific and nonspecific amplification in dLAMP, and thus, differentiate true from false positives.

We foresee two separate situations of dLAMP analysis using HRM. The first is where HRM is not incorporated in the final assay, but is used during assay development. Second is the ideal situation for quantitative performance, where HRM is incorporated into the final LAMP assay. We expect the first group of LAMP assays to exist because collecting Tm data adds additional time to an assay and requires more advanced hardware to run. This may be unideal in situations requiring more rapid diagnostics or limited-resource and field settings where the hardware may be impractical. Nonetheless, running HRM is still useful during LAMP assay development to select the optimal combination of parameters for end-point or real-time LAMP without using Tm. Hence, Tm allows one to identify the correct combination of assay parameters, and how to analyze the data for best LOD.

LOD is a key parameter when optimizing clinical assays because pathogen load is low in many infections (e.g. in blood infections or asymptomatic sexually transmitted infections). We thus illustrated the optimization of parameters using improved LOD as the selection criteria. The combination of real-time dLAMP with HRM can uniquely define LOD because of the combination of digital and Tm. Unlike bulk assays, which require a concentration titration curve (and are thus dependent on integrated signal intensity and enzymatic turnover), digital assays only require that an event (target molecule) is or is not observed, and can be counted relative to the partition volume (40,41). The minimum LOD for any digital assay corresponds to one target or amplification event per partition volume. Hence, we can define LOD from a single concentration point by Eq. 1:

**Equation 7-1**

$$LOD = \frac{C_{True}}{[N_{True} - (N_{False} + 3 \times \sqrt{N_{False}})]/N_{CI}}$$

where $C_{True}$ is the concentration of target molecules loaded by ddPCR counts in copies per microliter, $N_{True}$ is the number of true positive (specific) amplification events observed on a chip, $N_{False}$ is the number of nonspecific amplification events observed on a chip, and $N_{CI}$ is the number of expected molecules for a given confidence interval. In this equation, the $N_{True}$ and $N_{False}$ are chip-specific, and take into account the total volume of the chip, the number of partitions, and the volume of partitions. Furthermore, in Eq. 1, amplification efficiency is implicitly taken into account via the $N_{True}$ parameter (in other words, for a less efficient amplification process, a given $C_{True}$ on a given chip would lead to a lower value of $N_{True}$). Finally, for simplicity, Eq. 1 makes the assumption that the measurements are performed at sufficiently low concentrations (as is typical for LOD experiments) that only a very small fraction of occupied partitions contain more than one molecule, and therefore, there is a linear relationship between $C_{True}$ and $N_{True}$.

The concentration loaded, $C_{True}$, generates N total counts of both true- and false-positive events. We can divide this concentration by the minimal number of counts needed to identify a specific amplification event and define this as the LOD. The minimum number of counts needed to guarantee a specific amplification event is observed is determined by $N_{True}$, $N_{False}$, and $N_{CI}$. $N_{True}$ and $N_{False}$ are determined empirically, whereas $N_{CI}$ is calculated from the desired expected number of molecules that will yield at least one detection event for a given confidence interval ($N_{CI}$) from the Poisson equation. If we require a 95% CI to observe a true positive across an entire chip, the minimum number of counted events is 3 (i.e. 5% of the time, the Poisson expected loading of 3 target molecules will still measure zero events). For a 98% CI, $N_{CI}$ would be 4 counts. Hence, all true-positive counts in excess of $N_{CI}$ are counts observed above the LOD. Uncertainty in the LOD is given by Supplementary Equations S1-S2.

Counting only true positives does not account for interference from false positives. In order to meet our minimum counts for detection, our equation must remove false counts ($N_{False}$.) The generally accepted procedure for LOD calculations with a 99.7% CI is to assign $N_{True}$ only when the counts exceed the background plus three standard deviations of the

background ($N_{False} + 3 \times \sqrt{N_{False}}$). We approximate the variance in the background using the counting error as three times the square root of the number of false-positive events counted and subtract those counts from the true-positive counts to yield the equation.

Using this calculation of LOD to optimize an assay has three limitations. First, Eq. 1 fails to produce a number with physical meaning when the number of true-positive events ($N_{True}$) is less than the number of false-positive events plus three times the standard deviation in false amplification ($N_{False} + 3 \times \sqrt{N_{False}}$). In this case, it is not possible to conclusively observe a true positive, and the LOD becomes irrelevant. Second, Eq. 1 gives an absolute LOD. The numerator (concentration of template molecules loaded on the chip, as determined by PCR) is corrected for the probability of observing a molecule amplify (efficiency) by the true-positive counts. $N_{False}$ accounts for the nonspecific amplification, and $N_{\mathrm{CI}}$ accounts for the Poisson probability associated with loading a target molecule. Third, this equation is specific to digital assays.

We first sought to demonstrate the selection of optimal parameters for situations where HRM is not incorporated into the final assay. Using this process, one can pick any threshold and use Tm to determine the optimal trade-off between true and false positives. All initial experiments testing the utility of LOD, juxtaposed against receiver operating characteristic (ROC) curves, to identify optimal parameters were done using *Bst* 3.0. We began by determining the optimal thresholds for max rate, fluorescence intensity, and amplification time. We demonstrate optimization of all three parameters, using Tm as the arbiter, to illustrate the utility of our method.

We tested the use of ROC curves (commonly used to indicate clinical sensitivity and specificity) to compare the performance in response to a given parameter. ROC curves provide a visual representation of the ability to distinguish between a true-positive and false-positive event, as a function of a given threshold, but can be difficult to use for optimal selection of LOD. ROC curves show the fractions of true and false positives, where the true-positive fraction is the number of true positives at a given threshold out of the total number

of true positives observed by Tm; and the false-positive fraction is the number of false positives counted at the given threshold, divided by the total number of false positives observed by Tm. A perfect classifying test will yield the largest true-positive fraction and smallest false-positive fraction.

When plotting the ROC curve for maximum rate (**Figure 7.19A**), we observed that rate initially performs very well for eliminating false positives (the false-positive fraction is very small for very high rates). However, as the digital threshold (analogous to ROC "cut-point") for rate decreases, a greater number of both false and true-positive values are counted. Closer examination of this range of thresholds (**Figure 7.19B**) emphasizes the Youden Index at 34.6 true-positive fraction and 4.6 false-positive fraction as a possible choice for optimum threshold, although the assay performance in terms of LOD is unclear. The choice for optimal final-intensity threshold is even less clear with the ROC curve (**Figure 7.19C**), as the ROC curves do not give clear indication of the optimal LOD (the ROC curve is a gentle concave slope). Even relatively high fluorescence thresholds do not give indications of the optimal cut-point (**Figure 7.19D**).

Filtering using LOD revealed a clear optimum. We plot the total number of events for both true and false positives and LOD as a function of maximum rate (**Figure 7.7A**). The LOD curve revealed a clear minima, corresponding to the optimal cut-point using rate. Selecting the threshold of 49.8 RFU/30 seconds generated an LOD of 2.11±0.92 cp/µL. Similarly, plotting LOD against final intensity resulted in a clear minima, despite the histogram appearing as a continuum and the cut-point being thus ambiguous (**Figure 7.7B**). Using final intensity, an LOD of 2.14±0.89 cp/µL can be achieved at 1393 RFU.

The ROC curve for TTP presented a narrow range of thresholds, with ~50% true-positive fraction and 2% false-positive fraction, although the precise optimal threshold was not obvious (**Figure 7.19E**). To refine this threshold, we plotted the LOD and the cumulative counts as a function of time in both linear (**Figure 7.7C**) and logarithmic scales (**Figure 7.7D**).

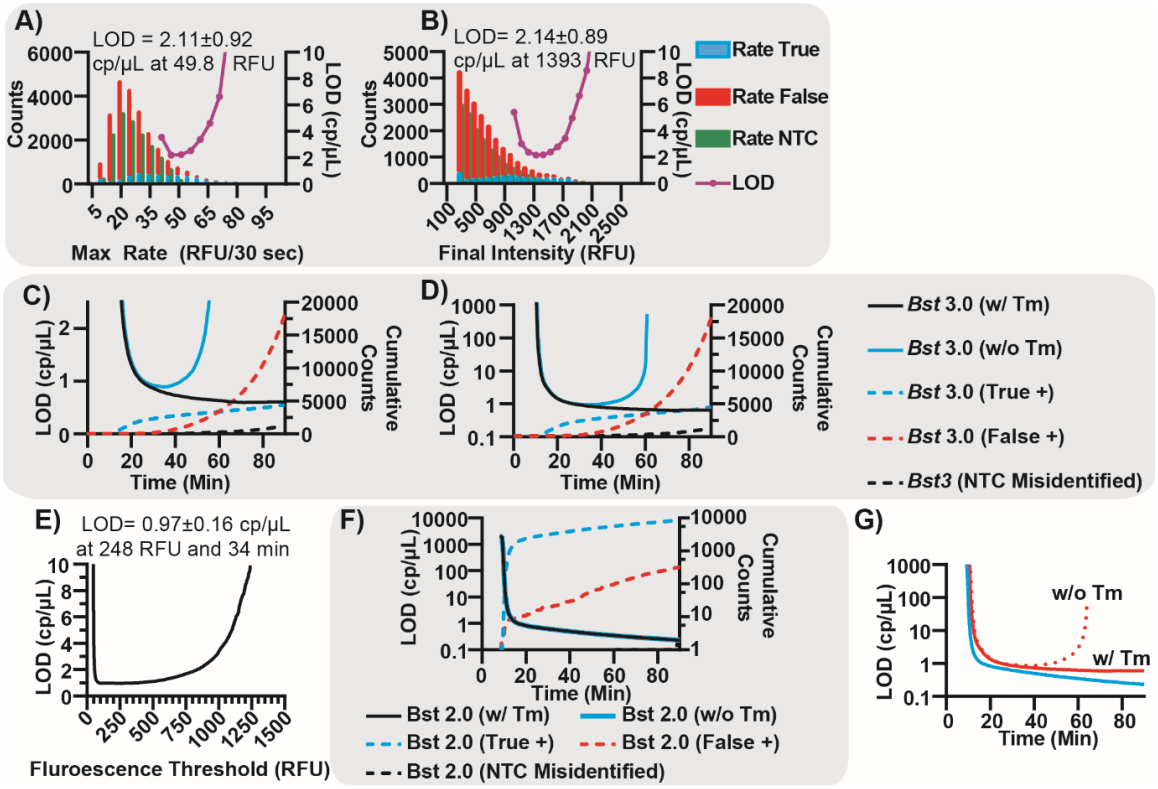


**Figure 7.7: Classification of amplification reactions using HRM to determine optimal performance of dLAMP assays.**

**(**A) Histogram of the false positives identified by Tm within the presence of template (red), true positives by Tm (blue), and false positives in the NTC (green), binned by max rate of the partition and a LOD curve plotted as a function of max rate using *Bst* 3.0. B) Histogram of the false positives identified by Tm within the presence of template (red), true positives by Tm (blue), and false positives in the NTC (green), binned by final intensity of the partition and an LOD curve plotted as a function of final intensity using *Bst* 3.0. C) LOD Curves using *Bst* 3.0 as a function of time without using Tm in the final assay (blue) and using Tm in the final device (black). Plots of cumulative counts of true positives (red dashed), false positives (blue dashed), and incorrectly identified partitions (black dashed). D) Logarithmic plot of LOD curves using *Bst* 3.0 as a function of time without using Tm in the final assay

(blue) and using Tm in the final device (black). Plots of cumulative counts of true positives (red dashed), false positives (blue dashed), and incorrectly identified partitions (black dashed). E) LOD plotted as a function of fluorescence intensity, when the assay is measured at the optimal TTP of 34 min. F) Logarithmic plot of LOD curves, using *Bst* 2.0, as a function of time without using Tm in the final assay (blue) and using Tm in the final device (black). The blue and black plots overlay. Plots of cumulative counts of true positives (blue dashed), false positives (red dashed), and incorrectly identified partitions (black dashed). G) Plot of LOD curves as a function of time comparing *Bst* 2.0 (solid blue with Tm, dotted blue without Tm) and *Bst* 3.0 (solid red with Tm, dotted red without Tm). Curves for *Bst* 2.0 overlap.

Assays employing HRM only during the development of the assay can improve the LOD of the final assays by selecting (making an informed choice of the optimum threshold). The LOD decreases (blue curve) as the true positives begin to amplify (blue dashed) and increase, as the false positives amplify (red dashed). The minima for this system occurs at 34 min and 0.93±16 cp/μL, striking a balance between allowing many true positives to amplify, and only a small amount of false positives to occur (53.6% true-positive fraction and 1.5% false-positive fraction) and is clearly defined using the linear scale (**Figure 7.7C**). Plotting of LOD on the logarithmic scale (**Figure 7.7D**) emphasizes improperly selecting a threshold can result in several orders of magnitude loss in assay performance (for example, stopping the assay too early or allowing the assay to run for too long). Although dLAMP is robust to perturbations, selecting the appropriate duration for amplification is important.

In contrast, assays using HRM as part of the final readout can distinguish false positives from the true positives and improve LOD further by excluding nonspecific amplification from the analysis. In some instances, a NTC may incorrectly identify partitions as true positives by Tm (black dashed). We incorporate these events as nonspecific amplification in case HRM is used in the final readout. If nonspecific amplification is eliminated, the assay LOD (**Figure 7.7C,F**, black solid) continues to improve with time, and is only dependent on the stochastic

probability that a true positive will initiate and amplify. In this scenario, there is no penalty allowing the assay to amplify for extended periods of time.

In this scenario the LOD equation simplifies to

**Equation 7-2**

$$LOD = \frac{C_{True}}{N_{True}/N_{CI}} = \sim \frac{N_{CI}}{Fraction\ copies\ detected}$$

Additionally, there is no limitation on the number of parameters that can be used to identify the optimal LOD. Using multiple parameters to filter the data may be useful for individuals not employing HRM in the final assay or in assays only employing end-point measurement (e.g. an assay without real-time measurements will be unable to generate data on rate, but still benefit from selecting optimal assay time and fluorescence threshold). As a demonstration, we filtered first by optimal TTP, then for the optima of a second parameter. In this case, we selected the optimal TTP of 34 min, and scanned for optimal fluorescence threshold. We plotted LOD as a function of fluorescence threshold and determined that the optimal fluorescence threshold at 34 min would be 248 RFU and correspond to an LOD of 0.97±0.16 cp/µL (**Figure 7.7E**).

Do filter parameters exhibit the same LOD minima when using *Bst* 2.0 as they did for *Bst* 3.0? *Bst* 2.0 had much lower nonspecific background than *Bst* 3.0, and could behave similarly or may behave differently.

First, does the ROC curve for TTP display a clear optimum? Similar to the TTP ROC for *Bst* 3.0 (**Figure 7.19E**), the TTP ROC for *Bst* 2.0 has a concave slope making choice of the optimum a matter of computation (**Figure 7.19F**). We can visually estimate the balance of true and false-positive fraction in the range of 50% true and 10% false. Similar curves for max rate and final intensity could be generated but are not shown here.

Second, is there an advantage to using HRM in the final assay with *Bst* 2.0? To answer this question, we plot LOD and the cumulative counts of true and false positives as a function of time for *Bst* 2.0 (**Figure 7.7F**). Similarly to *Bst* 3.0, we observe LOD improve rapidly as true-positive events are counted. However, unlike *Bst* 3.0, the nonspecific amplification events are few, and their presence does not have an impact on LOD. Thus, when using *Bst* 2.0, the curves representing LOD with or without HRM in the final assay overlay and indicate using HRM in the final assay has no additional benefit. Furthermore, the continuously decreasing LOD with time for either case indicates that use of ROC curves to determine an optimum can be misleading. While the ROC implies that an optimum exists, the false-positive incidence is rare enough that a TTP optimum selected by LOD does not exist. Hence, assay developers may select assay time based on requirements other than LOD.

We next assessed whether we could use HRM to compare the performance of the two polymerases, to see which one would give the best LOD and which combination of hardware components would give the optimum assay performance. (**Figure 7.7G**) For both polymerases, we observed a similar, rapid decrease in LOD in the initial moments as true-positive events are detected. However, we also noticed several differences. *Bst* 2.0 has a lower LOD than *Bst* 3.0 at any amplification time. We attribute this difference to the higher incidence of false positives when using *Bst* 3.0 compared with *Bst* 2.0. An additional consequence of the low false-positive incidence using *Bst* 2.0, regardless of the use of HRM in the assay, is the LOD continues to improve with time as additional true positives are counted. In contrast, *Bst* 3.0 benefits greatly from use of HRM in the final assay. If HRM is not included in the assay (**Figure 7.7G**, red dashed), a clear optimum for LOD occurs at 34 min and 0.93±0.16 cp/µL. However, if HRM is employed in the assay, the LOD more closely resembles the LOD curve for *Bst* 2.0 and improves with increased detection of true-positive events.

We made several overarching conclusions regarding improving the LOD of dLAMP using a combination of digital real-time parameters and Tm. First, filter parameters can be used singly or in combination to improve the performance (LOD) of dLAMP. In certain assays,

one parameter may perform better than another for this selection. For this primer set, LOD for *Bst* 3.0 was lower (better) when using TTP (0.93±0.16 cp/µL) than max rate (2.11±0.92 cp/µL) or final intensity (2.14±0.89 cp/µL). Second, incorporation of HRM into the final assay readout will benefit some assays more than others. We observed incorporation of HRM as a part of the final assay improved the perofmance of *Bst* 3.0 greater than the perofmance of *Bst* 2.0, and was vital for long assay times.

*Classification demonstrates host genomic DNA alters specific and nonspecific amplification in dLAMP*

Assays with high clinical sensitivity and specificity are critically needed. Clinical samples of CT, originating from urine and swabs, pose an intrinsic challenge because they contain variable levels of host DNA and DNA from other flora. The analysis of these clinical samples needs not only to be sensitive (good LOD), but also to be able to function in the presence of nonspecific, potentially amplifiable genomic secondary structures and other possible environmental contaminants, while remaining consistent between samples.

We sought to investigate the impact of host human genomic DNA (hgDNA) on nonspecific background amplification. We hypothesized that nonspecific structures (like hairpins and regulatory elements), may amplify in the presence of LAMP and contribute to nonspecific background amplification. We titrated sheared buffy coat gDNA (i.e. leukocytes) concentrations from zero to $2.5x10^3$ cells per µL, a concentration 2.5x greater than that expected to cause interference (8), and observed the impact on specific and nonspecific amplification of CT (**Figure 7.8**). We measured the concentration of hgDNA in Human Haploid Genome Equivalents (HHGE) or half the total amount of hgDNA in a diploid cell. For each concentration of host DNA and enzyme, we ran at least three chips in the presence of CT template and three in the absence of template across multiple days and sample lots. In total, we observed 1,196,038 different reaction partitions. At the highest concentration of hgDNA, there was 3,030,000 times more hgDNA than bacterial DNA by mass.

We first asked how background DNA impacted TTP qualitatively. We observed for both *Bst* 2.0 and *Bst* 3.0 enzymes, specific and nonspecific amplification were qualitative similar independent of background DNA concentration below 5000 HHGE per µL. As with previous measurements, *Bst* 2.0 rarely produced low-Tm nonspecific events; whereas *Bst* 3.0 produced both high- and low-Tm nonspecific events. Further, there were more nonspecific amplification events for *Bst* 3.0 than *Bst* 2.0 at both high and low Tm.

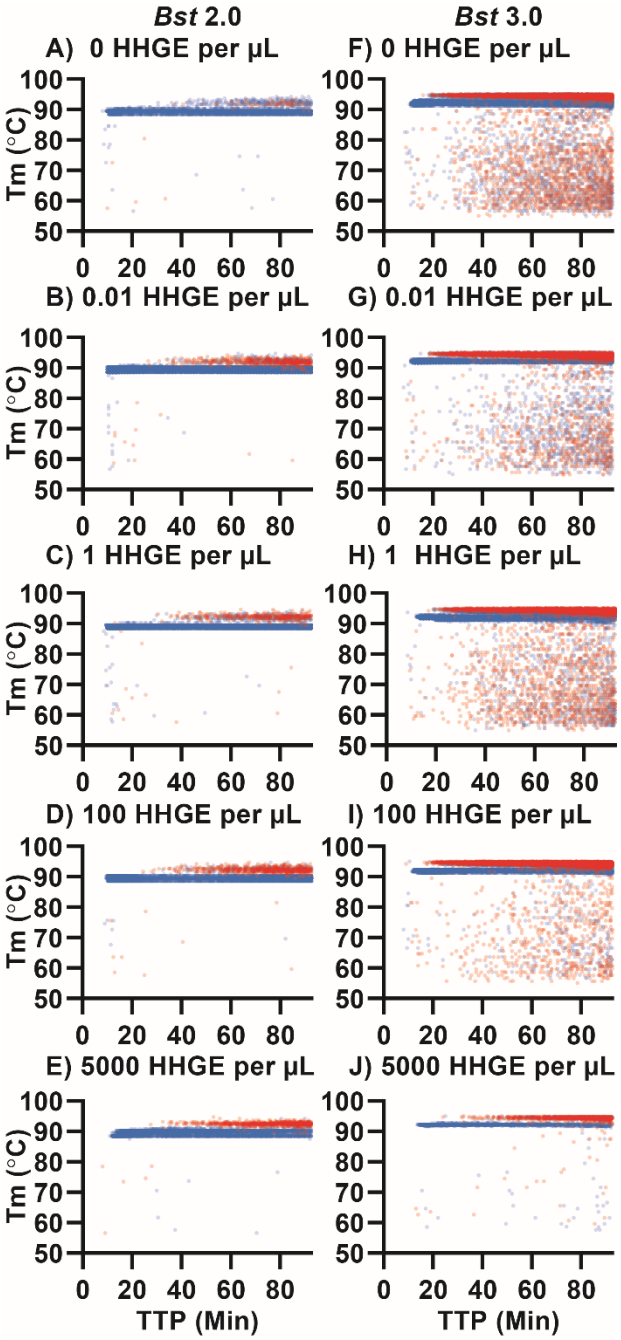


**Figure 7.8: Impacts of host (human) genomic DNA in human haploid genome equivalents (HHGE) on specific and nonspecific amplification.**

Plots of Tm as a function TTP using *Bst* 2.0 at (A) 0 HHGE per µL; (B) 0.01 HHGE per µL, C) 1 HHGE per µL, D) 100 HHGE per µL, and E) 5000 HHGE per µL; and using *Bst* 3.0 at (F) 0 HHGE per µL, (G) 0.01 HHGE per µL, H) 1 HHGE per µL, I)

100 HHGE per µL J) 5000 HHGE per µL in the presence of template (blue) and NTC (red). N = 3 for all conditions, except *Bst* 3.0 at 0 and 100 HHGE per µL in the presence of template, where N = 6.

We next asked how background hgDNA impacts specific and nonspecific amplification quantitatively. We categorized amplification events as specific and nonspecific based on Tm as previously. First, we asked: Is there a relationship between fraction of template molecules amplified in dLAMP and amplification time? We then determined the total number of template copies loaded into a chip relative to the copies measured by ddPCR. If amplification initiation is stochastic, as observed in **Figure 7.5F** and **Figure 7.6A-B**, does longer assay time increase ”efficiency” and thereby improve LOD when using Tm (as seen in **Figure 7.7C,F**)? We observe that for *Bst* 2.0, a large number of partitions amplify at in the first 11.5 min, followed by a second phase after 20 min where additional partitions amplify with lower frequency (**Figure 7.9A**). The mode TTP for concentrations less than 5000 HHGE per µL was ~11.6±0.2 min (**Table 7-8, Figure 7.20A, Figure 7.21C**). After the mode TTP, the frequency of observing specific amplification in the absence of HHGE decreases from a maximum frequency of 1.2±0.1% copies detected per 30 sec to a lower average frequency of 0.23±0.04 % copies per 30 sec from 20 to 90 min (**Figure 7.9A**). For ***Bst* 3.0** (**Figure 7.20A**), we observe a similar trend temporally, though mode TTP was at least 2 min slower and had greater variability than *Bst* 2.0 (**Table 7-8, Figure 7.20B, Figure 7.21D**). Further, *Bst* 3.0 consistently amplified fewer target molecules than *Bst* 2.0 at all time points. This highlights the stochastic nature of amplification using LAMP and the importance in choice of enzyme on sensitivity. In theory, assays employing Tm could be run until all partitions amplify as either a false or true positive. Allow all partitions to amplify would give the highest possible number of target copies amplified and lowest possible LOD when using Tm in the final assay.

Second, we asked, what is the impact of hgDNA on efficiency as a function of time? For both *Bst* 2.0 and 3.0 (**Figure 7.19A, Figure 7.20A**), when comparing within a given enzyme,

we observed that the fraction of copies detected, and the moment the majority of reactions initiate, were indistinguishable for concentrations less than 5000 HHGE per µL. At 5000 HHGE per µL, a decrease in the fraction of copies detected and a delay in amplification initiation was observed (see also **Figure 7.21C,D**). *Bst* 2.0 had a mode TTP of delay of 4.7 min to 16.3±2.7 min, whereas in *Bst* 3.0, the mode TTP was 17.2±2.1 min at 5000 HHGE per µL (**Table 7-8, Figure 7.21**). Thus, high concentrations of hgDNA may suppress specific amplification.

Third, we asked, what is the impact of hgDNA and time on nonspecific amplification? For *Bst* 2.0, we observed consistent nonspecific amplification products with high and low Tm, regardless of concentration of hgDNA. Single digital partition counts were observed at low-Tm nonspecific amplification in both the presence of template and the NTC and independent of hgDNA concentration (**Figure 7.19B-C**). The fraction of partitions generating a false-positive amplification at low Tm was less than $3.3x10^{-4}$ through 45 min (i.e. 7 or fewer events in 20,000 partitions per chip). Similarly, partition counts of high-Tm nonspecific amplification are <10 per chip until 45 min. After 90 min, high-Tm nonspecific amplification is more prevalent than low-Tm nonspecific amplification, and the reactions finish with fewer than nonspecific 260 counts in 20,000 partitions corresponding to a false-positive fraction of $1.3 \times 10^{-2}$. One exception is the nonspecific high-Tm amplification in the absence template and HHGE. This condition appears to have lower nonspecific background than other conditions. We collected each replicate on separate days and were able to observe the experimental variability between the presence and absence fo template, which might be otherwise lost when examining the NTC alone. This experiment emphasizes the advantage of determining nonspecific amplificaiton using Tm from the same experiment as specific amplification is counted. At low background rates, such as when using *Bst* 2.0, inherent variability exists in the false-positive fraction and can impact LOD. Meauring nonspecific amplificaiton from within an experiment eliminates the assumption that the false-positive rate remains identical to the NTC or between experimental runs.

For *Bst* 3.0, nonspecific amplification was variable, but tended to be fewer for higher concentrations of hgDNA. At any given time, high-Tm nonspecific amplification was on average ~30 fold more likely to occur than a low-Tm nonspecific product. At 45 min, low-Tm nonspecific amplification had false-positive fraction less than $3.1x10^{-3}$ (62 or fewer events per chip), amplification events with high Tm had a false-positive fraction less than $1.9x10^{-2}$ (386 or fewer events per chip). At the completion of the experiment, high-Tm nonspecific amplification events account for as much as 35% of the total partitions per chip; a value exceeding the total observed true-positive events. In these scenarios, utilization of Tm to identify true and false amplification will be critical to successful quantification of target analytes.

For this CT primer set, both *Bst* 2.0 and *Bst* 3.0 similarly demonstrate that the presence of high concentrations of hgDNA may suppress the likelihood of nonspecific amplification occurring. In general, for this primer set and target, we find that *Bst* 2.0 performs significantly better than *Bst* 3.0 as a consequence of having higher probability of detecting a target molecule and low likelihood of generating a nonspecific amplification event.

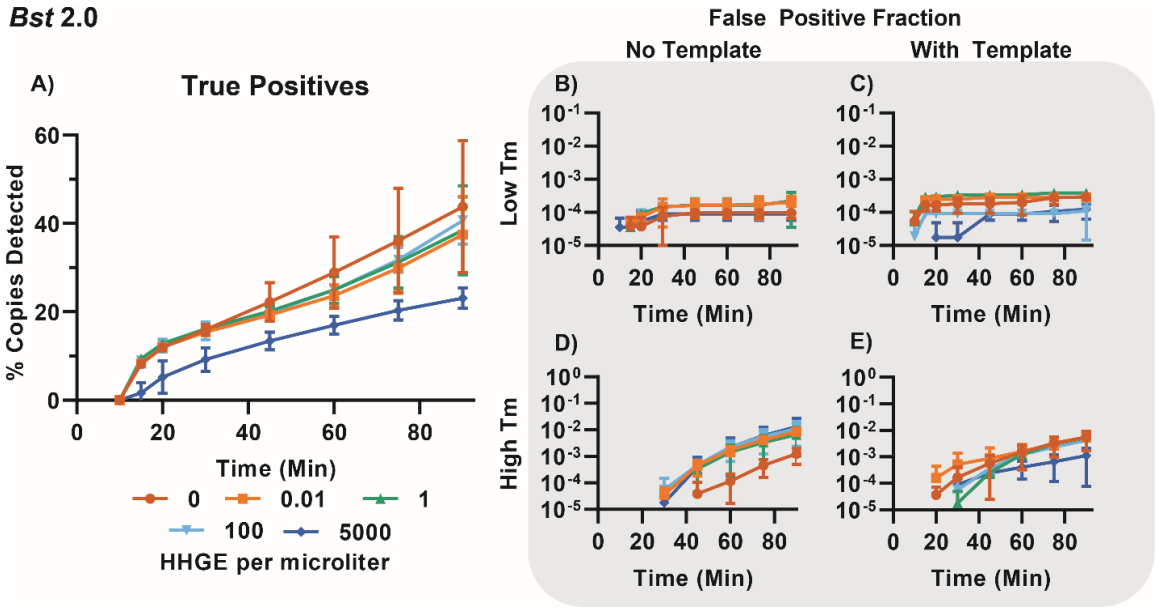


**Figure 7.9: Quantification of the impact of hgDNA on specific and nonspecific amplification using *Bst* 2.0 a as a function of time.**

(A) Plot of the % copies detected (specific amplification) as a function of time. (B-C) The fraction of partitions with nonspecific amplification with Tm less than the specific amplification in the NTC (B) and in the presence of template (C) as a function of time. (D-E) The fraction of partitions with nonspecific amplification with Tm greater than the specific amplification in the NTC (D) and in the presence of template (E) as a function of time. Panel (A) is available in tabular form as Supplementary **Table 7-9**.

Fourth, we asked, is maximum rate impacted by the concentration of hgDNA? We hypothesize that background hgDNA may compete for the binding site of the polymerase with the target DNA or generate competing amplification events and thus, decrease the maximum observed velocity in a given partition. This phenomena would be challenging to untangle in bulk. We find that maximum rates are similar for a given enzyme, until 5000 HHGE per µL for *Bst* 2.0 (**Figure 7.21A**), and above 100 HHGE per µL for *Bst* 3.0 (**Figure 7.21B**). Thus demonstrating that high concentrations of HHGE may slow the rate of

amplification. Furthermore, in general, and echoing the conclusions of **Figure 7.6G,I**, we observe that *Bst* 2.0 has faster maximum rate than *Bst* 3.0, regardless of the hgDNA concentration.

Fifth, we asked, how is LOD impacted by the concentration of hgDNA? For *Bst* 2.0 (**Figure 7.21E**), the LOD at a given time was similar for concentrations less than 5000 HHGE per µL. Meanwhile, the LOD in the presence of 5000 HHGE per µL was slightly worse as evidenced by the detection of fewer target molecules (e.g. 0.7 vs 0.5 cp/µL at 45 min). As previously, incorporation of HRM into the final assay does not impact the LOD when using *Bst* 2.0. When using *Bst* 3.0 (**Figure 7.21F**) and HRM to remove nonspecific amplification, LOD tracks with the number of true-positive events. Thus, LOD becomes worse when efficiency is lower (i.e., at 5000 HHGE per µL). Similarly, when HRM is not incorporated in the assay, higher concentrations of HHGE tend to result in a worse LOD. However, at long amplification times, high concentrations of HHGE suppress nonspecific amplification more than specific amplification, resulting in LOD enhancement relative to low concentrations of HHGE.

Cumulatively, these data show high background DNA may reduce the probability of detecting a specific molecule (analytical sensitivity), suppress the false-positive fraction (analytical specificity), reduce the velocity of amplification, and delay the start of amplification at clinically relevant concentrations of hgDNA. Thus, we conclude background hgDNA impacts dLAMP for this primer set. Generally, investigators should examine their own primer sets in the presence of high concentrations of hgDNA and take caution when examining clinical samples with high leukocyte concentrations (as reported by urinanalysis). For example, CT infection is not inherently associated with high concentrations of leukocytes, and many infections are asymptomatic. Ultimately, these experiments underscore the value of quantifying nonspecific amplificaiton variability, using HRM, from within the same experiment as a target is quantified. Because nonspecific amplificaiton is measured within a given sample, one no longer needs to assume it remains identical to the NTC or between experimental runs.

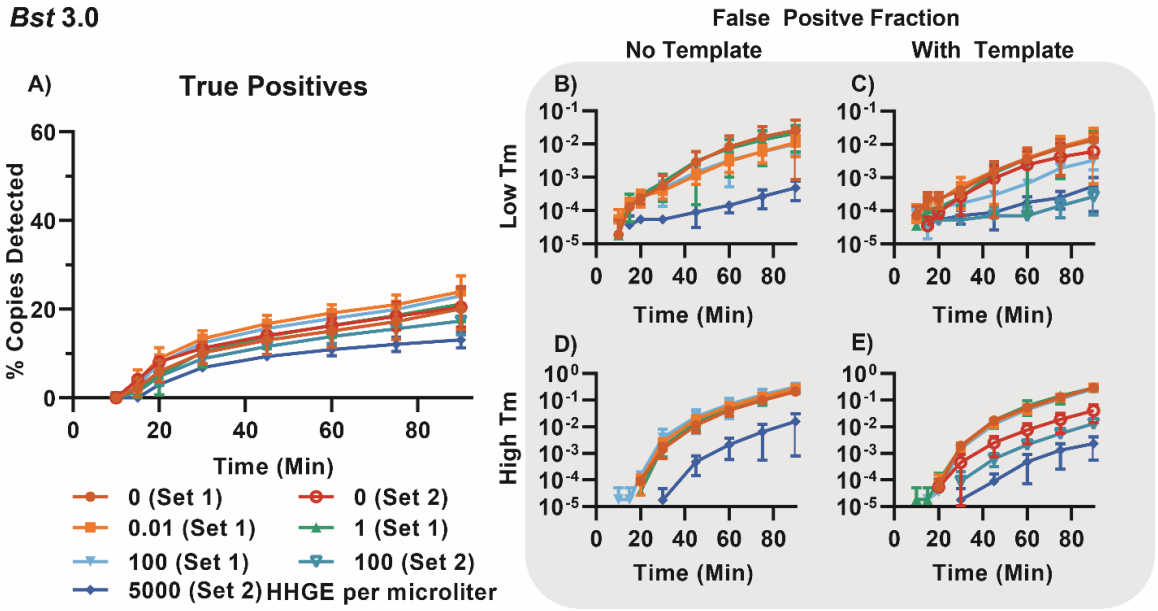


**Figure 7.10: Quantification of the impact of hgDNA on specific and nonspecific amplification using *Bst* 3.0 as a function of time.**

(A) The percentage copies detected (specific amplification) as a function of time. (B-C) The fraction of partitions with nonspecific amplification with Tm less than the specific amplification in the NTC (B) and in the presence of template (C) as a function of time. (D-E) The fraction of partitions with nonspecific amplification with Tm greater than the specific amplification in the NTC (D) and in the presence of template (E) as a function of time. Panel (A) is available in tabular form as Supplementary **Table 7-10**.

## Conclusions

We predict that the combination of HRM and real-time dLAMP will be invaluable for answering many questions across a wide variety of applications, and thus our approach was designed to be accessible to most standard labs. We employed commercial chips for digitization, a commercial thermoelectric unit for heating and cooling, a commercial

microscope for optical analyses, and we made our data-processing script freely available. Our intention was to design an accessible system with readily available components to enable others to access the advantages of digital microfluidics to study and optimize primer sets, enzymes, and reaction conditions of interest to them. We predict these capabilities will be particularly valuable for people working with variable sample matrixes, high background DNA, poorly performing primer sets, or poorly performing enzymes.

We derived four major lessons from this study. First, LAMP can produce nonspecific amplicons with high Tm. The formation of these nonspecific amplicons occurs from the interaction of multiple primers and the use of a polymerase with template switching ability, terminal transferase activity, and lacking 3′–5′ exonuclease activity. Interaction of primers may lead not only lead to rising background fluorescence (37), but to spontaneous exponential amplification as well. Primer design and enzyme selection therefore should be judicious to avoid formation of hairpins within primers, as well as microhomology at the 3' with any other primer, in order to prevent nonspecific amplification.

Second, HRM in LAMP is a useful method for differentiating specific and nonspecific amplification events. Digital experiments measure the fate and rate of each template, in contrast, bulk experiments are biased towards early amplification events. The combination of dLAMP and HRM allows observation of many amplification events and assignment of the nature of that amplification as true or false. Further, dLAMP with HRM quantifies nonspecific amplification experimentally in the presence of specific amplification, eliminating the assumption that incidence of false positives in the presence of template remains identical to the NTC or between experimental runs.

Third, by differentiating specific and nonspecific amplification, HRM is helpful in determining the combination processing and assay parameters that will lead to the best LOD in a digital assay. When HRM is incorporated into a dLAMP assay, true and false-positive amplification events can easily be separated. LOD is improved by elimination of nonspecific background and thus becomes dependent on the number of molecules that amplify (i.e. amplification efficiency or fraction of copies detected), without dependence on the incidence

of false positives. In contrast, if HRM were employed in a bulk reaction, the LOD would still be limited by the competition between specific and nonspecific amplification (which amplifies first) and would require a high number of trials to achieve sufficient statistical power. Importantly, even when HRM will not be used in the final assay, it can still be incorporated during the assay-development stage to improve the assay's LOD by determining the optimal choice of parameters based on rate, TTP, final intensity, or any combination of these parameters. Furthermore, our mathematical description of LOD is generalizable to other amplification methods that are measured in digital and can separate specific and nonspecific amplification.

Fourth, high levels of nonspecific host gDNA suppress analytical sensitivity and specificity, reduce amplification velocity, and delay the start of amplification. However, low-to-moderate levels of nonspecific host gDNA do not impact the analytical specificity or sensitivity of dLAMP. We ran our assays through clinically relevant concentrations of background DNA and did not observe interference until the upper range of concentrations expected to cause interference to demonstrate the clinical utility of real-time dLAMP with HRM.

Real-time dLAMP with HRM will enable the mechanistic optimization of primers and myriad assay conditions (such as buffer, $Mg^{2+}$, and reaction temperature). Because real-time dLAMP with HRM reveals the incidence of nonspecific amplification products with high and low Tm as a function of time, dLAMP with HRM can be used to investigate approaches that will eliminate different nonspecific products. For example, fast or early nonspecific events in digital may indicate primers or conditions that will be especially vulnerable to failure in a bulk reaction. Thus, real-time dLAMP with HRM could be used to design primers that will suppress nonspecific amplification in bulk, by generating only nonspecific amplicons that occur at slow rates and late TTP.

Future efforts should investigate the combination of real-time dLAMP (and other digital isothermal amplification technologies) and HRM as a way to increase multiplexing of dLAMP when using a single reporter. In PCR, HRM has been used to differentiate among

multiple amplification products by measuring differences in Tm (42-46), with applications that include among others multiplexed pathogen identification and antibiotic susceptibility testing. Finally, studies with clinical samples should be performed using the dLAMP with HRM method to understand the carryover effects from relevant matrices.

## Data Availability

The complete sequencing data generated during this study are available in the National Center for Biotechnology Information Sequence Read Archive repository with the BioProject ID: PRJNA574638.

The MATLAB script described here has been deposited in the open-access online repository GitHub and may be accessed using the following direct link:

https://github.com/IsmagilovLab/Digital_NAAT_2Ch_MeltCurve_Analyzer

## References

1. Kong, J.E., Wei, Q., Tseng, D., Zhang, J., Pan, E., Lewinski, M., Garner, O.B., Ozcan, A. and Di Carlo, D. (2017) Highly Stable and Sensitive Nucleic Acid Amplification and Cell-Phone-Based Readout. *ACS Nano*, **11**, 2934-2943.

2. Phillips, E.A., Moehling, T.J., Bhadra, S., Ellington, A.D. and Linnes, J.C. (2018) Strand Displacement Probes Combined with Isothermal Nucleic Acid Amplification for Instrument-Free Detection from Complex Samples. *Anal. Chem.*, **90**, 6580-6586.

3. Notomi, T., Okayama, H., Masubuchi, H., Yonekawa, T., Watanabe, K., Amino, N. and Hase, T. (2000) Loop-mediated isothermal amplification of DNA. *Nucleic Acids Res.*, **28**, e63-e63.

4. Somboonna, N., Choopara, I., Arunrut, N., Sukhonpan, K., Sayasathid, J., Dean, D. and Kiatpathomchai, W. (2018) Rapid and sensitive detection of Chlamydia trachomatis sexually transmitted infections in resource-constrained settings in Thailand at the point-of-care. *PLoS Negl. Trop. Dis.*, **12**, e0006900-e0006900.

5. Ljubin-Sternak, S. and Meštrović, T. (2014) Chlamydia trachomatis and Genital Mycoplasmas: Pathogens with an Impact on Human Reproductive Health. *Journal of pathogens*, **2014**, 183167-183167.

6. Su, W.H., Tsou, T.S., Chen, C.S., Ho, T.Y., Lee, W.L., Yu, Y.Y., Chen, T.J., Tan, C.H. and Wang, P.H. (2011) Diagnosis of Chlamydia infection in women. *Taiwan. J. Obstet. Gynecol.*, **50**, 261-267.

7. McEnroe, R.J., Burritt, M.F., Powers, D.M., Rheinheimer, D.W. and Wallace, B.H. (2018), pp. 112.

8. CLSI. (2005) *Interference Testing in Clinical Chemistry, EP07-A2*. Clinical and Laboratory Standards Institute, Wayne, PA.

9. Schneider, L., Blakely, H. and Tripathi, A. (2019) Mathematical model to reduce loop mediated isothermal amplification (LAMP) false-positive diagnosis. *Electrophoresis*, **40**, 2706-2717.

10. Chou, P.H., Lin, Y.C., Teng, P.H., Chen, C.L. and Lee, P.Y. (2011) Real-time target-specific detection of loop-mediated isothermal amplification for white spot syndrome virus using fluorescence energy transfer-based probes. *J. Virol. Methods*, **173**, 67-74.

11. Gadkar, V.J., Goldfarb, D.M., Gantt, S. and Tilley, P.A.G. (2018) Real-time Detection and Monitoring of Loop Mediated Amplification (LAMP) Reaction Using Self-quenching and De-quenching Fluorogenic Probes. *Sci. Rep.*, **8**, 5548.

12. Ball, C.S., Light, Y.K., Koh, C.-Y., Wheeler, S.S., Coffey, L.L. and Meagher, R.J. (2016) Quenching of Unincorporated Amplification Signal Reporters in Reverse-Transcription Loop-Mediated Isothermal Amplification Enabling Bright, Single-Step, Closed-Tube, and Multiplexed Detection of RNA Viruses. *Anal. Chem.*, **88**, 3562-3568.

13. Tanner, N.A., Zhang, Y. and Evans, T.C. (2012) Simultaneous multiple target detection in real-time loop-mediated isothermal amplification. *BioTechniques*, **53**, 81-89.

14. Kouguchi, Y., Fujiwara, T., Teramoto, M. and Kuramoto, M. (2010) Homogenous, real-time duplex loop-mediated isothermal amplification using a single fluorophore-labeled primer and an intercalator dye: Its application to the simultaneous detection of Shiga toxin genes 1 and 2 in Shiga toxigenic Escherichia coli isolates. *Mol. Cell. Probes*, **24**, 190-195.

15. Kubota, R., M. Alvarez, A., Su, W.W. and M. Jenkins, D. (2011) FRET-Based Assimilating Probe for Sequence-Specific Real-Time Monitoring of Loop-Mediated Isothermal Amplification (LAMP). *Biological Engineering Transactions*, **4**, 81-100.

16. Jiang, Y.S., Bhadra, S., Li, B., Wu, Y.R., Milligan, J.N. and Ellington, A.D. (2015) Robust strand exchange reactions for the sequence-specific, real-time detection of nucleic acid amplicons. *Anal. Chem.*, **87**, 3314-3320.

17. Liu, W., Huang, S., Liu, N., Dong, D., Yang, Z., Tang, Y., Ma, W., He, X., Ao, D., Xu, Y. *et al.* (2017) Establishment of an accurate and fast detection method using molecular beacons in loop-mediated isothermal amplification assay. *Sci. Rep.*, **7**, 40125.

18. Bhadra, S., Jiang, Y.S., Kumar, M.R., Johnson, R.F., Hensley, L.E. and Ellington, A.D. (2015) Real-Time Sequence-Validated Loop-Mediated Isothermal

Amplification Assays for Detection of Middle East Respiratory Syndrome Coronavirus (MERS-CoV). *PLoS One*, **10**, e0123126.

19. Li, B., Chen, X. and Ellington, A.D. (2012) Adapting enzyme-free DNA circuits to the detection of loop-mediated isothermal amplification reactions. *Anal. Chem.*, **84**, 8371-8377.

20. Wan, L., Chen, T., Gao, J., Dong, C., Wong, A.H.-H., Jia, Y., Mak, P.-I., Deng, C.-X. and Martins, R.P. (2017) A digital microfluidic system for loop-mediated isothermal amplification and sequence specific pathogen detection. *Sci. Rep.*, **7**, 14586-14586.

21. Selck, D.A., Karymov, M.A., Sun, B. and Ismagilov, R.F. (2013) Increased robustness of single-molecule counting with microfluidics, digital isothermal amplification, and a mobile phone versus real-time kinetic measurements. *Anal. Chem.*, **85**, 11129-11136.

22. Sun, B., Shen, F., McCalla, S.E., Kreutz, J.E., Karymov, M.A. and Ismagilov, R.F. (2013) Mechanistic evaluation of the pros and cons of digital RT-LAMP for HIV-1 viral load quantification on a microfluidic device and improved efficiency via a two-step digital protocol. *Anal. Chem.*, **85**, 1540-1546.

23. Rolando, J.C., Jue, E., Schoepp, N.G. and Ismagilov, R.F. (2019) Real-Time, Digital LAMP with Commercial Microfluidic Chips Reveals the Interplay of Efficiency, Speed, and Background Amplification as a Function of Reaction Temperature and Time. *Anal. Chem.*, **91**, 1034-1042.

24. Selck, D.A. and Ismagilov, R.F. (2016) Instrument for Real-Time Digital Nucleic Acid Amplification on Custom Microfluidic Devices. *PLoS One*, **11**, e0163060.

25. Njiru, Z.K., Mikosza, A.S.J., Armstrong, T., Enyaru, J.C., Ndung'u, J.M. and Thompson, A.R.C. (2008) Loop-mediated isothermal amplification (LAMP) method

for rapid detection of Trypanosoma brucei rhodesiense. *PLoS Negl. Trop. Dis.*, **2**, e147-e147.

26. Tone, K., Fujisaki, R., Yamazaki, T. and Makimura, K. (2017) Enhancing melting curve analysis for the discrimination of loop-mediated isothermal amplification products from four pathogenic molds: Use of inorganic pyrophosphatase and its effect in reducing the variance in melting temperature values. *J. Microbiol. Methods*, **132**, 41-45.

27. Uemura, N., Makimura, K., Onozaki, M., Otsuka, Y., Shibuya, Y., Yazaki, H., Kikuchi, Y., Abe, S. and Kudoh, S. (2008) Development of a loop-mediated isothermal amplification method for diagnosing Pneumocystis pneumonia. *J. Med. Microbiol.*, **57**, 50-57.

28. Liu, N., Zou, D., Dong, D., Yang, Z., Ao, D., Liu, W. and Huang, L. (2017) Development of a multiplex loop-mediated isothermal amplification method for the simultaneous detection of Salmonella spp. and Vibrio parahaemolyticus. *Sci. Rep.*, **7**, 45601.

29. Ayukawa, Y., Hanyuda, S., Fujita, N., Komatsu, K. and Arie, T. (2017) Novel loop-mediated isothermal amplification (LAMP) assay with a universal QProbe can detect SNPs determining races in plant pathogenic fungi. *Sci. Rep.*, **7**, 4253.

30. Hafner, G.J., Yang, I.C., Wolter, L.C., Stafford, M.R. and Giffard, P.M. (2001) Isothermal amplification and multimerization of DNA by Bst DNA polymerase. *BioTechniques*, **30**, 852-856, 858, 860 passim.

31. Wang, G., Ding, X., Hu, J., Wu, W., Sun, J. and Mu, Y. (2017) Unusual isothermal multimerization and amplification by the strand-displacing DNA polymerases with reverse transcription activities. *Sci. Rep.*, **7**, 13928.

32. Zyrina, N.V., Zheleznaya, L.A., Dvoretsky, E.V., Vasiliev, V.D., Chernov, A. and Matvienko, N.I. (2007) N.BspD6I DNA nickase strongly stimulates template-independent synthesis of non-palindromic repetitive DNA by Bst DNA polymerase. *Biol. Chem.*, **388**, 367-372.

33. Garcia, P.B., Robledo, N.L. and Islas, A.L. (2004) Analysis of non-template-directed nucleotide addition and template switching by DNA polymerase. *Biochemistry*, **43**, 16515-16524.

34. Ramadan, K., Shevelev, I.V., Maga, G. and Hübscher, U. (2004) De Novo DNA Synthesis by Human DNA Polymerase λ, DNA Polymerase μ and Terminal Deoxyribonucleotidyl Transferase. *J. Mol. Biol.*, **339**, 395-404.

35. Zyrina, N.V., Antipova, V.N. and Zheleznaya, L.A. (2014) Ab initio synthesis by DNA polymerases. *FEMS Microbiol. Lett.*, **351**, 1-6.

36. Voisey, J., Hafner, G.J., Morris, C.P., van Daal, A. and Giffard, P.M. (2001) Interrogation of Multimeric DNA Amplification Products by Competitive Primer Extension Using Bst DNA Polymerase (Large Fragment). *BioTechniques*, **31**, 1122-1129.

37. Meagher, R.J., Priye, A., Light, Y.K., Huang, C. and Wang, E. (2018) Impact of primer dimers and self-amplifying hairpins on reverse transcription loop-mediated isothermal amplification detection of viral RNA. *Analyst*, **143**, 1924-1933.

38. Khorosheva, E.M., Karymov, M.A., Selck, D.A. and Ismagilov, R.F. (2016) Lack of correlation between reaction speed and analytical sensitivity in isothermal amplification reveals the value of digital methods for optimization: validation using digital real-time RT-LAMP. *Nucleic Acids Res.*, **44**, e10.

39. Tanner, N.A. and Evans, T.C. (2014) Loop-Mediated Isothermal Amplification for Detection of Nucleic Acids. *Curr. Protoc. Mol. Biol.*, **105**, 15.14.11-15.14.14.

40. Rissin, D.M., Kan, C.W., Campbell, T.G., Howes, S.C., Fournier, D.R., Song, L., Piech, T., Patel, P.P., Chang, L., Rivnak, A.J. *et al.* (2010) Single-molecule enzyme-linked immunosorbent assay detects serum proteins at subfemtomolar concentrations. *Nat. Biotechnol.*, **28**, 595-599.

41. Rissin, D.M. and Walt, D.R. (2006) Digital Concentration Readout of Single Enzyme Molecules Using Femtoliter Arrays and Poisson Statistics. *Nano Lett.*, **6**, 520-523.

42. Athamanolap, P., Hsieh, K., Chen, L., Yang, S. and Wang, T.-H. (2017) Integrated Bacterial Identification and Antimicrobial Susceptibility Testing Using PCR and High-Resolution Melt. *Anal. Chem.*, **89**, 11529-11536.

43. Velez, D.O., Mack, H., Jupe, J., Hawker, S., Kulkarni, N., Hedayatnia, B., Zhang, Y., Lawrence, S. and Fraley, S.I. (2017) Massively parallel digital high resolution melt for rapid and absolutely quantitative sequence profiling. *Sci. Rep.*, **7**, 42326.

44. O'Keefe, C.M., Pisanic, T.R., Zec, H., Overman, M.J., Herman, J.G. and Wang, T.-H. (2018) Facile profiling of molecular heterogeneity by microfluidic digital melt. *Science Advances*, **4**, eaat6459.

*45.* Athamanolap, P., Hsieh, K., O'Keefe, C.M., Zhang, Y., Yang, S. and Wang, T.H. (2019) Nanoarray Digital Polymerase Chain Reaction with High-Resolution Melt for Enabling Broad Bacteria Identification and Pheno-Molecular Antimicrobial Susceptibility Test. *Anal. Chem.*

46. O'Keefe, C.M., Kaushik, A.M. and Wang, T.H. (2019) Highly Efficient Real-Time Droplet Analysis Platform for High-Throughput Interrogation of DNA Sequences by Melt. *Anal. Chem.*, **91**, 11275-11282.

**Supporting Information**

*Primer Sequences*

Primers had the following sequences:

- BIP: AAG CAC GCG GAC GAT TGG AAA AAA GCG GAT TTG CCT AAC CG
- BOP: CGA ACA TTC CCC TTG ATC GC
- FIP: GCT GCT CCA TCG TCT ACG CAG TTT TGC TCG TCT TCC CTG GGT T
- $FIP_{Short}$: GCT GCT CCA TCG TCT ACG CAG TTT TGC TCG TCT TCC CTG GG
- FOP: CCA AGG TTT CCA GGG TCA A
- LoopB: CCG TAG AGC GAT GAG AAC G
- LoopF: GCC TCA ACT TAG GGG CCG

*Fabrication of thermoelectric unit mount*

Starting from 1/4" thick aluminum stock; a block was squared and milled to 58x61 mm and slightly less than ¼” thick. Both the side in contact with the microfluidic chips and with the thermoelectric unit were finished with a single pass of a ½” fly bit to generate a mirror finish. Four holes for screws holes were counter bored to ensure the heads remained below the surface of the block and mounted to a 1.1 °C/W Half Brick DC Converter Heat Sink (AAVID, via Newark Electronics, 241214B92200G) using four #6-32, 5/8” long screws. A 7/16” hole was clearance drilled into the side of the aluminum to ¾” depth and a thermistor (TE Tech, MP-3002) was inserted and mounted using Thermal Compound (Arctic Alumina Silver Ceramic Polysynthetic). The thermoelectic unit was mounted between the aluminum block and heat sink using Thermal Compound and the screws finger tightened. Desired torque was calculated to be 0.89-7.175 ft*lbs per screw (total pressure 70-170 psi).

Once mounted, a QuantStudio chip was place on top of the block (to mimic total load on the instrument) and the PID tuned following instructions from the TC-720 Controller manual. With I&D set at zero; P was found to oscillate at 1.35 at 70 °C (the expected dLAMP temperature). The oscillation period was 6 seconds. Thus, the Proportional BW was set at 1.7*1.35 = **2.3**. The Integral gain was calculated as I = 1.2/T in min = 1.2/0.1 = **12**. The derivative gain was calculated as 0.075xT=0.075*0.1= 0.0075 min. With these settings, the observed temperature overshoot from room temperature to 70 °C at maximum output was 0.05 °C, whereas at 95 °C the observed overshoot was 1 °C.

The ability of the embedded thermocouple to accurately assess temperature of the aluminum block was verified with an independent K-type mini-thermcouple read through a General IRT659K [IR] Thermometer.

*MATLAB script*

The MATLAB script works as follows: First, the TIF stack containing 2-channel images of the LAMP amplification and melt curve along with a .txt file containing temperature over time data are loaded into memory. We used the first image of the ROX channel to define all of the partitions. A custom iterative thresholding algorithm was applied to detect partitions despite lighting non-uniformities, imaging artifacts, or possible debris. The size of a well was pre-defined using the areaBound parameter. For our study, we defined partitions as having areas between 20 to 45 pixels. The algorithm scans through increasing threshold sensitivities, applies the partition size filter, and combines the results into a final mask. This is repeated for each image in the stack.

In order to track the partition intensities over time, it is important to track the same partition. This is challenging because partition move due to thermal expansion during the LAMP heating and melt curve, partitions touching the edge of the image may appear or disappear from the field of view, and bubbles during the melt curve can distort image. To account for

this, we applied the built-in MATLAB labeling function to the first image of the stack to assign a unique number to each partition. We assume that a partition will not translate a distance greater than its radius from frame to frame. Using this, we find the centroid of each labeled partition in the first frame and overlay this with the second frame. If a labeled centroid overlaps a partition, the entire partition is assigned the label. If not, the partition was not found and was discarded from the analysis. This method is repeated for the centroids of the second frame onto partition of the third frame and so on. On average, more than 18,000 of the 20,000 partitions were attained for analysis, which is plenty for statistical confidence.

To analyze partitions, the intensity of each partition is averaged for each frame and plotting against time for the LAMP curve. The data is smoothed using a Gaussian blur, using the gaussWinSize parameter, with window size of 5 frames. The background baseline is subtracted from the LAMP curve. It is calculated by averaging the intensities from the six frames after the temperature of the experiment reached the optimal LAMP temperature. Time to positive (TTP) was calculated as the frame at which the intensity crossed a threshold of 250 RFU, defined using the "threshold" parameter. The derivative of the LAMP curve was calculated and the maximum slope was determined for each curve.

Partitions of interest for melt curve analysis were identified by exceeding a minimum intensity or slope (rate) threshold. Once selected, the average partition intensities during HRM were determined and smoothed similarly as for the LAMP curves. Using the temperature and time data from the .txt file, the melt intensities were replotted with temperature as the x-axis. The negative derivative of the melt curve was used to calculate the peak melt temperature for each partition. We have reported other processing parameters previously (22).

The following processing parameters were used:

- mask_thresh = .08:.002:.16;
- areaBound = [20 45] Pixels;

- threshold = 250 RFU;
- gaussWinSize = 5 Frames;
- maxSlope = 200 RFU/Frame;
- maxSlopeThreshold = 30 RFU/Frame;
- time between Frames (“time_spacing”) = 30 sec;
- LAMP Start (“LAMP_start”) = Frame 1;
- LAMP End (“LAMP_end”) = Frame 185;
- melt Curve Start (“MC_start”) = Frame 194;
- melt Curve End (“MC_end”) = Frame 241;

*Propagation of LOD uncertainty*

The digital loading of molecules onto a chip is a Poisson process. However, because the number of counting events is large, we can assume the counting events are approximately normally distributed, parameterized by a mean and standard deviation, σ. When measured quantities are normally distributed, then the error in any derived quantities can be found with the following expression (46):

**Equation 7-3**

$$\sigma_x^2 = \left(\frac{\delta x}{\delta a}\right)^2 \sigma_a^2 + \left(\frac{\delta x}{\delta b}\right)^2 \sigma_b^2 + \ldots \left(\frac{\delta x}{\delta n}\right)^2 \sigma_n^2$$

In our specific scenario, the variance of the derived quantity LOD (Equation 1) can be expressed as:

**Equation 7-4**

$$\sigma_{LOD}^2 = \left(\frac{1}{[N_{True} - (N_{False} + 3\sqrt{N_{False}})]/N_{CI}}\right)^2 \left(\sigma_{C_{True}}\right)^2 + \left(-\frac{C_{True}}{\left([N_{True} - (N_{False} + 3\sqrt{N_{False}})]/N_{CI}\right)^2}\right)^2 \left(\sigma_{N_{True}}\right)^2 + \left((-\frac{C_{True}}{\left([N_{True} - \left(N_{False} + 3\sqrt{N_{False}}\right)]/N_{CI}\right)^2})(-\frac{1}{N_{CI}} - \frac{3}{2N_{CI}\sqrt{N_{False}}})\right)^2 \left(\sigma_{N_{False}}\right)^2$$

*Impact of buffer conditions on specific and nonspecific amplification and Tm*

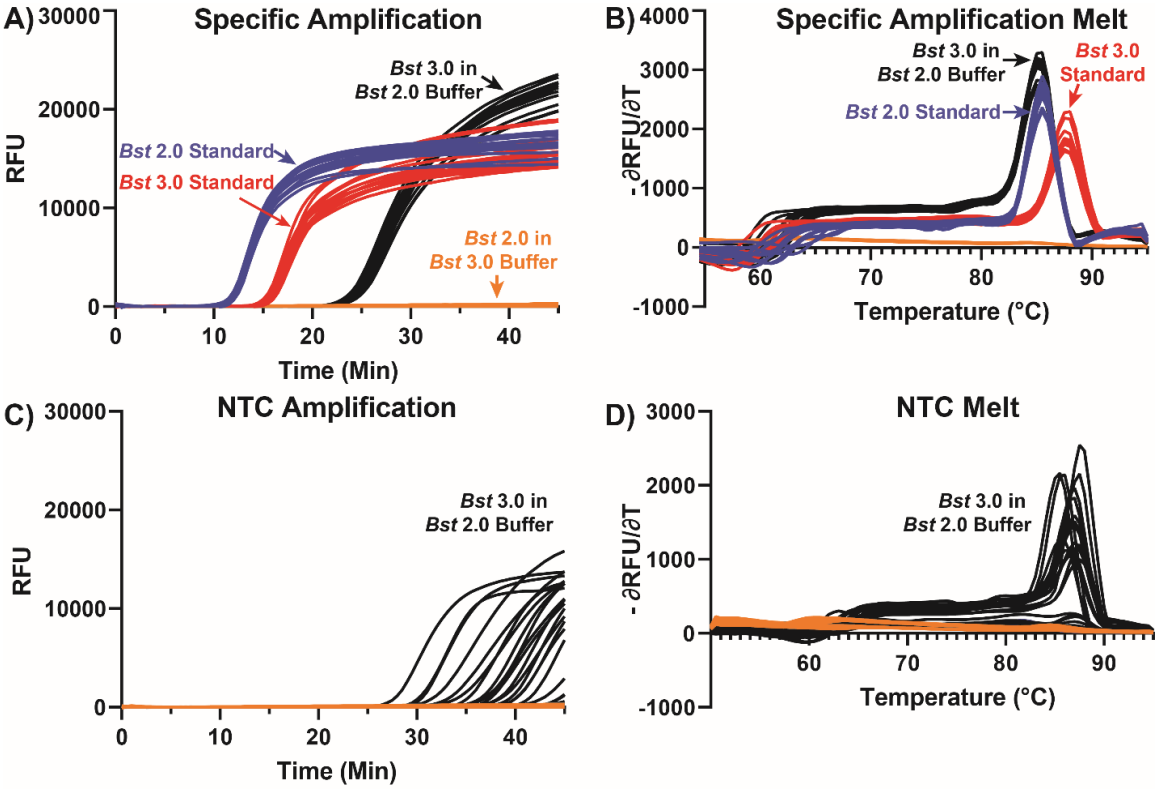


**Figure 7.11: Amplification and melting temperature (Tm) curves of *Chlamydia trachomatis* in bulk reactions indicate enzyme sensitivity to varying buffer conditions.**

(A-B) Amplification curves in the presence of template (A) and Tm curves (B). (C-D) Nonspecific amplification curves in the no-template control (NTC) (C) and the associated Tm curves (D).

**Table 7-1: Summary table of LAMP time to positive (TTP) and product melting temperature (Tm) of *Chlamydia trachomatis* amplicons under a range of buffer conditions.**

| Condition | Sample | TTP (Min) | Tm (°C) | Amplifications |
|---|---|---|---|---|
| + Control | *Bst* 2.0, Standard (7mM $Mg^{2+}$) | 12.71±0.23 | 85.50±0.00 | 12/12 |
| + Control | *Bst* 3.0, Standard (8mM $Mg^{2+}$) | 16.33±0.30 | 87.58±0.19 | 12/12 |
| + Control, NTC | *Bst* 3.0, Standard (8mM $Mg^{2+}$), NTC | 37.84±1.59 | 91.00±0.20 | 44/45 |
| Switch Buffers | *Bst* 2.0, *Bst* 3.0 Buffer | N/A | N/A | 0/24 |
| Switch Buffers | *Bst* 3.0, *Bst* 2.0 Buffer | 24.95±0.41 | 85.08±0.19 | 12/12 |
| Switch Buffers, NTC | *Bst* 2.0, *Bst* 3.0 Buffer; NTC | N/A | N/A | 0/24 |
| Switch Buffers, NTC | *Bst* 3.0, *Bst* 2.0 Buffer; NTC | 30.75±7.62 | 86.85±0.72 | 20/24 |

We next wished to determine if the behavior associated with nonspecific amplification was inherent to the polymerase or the buffer for both *Bst* polymerases. Buffer composition may influence nonspecific amplification more than the selection of polymerase. We conducted bulk reactions in the presence and absence of template using the standard buffer compositions (Materials and Methods) and the same reactions with each polymerase in the opposite buffer. When we used *Bst* 2.0 polymerase with the *Bst* 3.0 buffer, amplification failed to occur in both the presence and absence of template. When we used *Bst* 3.0 polymerase with *Bst* 2.0 buffer, we observed (i) an 8.6 min delay in TTP (from 16.33±0.30 min to 24.95±0.41 min) in the presence of template (ii) earlier nonspecific amplification in the absence of template, and (iii) greater variation in TTP (from 37.84±1.59 min to 30.75±7.62 min). From these data, we concluded that the difference in nonspecific amplification between conditions was an issue inherent to polymerase selection.

We next tested if the differences in Tm of the target amplicons were due to buffer components. We observed similar sequencing results for these products, but differing Tm. We conducted bulk reactions in the presence of template using the standard buffer

composition (Materials and Methods) and the same reactions with each polymerase in the opposite buffer. When all buffer components were switched between the polymerases, *Bst* 2.0 failed to amplify, whereas *Bst* 3.0 resulted in amplicons with Tm similar to *Bst* 2.0 in standard conditions (85.08±0.19 °C). We concluded the *Bst* polymerase produced similar specific products and differences in Tm were due to differences in buffer conditions.

**Table 7-2: List of abbreviations used in Figure 7.2, Figure 7.4.**

| Abbreviation | Long Form |
|---|---|
| BIP | Backward Inner Primer |
| rcBIP | Reverse Compliment of BIP |
| prcBIP | Partial Reverse Compliment of BIP |
| FIP | Forward Inner Primer |
| rcFIP | Reverse Compliment of FIP |
| pFIP | Partial FIP |
| loopB2 | Backward Loop Primer |
| rcloopb2 | Reverse Compliment of Backward Loop Primer |
| TargetDNA | CT Target DNA sequence |
| rcTargetDNA | Reverse Compliment CT Target DNA sequence |
| Rand | Random Insert |

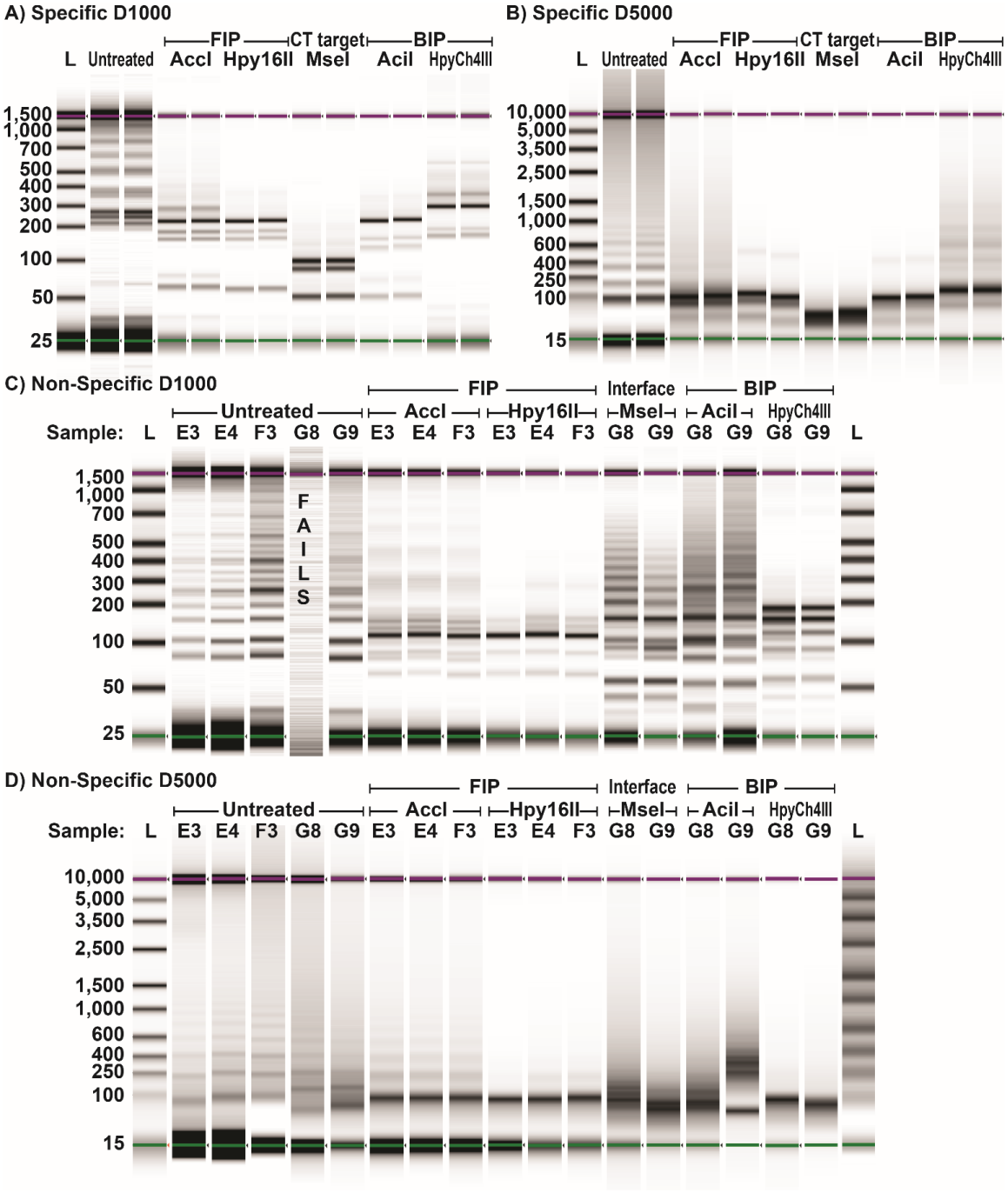


**Figure 7.12: Composite images of restriction digestion of *Chlamydia trachomatis* (CT) bulk amplification products.**

Digestion of specific amplification products using a D1000 DNA ScreenTape (A) and a D5000 DNA ScreenTape (B). Digestion of nonspecific amplification products

using a D1000 DNA ScreenTape (C) and a D5000 DNA ScreenTape (D). AccI and Hpy16II target restriction site in FIP, MseI in the specific products targets a region within the CT sequences, and in the presence of nonspecific amplification products targets the interface (synthesis across a discontinuous junction) of FIP and BIP. AciI and HpyCh4III target restriction endonuclease sites within BIP.

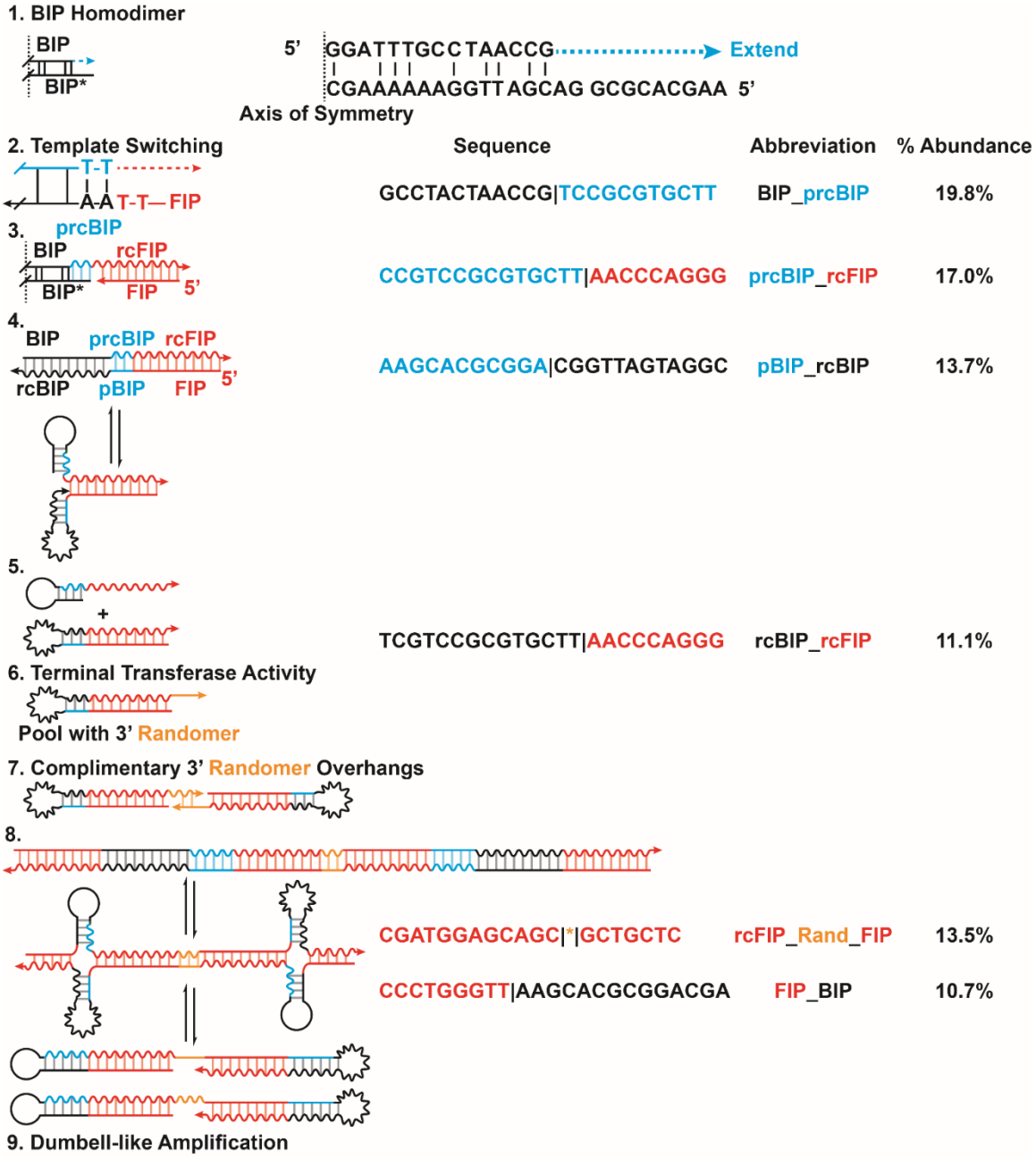


**Figure 7.13: Illustration of a simplified mechanism for nonspecific amplification products in LAMP reactions.**

Structures and intermediates are labeled with numbers. Percentage abundance reported from **Figure 7.2, Sample E2**.

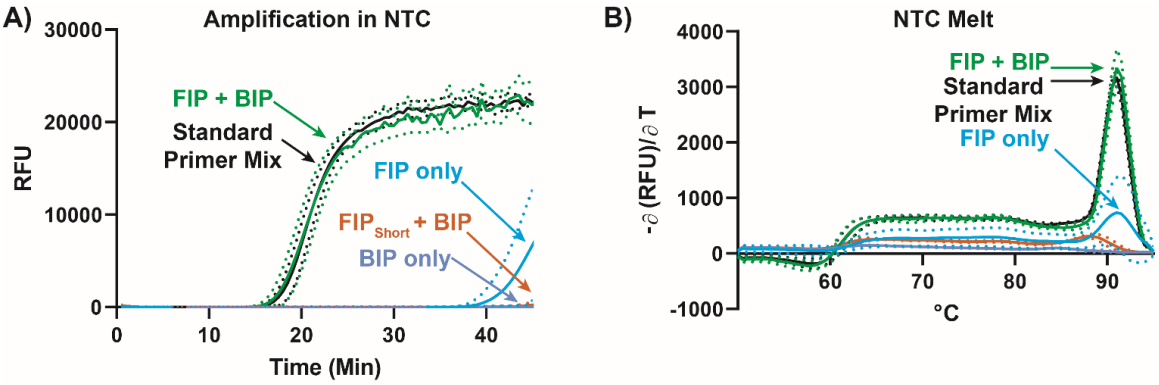


**Figure 7.14: Amplification and melting temperature (Tm) curves of *Chlamydia trachomatis* (CT) in a bulk reaction using multiple primer sets show reduced nonspecific amplification upon elimination of primer microhomology.**

Plots of average fluorescence as a function of time during the LAMP reaction in the NTC (A) and the corresponding derivative plot of fluorescence as a function of temperature (B). N per condition = 12.

**Table 7-3: Time to mean positive and Tm in bulk reactions using multiple primer sets.**

N per condition = 12.

| Sample | Time to Positive (Min) | Tm (°C) |
|---|---|---|
| FIP only | 42.3±1.8 | 91.7±0.8 |
| BIP only | n/a | n/a |
| FIP + BIP only (No Other Primers) | 18.1±1.1 | 91.0±0.1 |
| Standard Primer Mix | 18.3±0.7 | 91.0±0.0 |
| $FIP_{Short}$ + BIP | n/a | n/a |

We analyzed multiple primer sets (**Table S3**) to determine if the nonspecific amplification species produced in the NTC were indeed produced from a combination of primers, as

described by the sequencing data in **Figure 7.2** and the mechanism proposed in **Figure 7.4.** We also wished to test whether nonspecific amplification could occur by single primers, as is known to occur. We conducted bulk reactions in the absence of template using *Bst* 3.0 and the standard primer mixture, FIP and BIP in combination, and the Inner Primers alone and compared the TTP and Tm of these mixtures. The standard primer mixture (consisting of Inner, Outer, and Loop primers) had nonspecific amplification at 18.3±0.7 min with uniform Tm of 91.0±0.0 °C. When the Outer and Loop primers were removed, leaving only FIP and BIP, the mixture amplified with similar TTP and Tm (18.1±1.1 min and 91.0±0.1 °C, respectively) as the standard mixture. In contrast, using BIP alone failed to amplify within 45 min, and FIP alone amplified much later (42.3±1.8 min) and with different Tm (91.7±0.8) than FIP and BIP together or the standard primer mixture. We thus concluded that both FIP and BIP were required to generate the nonspecific products we observed.

The mechanism proposed in **Figure 7.4** requires an interaction between BIP and FIP via microhomology of the 3' of FIP. To confirm the suspected interaction between FIP and BIP, we removed two bases from the 3' end of the FIP primer (hereafter $FIP_{Short}$). In bulk reactions using $FIP_{Short}$ and BIP with *Bst* 3.0 in the absence of template, we did not observe nonspecific amplification within 45 min. Consequently, we concluded, some of the nonspecific amplification was due to an interaction of the 3' of FIP with BIP.

We next ran the modified primer set in digital LAMP using *Bst* 3.0 to improve our understanding of what occurs at the single-molecule level when primer microhomology is eliminated. We ran three chips in the presence of template and three chips in the absence of template, using the standard primer set (**Figure 7.14A**), and compared the results to the same experiments run with a primer set with $FIP_{Short}$ (**Figure 7.14B**). We observed a significant increase in the percentage of copies detected when using $FIP_{Short}$ (**Figure 7.14C**) using a two-tailed paired t-test ($P = 0.002$), without a difference in TTP (**Table 7-3**). The use of $FIP_{Short}$ did not significantly impact nonspecific amplification products with low Tm in any pairwise ANOVA comparison (**Figure 7.14D,E**). However, we observed a 10-100 fold decrease in nonspecific products with high Tm (**Figure 7.14F, G**). In the absence of template,

nonspecific amplification was reduced (**Figure 7.14E**); whereas in the presence of template, the number of nonspecific amplification products with high Tm was significantly lower at all time points (**Figure 7.14G**).

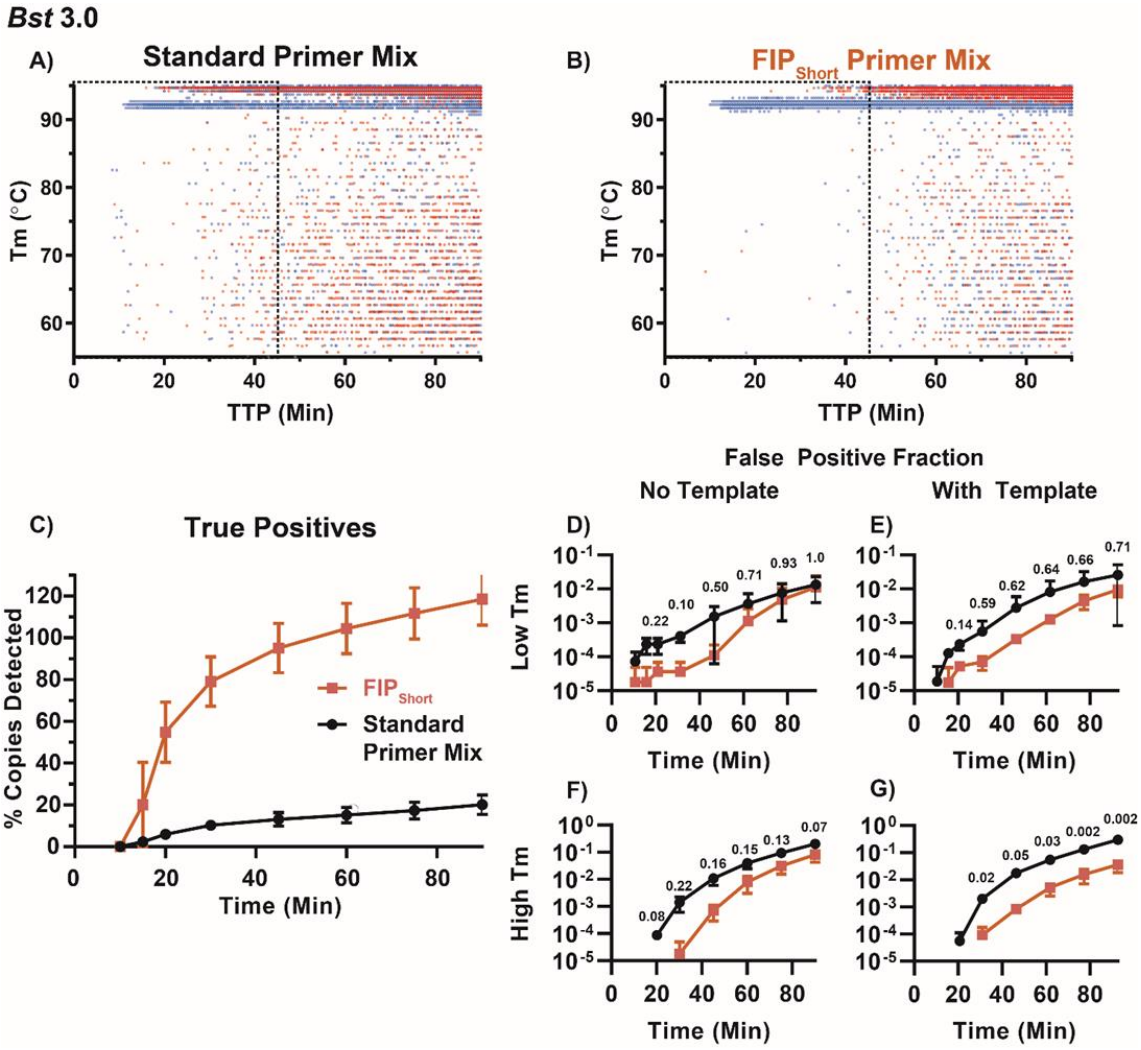


**Figure 7.15: Digital, single-molecule plots of specific and nonspecific amplification for multiple primer sets of *Chlamydia trachomatis* show significantly reduced nonspecific amplification with high melting temperature (Tm) upon elimination of primer microhomology.**

(A-B) Individual amplification events using *Bst* 3.0 and a primer mixture where FIP is replaced with $FIP_{Short}$ (A) and the standard primer mixture (B). Blue indicates amplification events in the presence of template; red indicates amplification in the absence of template (NTC). A box is placed around events that occur within 45 min, corresponding to the bulk amplification time. Partitions are rendered at 50% opacity. (C) Plot of the percentage of copies detected (specific amplification) as a function of time. (D-E) The fraction of partitions with nonspecific amplification with Tm less than the specific amplification as a function of time in the absence of template (D) and in the presence of template (E). (F-G) The fraction of partitions with nonspecific amplification with Tm greater than the specific amplification in the NTC as a function of time (F) and in the presence of template (G). Within panels D-G, pairwise *P*-values by t-test are written above each time point.

**Table 7-4: Digital, single-molecule comparison of specific and nonspecific amplification for multiple primer sets of *Chlamydia trachomatis* using *Bst* 3.0.**

| | Time to mode positive (min) |
|---|---|
| Standard Primer (Set 1) | 15.7±2.7 |
| (Set 2) | 13.7±0.9 |
| Modified Primer | 15.0±1.7 |

The decrease in nonspecific products with high Tm, upon elimination of the microhomology between FIP and BIP, is consistent with the formation of a nonspecific product predicted by the proposed mechanism in **Figure 7.4**. However, the continued existence of nonspecific products indicates it is possible to form a variety of nonspecific products. Our results indicate that nonspecific products with high-Tm occur even with further primer optimization. The formation of products with high Tm is consistent with our proposed mechanism of branched, mesh-like network. Further investigation should determine if this problem is ubiquitous, even in optimized systems. Additionally, the delay in nonspecific amplification in digital could

explain why we did not observe these products in bulk (and thus cannot sequence them).

We believe the mechanism described in **Figure 7.4** is potentially applicable to other primer sets. Amplification observed by FIP alone may follow a similar amplification scheme to **Figure 7.4** via homo-dimerization (**Figure 7.16A**), non-templated synthesis, hairpin dimerization (**Figure 7.16B**), and eventually dumbbell-like amplification (**Figure 7.16D,E**). We observe products consistent with these structures in some of the sequencing data (e.g. **Figure 7.2, Well E1**, which contains elevated rcFIP_pFIP and rcpFIP_FIP).

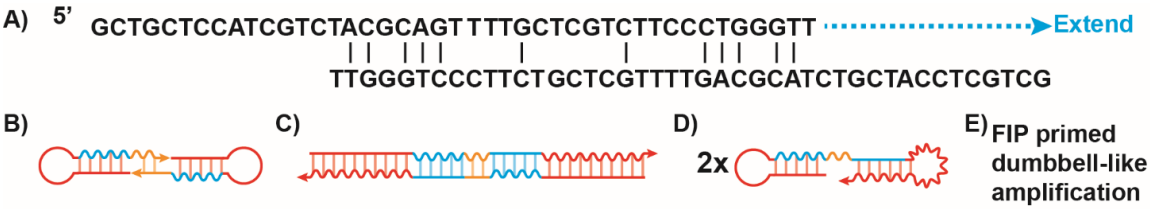


**Figure 7.16: Illustration of a mechanism for amplification of FIP alone.**
After 3' extension of a FIP homodimer (A), random nucleotides may be incorporated (orange) resulting in self-complimentary hairpins (B). The extension of these hairpins products produce (C): top strand, FIP-prcFIP-rand-pFIP-rcFIP. Upon melting, two self-amplifying dumbbell structures can be produced (D), and undergo further LAMP-like amplification primed by FIP (E).

**Table 7-5: Table group of NGS of Randomer inserts within Bulk Sample E1.**

| E1 | |
|---|---|
| **Length** | **Percent** |
| 4 | 53.1 |
| 2 | 41.0 |
| 3 | 2.6 |
| 5 | 1.8 |
| 6 | 1.1 |

| E1: Length n=4 | |
|---|---|
| **Sequence** | **Percent** |
| CGTT | 38.6 |
| AACG | 33.1 |
| AGTT | 8.1 |
| AACT | 7.5 |
| GGTT | 2.5 |
| AACC | 2.5 |
| CGTC | 1.4 |
| GACG | 1.2 |

| E1: Length n=2 | |
|---|---|
| **Sequence** | **Percent** |
| AT | 28.4 |
| GT | 15 |
| AC | 13.8 |
| CC | 10.3 |
| GG | 10.2 |
| CT | 9.1 |
| AG | 8.3 |
| GC | 3.8 |

**Table 7-6: Table group of NGS of Randomer inserts within Bulk Sample E2.**

| E2 | |
|---|---|
| **Length** | **Percent** |
| 3 | 53.4 |
| 11 | 13.8 |
| 4 | 12.7 |
| 2 | 9.0 |
| 5 | 3.7 |
| 8 | 2.9 |
| 14 | 1.7 |

| E2: Length n=3 | |
|---|---|
| **Sequence** | **Percent** |
| CGT | 17.9 |
| ACG | 16.5 |
| ACT | 12.6 |
| AGT | 12.4 |
| ACC | 7.2 |
| GGT | 6.5 |
| CCC | 6.1 |
| GGG | 5.3 |

| E2: Length n=11 | |
|---|---|
| **Sequence** | **Percent** |
| AGCAGCAGCAG | 20.2 |
| CTGCTGCTGCT | 18.9 |
| ATGCTGCTGCT | 19.7 |
| AGCAGCAGCAT | 18.4 |
| AGCAGCAGCAC | 4.7 |
| GTGCTGCTGCT | 4.6 |

**Table 7-7: Table group of NGS of Randomer inserts within Bulk Sample F1.**

| F1 | |
|---|---|
| **Length** | **Percent** |
| 5 | 47.9 |
| 3 | 32.1 |
| 4 | 16.6 |
| 2 | 2.4 |

| F1: Length n=5 | |
|---|---|
| **Sequence** | **Percent** |
| GTTGT | 17.8 |
| ACAAC | 16.3 |
| GTTGC | 15.3 |
| GCAAC | 13.4 |
| ATTGC | 8.4 |
| GCAAT | 8.4 |
| ATTGT | 7.7 |
| ACAAT | 7.2 |

| F1: Length n=3 | |
|---|---|
| **Sequence** | **Percent** |
| CGT | 14.8 |
| ACG | 13.7 |
| CGC | 13.7 |
| GCG | 12.3 |
| AGC | 8.9 |
| GCT | 8.3 |
| ACT | 8.3 |
| AGT | 8.3 |

*Does removing outliers impact the distribution of maximum rates?*

Occasionally, we observed outlier data points in maximum rate. We asked what caused one point (green circle, max rate 56 RFU, **Figure 7.12A**) to separate from the majority of the data (17 to 30 RFU/30 sec), if these points were common, and if these points were likely to misrepresent the max rate data. We determined the individual trace corresponding to the outlier amplification event (green trace, **Figure 7.12B**) and observed that the maximum rate for this partition was at 52.5 min, corresponding to a fluctuation in the plateau phase of amplification (dotted line).

We hypothesized that the maximum rate should occur at the observed initial moment of exponential amplification, often slightly before the fluorescence TTP threshold (250 RFU) is reached. To test this hypothesis, we determined the frame (2 per minute) where the amplification trace reached the TTP. From this frame, we subtracted the frame where maximum rate was calculated and plot it against maximum rate (**Figure 7.12C**). Values greater than zero represent partitions where the frame the maximum rate occurs before the fame of TTP, while negative values occur when fame the max rate occurs is after the frame

of TTP. We draw a vertical line separating partitions that occur more than 15 min after the TTP (left), from all other partitions.

For the case of *Bst* 2.0, we observed that the mode max rate occurred before the fluorescence TTP by 1 frame (30 sec). Of the 9099 partitions exceeding the 250 RFU threshold, 821 (9.02%) were more than 15 min after the TTP. We expect these partitions to have max rate within the noise of the plateau phase.

A similar trend was observed for *Bst* 3.0 (**Figure 7.12D**). With *Bst* 3.0, the mode max rate occurred 2 frames before the fluorescence TTP (1 min). This value is later than *Bst* 2.0 and is consistent with a slower max rate for *Bst* 3.0 than for *Bst* 2.0. Of the 24,466 partitions reaching the 250 RFU threshold, 1113 (4.55%) were more than 15 min after TTP.

To determine whether removing the partitions with max rate more than 15 min after the TTP impacted the distribution of enzymatic rates, we plotted the fractional cumulative distribution function (CDF) of max rate for all partitions (blue), and the same fractional CDF removing those points more than 15 min after the fluorescence intensity based TTP (red) for *Bst* 2.0 (**Figure 7.12E**) and *Bst* 3.0 (**Figure 7.12F**). Performing a non-parametric based Kolmogorov–Smirnov test to compare the exclusion of partitions with late max rate indicated non-significance between the two CDFs (*Bst* 2.0 P=0.3255, and *Bst* 3.0 $P = 0.1236$). Thus, we concluded removing late max rate data from the distributions did not impact the CDFs, and therefore does not significantly impact the integrity of our data reporting.

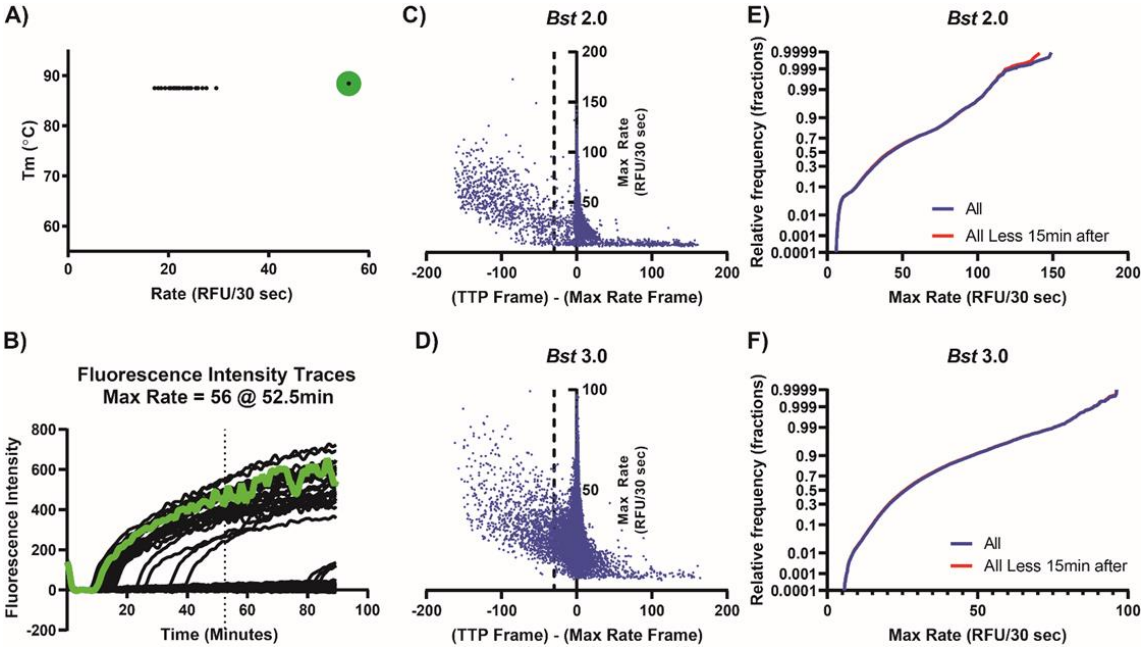


**Figure 7.17: Removing outlier data in max rate does not significantly impact summary data.**

Plot of observed melting temperature (Tm) as a function of maximum rate, with a possible outlier point highlighted in green (A). Fluorescence traces of individual partition amplification events, with the possible outlier partition's trace highlighted in green (B). The maximum rate for the green trace occurred at 52.5 min (dotted line), corresponding to a fluctuation in the plateau phase of amplification. Plot of maximum rate as a function of the difference between the TTP and max rate frames using *Bst* 2.0 (C) and *Bst* 3.0 (D). Partitions lower than the dashed vertical line represent partitions whose max rate occurred more than 15 min after the TTP frame. Fractional Cumulative Distribution Plots of maximum rate for *Bst* 2.0 (E) and *Bst* 3.0 (f), where the CDF includes all possible partitions (blue), and the same fractional CDF removing those points more than 15 min after the Fluorescence Intensity based TTP (red).

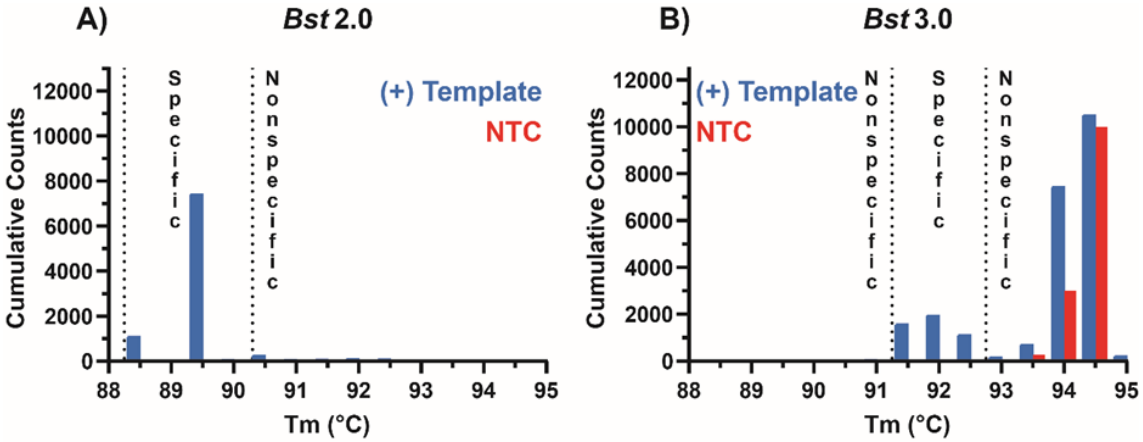


**Figure 7.18: Histogram plots of Tm after 90 min of digital LAMP targeting CT in the presence of template (blue) and NTC (red) can be used to distinguish specific from nonspecific amplification.**

Tm of amplification using *Bst* 2.0 (A) and *Bst* 3.0 (B). Dashed lines indicates the upper and lower bounds used for separating specific and nonspecific amplification. *Bst* 2.0: 88.5-90.3°C, *Bst* 3.0: 91.25-92.75 °C. Bin width in both graphs 0.5 °C, with the (+) template left of the tick and NTC right of the tick. NTC is illustrated with red bars, and the presence of template with blue bars.

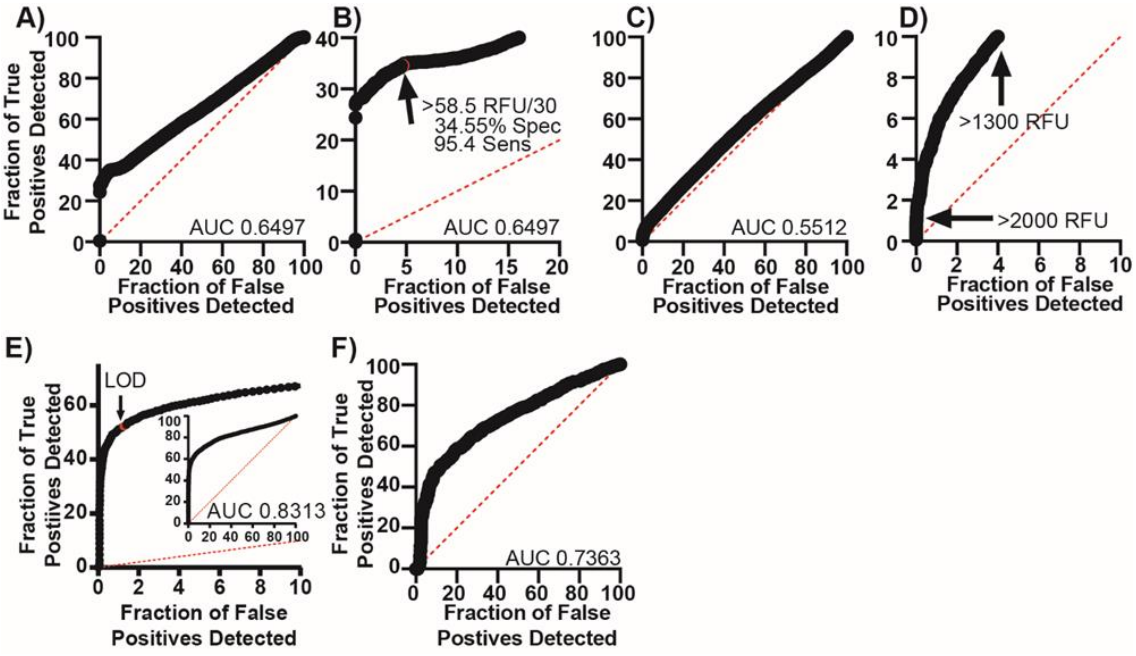


**Figure 7.19: Receiver operating characteristic (ROC) curves using HRM to determine optimal performance of dLAMP assays.**

(A) ROC curve using *Bst* 3.0, plotting the fraction of true positives detected versus the fraction of false positives detected using a threshold on max rate. (B) ROC curve using *Bst* 3.0, plotting the fraction of true positives detected less than 40% versus the fraction of false positives detected less than 20% using a threshold on maximum rate. Arrow indicates corresponding LOD. (C) ROC curve using *Bst* 3.0, plotting the fraction of true positives detected versus the fraction of false positives detected using a threshold on final intensity of the partition. (D) ROC curve using *Bst* 3.0, plotting the fraction of true positives detected less than 10% versus the fraction of false positives detected less than 10% using a threshold on final intensity of the partition. Arrows indicate final-intensity thresholds of >2000 RFU and >1300 RFU. (E) ROC curve using *Bst* 3.0, plotting the fraction of true positives detected versus the fraction of false positives detected using a threshold on TTP. Arrow indicates LOD. (F) ROC curve using *Bst* 2.0, plotting the fractions of true versus false positives detected using a threshold on TTP.

*Summary Data of Mode TTP*

**Table 7-8: Time to mode positive in minutes.**

N=3 chips per set. Human Haploid Genome Equivalents (HHGE) are per microliter.

| HHGE per µL | 0 | 0.01 | 1 | 100 | 5000 |
|---|---|---|---|---|---|
| *Bst* 2.0 | 11.8 ± 0.2 | 11.7±0.2 | 11.3±0.2 | 11.7±0.6 | 16.3±2.7 |
| *Bst* 3.0 (Set 1)<br>(Set 2) | 15.7± 2.7<br>13.7± 0.9 | 13.8±1.2 | 18.2 ±4.4 | 14.7± 1.7<br>17.2± 2.1 | <br>17.2± 2.1 |

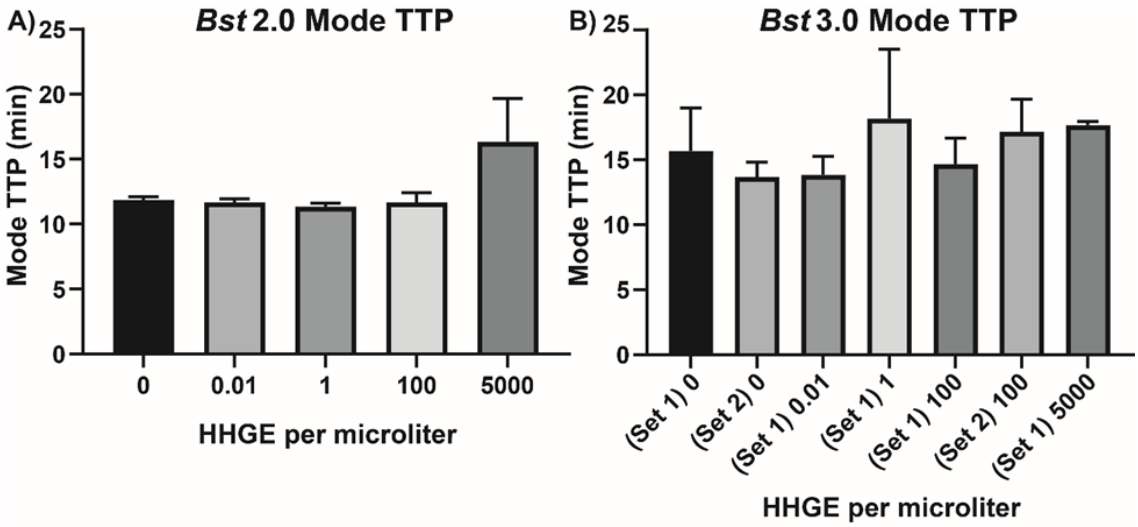


**Figure 7.20: Time to mode positive for *Bst* 2.0 (A) and *Bst* 3.0 (B) under variable concentrations of host human genomic DNA (hgDNA).**

Human Haploid Genome Equivalents (HHGE) are per microliter.

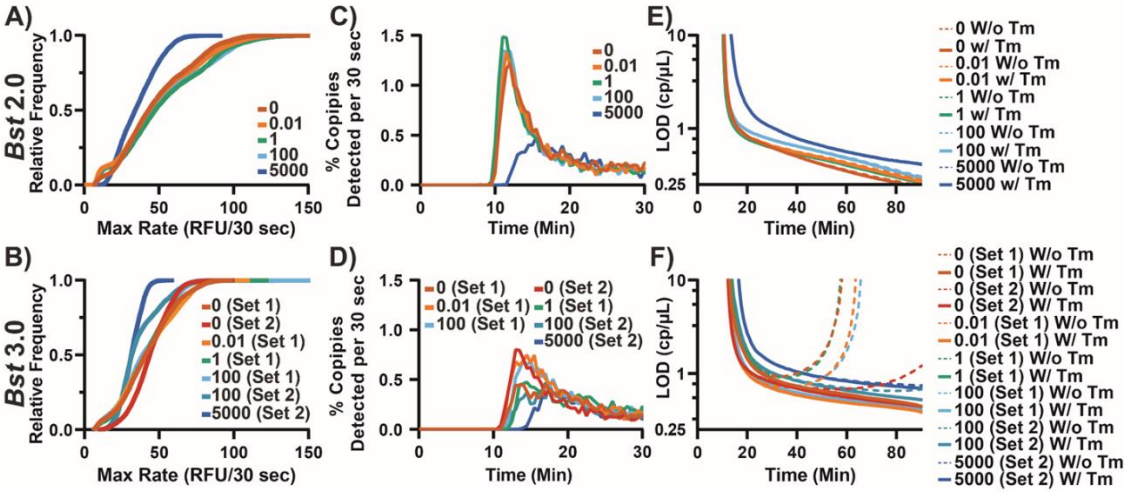


**Figure 7.21: Evaluation of the impact of gDNA on assay performance.**

Fractional cumulative distribution function (CDF) of maximum rates of amplification using *Bst* 2.0. (A) and *Bst* 3.0 (B) CDFs are plotted as the sum of replicates. Distribution plot of time to fluorescence threshold for *Bst* 2.0 (C) and *Bst* 3.0 (D) using arithmetic mean. LOD as a function of time using *Bst* 2.0. (E) and *Bst* 3.0 (F).

**Table 7-9: Tabular form of % copies detected from Figure 7.9 using *Bst* 2.0.**

| Time (Min) | 0 HHGE per µL | 0.01 HHGE per µL | 1 HHGE per µL | 100 HHGE per µL | 5000 HHGE per µL |
|---|---|---|---|---|---|
| 10 | 0.01±0.02 | 0.00±0.00 | 0.04±0.03 | 0.02±0.02 | 0.00±0.00 |
| 15 | 8.21±0.72 | 8.35±0.56 | 9.42±0.56 | 8.98±0.81 | 1.67±2.32 |
| 20 | 11.92±0.35 | 12.04±0.20 | 12.86±0.54 | 12.34±1.44 | 5.24±3.69 |
| 30 | 15.94±1.13 | 15.41±0.36 | 16.15±0.66 | 15.65±1.98 | 9.19±2.66 |
| 45 | 22.20±4.37 | 19.30±0.85 | 20.16±1.12 | 19.84±1.73 | 13.42±1.99 |
| 60 | 28.88±8.07 | 23.68±2.49 | 24.94±3.05 | 25.00±1.11 | 16.96±2.03 |
| 75 | 36.10±11.86 | 29.93±5.30 | 31.24±5.83 | 31.81±2.83 | 20.34±2.17 |
| 90 | 43.77±14.98 | 37.47±8.62 | 38.47±10.05 | 40.69±5.32 | 23.12±2.35 |

**Table 7-10: Tabular form of % copies detected from Figure 7.10 using *Bst* 3.0.**

| Time (Minutes) | 0 HHGE per µL (Set 1) | 0 HHGE per µL (Set 2) | 0.01 HHGE per µL (Set 1) | 1 HHGE per µL (Set 1) | 100 HHGE per µL (Set 1) | 100 HHGE per µL (Set 2) | 5000 HHGE per µL (Set 2) |
|---|---|---|---|---|---|---|---|
| 10 | 0.00±0.00 | 0.00±0.00 | 0.00±0.01 | 0.00±0.00 | 0.00±0.00 | 0.00±0.00 | 0.00±0.00 |
| 15 | 2.28±1.99 | 4.13±0.98 | 3.83±2.47 | 1.71±1.54 | 2.86±1.04 | 1.37±1.89 | 0.05±0.08 |
| 20 | 5.96±2.47 | 8.15±0.31 | 8.93±2.44 | 5.21±4.50 | 7.89±0.66 | 4.81±2.04 | 3.04±0.93 |
| 30 | 10.19±2.48 | 11.23±0.23 | 13.33±1.84 | 10.26±3.32 | 12.41±0.24 | 8.82±1.06 | 6.86±1.05 |
| 45 | 13.02±3.28 | 14.07±0.80 | 16.74±1.87 | 13.92±2.80 | 15.67±0.38 | 11.60±1.12 | 9.35±1.09 |
| 60 | 15.09±3.68 | 16.28±1.71 | 19.13±1.83 | 16.37±2.69 | 17.89±0.29 | 13.81±1.70 | 10.92±1.38 |
| 75 | 17.25±4.02 | 18.38±3.13 | 21.00±2.20 | 18.61±3.05 | 19.95±0.45 | 15.62±2.34 | 12.11±1.16 |
| 90 | 20.11±4.71 | 20.44±4.50 | 23.97±3.58 | 21.13±3.99 | 23.00±0.87 | 17.37±3.16 | 13.10±1.81 |

*Caption for 4D videos*

Videos plot the TTP, max rate, final intensity, and Tm data of both specific and nonspecific amplification reactions using either *Bst* 2.0 (Video 1) and using *Bst* 3.0 (Video 2). Time to positive (TTP), max rate, and melting temperature (Tm) are plotted on the axes; final intensity is indicated by the color of each data point (scale provided in **Figure 7.6Q-R**).

*Chapter 8*

# ADDITIONAL TOOLS FOR SAMPLE-TO-ANSWER POINT-OF-CARE NUCLEIC ACID AMPLIFICATION TESTING

## Introduction

The development of a fully-integrated sample-to-answer point-of-care NAAT which meets all of the ASSURED criteria remains a critical challenge for the diagnostics field. NAAT is inherently complex, and to realize a fully-integrated sample-to-answer point-of-care diagnostic requires many components which can perform multiple steps: sample transfer, nucleic acid extraction, nucleic acid amplification, readout, and analysis. Each component must fulfill the ASSURED criteria individually (e.g. Affordable, User-friendly, Rapid, Robust, Equipment-free, Deliverable). These characteristics must further be retained when these components are combined, and the fully-integrated test must additionally be Sensitive and Specific. A system which integrates of all of these components while meeting performance requirements has yet to be realized.

In this chapter, I develop a fully-integrated sample-to-answer point-of-care NAAT kit.[1] The test kit is composed of the following components: (1) meter-mix device presented in Chapter 4, (2) sample preparation module, (3) amplification module, (4) cell-phone readout, (5) automated MATLAB image processing, and (6) an automated base station. I will elaborate on the design of each component (with the exception of the meter-mix device) followed by an evaluation of integrated device performance.

## Sample preparation module

EJ designed the simultaneous pre-pressurization pumping lid approach and contributed to sealing surface improvements. Created the 6x pressure sensor capable of measuring all chambers simulataneously using an adaptation of David Selck's previously developed LabView script.

Daan Witters, Stefano Begolo, and Feng Shen all contributed to the design of the sample preparation module.

*Design*

The sample preparation module takes lysed sample (mixed with Zymo buffers DNA/RNA shield and DNA/RNA lysis buffer) as input. Both DNA and RNA are purified on a silica column using NA extraction buffers and eluted with either water or Tris-EDTA (TE) buffer. There are three innovations which improve the performance of the sample preparation module over existing centrifugation protocols. First, the sample preparation module uses an additional two-phase wash buffer as presented in Chapter 2, which improves extraction purity. Secondly, the sample preparation module uses positive pressure to push liquids through the column rather than a centrifugation. This allows the sample preparation module to be smaller, more portable, and 3D-printed. Lastly, the sample preparation module uses SlipValve technology, which reduces user interactions resulting in a quick 4-min extraction.

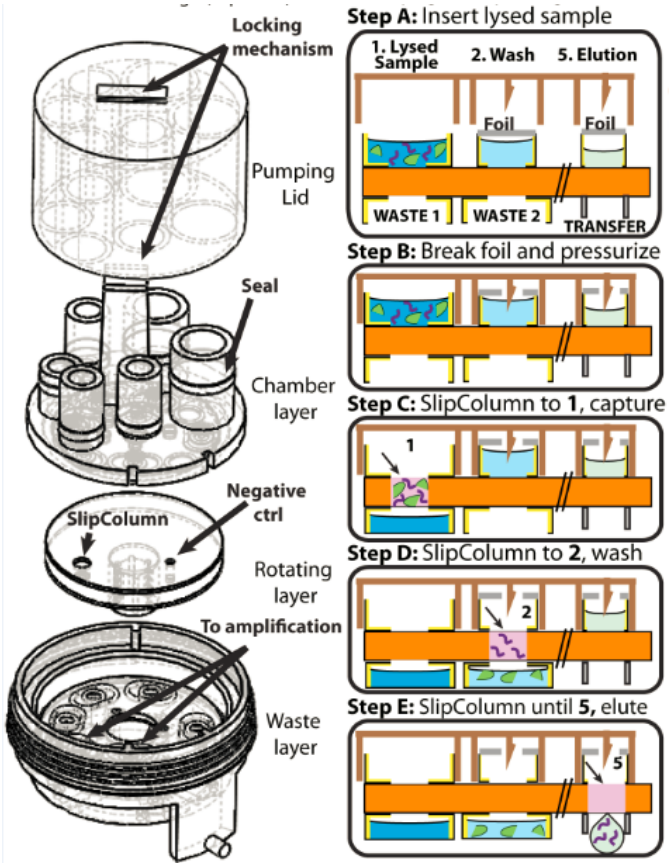


**Figure 8.1: Sample preparation module design**

(left) Solidworks exploded view showing pumping lid to generate and hold positive pressure, chamber layer to hold (1) lysed sample, (2) Zymo viral wash buffer, (3) 1-undecanol two-phase wash, (4) air push, (5) elution, and (6) negative control, rotating layer which houses the SlipColumn, and a waste layer to capture flow-through waste. (right) Schematic showing the steps to use the sample preparation module. The user adds the lysed sample (step A), pushes down the pumping lid (step B), and presses start (steps C-E).

*Pressurization and SlipValving*

The positive pressurize mechanism works by pushing the pumping lid onto the chamber layer. In this moment, all 6 chambers are simulataneous pre-pressurized and the pumping lid

locks into place due to the snap-fit feature. Because the chambers are well-sealed, the pressure in each chamber is maintained over the course of the 4 min extraction. When the user presses start, the motor of the base station activates the rotating layer, bringing the SlipValve (containing the silica column) below each chamber sequentially. Once the SlipValve transits below the first chamber where the lysed sample is stored, the lysed sample pushes through the silica column thereby binding DNA and RNA to the column. The motor pauses to allow all of the lysed sample to pump through to the waste layer, and then the motor automatically rotates again to the next position to pump through wash buffer. This repeat until the elution step, and the elution containing purified DNA and RNA routes automatically to the amplification module.

*Holding Pressure Validation*

To ensure that pressure is held in each chamber, I developed a pressure sensor capable of measuring the pressure in all six chambers in real-time. The pressure sensor software was developed in LabView (adaptation of program originally programmed by Dr. David Selck), and the pressure sensors were physically wired on a solderable prototyping board. After placing the pumping lid, we observed that the pressure held constant for at least 30 min. When the base station operates the rotating layer according to the pre-programmed rotation schedule, a pressure drop is observed at the appropriate time (**Figure 8.2**).

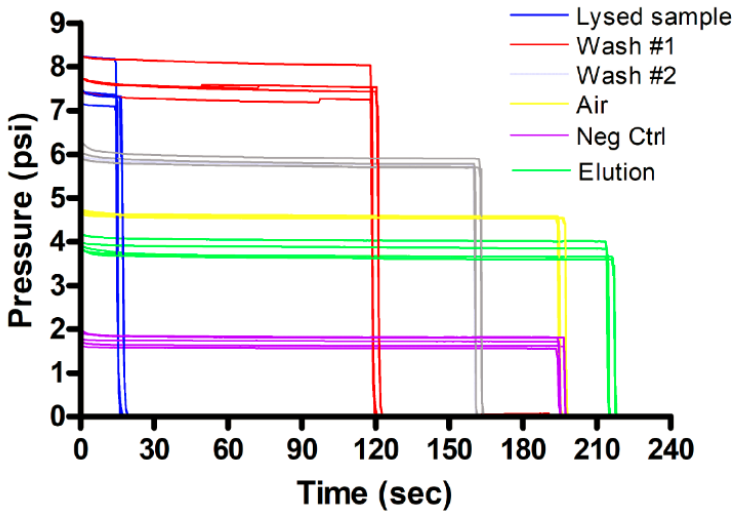


**Figure 8.2: Sample preparation module holding pressure validation**

Four repeated experiments showing the initial pre-pressurization of six chambers by placing the pumping lid onto the sample preparation module. The motor automatically moves the rotating layer and SlipValve below each chamber at the pre-programmed time.

**Parallel-filled amplification module**

EJ designed the parallel-filling to dead-end hydrophobic membrane strategy. EJ contributed to material selection and assembly practices

DW (Daan Witters) contributed to material selection and assembly practices

*Design*

Here we present the design for an easy-to-fabricate 5-plex uL volume SlipChip for running NAAT reactions. There are 2 inlets, one for the test which accesses 3 of the 5 wells and one for the control which accesses the remaining 2 wells. The bottom plate have 5 wells where

lyophilized reagents (LAMP) are pre-stored. The top plate has channels from the inlets to each well and from each well to a separate outlet. The outlet has a hydrophobic membrane to allow air to escape but blocks the flow of fluid. This strategy allows parallel filling whereby a single input fluid fills many wells at once, each containing its own set of lyophilized reactants. After well filling, the device is slipped rotationally to isolate each well. With this design, we expect no cross-contamination of rehydrated amplification reagents between different wells. Features on the outer edge of the device constrain slipping to rotation.

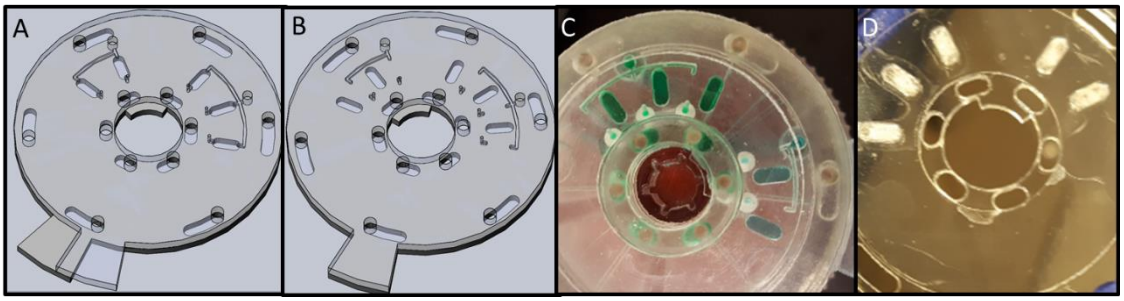


**Figure 8.3: Parallel filling of amplification modules.**

(A-B) Solidworks 3D models of parallel filling amplification modules in (A) unslipped and (B) slipped positions. (C) Parallel filling of the amplification module integrated with multi-chamber sample preparation module and filled with green (representing eluent) and blue (representing negative control) dyes. The multi-chamber pumping lid from the sample preparation module provides the filling pressure. (D) LAMP reagents lyophilized in the wells of the bottom plate.

*Fabrication and assembly*

The geometry of the amplification module was designed in CAD software and fabricated using a combination of laser cutting (Epilog Zing 24) and multi-material 3D printing. There are 4 primary components: (i) top plate, (ii) bottom plate, (iii) inner and outer pins, and (iv) inner and outer clamps. A layer of 3M 300 LSE was laminated on the top and bottom side of

the bottom plate. The top (2.1 mm) and bottom plates (1.5mm) were laser cut from cast acrylic (McMaster), using vector cutting to generate the outline, wells, and outlets and using engraving for the channels. A laser-cut donut of 0.175mm PMMA (Goodfellow Cambridge Limited) was attached to the bottom 300LSE on the bottom plate. A thin coat of Krytox GPL 205 was applied by smearing Krytox between two glass slides and stamping the top 300LSE of the bottom plate with Krytox. The appropriate LAMP mix (see below) was added to each respective well and bottom plates were lyophilized overnight. The bottom side of the top plate (without 300LSE) was smeared with a thin layer of Krytox GPL 205. A layer of pre-cut 300LSE that matches the top plate pattern was attached to the top plate. 3 mm discs polypropylene hydrophobic membranes (Sterlitech, 0.22 micro) were applied to the top 300LSE of the top plate to cover the well outlets.

For lyophilization, the 2.5% mannitol was added to the LAMP reaction, glycerol-free Bst 2.0 and AMV RT were used, and the addition of water was minimized. The AdVantage Pro EL lyophilizer shelves were set to precool at -50C with frost seal. Bottom plates were placed onto a tray and inserted into the lyophilizer. The lyophilizer performed thermal treatment by holding -50 °C with 75 min ramp and 60 min hold. Drying had 4 steps: -45 °C with 0 min ramp, 840 min hold at 100 mTorr, -20 °C with 60 min ramp, 5 min hold at 100 mTorr, 0 °C with 60 min ramp, 5 min hold at 100 mTorr, and 25 °C with 120 min ramp, 60 min hold at 100 mTorr. Product was held at 25 C and 100 mTorr until removed from the lyophilizer.

Following lyophilization, bottom plates were removed from the lyophilizer under dry nitrogen and placed into a dry nitrogen glove bag. Bottom and top plates were sandwiched together, and mostly assembled except the final clamping step using the 3D printed inner and outer pin and clamp sets. Nearly assembled amplification modules were stored with desiccant and vacuum sealed (Weston Pro-2300) under dry nitrogen in mylar bags (4 mil).

*Validation*

To validate the stability of the lyophilized reagents in the amplification module, purified nucleic acids from *Neisseria Gonorrhoeae* at 500 CFU/mL and nuclease-free water were used to rehydrate the lyophilized reagents on the amplification module. Real-time imaging was used to monitor the RT LAMP reaction in the amplification module. As shown in **Figure 8.4**, the wells containing purified nucleic acids ("positive wells") displayed increased fluorescence, with a TTP of 13.6 min, compared with 11.6 min when using standard liquid LAMP reagents in an ECO plate. The observed 2 min delay is presumably due to the delay in heating of reagents in our amplification module (~90 sec) compared with the standard ECO-machine (Illumina) heating elements.

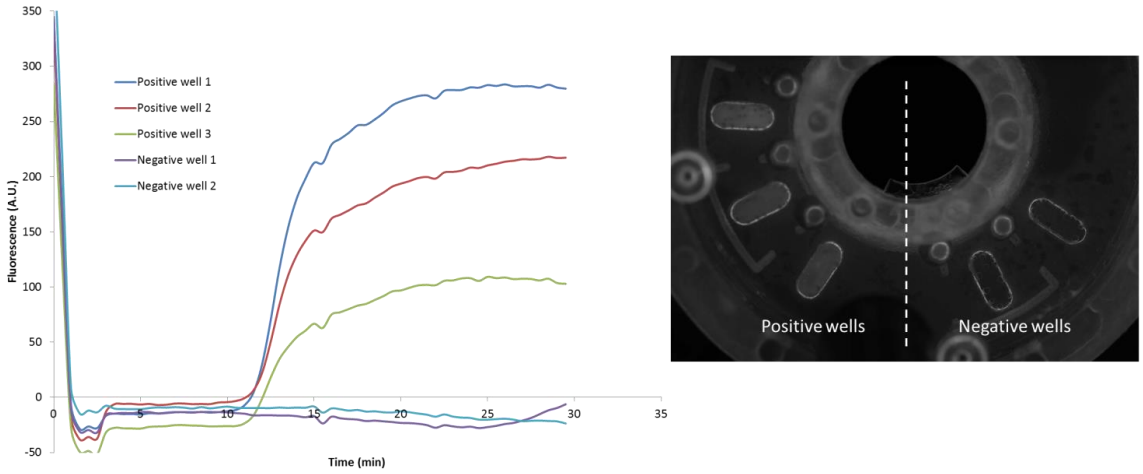


**Figure 8.4: (A) Amplification data and (B) fluorescence image showing real-time imaging of an amplification module that contained lyophilized reagents for the detection of NG.**

The positive wells of the amplification module were loaded with purified nucleic acids from NG, whereas the negative wells were loaded with nuclease-free water. The time-to-positive for the positive wells was 13.6 min, whereas there was no significant increase in fluorescence intensity in the negative wells.

**Cell-phone readout and automated analysis**

EJ designed and printed the cell-phone dongle and programmed the MATLAB code.

A cell-phone dongle was designed, 3D printed, and painted black to block out ambient light. The sample preparation and amplification module assembly directly connects to the cell-phone dongle to allow fluorescent readout of the wells. The cell-phone dongle is powered by connecting to the base station. A blue LED passes through a blue filter and shines onto each well. A cell-phone with a yellow filter on the camera is placed onto the dongle and a photo was taken. Following image capture, the photo is automatically uploaded to the cloud for automated image analysis and email delivery of results.

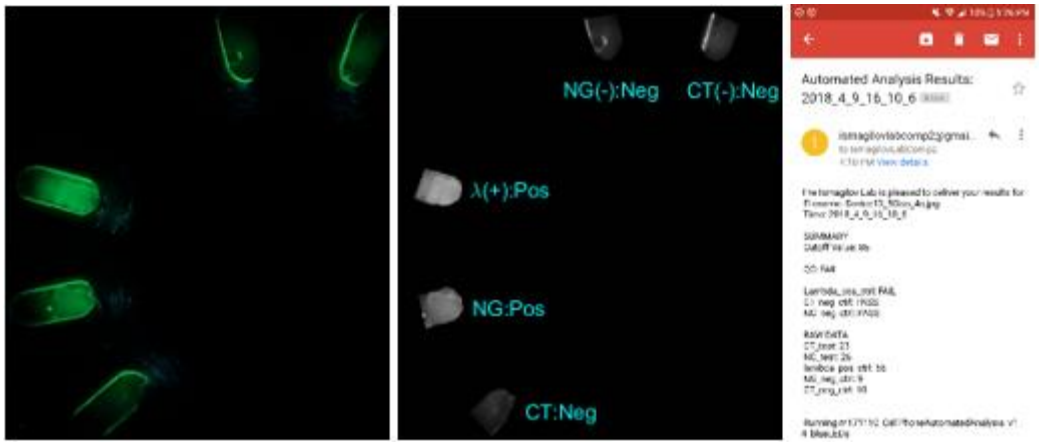


**Figure 8.5: Automated cell-phone image processing.**
(Left) un-processed cell-phone image, (middle) MATLAB processed image, and (right) automated email delivery of results.

**Automated base station**

AS (Andrey Shur) designed the basic circuit and Arduino code for rotation and heating

EJ further modified the circuit, Arduino code, integrated the base station with other components, and validated the device.

We have successfully built a prototype base station controlled with an $8.50 Arduino Mini Pro operating on 6 AA rechargeable battery pack which performs combined heating and rotations (**Figure 8.6A**). Power may alternatively be provided by an AC adapter which has greater voltage and amperage capabilities. Heating is performed with a proportional control algorithm, thermistor, and thin-film heater attached to an aluminum disk for even heat distribution. The heater reaches 68°C within 95s and is capable of maintaining temperature within a range of 1°C for at least 40 min. Rotation is controlled by the Arduino and a $5 Polulu DRV8880 Motor Driver connected to a bipolar-modified 28BYJ-48 stepper motor with a 3D-printed gear train (gear ratio of 11.3). Using a TRH605 Futek Torque Sensor, we measured base station output torque at 1.1 N-m and the torque required to turn the SlipColumn at 0.7 N-m. The base station rotation is responsible for controlling the position of the slip valve of the sample preparation module and for automated slipping of the amplification module (by rotating in the opposite direction). The motor draws little power, and its full sequence (6 rotations and slipping) can be run at least 40 times without recharging. The base station could instead be designed to operate using an AC power supply, which has fewer power restrictions.

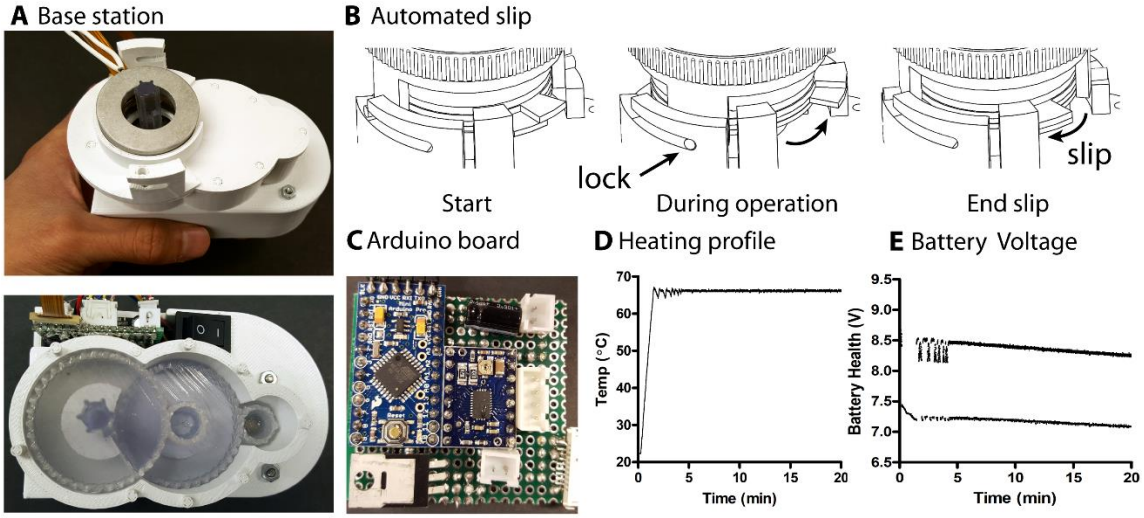


**Figure 8.6: Automated base station components.**

(A) Angled-view and top-down view of the gear rotation mechanism. (B) 3 panels showing automated slip step using rotation. (C) A photo of the Arduino board. (D) Heating profile measured by Arduino and a thermistor connected to the heater. (E) A measure of battery voltage over time. Under no-load, the voltage is high (8.5 V) and while heating the voltage drops (7.5). Voltage switching is rapid giving the appearance of two curves.

## Integrated device performance

We tested three sample-to-answer experiments using the NAAT kit and either *Chlamydia Trachomatis* (CT), *Neisseria Gonorrhoeae* (NG), or both pathogens spiked into normal human donated urine samples at 5000 CFU or IFU/mL. We found that the kit accurately detected the CT samples, but sometimes the kit failed to detect the NG samples (**Figure 8.7**). Follow-up experiments also confirmed this result. After analyzing the number of NA copies we would expect to find in the final LAMP reaction (stock concentration times input volume times extraction efficiency times reaction volume divided by elution volume), we calculated that there would be up to 340,000 NG RNA copies. For a lyophilized LAMP reaction, we

measured a limit-of-detection around 4000 copies. Therefore, our assay kit sometimes failed to detect NG even though we expect 85x more copies than the limit-of-detection.

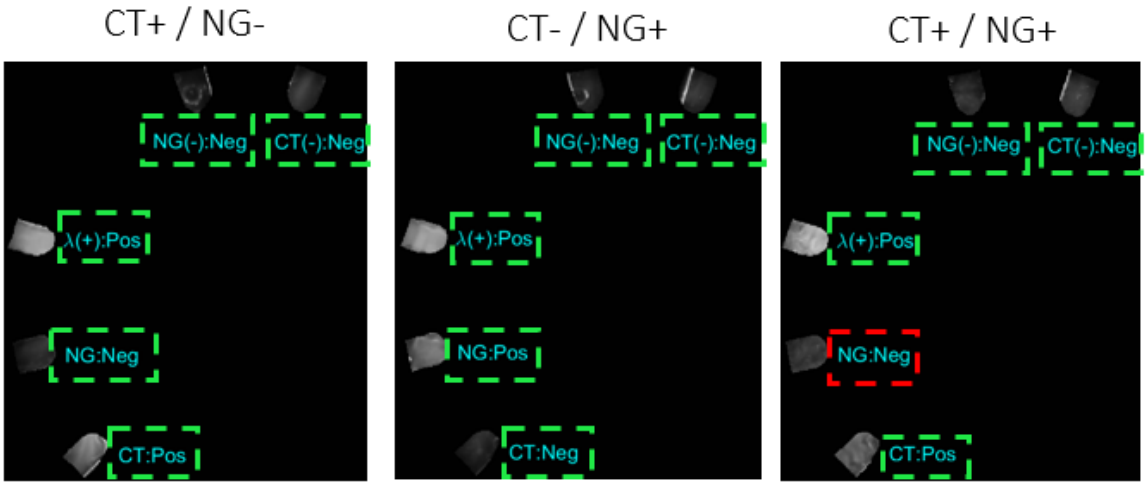


**Figure 8.7: Integrated NAAT kit performance**

(left) Accurate detection of CT at 5000 IFU/mL in a urine sample on the integrated NAAT kit platform. (middle) Accurate detection of NG at 5000 CFU/mL. (right) Accurate detection of CT at 5000 IFU/mL but inaccurate detection of NG at 5000 CFU/mL.

## Conclusions

In this chapter, we demonstrated a fully-integrated sample-to-answer device capable of processing 250 µL of urine sample. The NAAT kit is portable with a total weight of less than 1 kilogram and can be held in the palm of a hand. The NAAT kit is rapid with a total assay time of 26 min. Lastly, the NAAT is easy-to-use with 1 min of hands-on time at the start of the assay and 30s hands-on time at the end. With this NAAT kit, we have nearly met our requirements for fulfilling the desired ASSURED criteria.

However, we observed that our assay sensitivity was lacking. In some (but not all) cases, we were unable to detect *Neisseria Gonorrhoeae* at a concentration that we expected to be 85x higher than our limit-of-detection. We suspect this is due to the greater carry-over of

extraction buffers when using a pressure-based approach as compared to centrifugation.

In Chapter 2, I demonstrated how extraction buffer carry-over can be mitigated by the addition of the two-phase wash. The next step of this project is to more carefully examine extraction buffer carry-over using the sample preparation module by applying similar experimental techniques from Chapter 2 (carefully controlled experiments which will determine the extent of carry-over). I anticipate that once buffer carry-over is characterized and understood, it will be possible to further reduce buffer carry-over by adjusting pressures, modifying the two-phase wash conditions, and/or changing device geometry. I am hopeful that these changes could improve the sensitivity of the NAAT kit, thereby meeting all of the ASSURED criteria for a sample-to-answer POC molecular test.

**References**

1. D. Witters, E. Jue, N.G. Schoepp, S. Begolo, J. Rodriguez-Manzano, F. Shen, H. Maamar, A. Shur, and R.F. Ismagilov “Autonomous and portable device for rapid sample-to-answer molecular diagnostics at the point-of-care”. Poster presentation at MicroTAS 2017, Savannah, Georgia, Oct. 2017